Effect of systematic variation in Co:Ni ratio on elemental partitioning, lattice misfit and oxidation behaviour of γ'-strengthened $(Ni,Co)_{75}Al_5Ti_5Cr_{15}$ (at.%) alloys

SIONED CATHERINE HUXLEY LLEWELYN

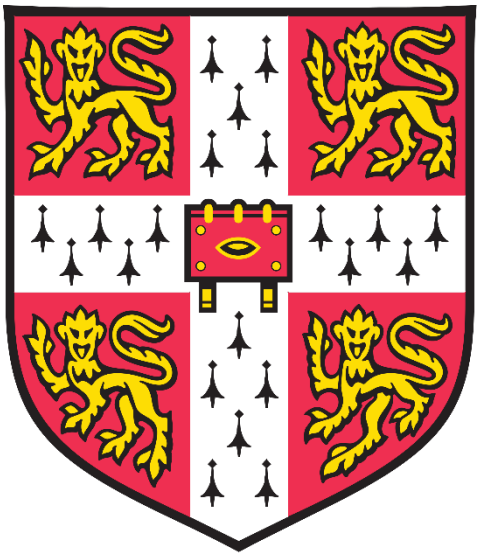

UNIVERSITY OF CAMBRIDGE

DEPARTMENT OF MATERIALS SCIENCE AND METALLURGY

ST. JOHN'S COLLEGE

THIS DISSERTATION IS SUBMITTED FOR THE DEGREE OF DOCTOR OF PHILOSOPHY

SEPTEMBER 2019

Preface

This dissertation is submitted for the degree of Doctor of Philosophy at the University of Cambridge. The research described herein was carried out at the Rolls-Royce University Technology Centre (UTC), Department of Materials Science and Metallurgy, University of Cambridge between October 2015 and September 2019. This dissertation is the result of my own work and includes nothing which is the outcome of work done in collaboration except as declared in the Preface and specified in the text. It is not substantially the same as any that I have submitted, or, is being concurrently submitted for a degree or diploma or other qualification at the University of Cambridge or any other University or similar institution except as declared in the Preface and specified in the text. I further state that no substantial part of my dissertation has already been submitted, or, is being concurrently submitted for any such degree, diploma or other qualification at the University of Cambridge or any other University or similar institution except as declared in the Preface and specified in the text. It does not exceed the prescribed word limit for the Degree Committee for the Faculty of Physics and Chemistry of 60,000 words.

The following journal paper was produced during the course of this research:

S.C.H. Llewelyn, K.A. Christofidou, V.J. Araullo-Peters, N.G. Jones, M.C. Hardy, E.A. Marquis, H.J. Stone, The Effect of Ni:Co Ratio on the Elemental Phase Partitioning in γ-γ′ Ni-Co-Al-Ti-Cr Alloys, *Acta Materialia*, vol. 131, pp. 296-304, 2017 (Chapter 2).

Acknowledgments

This work was supported by the Rolls-Royce Engineering and Physical Sciences Research Council (EPSRC) Strategic Partnership. I should like to express my sincere thanks to Dr Howard Stone and Dr Nicholas Jones of the University of Cambridge and to Dr Mark Hardy of Rolls-Royce plc. for this research opportunity.

I should like to thank the Marquis Research Group (Associate Professor Emmanuelle Marquis and Dr Vicente Araullo-Peters), Department of Materials Science and Engineering, University of Michigan for the collaborative use of atom probe tomography (APT), Dr Richard Chater for his kind assistance with secondary ion mass spectrometry (SIMS) at Imperial College, London and Professor David Dye, Ioannis Bantounas, Tom McAuliffe and Thomas Kwok at Imperial College, London for their assistance in hot rolling of the $(Ni,Co)_{75}Al_5Ti_5Cr_{15}$ (at.%) series of model superalloys.

In addition, I wish to thank Dr Helen Playford of the Rutherford Appleton Laboratory ISIS Neutron and Muon Source, for her assistance on the POLARIS diffractometer during the neutron diffraction experiment. Finally, I wish to thank Dr Lewis Owen, University of Cambridge for his invaluable contribution to the neutron diffraction experiment and data analysis.

Contents

Abstract

Ni-based superalloys currently in service as aero-engine turbine discs are operating at the limit of their high-temperature capability. Next-generation turbine disc superalloys must be capable of sustaining the higher operating temperatures (approaching 800°C) and stresses required for greater thermal efficiency, whilst maintaining mechanical integrity and excellent oxidation resistance. Studies on the emerging γ'-strengthened Co-based superalloys based on the Co-Al-W and Co-Al-Mo-Nb/Ta systems have been successful in mitigating the respective drawbacks of high mass density and low γ' solvus temperature by incorporation of Ni, Ti or Cr. However, detailed systematic investigation of the fundamental quinary system, Ni-Co-Al-Ti-Cr, is essential to provide a baseline against which to compare the influence of higher-order alloying with elements, such as W, that potentially confer superior high-temperature properties.

To this end, seven γ'-strengthened model superalloys of composition $(Ni,Co)_{75}Al_5Ti_5Cr_{15}$ (at.%) were fabricated, aged at 800°C for 1000 hours, and the effect of increasing Co:Ni ratio on their resultant microstructural characteristics and critical properties was determined. For alloys of Co content 0, 9, 19, 28, 38, 47 and 56 at.%, γ' solvus temperature decreased with increasing Co:Ni ratio, whilst alloy mass density remained fairly constant across the alloy series at ~8.1 $g.cm^{-3}$. Atom probe tomography (APT) was used to determine the elemental partitioning behaviour and γ' volume fraction for each of the seven alloys, denoted 0Co, 9Co, 19Co, 28Co, 38Co, 47Co and 56Co. From APT, a non-monotonic trend in Ti, Al and Cr partitioning was observed as Co:Ni ratio increased, with a transition at ~19 at.% Co. From neutron diffraction analysis, the γ-γ' lattice misfits of alloys 0-47Co were found to be positive at all test temperatures (ambient, 400, 600, 700 and 800°C) and the magnitude of lattice misfit increased as Co content increased from 0-38 at.%. Lattice misfit values decreased with increasing temperature, the lowest values being obtained for 800°C.

Crucially, this study also investigated the effect of a systematic increase in Co:Ni ratio on oxidation performance of γ-γ′ alloys of composition $(Ni,Co)_{75}Al_5Ti_5Cr_{15}$ (at.%). The seven model superalloys (0Co, 9Co, 19Co, 28Co, 38Co, 47Co and 56Co) underwent isothermal oxidation in air at 800°C using both thermogravimetric analysis (100 hours) and box-furnace exposure (1000 hours). X-ray diffraction was carried out to identify surface oxide phases present. Scanning electron microscopy (SEM)-energy dispersive X-ray spectroscopy (EDS) and secondary ion mass spectrometry were performed to map elemental distribution and to provide precise chemical analysis of any thin surface oxide layers present. Following 1000

hours oxidation at 800°C, the 28Co, 38Co and 47Co alloys were observed to exhibit a flat, compact, well-defined external scale and Cr_2O_3 layer with minimal oxygen ingress, together with a distinct Al_2O_3 sub-scale.

This work represents the first detailed systematic study on the fundamental quinary Ni-Co-Al-Ti-Cr alloy system describing the effect of variation in Co:Ni ratio on the evolution of surface oxides and on the partitioning of elements to γ and γ' phases and associated lattice misfit.

The influence of 3 at.% W addition to the base alloy Ni-Co-5Al-5Ti-15Cr (at.%) system was investigated by examining the effect of increasing Co:Ni ratio on microstructure, phase transition temperatures (γ' solvus, solidus and liquidus), mass density and Vickers microhardness. 3 at.% W was substituted for 1.5 at.% Ni and 1.5 at.% Co to achieve a series of six alloys of composition $(Ni,Co)_{72}Al_5Ti_5Cr_{15}W_3$ (at.%), denoted 0Co-3W, 17Co-3W, 27Co-3W, 36Co-3W, 45Co-3W and 55Co-3W. These alloys were homogenised (1250°C) and subsequently aged for 1000 hours at 800°C. With 3 at.% W incorporation, γ' solvus temperature decreased with increasing Co:Ni ratio following the same trend as seen for the W-free alloys, although values were consistently higher in the W-containing alloys. Of the W-free alloys, the 19Co alloy exhibited an optimal combination of high γ' solvus temperature (1113°C) and maximal Vickers microhardness (~425 HV). Of the W-containing alloys, the 27Co-3W alloy exhibited a γ' solvus temperature of 1122°C (Vickers microhardness ~436 HV), although the 17Co-3W alloy exhibited a higher γ' solvus temperature of 1143°C (Vickers microhardness 424 HV). 3 at.% W addition to the quinary Ni-Co-5Al-5Ti-15Cr (at.%) alloy series led to an increase in alloy mass density from ~8.1 $g.cm^{-3}$ to ~8.5 $g.cm^{-3}$. Incorporation of 3 at.% W into the base alloy Ni-Co-5Al-5Ti-15Cr (at.%) thus permits a novel systematic comparison between the fundamental properties of the senary and W-free quinary alloy systems with respect to the influence of increasing Co:Ni ratio.

1. Introduction: The Role of Alloying Elements in Polycrystalline Superalloy Design for Aero-engine Turbine Discs

Ni-based superalloys have been extensively employed in the hot section of gas turbines as they offer an excellent balance of high-temperature strength, creep resistance and fatigue performance as well as resistance to high-temperature oxidation and corrosion. Much of the literature concerning Ni-based superalloys relates to their use as single-crystal turbine blades, which are protected by a thermal barrier coating and further insulated from the hot gas stream by film cooling, in which cool air is bled from the compressor and ducted through small holes in the blade wall, allowing the blades to operate in a gas stream at temperatures above their melting point. In contrast, polycrystalline Ni-based superalloys for aero-engine turbine disc applications are typically uncoated and are required to sustain rim temperatures of ~700-800°C, requiring a diffusion-resistant, continuous oxide scale to protect the underlying alloy from further oxidative degradation. Thus, turbine discs must be engineered to possess adequate creep resistance at the rim as well as a combination of excellent high-temperature strength, dwell fatigue crack growth resistance, oxidation resistance and toughness.

The excellent high-temperature strength exhibited by Ni-based superalloys currently deployed as aero-engine turbine discs derives principally from the $L1_2$ precipitates (γ') based on Ni_3Al, coherently embedded in an FCC Ni-rich solid solution matrix (γ). Since the 1940s, progressive improvements in aero-engine thermal efficiency have been achieved by increasing the turbine entry temperature [1], requiring progressive improvements in the temperature capability of superalloys used for both turbine blades and discs. However, more recently, the incremental improvements in the temperature capability of conventional Ni-based superalloys achieved by judicious alloying and advances in processing are tending towards a plateau. The next challenge, therefore, is to develop an alloy system for turbine discs that retains mechanical integrity and oxidation resistance in a high-stress environment at temperatures approaching 800°C, without the physical application of a protective coating. It is therefore fortuitous that Lee, 1971 [2] carried out extensive studies on the formation of a strengthening $L1_2$-γ' phase in Co alloys and reported an apparent ordered superlattice phase in the Co-Al-W system, analogous to the $L1_2$ $Ni_3(Al,Ti)$ precipitate phase in conventional Ni-based superalloys. Over the last decade, research has intensified on $L1_2$ γ'-strengthened Co-based superalloys and recently, more studies have accrued to suggest that beneficial high-temperature properties may be derived from alloys intermediate between Ni-based and Co-based compositions.

1.1 Polycrystalline γ'-strengthened Nickel-based Superalloys

Polycrystalline Ni-based superalloys currently in service as high-pressure turbine discs typically comprise a Ni-rich solid solution (γ phase) of face-centred cubic (A1 in Strukturbericht notation) crystal structure [3] strengthened by precipitates of an ordered intermetallic Ni_3Al (γ' phase), of primitive cubic $L1_2$ superlattice structure [4, 5] (Figure 1.1). Between 8 and 12 additional elements are typically incorporated into the superalloy to optimise the critical properties of high-temperature strength, creep resistance and oxidation resistance. Other important properties required for turbine disc alloys include low mass density, low cost and ease of processability.

Diagram showing A1 and $L1_2$ unit cells removed for copyright reasons. Copyright holder is R.C. Reed, Cambridge University Press.

Figure 1.1. Unit cells of the disordered FCC (A1) γ matrix phase (left) and ordered $L1_2$ γ' precipitate phase in which Ni and Al have specific site occupancies (right). Adapted from [1].

The A1 crystal structure of Ni not only favours high ductility of the γ phase [6] but also the low rate of elemental diffusion required for microstructural stability and creep resistance [1]. Furthermore, Ni is stable in the FCC form from ambient temperature up to its melting point, thus avoiding any potential phase transformation that might lead to expansion or contraction thereby complicating its use in high-temperature components [1]. Ni as a solvent provides good solid solubility for alloying elements such as Cr that can strengthen the γ phase through solid solution hardening [5, 7] (section 1.1.1 *v*). However, it is the $L1_2$ γ' precipitate phase (Figure 1.2) that confers the characteristic increase in proof stress with increasing temperature that has been so pivotal to the success of Ni-based superalloys as aero-engine turbine components (section 1.1.1 *i*). This geometrically close-packed (GCP) γ' phase [5, 8, 9] is inherently ductile [10, 11, 12] and precipitates coherently with the A1 γ-Ni matrix [5, 11], adopting a cube-cube orientation relationship with the parent γ [1]:

$$\{100\}_{\gamma} // \{100\}_{\gamma'} \qquad <010>_{\gamma} // <010>_{\gamma'}$$

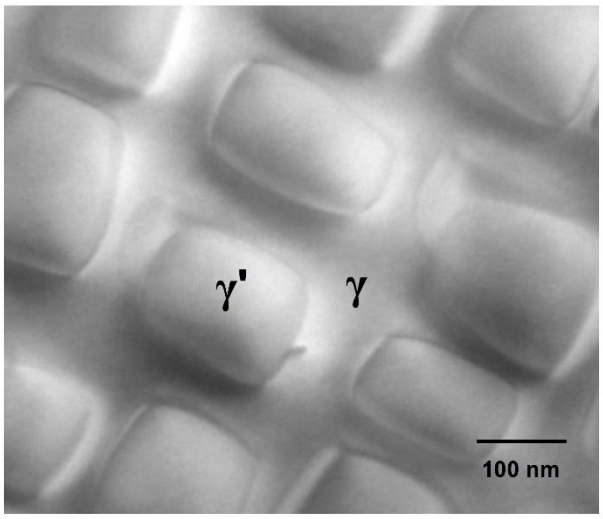

Figure 1.2. High angle annular dark field (HAADF) scanning transmission electron microscopy (STEM) image of a Ni-28Co-5Al-5Ti-15Cr (at.%) model superalloy aged at 800°C for 1000 hours, showing γ' precipitates embedded within a γ matrix. Image acquired using an FEI Tecnai Osiris transmission electron microscope.

The Ni-Al binary phase diagram (Figure 1.3) indicates that addition of >10 at.% Al to Ni stabilises formation of the $L1_2$ Ni_3Al (γ') phase at temperatures above ~300°C. This γ' phase, shown to remain fully ordered up to a temperature approaching its melting point [4, 5, 13, 14], precipitates from γ-Ni on cooling through the γ' solvus temperature. The γ' solvus temperature should be sufficiently above the superalloy operating temperature to retain a γ-γ' microstructure in service, but sufficiently below the alloy solidus temperature to provide an adequate heat treatment window, ΔT, in which A1 γ is established as the thermodynamically stable phase (Figure 1.4). This is essential for homogenisation heat treatment following solidification to eliminate residual micro-segregation [1, 5]. The γ'-Ni_3Al intermetallic exhibits considerable solubility for substitutional elements such as Ti and Nb [4], which significantly influence the γ' solvus temperature. In general, the equilibrium γ' mole fraction increases with decreasing temperature below the γ' solvus, as illustrated in Figure 1.4 for the model superalloy Ni-28Co-5Al-5Ti-15Cr (at.%).

Ni-Al binary phase diagram removed for copyright reasons. Copyright holder is ASM International.

Figure 1.3. Phase diagram of the Ni-Al binary alloy system, where the blue and white regions indicate single-phase and two-phase fields respectively [15].

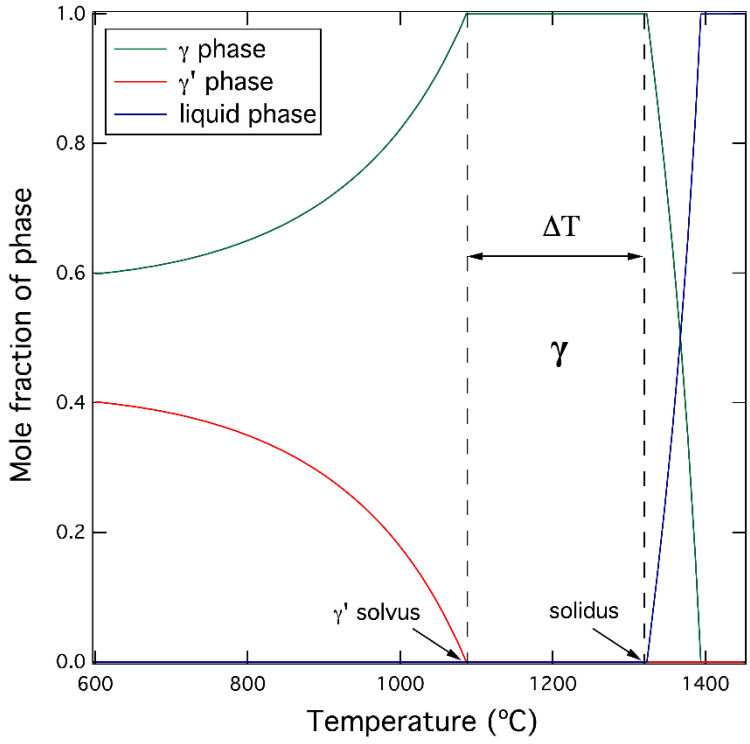

Figure 1.4. Graph showing equilibrium mole fraction of the A1-γ phase (green line), $L1_2$-γ' phase (red line) and liquid phase (blue line) as a function of temperature computed for the Ni-28Co-5Al-5Ti-15Cr (at.%) model superalloy using Thermo-Calc software with the TCNi8 database. The heat treatment window (ΔT) is indicated, in which γ is the established thermodynamically stable phase.

1.1.1 Optimising High-Temperature Strength and Creep Resistance

The γ-Ni phase possesses the A1 crystal structure in which operative slip systems are of the type $\frac{a}{2} < 110 > \{111\}$ where a is phase lattice parameter [1]. Thus, unit (perfect) dislocations in the γ phase (i.e. those not affecting the stacking sequence of the crystal) exhibit a Burgers vector (b) of the form $\frac{a}{2} < 110 >$ and glide on the crystallographic {111} planes [16].

(i) Order Strengthening Conferred by the γ′ Phase

A major strengthening mechanism in Ni-based superalloys is the order hardening conferred through precipitation of the $L1_2$ γ'-Ni_3Al intermetallic phase from the γ-Ni solid solution. Under moderate stress, a perfect $\frac{a}{2} < 110 > \{111\}$ dislocation in the γ phase can glide through the γ' superlattice to become a partial dislocation (superpartial), interrupting the atomic stacking sequence and forming an anti-phase boundary (APB) fault, thereby incurring a substantial energy penalty [1, 17]. The original ordered γ' stacking sequence is restored by glide of a trailing superpartial, which can enter the γ' precipitate at lower applied stress [18]. Superpartial dislocations thus travel in pairs separated by an APB and this assembly is referred to as a superdislocation [19].

For the $L1_2$ Ni_3Al γ' phase, increasing temperature up to ~780°C is reportedly associated with an increase in 0.2% flow stress [20] (Figure 1.5). Addition of Nb, Ti or Cr was observed to influence the magnitude of peak flow stress and the temperature at which peak flow stress occurred [20].

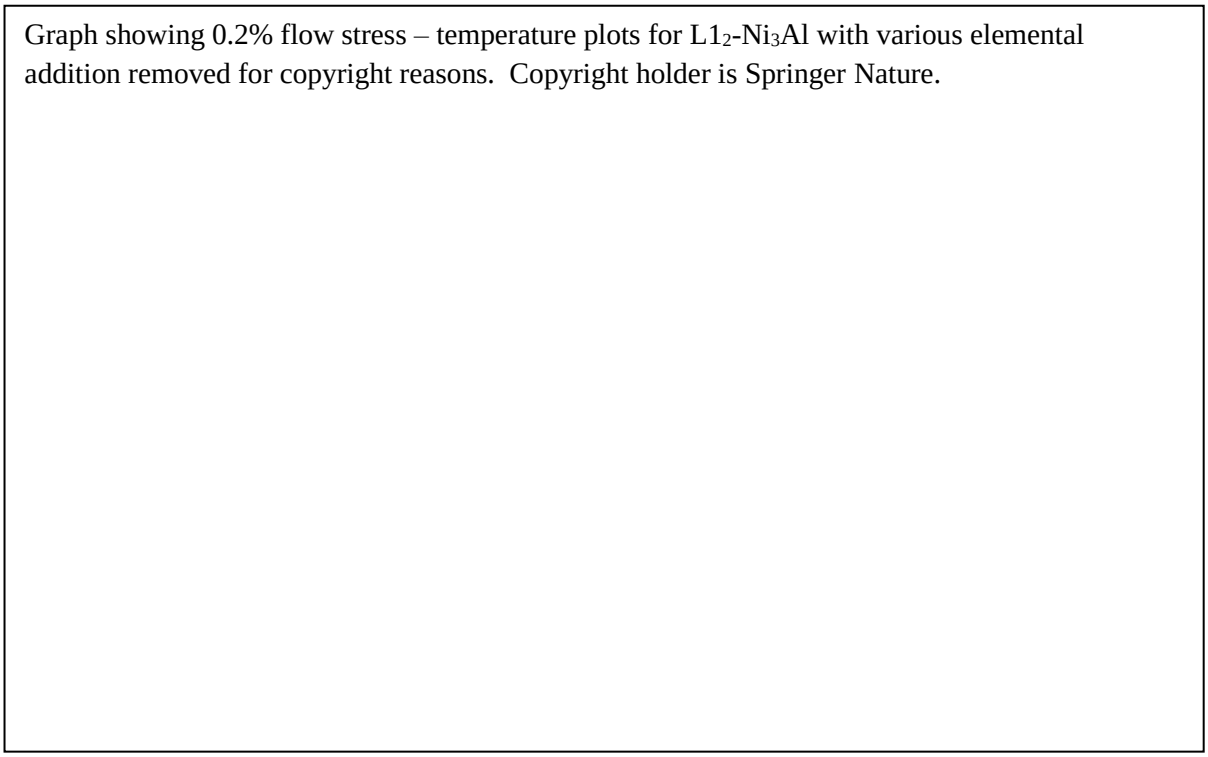

Figure 1.5. Temperature dependence of 0.2% flow stress for $L1_2$-Ni_3Al (γ') (black circles). The effect of elemental addition is shown by open symbols [20].

The mechanism by which 0.2% flow stress of Ni_3Al increases with increasing temperature up to ~780°C is generally considered to derive from thermally-activated cross-slip of a screw segment of a leading γ' superpartial from the glissile {111} slip planes to the sessile {100} planes, which are associated with lower APB energy [1, 21, 22, 23]. This configuration, the Kear-Wilsdorf lock [22, 24] (Figure 1.6), restricts dislocation glide on {111} planes as the cross-slipped screw segment cannot glide without formation of a trailing APB, rendering the assembly immobile [1, 25]. However, above a critical temperature (typically ~800°C) the flow stress of γ' decreases with further increases in temperature, an effect attributed to thermal activation of dislocation glide on {100} planes [1, 26].

a) Diagram showing Kear-Wilsdorf lock cross-slip mechanism removed for copyright reasons. Copyright holder is Elsevier.

b) Diagram showing detail of dissociated screw dislocation removed for copyright reasons. Copyright holder is Taylor and Francis.

Figure 1.6. (a) Kear-Wilsdorf lock cross-slip mechanism, as originally proposed by Kear and Wilsdorf, 1962 [24]. Each black circle represents a Shockley partial (adapted from [22]). (b) Zoom in of the dissociated screw dislocation in (a) showing an $L1_2$ Ni_3Al $a[110]$ superdislocation dissociated into two $\frac{a}{2}[110]$ superpartials separated by an APB. Each superpartial has dissociated into its component Shockley partials (black circles) separated by a complex stacking fault (adapted from [19]). Note that a is phase lattice parameter.

The lower APB energy of the {100} planes compared with the {111} planes is considered a major driving force for dislocation cross-slip from {111} to {100} [17, 27]. Therefore, in superalloy design, the aim is to raise the APB energy of the γ' phase on its {111} planes at the intended service temperature. One way of achieving this may be through increasing the Ta:Al concentration ratio of the γ' phase [28].

(ii) Influence of γ' Volume Fraction

In γ-γ' alloys based on the Ni-Cr-Al system, increasing volume fraction of γ' precipitates (0.5 μm diameter) increased 0.2% flow stress at high temperature (≥900°C) [4]. Alloys with large γ' volume fraction reportedly deformed by precipitate shear whereas alloys with low γ' volume fraction deformed by bowing of unpaired dislocations within the A1 matrix [4]. For Ni-based superalloys at temperatures in the range 705-980°C, an increase in γ' volume fraction reportedly increased creep resistance [6, 29] (Figure 1.7). Figure 1.7 indicates that, in driving the temperature capability of turbine disc alloys toward 800°C, it is desirable to increase γ' volume fraction to retain the same level of creep resistance. This may be accomplished by adding higher concentrations of γ'-formers, namely Al, Ti, Nb and Ta [12]. However, this should be weighed against potential deterioration in fatigue crack growth resistance, associated with high γ' volume fraction [30]. Most conventional disc alloys incorporate a γ' volume fraction in the range of 0.40-0.55 [1]. As turbine blades demand superior creep resistance, the single-crystal Ni-based superalloys used in blade applications require a greater γ' volume fraction (0.60-0.70) [31]. This permits reduction in width of the γ channels separating γ' precipitates, corresponding to an increase in Orowan stress and thus to enhanced creep resistance [1, 31].

Graph showing rupture stress as a function of γ' volume fraction removed for copyright reasons. Copyright holder is Springer Nature.

Figure 1.7. Rupture stress (σ) after 100 hours as a function of γ' volume fraction in superalloys at temperatures between 705 and 980°C [6].

(iii) Influence of γ′ Precipitate Size

The critical resolved shear stress (τ_{CRSS}) of a Ni-based superalloy is dependent on the mean size of coherent γ' precipitates relative to the distance between paired superpartial dislocations (Figure 1.8). Characteristic of the under-aged condition, the distance separating paired superpartials is large compared with γ' precipitate diameter, such that the trailing superpartial lags behind the first, allowing faulted γ' precipitates to reside between the two superpartials [1]. This is referred to as weak coupling of paired superpartials, for which the extent of hardening is proportional to the square root of precipitate radius, r [1, 32, 33]. Conversely, for the over-aged condition, the spacing between paired superpartials becomes comparable to the γ' precipitate diameter such that a single precipitate may contain a superpartial pair. This is referred to as strong coupling, for which the degree of hardening is inversely proportional to $\sqrt{r}$ [1, 32, 33]. Maximum τ_{CRSS} is achieved when precipitate size favours the mechanism of precipitate shear that lies at the transition between weakly-coupled and strongly-coupled superpartials [34, 35] (Figure 1.8). Therefore, particle size distribution (PSD) within a superalloy is pivotal in governing alloy strength and can be optimised through controlled heat treatment schedules [33, 36, 37]. A physics-based model for predicting yield stress of superalloys, accounting for unimodal and multimodal γ' PSD, has been proposed by Galindo-Nava *et al*. 2015 [38].

Diagram showing critical resolved shear stress as a function of precipitate size removed for copyright reasons. Copyright holder is Elsevier.

Figure 1.8. Schematic representation of critical resolved shear stress (τ_{CRSS}) as a function of γ' precipitate size [33]. The predominant mechanism by which shearing of the γ' precipitates occurs is indicated by the shaded region. For maximum τ_{CRSS}, precipitate size is such that the active shearing mechanism corresponds to the transition between weak and strong superpartial coupling modes.

It should be noted that, in polycrystalline disc superalloys, the intragranular γ' PSD has a significant influence on alloy resistance to dwell fatigue crack growth. For superalloy RR1000, slower dwell fatigue crack growth rates have been reported for a microstructure comprising coarser and/or fewer γ' precipitates [39].

(iv) Importance of Coherence of the γ-γ′ Interface

The degree of coherence of the γ-γ′ interface influences γ′ precipitate morphology [40], γ′ coarsening kinetics [4] and the resultant mechanical properties of the superalloy. At a given temperature, the lattice parameter (a) of the γ and γ' is related to lattice misfit (δ) by Equation 1.1 [1, 5, 41]:

$$\delta = 2\frac{[a_{\gamma'} - a_{\gamma}]}{[a_{\gamma'} + a_{\gamma}]} \qquad \text{Equation 1.1}$$

Provided that elemental partitioning between γ and γ' phases at service temperature results in comparable lattice parameters, then the magnitude of δ is small, the γ-γ' interface is coherent and the interfacial strain energy is low [1]. A large magnitude of lattice misfit generates coherency strain fields in the γ matrix that interact with the strain fields of edge dislocations [42, 43] and hinder their glide. This strengthening mechanism is important for turbine disc alloys designed to operate at lower temperatures i.e. $<0.6T_m$, where T_m denotes superalloy melting temperature [12]. At higher temperatures there is an increased driving force for Ostwald ripening (coarsening) of the γ' [44], which can facilitate dislocation bypass [45], adversely affecting creep resistance [11, 12, 46]. Therefore, to maintain stability of the precipitate array at higher in-service temperatures in Ni-based superalloys, turbine disc alloy design strives toward a near-zero γ-γ' lattice misfit at operating temperature. This may be achieved by controlling superalloy composition such that elemental partitioning between γ and γ' phases generates similar lattice parameters of the two phases [4].

To understand the influence of solute elements on phase lattice parameters it is useful to consider Vegard's relation:

$$a_{\gamma} = a_0^{\gamma} + \Sigma_i(\Gamma_i^{\gamma} x_i^{\gamma}) \qquad \text{Equation 1.2}$$

$$a_{\gamma'} = a_0^{\gamma'} + \Sigma_i(\Gamma_i^{\gamma'} x_i^{\gamma'}) \qquad \text{Equation 1.3}$$

where a_0^{γ} and $a_0^{\gamma'}$ are the lattice parameters of pure Ni and Ni_3Al respectively; Γ_i^{γ} and $\Gamma_i^{\gamma'}$ are the Vegard coefficients of element i in γ and γ' respectively; x_i^{γ} and $x_i^{\gamma'}$ are the concentrations

of i in γ and γ' respectively [1]. Equations 1.2 and 1.3 define the relationship between phase elemental content (x_i) and the efficacy of solute per at.% (Γ_i) in expanding the γ and γ' lattice parameters. Achieving a near-zero lattice misfit therefore requires consideration of preferential partitioning of elements and of the magnitude of elemental Vegard coefficients in γ and γ' [1] (Figure 1.9). Adjustments in alloy chemistry required to achieve a low lattice misfit at a given temperature inevitably have a concomitant effect on γ' APB energy, which must be taken into account in alloy design. Additionally, it should be noted that the degree of misfit of an alloy is influenced by its homogenisation and ageing heat treatments and subsequent cooling rates [47, 48, 49].

a) Diagram showing Vegard coefficients for the A1-Ni phase removed for copyright reasons. Copyright holder is R.C. Reed, Cambridge University Press.

b) Diagram showing Vegard coefficients for the $L1_2$-Ni_3Al phase removed for copyright reasons. Copyright holder is R.C. Reed, Cambridge University Press.

Figure 1.9. Vegard coefficient shown in relation to elemental position in the transition metal series: (a) disordered A1 Ni-rich solid solution (γ); (b) ordered $L1_2$ Ni_3Al (γ') phase. Figure from [1]; data from [50]. (Note that in Figure 1.9a values for Mo and W have been transposed.)

(v) Solid Solution Hardening of γ and γ' Phases

Due to the considerable solid solubility of austenitic superalloys for many alloying elements, extensive solid solution hardening of both γ' and γ phases can be achieved. Differences in atomic radius between solvent atoms and substitutional solute atoms distort the crystal lattice and generate elastic strain fields that interact with those of edge dislocations [51, 52, 53], hindering their migration such that yield stress increases. Within solid solubility limits, this strengthening effect appears to increase with increasing concentration of solute elements and with atomic size misfit and therefore Vegard coefficient [4, 7, 53] (Figure 1.9). An atomic size misfit exceeding ~15% reportedly limits solid solubility of substitutional elements [7, 54]. Hence, the most potent solid solution hardeners of γ and γ' phases are solute elements that exhibit moderate atomic size misfit with the solvent lattice. Solid solution hardening of the γ phase provides a baseline strength level as well as resistance to primary (transient) creep [1].

(vi) Lowering Stacking Fault Energy (SFE) Within the γ Phase

One mechanism by which creep resistance of a Ni-based superalloy can be increased is by hindering dislocation cross-slip (i.e. change of slip-plane) through reducing the stacking fault energy (SFE) of the γ phase. It is energetically favourable, by Frank's rule, for each unit dislocation in the γ phase to dissociate into two Shockley partial dislocations [1, 16]:

$$\frac{a}{2}<110>\rightarrow\frac{a}{6}<12\bar{1}>+\frac{a}{6}<211>$$

Passage of a single Shockley partial through the A1 γ phase disrupts the atomic stacking sequence of the close-packed {111} planes (originally ABCABCABC) to produce 4 adjacent planes of A3 hexagonal close-packing (ABCACABC) [16]. Passage of the second Shockley partial through the faulted crystal restores the stacking sequence back to that characteristic of A1 [16]. Equilibrium partial separation is achieved by balancing the force of elastic repulsion between paired partials with the energy of the planar defect created (SFE) [1, 55]. Therefore, it follows that lower SFE leads to more widely-spaced partials. Crucially, Shockley partials must locally recombine for cross-slip of screw segments of unit dislocations to occur around obstacles such as precipitates [1]. Partials that are more widely-spaced do not recombine as readily. Thus, lower SFE impedes dislocation cross-slip [56], thereby retarding creep strain accumulation [57].

The degree of faulting in the γ phase of Ni-based superalloys and their resultant creep resistance is highly dependent on alloy composition. For example, Co possesses a stable A3 allotrope and can thus decrease SFE of the γ-Ni phase [58], promoting planar dislocation slip rather than cross-slip [56] and consequently slower steady-state creep rates [59].

1.1.2 Effect of Composition on Elemental Phase Partitioning, Microstructure and Strength

The relative concentration of elements within a Ni-based superalloy determines the extent to which elements partition to the γ and γ' phases, thereby defining alloy microstructure and properties. Various alloying elements may be added to the Ni-Cr-Al-Ti quaternary system that is generally deployed for describing the γ-γ' phase equilibria of Ni-based superalloys [60, 61]. Common elemental additions include Co, Mo, W, Nb and Ta, with small concentrations of C, B and Zr often incorporated into polycrystalline superalloys [3, 4, 5]. Alloying elements may be categorised into three classes according to preferential partitioning (Figure 1.10). The first class includes elements such as Cr, Co and Mo that reportedly partition preferentially towards the γ phase. The second class comprises elements that stabilise the γ' phase, namely Al, Ti, Nb and Ta. The third class includes the elements that reportedly segregate to γ grain boundaries, such as C, B and Zr [1, 11, 12].

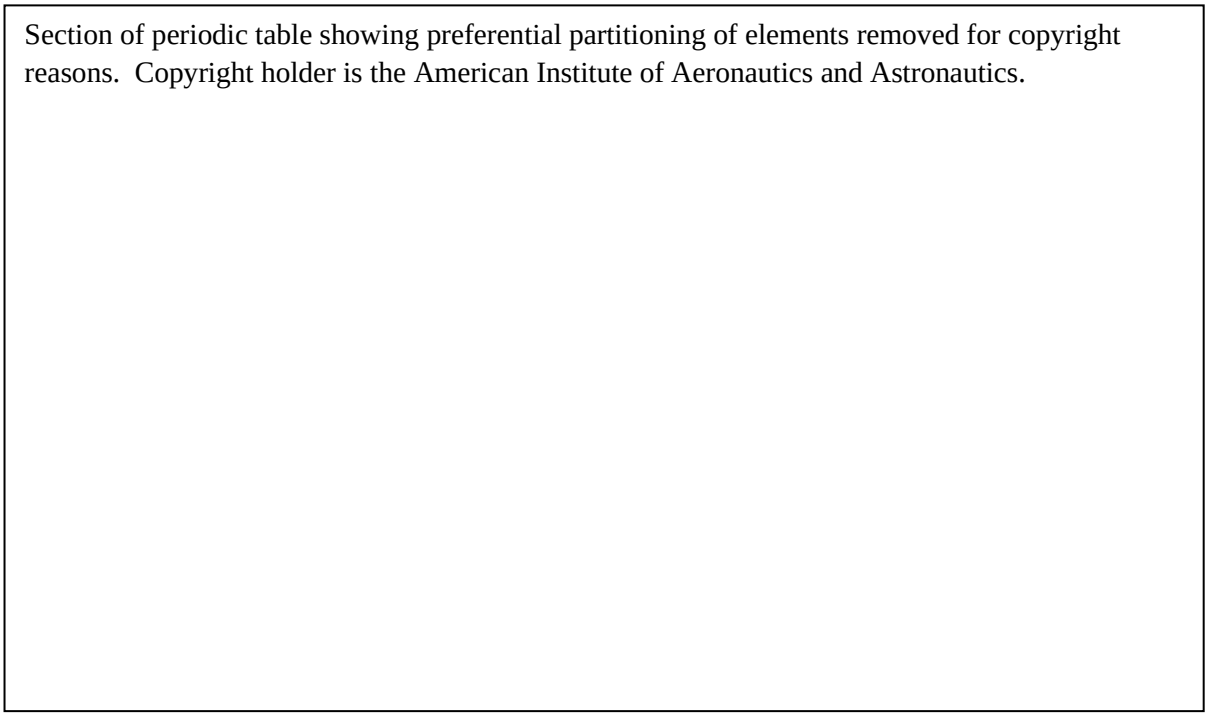

Figure 1.10. Preferential partitioning of alloying elements in Ni-based superalloys [41].

The extent to which alloying elements partition preferentially toward γ or γ' can be described quantitatively by the elemental partitioning coefficient (k_i), defined as the ratio of the concentration of element *i* in the γ' precipitate phase ($C_i^{\gamma'}$) to the concentration of the same element in the γ matrix phase (C_i^{γ}) according to Equation 1.4:

$$k_i = \frac{C_i^{\gamma'}}{C_i^{\gamma}} \qquad \text{Equation 1.4}$$

Elemental partitioning coefficients for selected elements in the polycrystalline disc superalloy RR1000 are displayed in Figure 1.11.

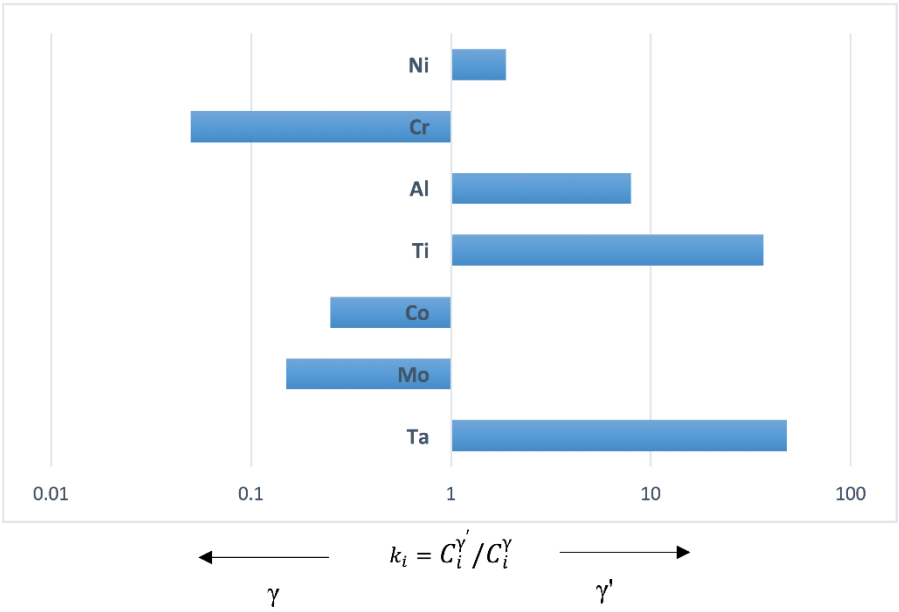

Figure 1.11. Elemental partitioning coefficients (k_i) for superalloy RR1000, calculated from Equation 1.4 using secondary γ' (~250 nm in size) and matrix phase compositions determined by atom probe tomography [62]. Ti, Ta and Al (and to a lesser extent Ni) partitioned preferentially to the γ' phase (k_i > 1) whilst Cr, Mo and Co partitioned preferentially to the γ phase (k_i < 1). Note logarithmic scale.

(i) Chromium (Cr)

Cr is a crucial addition in polycrystalline Ni-based superalloys as it imparts high-temperature oxidation resistance and hot-corrosion resistance via formation of a near-stoichiometric, diffusion-resistant chromia (Cr_2O_3) scale [5, 12]. In conventional Ni-based disc superalloys, Cr partitions preferentially to the γ phase (k_i < 1) [4] and, critically, the alloy must contain a sufficient level of Cr to form and maintain a *continuous* layer of protective oxide [63, 64, 65]. Because of the relatively high Cr content of Ni-based superalloys (~15 wt.% Cr in RR1000, [30]) and the considerable solubility of Cr in Ni, the contribution of Cr to solid solution hardening of the γ phase can be significant [7]. In addition, Cr can improve fatigue

crack growth resistance at elevated temperature, an effect putatively attributed to formation of (Cr-rich) $M_{23}C_6$ and M_6C (M = metal) at γ grain boundaries promoting transgranular crack growth [30, 66].

With respect to the γ' phase, Cr may substitute on either the Ni sub-lattice or the Al sub-lattice [5, 11, 12, 67]. Gorbatov *et al*., 2016 [68] have described a non-monotonic relationship between Cr concentration and γ' APB energy: using *ab initio* calculations, γ'-Ni_3Al APB energy increased with Cr content of up to 5 at.% but decreased with Cr content above 5 at.%.

Unfortunately, formation of the $M_{23}C_6$ carbide phase can deplete the γ phase of Cr [11, 69], potentially compromising environmental resistance and decreasing solid solution hardening of the γ phase. Furthermore, the $M_{23}C_6$ carbide exhibits a crystal structure analogous to that of the embrittling topologically close-packed (TCP) σ phase (section 1.1.3), the high coherency between the two phases favouring σ nucleation at $M_{23}C_6$ particles [5, 8, 11, 69]. Compositional design of superalloys therefore demands an optimal Cr concentration such that growth of a continuous Cr_2O_3 scale is permitted whilst precipitation of undesirable phases is avoided.

(ii) Aluminium (Al)

The element Al is incorporated into turbine disc (and blade) alloys primarily to impart high proof stress and creep resistance through its efficacy as a γ'-former. For example, for the turbine disc superalloy RR1000, $k_{Al} \approx 8$ (Figure 1.11). Increasing Al content increases γ' solvus temperature (Figure 1.3), which can narrow the homogenisation heat treatment window ΔT [70] (Figure 1.4).

Al can enhance oxidation resistance of turbine disc alloys by promoting formation of a stable Cr_2O_3-rich scale [71, 72]. This chromia scale can produce sufficient reduction in oxygen partial pressure at the scale-alloy interface to cause preferential oxidation of Al within the alloy [63, 71], consistent with the thermodynamics of the Ellingham diagram [73]. Formation of internal Al_2O_3 intrusions is undesirable as partitioning of Al from the γ' phase to form these oxides can deplete the alloy of its strengthening precipitate phase [74] (Figure 1.12). Furthermore, in terms of fatigue crack growth resistance, the intergranular Al_2O_3 intrusions, which often have an acicular morphology, can act as preferential crack initiation sites [75, 76].

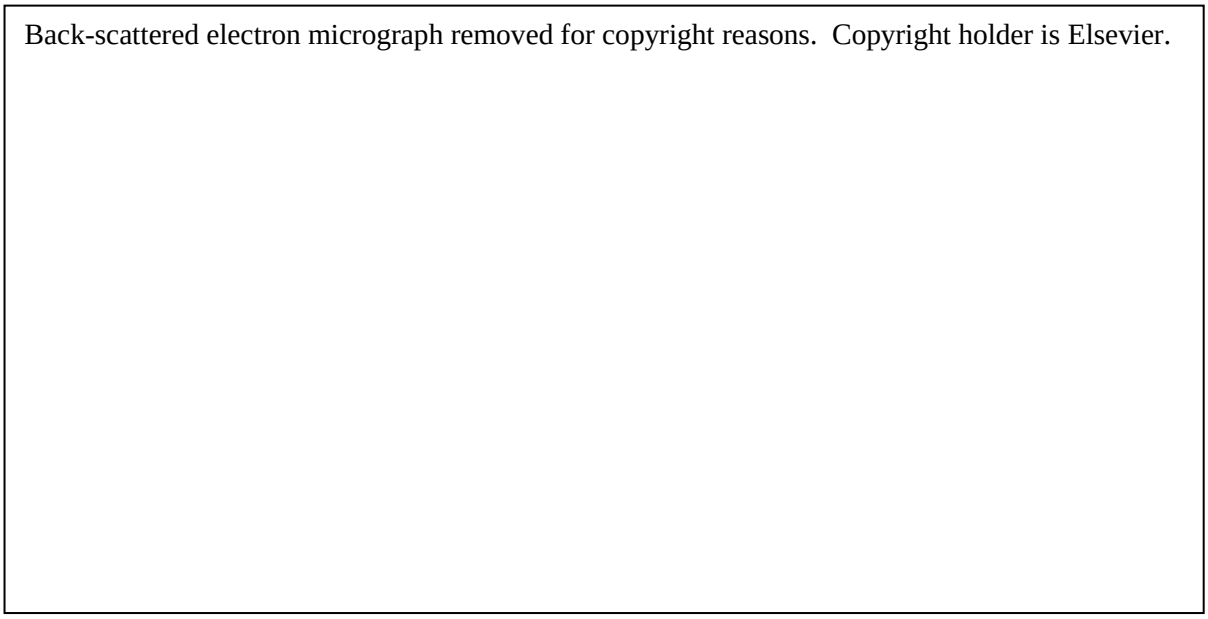

Figure 1.12. Back-scattered electron image of the sub-surface of superalloy RR1000 oxidised at 800°C for 2000 hours [77]. Beneath the external chromia-rich scale (indicated as oxide) are internal alumina precipitates residing within a γ'-denuded zone.

(iii) Titanium (Ti)

Ti partitions strongly toward the γ' phase in Ni-based superalloys [4, 78, 79], raising γ' solvus temperature [80] and γ' volume fraction in the superalloy. Figure 1.11 indicates a value of $k_{Ti} \approx 37$ for the superalloy RR1000. Ti occupies the Al sub-lattice of γ'-Ni_3Al [1, 12, 67, 81] and reportedly increases the APB energy on the (111) planes to a greater extent than on the (001) planes [28]. Using computational modelling of supercell shearing, substitution of one Ti atom for one Al atom in the shearing plane of Ni_3Al elicited values for the resultant increase in APB energy of 81.87 $mJ.m^{-2}$ for the (111) plane compared with 44.26 $mJ.m^{-2}$ for the (001) plane [28]. This differential APB energy promotes dislocation cross-slip in the γ' phase, which would be expected to increase flow stress within the anomalous temperature range (that for which flow stress increases with increasing temperature) [28].

Ti expands the γ' lattice parameter [4, 82] (Figure 1.9b), promoting solid solution hardening of the γ' phase [51, 67] without the prohibitive weight penalty incurred by addition of certain refractory metal elements. However, a high Ti:Al concentration ratio reportedly increases propensity for precipitation of the GCP η (Ni_3Ti) phase (Figure 1.13), which possesses the ordered $D0_{24}$ crystal structure [9] and is generally considered detrimental to the mechanical integrity of the alloy [83]. In addition, Ti substitution on the γ′ Al sub-lattice can reduce γ′ solubility for Mo and Cr, thereby increasing partitioning of these elements to the γ matrix and thus facilitating precipitation of deleterious TCP phases in the γ phase [80].

Diagram showing isothermal section of Ni-Al-Ti phase diagram for 800°C removed for copyright reasons. Copyright holder is ASM International.

Figure 1.13. Isothermal section of the Ni-Al-Ti ternary system for 800°C, showing single-phase fields (blue), two-phase fields (white) and three-phase fields (yellow) [84].

With respect to oxidation resistance of Ni-based disc superalloys, Ti can have a detrimental effect by compromising the inherently slow-growing (protective) nature of chromia [85]. Rutile (TiO_2) formation can occur at the external surface of the Cr_2O_3 scale [63, 77] and within the superalloy [63], potentially contributing to the formation of a γ'-denuded zone in the alloy sub-surface [74], thus impacting alloy strength.

(iv) Cobalt (Co)

Increasing Co content within Ni-based superalloy systems reportedly improves creep resistance by inhibiting dislocation cross-slip through reducing stacking fault energy of the γ phase [59, 86]. Tian *et al*., 2014 [59] reported that systematic substitution of Co (up to 22 at.%) for Ni in a Ni-based superalloy reduced γ phase SFE and led to increased creep life. This parallels the study by Yuan *et al*., 2011 [86], who described an initial decrease in γ phase SFE with increasing alloy Co content from 14.2 to 24.0 at.%, corresponding to an increased γ phase Co concentration from 19.8 to 34.0 at.% (calculated using a Thermal-cal program with a Ni-RUMN database). A subsequent increase in SFE was reported as γ phase Co concentration increased further to 34.7 at.% [86].

Co is known to partition preferentially to the γ phase of Ni-based superalloys ($k_{Co} < 1$, Figure 1.11), markedly influencing partitioning of other elements between the γ and γ' phases [79, 87, 88, 89]. Co addition (up to ~15-20 wt.%) has been shown to increase the γ' volume fraction in conventional Ni-based superalloys [81, 90, 91], an effect attributed to the role of Co in lowering solubility of Ti and Al within the γ phase [81, 89, 92].

(v) Refractory Metals: Molybdenum (Mo) and Tungsten (W)

Both Mo and W exhibit a relatively large Vegard coefficient in the γ-Ni phase [82] (Figure 1.9a) and are thus considered effective γ solid solution hardeners [52, 53]. For Ni-based superalloys at operating temperatures above $0.6T_m$, γ strengthening reportedly becomes diffusion-dependent [11, 12]. Rehman, 2016 [53] noted that, for a strain rate of 10^{-5} s^{-1}, the deformation mechanism at intermediate temperature (~800°C) is governed by lattice distortion whereas at high temperature (~1200°C) the deformation mechanism no longer depends on solute size and diffusion-controlled processes predominate. Thus, the slowly diffusing elements Mo and W [93, 94] are anticipated to be potent solid solution hardeners of the γ phase at elevated temperature [11, 12, 53]. Furthermore, Mo and W addition has been shown to reduce the diffusivity of Ti and Cr at 900°C [11, 12], which may contribute to the reduction in γ' coarsening rates observed [5]. Both Mo and W are reportedly more potent than Co in reducing SFE of γ-Ni [58, 95].

Dreshfield and Wallace, 1974 [78] studied the elemental partitioning in the γ-γ' region of the Ni-Al-Cr-Ti-W-Mo system at 850°C. For the γ phase, increasing the W content from 0 to 1 at. % increased Al solubility in γ whereas further increases in W content reduced γ Al solubility. For the γ phase, in which Cr concentration ranged from 6.6-30.7 at.%, increasing Mo content increased slightly the Al solubility in γ at high Cr content but decreased Al solubility in this phase at lower Cr content [78]. Loomis *et al*., 1972 [80] reported that Mo addition to the Ni-Cr-Al system raised γ' volume fraction and solvus temperature, although these effects were less pronounced in Ti-containing alloys.

Unfortunately, a high Mo and W content of superalloys promotes precipitation of M_6C and $M_{23}C_6$ carbides such as $(Ni,Co)_3Mo_3C$ and $Cr_{21}(Mo,W)_2C_6$ [5, 11], which can act as nucleation sites for embrittling TCP μ and σ phases respectively [8] (section 1.1.3).

(vi) Refractory Metals: Niobium (Nb) and Tantalum (Ta)

Nb and Ta are reportedly more potent than Mo and W in expanding the lattice parameter of the disordered A1 Ni-rich solid solution (γ) [82] (Figure 1.9a) and are therefore considered effective solid solution hardeners of the γ phase [96]. However, Nb and Ta are known to partition strongly to the γ' phase ($k_i > 1$) of Ni-based superalloys [5], and so their contribution to solid solution hardening of the γ phase inevitably diminishes on γ' precipitation. Nb and Ta reportedly substitute onto the Al sub-lattice of the γ'-Ni_3Al [11, 67] and increase the volume fraction and solvus temperature of the γ' phase [5]. Nb or Ta can reportedly elevate APB energy on the {111} planes of $L1_2$ $Ni_3Al_{1-x}R_x$ (where R=Nb or Ta) with peak APB energy of ~600 $mJ.m^{-2}$ calculated for $x \approx 0.2$ [97]. This value of APB energy is approximately twice that for Ni_3Al [97]. Furthermore, the high Vegard coefficients of Nb and Ta in the γ' phase [82] (Figure 1.9b) permit substantial solid solution hardening therein [51, 67]. In addition, Nb and Ta are MC carbide-formers [7, 11, 98] and may suppress transformation to secondary $M_{23}C_6$/M_6C carbides [5, 11].

The use of Nb is preferred over that of Ta due to the lower density and lower cost of Nb [5]. Mignanelli *et al*., 2014 [99] reported that increasing Nb:Al concentration ratio in γ-γ' Ni-Cr-Al-Nb alloys was associated with decreased γ' volume fraction and precipitate size, together with a decrease in lattice misfit of the alloy, which overall appeared to result in increased alloy strength. Thornton *et al*., 1970 [20] reported that addition of 6 at.% Nb to γ′-Ni_3Al at the expense of Al increased 0.2% flow stress of by a factor of ~2 at temperatures between 600 and 800°C (Figure 1.5). However, a high Nb:(Al+Ti) concentration ratio in Ni-based superalloys has been shown to promote transformation of γ'-Ni_3(Al,Ti) to γ''-Ni_3Nb [12, 100], which has the ordered $D0_{22}$ crystal structure [9] capable of strengthening superalloys operating at temperatures of up to ~650°C [101]. Above ~650°C, γ'' can transform to δ-Ni_3Nb, which exhibits the orthorhombic $D0_a$ crystal structure [96] and is generally considered deleterious to alloy strength [1].

1.1.3 Topologically Close-Packed (TCP) Phases

Mo, W and Cr are known to promote precipitation of M_6C and $M_{23}C_6$ carbides in Ni-based superalloys, which can act as preferential nucleation sites for μ and σ TCP phases respectively [8] as the carbide crystal structures resemble those of these TCP phases [11]. These undesirable compounds exhibit complex crystal structures with large unit cells characterised by exclusively tetrahedral interstices and thus exhibit a high and uniform atomic packing density [102] (Table 1.1).

Table 1.1. TCP phases commonly observed in Ni-based superalloys. Data from [1, 102, 103].

Phase	***Examples***	***Lattice type***	***Atoms /unit cell***	***Space group (No.)***	***Lattice parameters (nm)***
σ	$Cr_{61}Co_{39}$	Tetragonal	30	*$P4_2/mnm$ (136)*	*a* = *b* = 0.912 *c* = 0.472
μ	Mo_6Co_7, W_6Co_7	Rhombohedral	13	*R-3m (166)*	*a* = *b* = 0.473 *c* = 2.554
P	$Cr_{18}Mo_{42}Ni_{40}$	Orthorhombic	56	*Pa (62)*	*a* = 1.690 *b* = 0.471 *c* = 0.904
R	$Cr_{18}Mo_{31}Co_{51}$	Rhombohedral	53	*R-3 (148)*	*a* = *b* =1.093 *c* = 1.934

Four coordination environments are permitted, specifically the four Kasper polyhedra with coordination numbers of 12, 14, 15, 16 [102, 104] (Figure 1.14). TCP phases often form basket-weave sheets aligned with {111} planes of the γ-Ni matrix [11, 41, 105] (Figure 1.15).

TCP phases tend to lack multiple slip systems and are therefore inherently hard, increasing susceptibility of the superalloy to embrittlement [8, 11, 106]. In addition, the depletion of refractory metals and Cr within the γ matrix accompanying TCP phase precipitation purportedly reduces the degree of solid solution hardening of the γ phase [8, 11, 69]. Removal of Cr, Mo and/or W from the γ phase during TCP phase formation plausibly modifies lattice misfit [8], which in turn influences γ' coarsening rates.

Diagram showing Kasper polyhedra removed for copyright reasons. Copyright holder is International Union of Crystallography.

Figure 1.14. The four Kasper polyhedra with coordination numbers of (a) 12, (b) 14, (c) 15, (d) 16. In (a) and (b), the two spheres below and above the central sphere (along the five-fold and six-fold axes respectively) are not displayed. In (d), the sphere below the central sphere is not displayed [104].

Secondary electron micrograph removed for copyright reasons. Copyright holder is Elsevier.

Figure 1.15. Secondary electron image of the experimental Ni-based blade alloy RR2073 (containing 3 wt.% Re) annealed at 950°C for 1000 hours, showing basket-weave sheets of the TCP σ phase from which P phase has formed [103].

1.1.4 Oxidation Characteristics of Conventional Nickel-based Superalloys

As mentioned in section 1.1.2 *i*, Cr is critical addition in polycrystalline Ni-based superalloys conferring high-temperature oxidation resistance and hot-corrosion resistance via formation of a near-stoichiometric, diffusion-resistant Cr_2O_3 scale [5, 12]. Pure chromia growth is dominated by the outward diffusion of Cr^{3+} cations through the scale to react with oxygen at the oxide-gas interface [107]:

$$2Cr^{3+} + 6e^{-} + \frac{3}{2}O_{2(g)} \rightarrow Cr_2O_{3(S)}$$

As cationic diffusion through Cr_2O_3 is slow, oxide growth rates are consequently slow [107] such that the underlying substrate is protected against further environmental degradation, providing that the oxide scale remains intact. This Cr_2O_3 scale protects the underlying alloy when exposed to temperatures up to 1000°C [63, 72, 108].

A study on established commercial Cr_2O_3-forming Ni-based superalloys, namely Waspaloy, Astroloy and Udimet 720 [63], reported that following isothermal oxidation at 750-1000°C, Ti can form TiO_2 at the external oxide surface in addition to forming TiO_2 and TiN within the alloy interior. These authors also reported Al_2O_3 formation as discrete oxides beneath the Cr_2O_3 scale, although isothermal oxidation of Astroloy at 1000°C reportedly elicited a semi-continuous layer of internal Al_2O_3, plausibly due to its higher Al content. At these temperatures, aluminium oxidises at lower partial pressures of oxygen than Cr in accordance with the thermodynamics of the Ellingham diagram [73], facilitating Al_2O_3 formation beneath the chromia scale. Formation of internal Al_2O_3 and TiO_2 intrusions is undesirable as partitioning of Al or Ti towards such oxide species potentially depletes the alloy of its strengthening γ' precipitate phase resulting in a γ'-depleted zone in the near-surface region [74]. Furthermore, internal oxide intrusions may potentially act as crack initiation sites.

1.2 Cobalt-based Superalloys Strengthened by an $L1_2$ Superlattice Phase

The excellent high-temperature strength exhibited by Ni-based superalloys currently deployed as aero-engine turbine discs derives predominantly from the $L1_2$ precipitates (γ') based on Ni_3Al, coherently embedded in an FCC (A1) Ni-rich solid solution matrix (γ). This γ-γ' (Ni-Ni_3Al) two-phase microstructure is responsible for the superior high-temperature strength of Ni-based superalloys over traditional carbide-hardened Co alloys and arises from the temperature-dependent order hardening conferred by the $L1_2$-Ni_3Al intermetallic γ' phase.

In contrast, Co alloys have traditionally derived their strength mainly from solid solution strengthening and from precipitation of carbide phases within the austenitic matrix [109, 110, 111]. Therefore, solid solution strengthened Co alloys have conventionally been deployed as aero-engine components operating at high temperature but relatively low stresses such as nozzle guide vanes [112, 113] and combustion chambers [110].

To improve aero-engine thermal efficiency, next-generation superalloys for turbine disc applications must be capable of sustaining operating temperatures approaching 800°C and of maintaining mechanical integrity in the resultant highly oxidising environment experienced by superalloy components in service. Nickel exhibits the FCC crystal structure and is therefore both ductile and tough. FCC metals, such as Ni, possess low diffusion rates, such that significant microstructural stability is conferred at elevated temperature. Other metals in the transition metal series that exhibit FCC crystal structure include certain of the platinum group metals, which are dense and very expensive. Of the hexagonally close-packed metals, only Co is of acceptable mass density and cost [1]. Although no stable $L1_2$ Co_3Al phase reportedly exists in the Co-Al binary system [114], Co-based superalloys comprising an FCC solid solution γ-Co phase strengthened by a γ' phase of $L1_2$-$Co_3(Al,W)$ have been intensively investigated in recent years. It was Lee, 1971 [2] who first reported the role of W in the formation of ordered $L1_2$ precipitates in the Co-Al-W system. These reportedly cuboidal precipitates distribute throughout the A1 γ-Co matrix in a manner analogous to that of the distribution of stable $L1_2$ $Ni_3(Al,Ti)$ in the A1 γ-Ni matrix.

Other $L1_2$ intermetallic compounds such as Co_3Ta or Co_3Ti had been considered as a strengthening precipitate phase in the Co-Ta or Co-Ti system respectively. However, the ordered Co_3Ta compound was reported as metastable at high temperature [115]. Although there was a drive in the 1970s to develop alloys based on the Co-Co_3Ti equilibrium [116, 117], discontinuous precipitation could be observed at 800°C [116, 117], which can adversely influence creep resistance [118]. Furthermore, the $L1_2$-Co_3Ti compound was shown to possess a lower solubility for ternary alloying elements than does $L1_2$-Ni_3Al [119]. In addition, binary and ternary alloys based on the Co-Co_3Ti equilibrium exhibited a relatively high γ-γ' lattice misfit (≥ 1%) following ageing at 700, 800 and 900°C, although Cr addition of ~10 at.% to the Co-9Ti alloy was found to reduce lattice misfit (to 0.31%) following ageing at 800°C [117].

Interest in development of γ'-strengthened Co-based superalloys therefore subsided until Sato *et al.*, 2006 [120] reported that addition of W to binary Co-Al alloys produced an

A1-$L1_2$ equilibrium at 900°C (1173 K) based on Co-Co_3(Al,W) with an appropriately low lattice misfit. Although Kobayashi *et al*., 2009 [121] revealed the ternary γ'-Co_3(Al,W) phase in the Co-Al-W system to be metastable at 900°C following extended ageing for 2000 hours, a number of elements including Ta, Ti, Nb (or high concentrations of Ni) have been shown to stabilise the γ'-Co_3(Al,W) phase and increase γ' solvus temperature [122]. Indeed, recent studies have shown significant advances toward commercial development of Co-Al-W based alloys to alleviate the inherent drawbacks of low γ' solvus temperature, attenuated yield stress anomaly and high mass density relative to Ni-based superalloys.

1.2.1 The Co-Al-W ternary system and $L1_2$ Co_3(Al,W) phase stability

The Co-rich region of the isothermal section of the Co-Al-W ternary system reported by Sato *et al*., 2006 [120] for 900°C (1173 K) is shown in Figure 1.16. The $L1_2$-Co_3(Al,W) γ' phase is indicated as γ'($L1_2$) and reportedly precipitated in the disordered γ FCC Co matrix at 900°C with high coherency and high melting point. Figure 1.17 shows cuboidal γ'-Co_3(Al,W) precipitates in an A1 γ matrix following annealing at 900°C for 72 hours. At 1000°C (1273 K), however, this $L1_2$ phase was reportedly metastable [120] and, as mentioned, Kobayashi *et al*. [121] reported this phase to be metastable at 900°C following extended ageing for 2000 hours.

Co-rich region of Co-Al-W phase diagram for 900°C removed for copyright reasons. Copyright holder is the American Association for the Advancement of Science.

Figure 1.16. Co-rich region of the isothermal ternary Co-Al-W phase diagram for 1173 K (900°C) [120]. The stable $L1_2$ Co_3(Al,W) phase (γ′) is indicated, together with A1-γ, B2 and Co_3W ($D0_{19}$) phases. The γ+γ′ two-phase field is shown as shaded. Data included from Sato *et al*., 2005 [123].

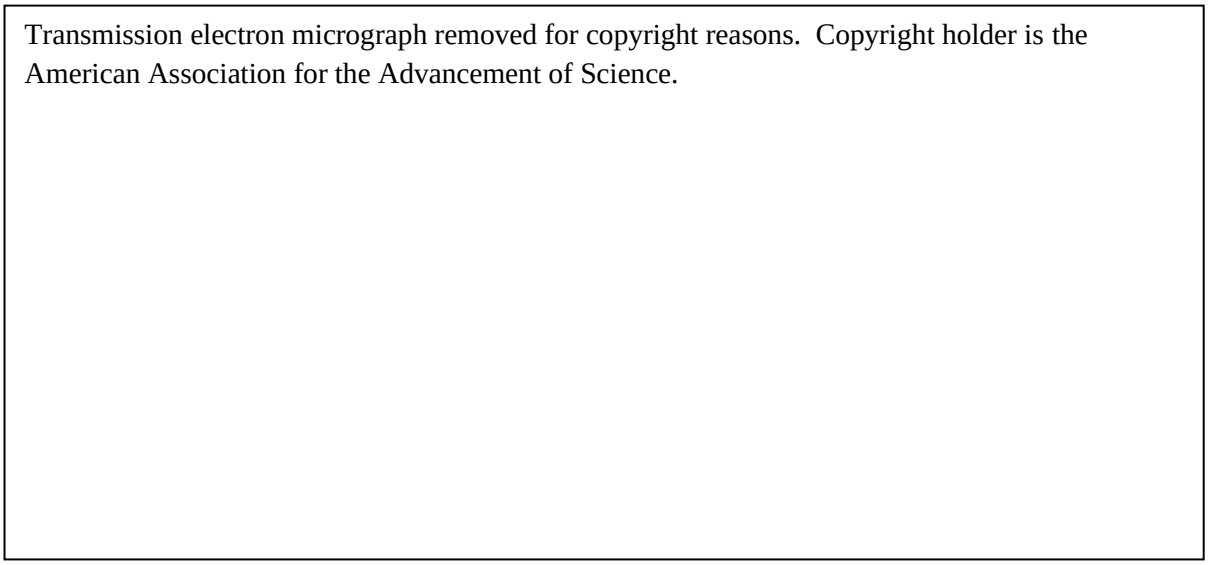

Figure 1.17. A: Transmission electron micrograph for Co-9Al-7.5W (at.%) following annealing at 1173 K (900°C) for 72 hours showing cuboidal γ′-Co_3(Al,W) precipitates in an A1 γ matrix. Inset (B) shows the corresponding selected area electron diffraction pattern, confirming the ordered $L1_2$ crystal structure of the γ′ phase aligned along the <001> directions [120].

The stable and metastable phase boundaries for the isothermal section of the Co-Al-W system at 900°C are shown in Figure 1.18. A narrow γ+γ' metastable two-phase region is apparent, wherein alloys slowly decompose into γ-Co, ß-CoAl (B2) and χ-Co_3W ($D0_{19}$) phases following ageing at 900°C for 2000 hours [121]. The crystal structures of these phases are shown in Figure 1.19.

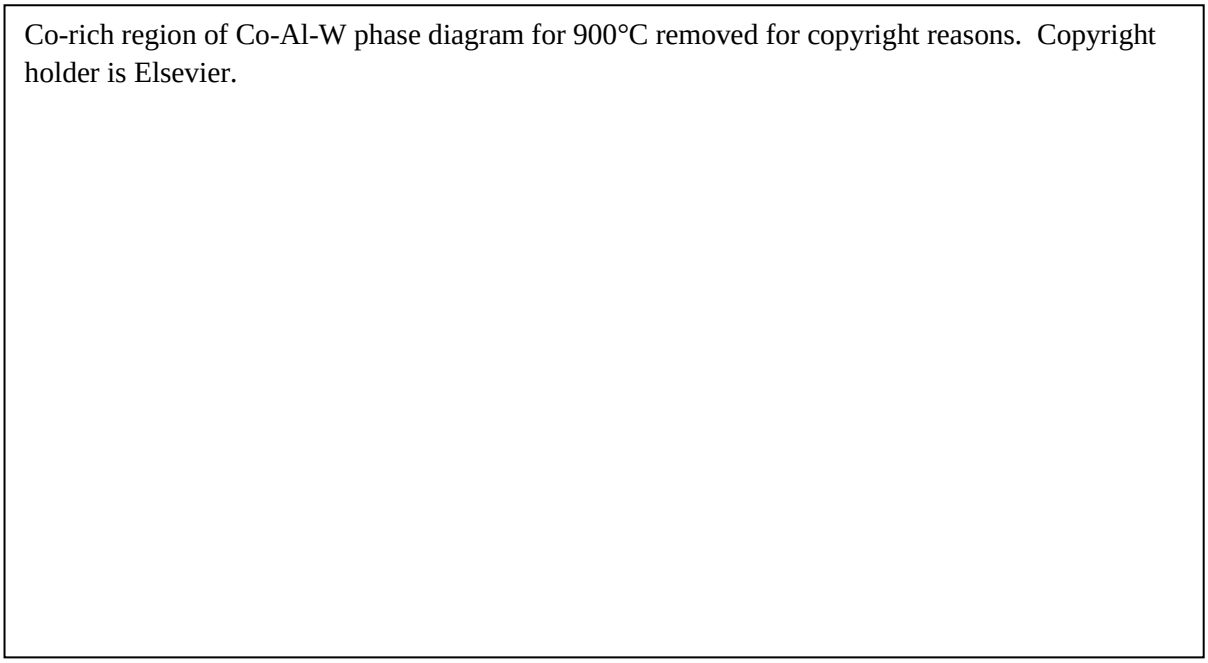

Figure 1.18. Co-rich region of the isothermal ternary Co-Al-W phase diagram for 1173 K (900°C), indicating that the γ′-Co_3(Al,W) phase is metastable and that the thermodynamically stable phases are γ-Co, ß-CoAl and χ-Co_3W phases [124].

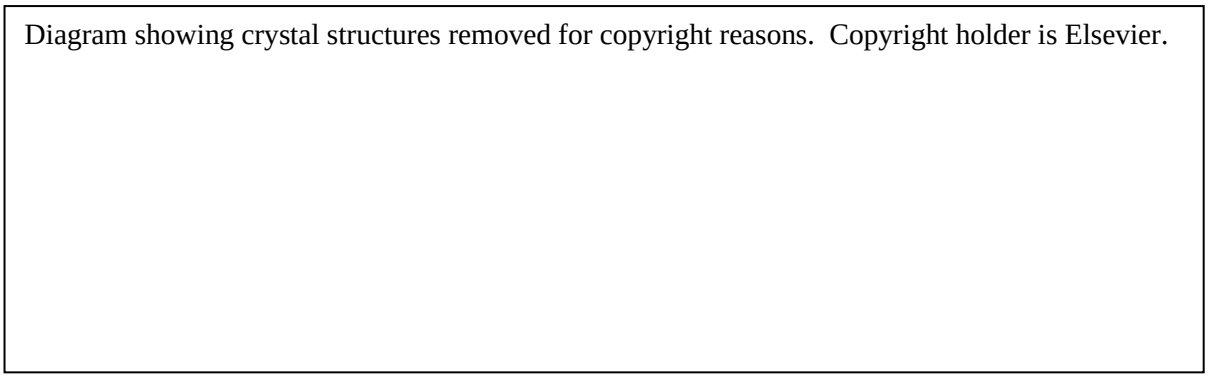

Figure 1.19. Crystal structures of the constituent phases in the Co-rich region of the Co-Al-W phase diagram for 1173 K (900°C): γ Co-based solid solution, γ′-Co_3(Al,W), ß-CoAl and χ-Co_3W [124].

1.2.2 Stabilising the $L1_2$ Co_3(Al,W) phase: effect of alloying elements

Although the γ'-Co_3(Al,W) phase in the ternary Co-Al-W system was revealed as metastable at 900°C and 1000°C, Ti is one of several elements shown to stabilise the γ'-Co_3(Al,W) phase and increase the γ' solvus temperature. Figure 1.20a indicates the efficacy of adding alloying elements (1 at.% by substitution for Co) in stabilising the γ'-Co_3(Al,W) phase in Co-Al-W ternary alloys, as determined by the resultant change in γ' solvus temperature [122]. From Figure 1.20a, Ta is the most efficacious element in increasing γ' solvus temperature, then Ti, Nb, W and Hf in descending order. Incorporating 1 at.% Ta apparently raises the γ' solvus temperature by ~45°*C,* whereas 1 at.% Ti raises the γ' solvus temperature by ~30°C. Ni or V addition increases γ' solvus temperature to a much lesser extent per atomic percent of quaternary elemental addition, whereas Cr, Mn or Fe addition reduces the γ' solvus temperature (Figure 1.20a). This is reflected in the elemental partitioning data on Co-Al-W based quaternary systems obtained by Omori *et al*., 2013 [124] as shown in Figure 1.20b, which indicate γ'-stabilising elements partitioning to the γ' phase ($k > 1$) whereas the γ'-destabilising elements, Cr, Mn and Fe, partition to the γ phase ($k < 1$) (Equation 1.4).

a) Diagram showing influence of transition metal elements on solvus temperature in the Co-Al-W alloy system removed for copyright reasons. Copyright holder is Annual Reviews.

b) Diagram showing correlation of elemental partitioning coefficient with change in solvus temperature removed for copyright reasons. Copyright holder is Annual Reviews.

Figure 1.20. From Suzuki *et al*., 2015 [122]: a) Change in γ′ solvus temperature per 1 at.% addition ($\Delta T_{\gamma'\text{-solvus}}$) of transition metal element to the Co-Al-W ternary system (data amalgamated from different sources); b) Correlation between elemental partitioning coefficient (k) [124] and $\Delta T_{\gamma'\text{-solvus}}$ of the alloying elements.

Yan *et al*., 2014 [125] reported a relatively low solvus temperature for γ'-Co_3(Al,W), specifically 854°C for a Co-7Al-7W (at.%) alloy. Addition of 2 at.% Ta or 2 at.% Ti reportedly raised the γ′ solvus temperature to 983°C and 919°C respectively [125]. Povstugar *et al*., 2014 [126] reported a γ' volume fraction for alloy Co-9Al-9W (at.%) of 0.38 ($\pm$0.02) and found that addition of 2 at.% Ta or 2 at.% Ti raised γ' volume fraction to 0.56 and 0.57 ($\pm$0.01) respectively for alloys aged at 900°C for 200 hours.

Figure 1.21 shows the change in γ' solvus temperature following addition of Ni, Cr or Fe to Co-Al-W ternary alloys [122]. The quaternary element was substituted for Co. Addition of 20 at.% Cr or Fe decreased γ' solvus by >100°C, destabilising the γ' phase. This is an important consideration in turbine disc alloys, for which Cr addition has traditionally been considered critical for oxidation resistance. The increase in γ' solvus temperature due to Ni addition, although modest per at.%, is potentially ~200°C for large amounts of Ni (~80 at.%) due to its high solubility, implying that beneficial high-temperature properties may be derived from alloys intermediate between Ni- and Co-based compositions [122].

Graph showing effect of elemental addition on solvus temperature of Co-Al-W based alloys removed for copyright reasons. Copyright holder is Annual Reviews.

Figure 1.21. From Suzuki *et al*., 2015 [122]. Effect of elemental addition (Ni, Cr or Fe) on γ′ solvus temperature of Co-Al-W-based alloys (data amalgamated from several sources). Data for Ni addition were acquired experimentally by Yan *et al*. [125] (solid grey line) and by Shinagawa *et al*. [127] (closed triangles) as well as by thermodynamic modelling (dotted grey line, [128]).

With respect to Ni addition in Co-Al-W alloys, Shinagawa *et al*., 2008 [127] reported that increasing the Ni:Co ratio of Co-(10-70)Ni-Al-W (at.%) alloys raised the γ' solvus temperature (Figure 1.22a) and reduced lattice misfit (Figure 1.22b). γ′ solvus temperature was found to increase with increasing Ni:Co ratio for both alloy compositions Co-Ni-10Al-10W (at.%) and Co-Ni-10Al-7.5W (at.%) whilst solidus temperature appeared little influenced. Increasing W content from 7.5 at.% to 10 at.% was found to shift the γ′ solvus temperature to higher values (Figure 1.22a). For the Co-Ni-10Al-7.5W alloy equilibrated at 900°C (Figure 1.22b), lattice parameter of γ and γ′ phases decreased with increasing Ni:Co ratio, accompanied by a decrease in lattice misfit (mismatch) from 0.4184% to 0.1958% for a Ni concentration range of 10-70 at.% [127].

a) Graph showing solvus and solidus temperatures for Co-Ni-Al-W alloys removed for copyright reasons. Copyright holder is The Japan Institute of Metals.

b) Graph showing lattice parameters and lattice misfit of Co-Ni-Al-W alloys removed for copyright reasons. Copyright holder is The Japan Institute of Metals.

Figure 1.22. From Shinagawa *et al*., 2008 [127]: a) γ′ solvus and solidus temperatures for alloys Co-Ni-10Al-10W (at.%) and Co-Ni-10Al-7.5W (at.%) homogenised at 1300°C for 24 hours; b) Lattice parameters and lattice misfit (mismatch) for the Co-Ni-10Al-7.5W alloy equilibrated at 900°C.

1.2.3 Effect of temperature on 0.2% flow stress of alloys based on the Co-Al-W system

Figure 1.23 shows the temperature dependence of flow stress for the ternary Co-9Al-9W (at.%) alloy together with a Ta-containing variant, compared with conventional solid solution strengthened Co-based alloys Haynes188 and MarM302. The γ-γ' Co-based alloys exhibited the so-called anomalous increase in flow stress with increasing temperature. For the γ-γ' Co-9Al-9W (at.%) alloy, the onset of the 0.2% flow stress anomaly occurred at ~650°C (923 K), with peak flow stress observed at ~700°C (973 K, Figure 1.23) [129, 130]. Addition of 2 at.% Ta to Co-9Al-10W produced a 0.2% flow stress comparable to that of the polycrystalline Ni-based superalloy MarM247 at 900°C (1173 K) [129, 130] (Figure 1.23). At lower temperatures, the flow stress of the two-phase γ-γ′ Co-based alloys (labelled 2Ta and 9Al-9W) was appreciably less than that observed for the Ni-based MarM247.

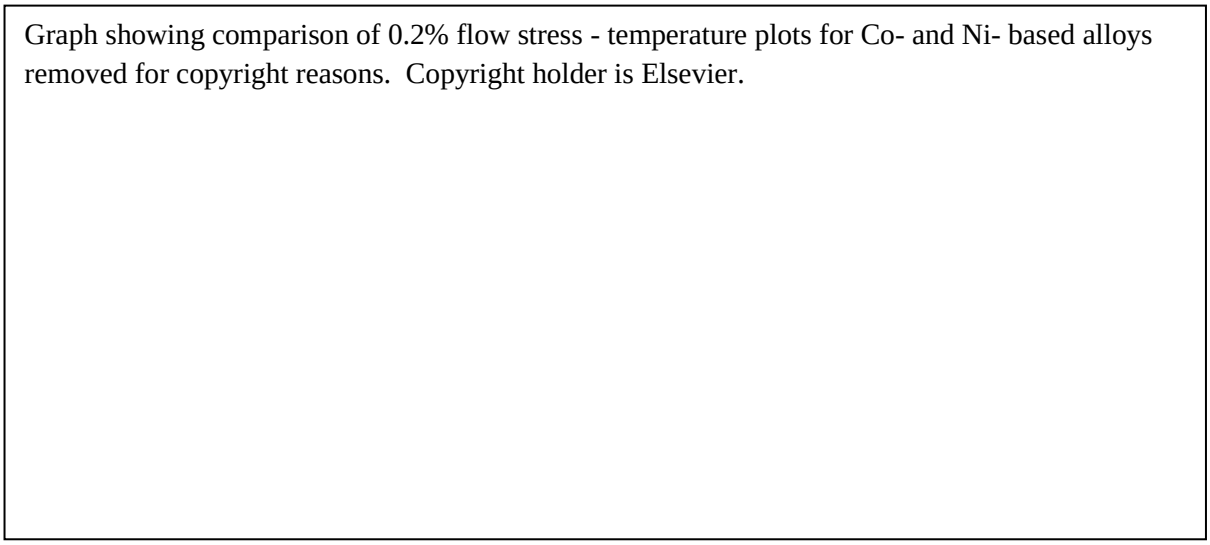

Figure 1.23. From Suzuki *et al*., 2007 [129]. 0.2% flow stress versus temperature for alloys Co-9Al-9W at.% (denoted 9Al-9W) and Co-9Al-10W-2Ta at.% (denoted 2Ta). Values are also shown for conventional solid solution strengthened Co-based alloys MarM302 (open symbols) and Haynes188 (solid triangles) and for polycrystalline Ni-based superalloy MarM247 (solid diamonds) [131]. Compression strain rate 10^{-4} s^{-1}.

1.2.4 0.2% flow stress of the $L1_2$-γ′ compound: comparing $Co_3(Al,W)$, $Ni_3(Al,W)$ and Co_3Ti

Figure 1.24 compares the 0.2% flow stress-temperature curves for $L1_2$ compounds, $Co_3(Al,W)$, $Ni_3(Al,W)$ and Co_3Ti [122]. The 0.2% flow stress for polycrystalline $L1_2$-$Co_3(Al,W)$ derived from Co-12Al-11W (at.%) falls rapidly initially as temperature increases from ~ -200°C up to room temperature [132] (Figure 1.24a). Values of 0.2% flow stress for $Co_3(Al,W)$ then tend to plateau for temperatures up to ~680°C, before displaying the anomalous increase in yield strength with increasing temperature between the relatively narrow temperature range ~680-830°C [132]. A precipitous drop in 0.2% flow stress is then observed for higher temperatures (above ~830°C) [132] (Figure 1.24a). Other $L1_2$ compounds exhibit much lower onset temperatures for the yield stress anomaly, for example ~ -200°C for $Ni_3(Al,W)$. The Co_3Ti compound also exhibits a significantly lower onset temperature for the yield stress anomaly i.e. ~400°C [133], compared with ~680°C for $Co_3(Al,W)$. Furthermore, the temperature range for the yield stress anomaly for Co_3Ti is appreciably wider than for $Co_3(Al,W)$ [133].

a) Graph showing yield stress - temperature plots for individual $L1_2$ compounds removed for copyright reasons. Copyright holder is Annual Reviews.

b) Graph showing normalised yield stress - temperature plots for individual $L1_2$ compounds removed for copyright reasons. Copyright holder is Annual Reviews.

Figure 1.24. From Suzuki *et al*., 2015 [122]: a) yield stress-temperature curves for $L1_2$ compounds $Co_3(Al,W)$ [132], Co_3Ti [133] and $Ni_3(Al,W)$ [134]; b) yield stress-temperature plot for each $L1_2$ compound [data from (a)] normalised to values at room temperature.

As indicated by the normalised yield stress-temperature data (Figure 1.24b), the intermediate- and high-temperature strength of the γ' $Co_3(Al,W)$ phase appears appreciably lower than that for the other $L1_2$ compounds Co_3Ti [133] and $Ni_3(Al,W)$ [134]. The intermediate- and high-temperature strength of the γ' $Co_3(Al,W)$ is reportedly lower than that for Ni_3Al [122].

1.2.5 Expanding the temperature range of the 0.2% flow stress for $L1_2$-$Co_3(Al,W)$

As with many $L1_2$ compounds, the yield stress anomaly for $Co_3(Al,W)$ has been attributed to thermal activation of cross slip of APB-coupled superpartial dislocations from (111) to (010) planes [132] (section 1.1.1 *i*). The APB and complex stacking fault (CSF) energies on (111) were reported as 146 and 137 $mJ.m^{-2}$ respectively for a Co-12Al-11W alloy [132]. This low CSF energy is believed responsible for the high onset temperature (~680°C) of the yield stress anomaly for $Co_3(Al,W)$ [132] and therefore for the inferior intermediate- and high-temperature strength compared to other $L1_2$ compounds, such as $Ni_3(Al,W)$ [134] and Co_3Ti [133].

The sharp decline in yield stress for $Co_3(Al,W)$ above ~830°C has been attributed to (111) slip in the γ phase, the experimental temperature being above the order-disorder transition temperature [122]. Increasing the stability of the $L1_2$-γ' phase to increase the γ' solvus temperature extends the temperature range of the yield stress anomaly up to higher

temperatures to the point where slip on (001) is initiated, thus improving the high-temperature strength of this γ' phase [122].

In addition to increasing the γ' solvus temperature to improve high-temperature strength of the γ' $Co_3(Al,W)$ phase, a lower onset temperature for the yield stress anomaly is essential to improve both intermediate- and high-temperature strength within the yield stress anomaly. The high onset temperature of the yield stress anomaly for $Co_3(Al,W)$ is believed to derive from the low CSF energy that impedes cross slip of APB-coupled dislocations from (111) to (010) planes [132]. Therefore, selecting alloying elements that can simultaneously increase the CSF energy of $Co_3(Al,W)$ as well as increasing γ' solvus temperature is important. Both parameters are improved by stabilising the $L1_2$ $Co_3(Al,W)$ phase, for example, by addition of Ta, Ti or Nb, or by incorporating significant amounts of Ni, as discussed in section 1.2.2. With addition of Ni, the onset temperature for the yield stress anomaly of the single-phase $L1_2$ compound $(Co_{0.8}Ni_{0.2})_3(Al,W)$ reportedly decreased from ~680°C to ~430°C [122].

1.2.6 Towards higher γ' solvus temperatures and lower mass density in Co-Al-W based alloys

Considerable progress has been made in increasing γ' solvus temperature of γ-γ' Co-Al-W based alloys by specific elemental addition, such as the incorporation of Ni, Ta or Ti, as described in section 1.2.2. Xue *et al*., 2013 [135] showed that alloy Co-7Al-8W-4Ti-1Ta (at.%) exhibited a γ' solvus temperature of 1131°C. A γ' solvus temperature of 1185°C was reported for alloy Co-20Ni-7Al-7W-4Ti-2Ta (at.%) [136], indicating the significant effect that Ni can have with respect to increasing γ′ solvus temperature. Lass, 2017 [137] designed an alloy, Co-30Ni-9Al-3Ti-7W-2Ta-0.1B (by mole percent), using computational thermodynamics, for which a γ' solvus temperature of 1218°C was experimentally derived. Increasing W concentration has been shown to raise γ' solvus temperature in the Co-9Al-W (at.%) ternary system, equating to ~25°C for 1 at.% W addition (in the range 7.4-10.3 at.%), whilst improving creep strength at 850°C and 900°C by increasing γ' volume fraction [138]. Unfortunately, however, W addition increases the mass density of the bulk alloy, restricting applications where strength-to-weight ratio is critical.

Mass density remains a significant challenge for Co alloys based on the Co-Al-W compositions described by Sato *et al*. [120] as these generally comprise a high W content of ~7-10 at.% (20-27 wt.%), which, due to the high mass density of W (19.3 $g.cm^{-3}$), results in alloy mass densities exceeding 9.0 $g.cm^{-3}$ [125]. Many Co superalloys developed to date have

targeted single-crystal blade applications of composition in the region Co-10Al-9(W+Ta) (at.%), possessing alloy mass densities > 9.0 g.cm^{-3} due to their high refractory metal content [139]. In comparison, Ni-based disc alloys generally exhibit a mass density < 8.5 g.cm^{-3} [139], for example ~8.2 g.cm^{-3} for Waspaloy, which is W-free. Therefore, for Co-based superalloys to realise their full potential, reducing alloy mass density toward that of conventional Ni-based superalloys is a priority.

1.2.7 W-free γ′-strengthened Co-based superalloys

Makineni *et al*., 2015 [140, 141] reported a reduced mass density in γ'-strengthened Co-based alloys on substitution of Mo and Nb [140], or Mo and Ta [141], for W. Mo possesses a density of 10.2 g.cm^{-3} compared with 19.3 g.cm^{-3} for W. Nb and Ta (density values 8.6 and 16.4 g.cm^{-3} respectively) in small concentrations stabilise the γ-γ′ microstructure in Co-Al-Mo-Nb/Ta alloys [142]. Unfortunately, these W-free alloys displayed considerably lower γ' solvus temperatures than those of Co-Al-W based alloys i.e. 866°C for Co-10Al-5Mo-2Nb at.% (density 8.36 g.cm^{-3}) and 928°C for Co-10Al-5Mo-2Ta at.% (density 8.61 g.cm^{-3}). However, the density values of these alloys compare well with values for Ni-based disc alloys (ideally < 8.5 g.cm^{-3}, [139]) and improve on the reported mass density for the ternary Co-9Al-9.8W alloy (9.82 g.cm^{-3}) [140, 141].

(i) Effect of Ni addition in the Co-Al-Mo-Nb system

Alloying with 10-30 at.% Ni improved γ' phase stability and raised the γ' solvus temperature of the Co-10Al-5Mo-2Nb (at.%) alloy [140]. For this alloy system, Ni addition increased γ' solvus temperature from 866°C in the absence of Ni, to 990°C for the alloy containing 30 at.% Ni (Figure 1.25a). Mass density of the base alloy Co-10Al-5Mo-2Nb (8.36 g.cm^{-3}) was not unduly influenced by addition of 10, 20 or 30 at.% Ni (Figure 1.25b). Alloy Co-30Ni-10Al-5Mo-2Nb exhibited a high specific 0.2% proof stress (0.2% proof stress per unit mass density) at room temperature (94.3 MPa/g.cm^{-3}) and at 870°C (63.9 MPa/g.cm^{-3}).

a) Graph showing effect of Ni addition on solvus temperature of alloy Co-10Al-5Mo-2Nb (at.%) removed for copyright reasons. Copyright holder is Elsevier.

b) Diagram showing comparison of mass density of Co-based alloys removed for copyright reasons. Copyright holder is Elsevier.

Figure 1.25. From Makineni *et al*., 2015 [140]. Effect of adding 10, 20 and 30 at.% Ni to the quaternary W-free Co-10Al-5Mo-2Nb (at.%) base alloy: a) γ′ solvus temperature. Inset shows differential scanning calorimetry (DSC) heating curves. b) mass density values compared with Co-9Al-9.8W and with conventional solid solution strengthened Co alloys MAR-M-302, Haynes 188 and L-605.

(ii) Effect of Ni addition in the Co-Al-Mo-Ta (±Ti) system

Makineni *et al*., 2015 [141] investigated alloys of basic composition Co-10Al-5Mo (at.%) with 2 at.% added Ta (denoted 2Ta) for stabilisation of the γ′ phase. Incorporation of 30 at.% Ni (Co-30Ni-10Al-5Mo-2Ta at.%, denoted 30Ni-2Ta in Figure 1.26) increased γ' solvus temperature by 86°C (from 928°C to 1014°C), Figure 1.26a. Additional incorporation of 2 at.% Ti (denoted 30Ni-2Ta-2Ti) pushed the γ' solvus temperature higher (to 1066°C). These W-free alloys (2Ta, 30Ni-2Ta and 30Ni-2Ta-2Ti) exhibited appreciably lower mass density than that reported for W-containing Co-based alloys (Figure 1.26b).

a) Diagram showing comparison of solvus temperatures of Co- and Ni-based alloys removed for copyright reasons. Copyright holder is Elsevier.

b) Bar chart showing comparison of mass density of Co-based alloys removed for copyright reasons. Copyright holder is Elsevier.

Figure 1.26. From Makineni *et al*., 2015 [141]. Effect of adding 30 at.% Ni (±2 at.% Ti) to alloy Co-10Al-5Mo-2Ta (denoted 2Ta): a) γ′ solvus temperature compared with Co-9Al-9.8W, Co-35Ni-9Al-10W and Waspaloy; b) mass density compared with Co-9Al-9.8W ±2Ta and with W-containing solid solution strengthened Co alloys MAR-M-302, Haynes 188 and L-605.

Alloy 30Ni-2Ta-2Ti (aged at 900°C for 50 hours) exhibited a particularly high specific 0.2% proof stress at 870°C (73.9 MPa/g.cm^{-3}) compared with alloy 30Ni-2Ta and with values for Co-Al-W based alloys and the Ni-based superalloys Waspaloy and MAR-M-247 (Figure 1.27). This value of specific 0.2% proof stress (73.9 MPa/g.cm^{-3}) was notably higher than that of the Co-30Ni-10Al-5Mo-2Nb alloy (63.9 MPa/g.cm^{-3}) at 870°C [140]. Alloy 30Ni-2Ta-2Ti also exhibited a higher γ′ solvus temperature i.e. 1066°C compared with 990°C for the Nb-containing alloy. Both alloys possessed a relatively low mass density (8.55 and 8.38 g.cm^{-3} respectively). As Nb possesses a density (8.6 g.cm^{-3}) of around half that of Ta (density 16.4 g.cm^{-3}), Nb confers a lower density to the base alloy.

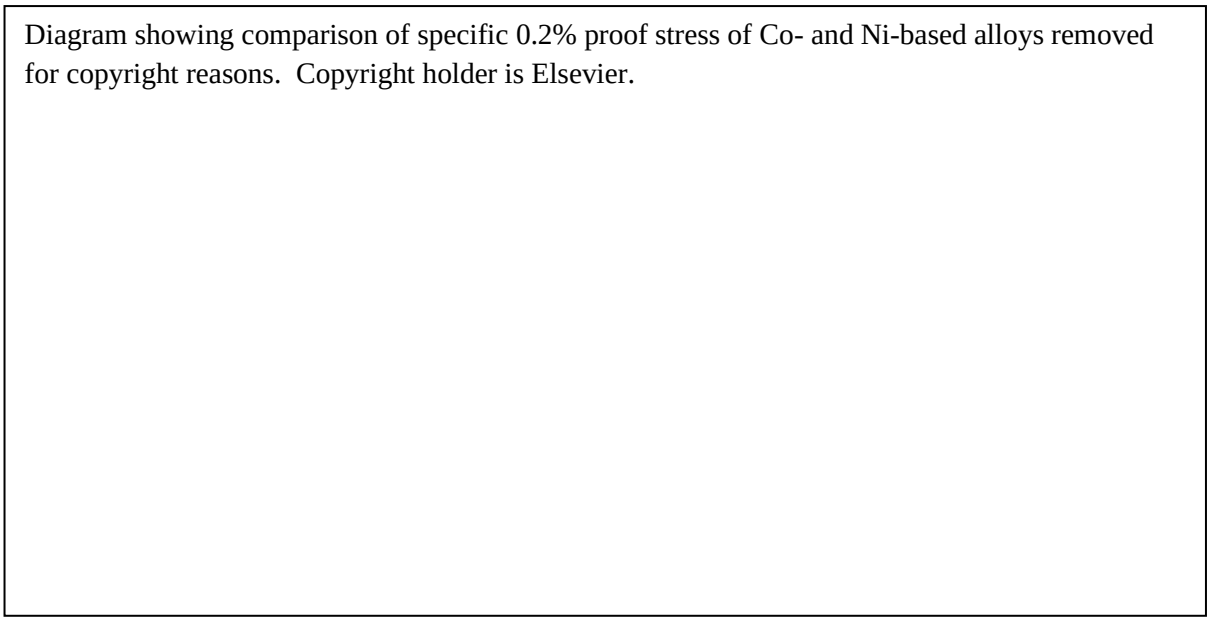

Figure 1.27. Specific 0.2% proof stress (0.2% proof stress per unit mass density) for 30Ni-2Ta and 30Ni-2Ta-2Ti (aged at 900°C for 50 hours). Values are compared with specific 0.2% proof stress of Co-9.4Al-11W, Co-8.8Al-9.8W-2Ta and the Ni-based superalloys, Waspaloy and MAR-M-247. All values were obtained for a test temperature of 870°C [141].

1.2.8 $L1_2$ γ'-strengthened Co-based superalloys with low W content

Lass *et al.*, 2018 [143] developed a range of Co-Ni-Al-Ti based alloys combining the benefits of increased γ' solvus temperature conferred by Ni, Ti and Ta addition in the Co-Al-W system and the decreased mass density achieved by replacing W with Mo and Nb. For the alloys investigated, alloy Co-30Ni-7Al-4Ti-3Mo-2W-1Nb-1Ta (by mole percent) (designated L19) exhibited a favourable combination of high γ' volume fraction (~0.65) and good γ-γ' microstructural stability at 900°C, together with a high γ' solvus temperature (1126 ±2°C) and a mass density of ~8.89 g.cm^{-3}. Atom probe tomography on alloy L19 (aged at 900°C, 4 hours) indicated preferential partitioning of Ni, Al, Ti, W, Nb and Ta to the γ' phase with preferential partitioning of Co to the γ phase and Mo segregating to the γ-γ' interface. Reducing the Ni mole fraction from 0.30 (alloy L19) to 0.10 (alloy L18) reduced Ti and Al partitioning to the γ' phase and increased partitioning of Ta, Nb, W, Mo and Co to the γ' phase, with a consequent reduction in γ' solvus temperature (from 1126 ±2°C to 1076 ±4°C) [143].

From section 1.2.2, Shinagawa *et al.*, 2008 [127] reported that increasing the Ni:Co ratio in Co-(10-70)Ni-Al-W (at.%) alloys raised the γ' solvus temperature (Figure 1.22a) and reduced lattice misfit (Figure 1.22b). In addition to stabilising the γ' phase, increasing Ni content was observed to expand the γ+γ' two-phase field to the low W region of the Co-(10-

70)Ni-Al-W (at.%) system at 900°C [127], reducing the amount of W necessary to stabilise the γ-γ' microstructure (Figure 1.28).

Diagram showing the influence of Ni on the Co-Ni-Al-W isothermal phase diagram at 900°C removed for copyright reasons. Copyright holder is The Japan Institute of Metals.

Figure 1.28. From Shinagawa *et al*., 2008 [127]. Section of isothermal phase diagram at 900°C for Co-10Ni-Al-W, Co-30Ni-Al-W, Co-50Ni-Al-W and Co-70Ni-Al-W. Pale grey lines delineate the phase boundaries in the Co-Al-W ternary system as reported by Sato *et al*. [120] for 900°C. Shaded areas represent the γ-γ' two-phase regions in the Co-Ni-Al-W quaternary system.

(i) Effect of systematic reduction of W in alloys based on the Co-Al-W system

Systematic reduction of W in the ternary Co-9Al-W (at.%) system reportedly reduces γ′ solvus temperature and γ′ volume fraction (Figure 1.29). Pyczak *et al*., 2015 [138] showed that reducing W from 10.3 to 7.4 at.% in the ternary Co-9Al-W system lowered γ' solvus temperature from 1036 to 960°C and reduced γ' volume fraction (from 0.73 to 0.34) (Figure 1.29). Ooshima *et al*., 2010 [144] reported that reducing W content from 8 to 6 at.% in a similar ternary Co-9Al-W system lowered γ' solvus temperature from 985 to 948°C and reduced γ' volume fraction (from 0.64 to 0.36). The values published by Pyczak *et al*. [138] and Ooshima *et al*. [144] are consistent with data shown in Figure 1.21 and Figure 1.22a, which indicate a γ′ solvus temperature of ~980°C for Co-9Al-9W and ~970°C for Co-10Al-7.5W.

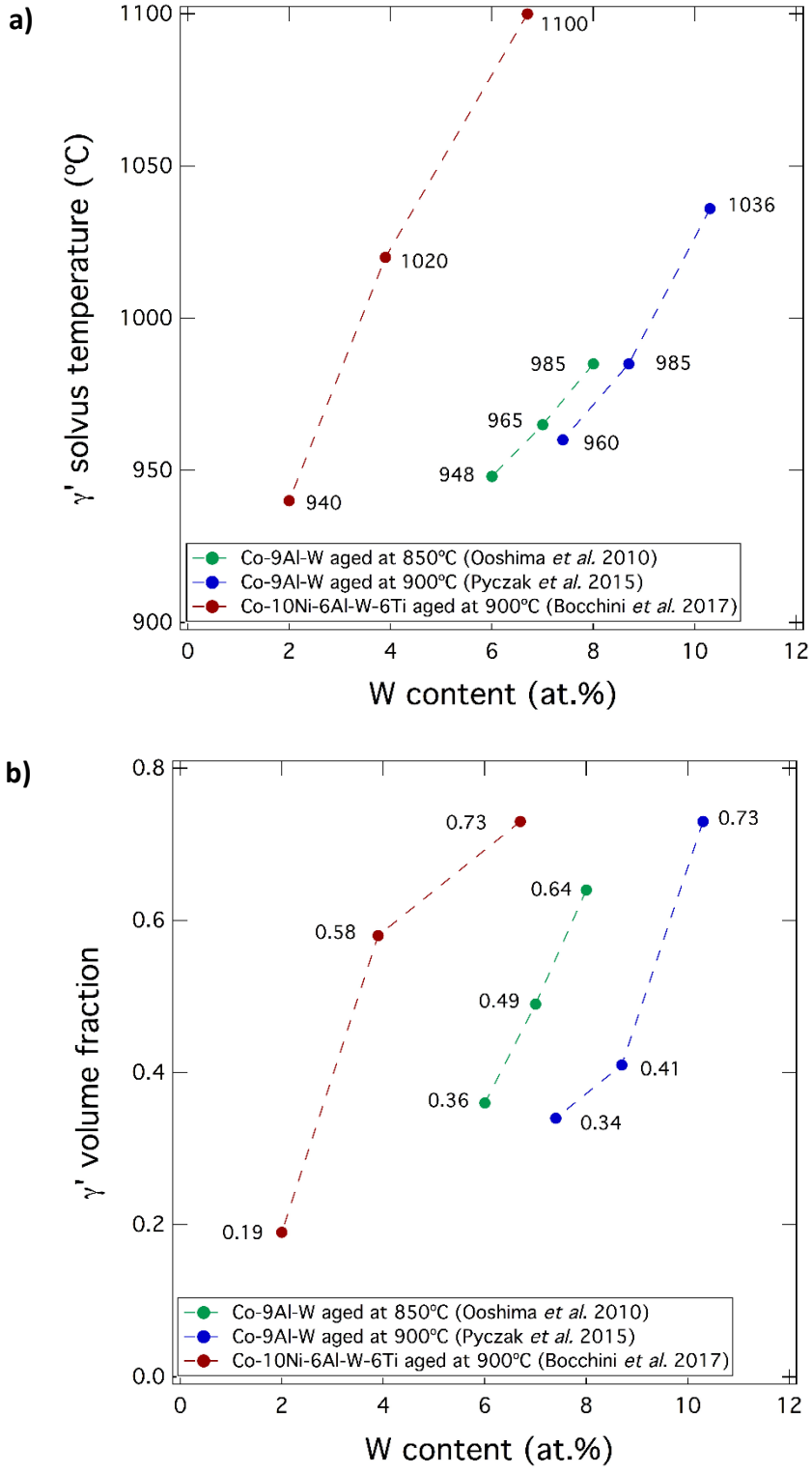

Figure 1.29. Effect of increasing W content on a) γ′ solvus temperature and b) γ′ volume fraction for alloys of the Co-9Al-W (at.%) system (Ooshima *et al.*, 2010 [144], Pyczak *et al.*, 2015 [138]) and for alloys of the Co-10Ni-6Al-W-6Ti (at.%) system (Bocchini *et al.*, 2017) [145]. For each alloy system, W was added at the expense of Co. Values of γ′ solvus from [145] are estimated.

Bocchini *et al*., 2017 [145] reported a steeper overall reduction in γ′ solvus temperature (from ~1100°C to ~940°C) on reducing the W content from 6.7 to 2.0 at.% in alloy Co-10Ni-6Al-W-6Ti (as well as a reduction in γ' volume fraction from 0.73 to 0.19) (Figure 1.29). This decrease in γ′ solvus temperature equates to ~40°C per 1 at.% W, which compares with the ~25°C and 18.5°C reduction (per 1 at.% W) reported for the Co-Al-W system by Pyczak *et al*. [138] and Ooshima *et al*. [144] respectively for the higher W concentration range of 7.4-10.3 at.% and 6-8 at.% respectively (Figure 1.29).

For the Co-10Ni-6Al-(2-6.7)W-6Ti (at.%) alloy series, a 1 at.% reduction in bulk W content reportedly lowered solidus and liquidus temperatures by only ~3°C and ~5°C respectively [145], with solidus temperatures remaining close to 1300°C i.e. comparable with Waspaloy (~1330°C) but ~150°C lower than for the ternary Co-9.2Al-9.0W alloy (~1450°C) reported by Sato *et al*. [120]. Of the Co-10Ni-6Al-(2-6.7)W-6Ti (at.%) alloy series, mass densities were reportedly 8.5 $g.cm^{-3}$ and 8.9 $g.cm^{-3}$ for alloys containing 2 and 4 at.% W respectively [145]. These values compare with a desired mass density for Ni-based disc alloys of < 8.5 $g.cm^{-3}$ [139].

For comparison with W-free alloys (section 1.2.7), the Co-10Al-5Mo-2Nb (at.%) alloys with Ni content 0-30 at.% (Figure 1.25) exhibited γ' solvus temperatures of 866-990°C and densities ~8.37 $g.cm^{-3}$ [140]. For the same base alloy (Co-10Al-5Mo), addition of 30Ni-2Ta-2Ti (Figure 1.26) resulted in a γ′ solvus temperature of 1066°C and density 8.55 $g.cm^{-3}$ [141]. These values compare with a γ′ solvus temperature for Waspaloy of 1030°C (Figure 1.26) and mass density of ~8.2 $g.cm^{-3}$.

(ii) Effect of systematic Ti substitution for Al and W in Co-Ni-Al-W-Ti alloys

In a further study, Bocchini *et al*., 2017 [146] substituted Ti (2, 4, 6 and 8 at.%) for W and Al in the Co-10Ni-(9-x)Al-(9-x)W-2xTi (at.%) alloy and observed an almost linear increase in γ' solvus temperature with increasing Ti addition, from ~985°C for the Ti-free alloy (Co-10Ni-9Al-9W, at.%) to ~1130°C for the Co-10Ni-5Al-5W-8Ti (at.%) alloy (denoted 8Ti) (Figure 1.30a). In contrast, solidus and liquidus temperatures decreased almost linearly with increasing Ti substitution: respectively from 1459°C and 1489°C (0Ti) to 1277°C and 1383°C (8Ti alloy) (Figure 1.30a) [146], conducive with the corresponding decrease in W, which possesses an inherently high melting point.

a) Graph showing effect of Ti content on phase transition temperatures of Co-Ni-Al-W-Ti alloys removed for copyright reasons. Copyright holder is Elsevier.

b) Graph showing effect of Ti content on 0.2% flow stress – temperature plots for Co-Ni-Al-W-Ti alloys removed for copyright reasons. Copyright holder is Elsevier.

Figure 1.30. From Bocchini *et al*., 2017 [146]: a) γ′ solvus, solidus and liquidus temperatures derived from differential thermal analysis (DTA) heating curves for Co-10Ni-(9-x)Al-(9-x)W-2xTi (at.%) alloys (heating rate 5°C min^{-1}); b) 0.2% flow stress for the same series of alloys (aged at 900°C, 168 hours) for a temperature range between ambient and 900°C at a strain rate of 10^{-4} s^{-1}. Different samples of the same alloy are shown by open or closed symbols of the same colour.

From Figure 1.30b, increasing Ti concentration from 0 to 8 at.% produced a systematic increase in 0.2% flow stress for temperatures between ambient and 900°C, with peak flow stress ~810 MPa for the 8Ti alloy. This compares with a value of ~575 MPa for the Ti-free alloy (Figure 1.30b) and just under 500 MPa for the ternary Co-9Al-9W (at.%) alloy (Figure 1.23). For the Ti-containing alloys, the flow stress anomaly reportedly had an onset temperature ~600°C (Figure 1.30b), compared with ~700°C for the Ti-free alloy and ~650°C for the Co-9Al-9W (at.%) alloy (Figure 1.23). Of note in regard to the proposed operating temperatures for turbine discs of ~800°C is the fact that the higher Ti alloys (containing 4, 6 and 8 at.% Ti) reportedly exhibited peak 0.2% flow stress at ~750°C compared with ~800°C for the 0Ti and 2Ti alloys (Figure 1.30b). Alloys Co-10Ni-6Al-6W-6Ti and Co-10Ni-5Al-5W-8Ti (at.%) exhibited a mass density of 9.17 $g.cm^{-3}$ and 8.84 $g.cm^{-3}$ respectively [146], which compare with the desired density for Ni-based disc superalloys of < 8.5 $g.cm^{-3}$ [139].

1.2.9 Effect of Cr addition in W-free γ-γ′ Co based alloys

Nithin *et al*., 2017 [142], building on the work of Makineni *et al*., 2015 [141], studied the effect of 10 at.% Cr addition to alloy Co-30Ni-10Al-5Mo-2Ta ±2Ti (Table 1.2). Addition of 10 at.% Cr increased γ' solvus temperature from 1014°C in the absence of Ti and 1066°C in the presence of Ti to 1038°C and 1078°C respectively. Incorporation of 10 at.% Cr reduced mass density from 8.55 $g.cm^{-3}$ for the Co-30Ni-10Al-5Mo-2Ta-2Ti (at.%) alloy to 8.41 $g.cm^{-3}$

for the Cr-containing alloy, such that alloy density approached that of Waspaloy (~8.2 g.cm^{-3}). 10 at.% Cr addition increased specific 0.2% proof stress at 870°C from 73.9 MPa/g.cm^{-3} for the Co-30Ni-10Al-5Mo-2Ta-2Ti (at.%) alloy to 85.6 MPa/g.cm^{-3} in the presence of Cr (Table 1.2), indicating that Cr is highly beneficial to alloy strength in this W-free alloy system.

Table 1.2. Comparison of fundamental properties of the W-free Co-10Al-5Mo-2Nb (at.%) and Co-10Al-5Mo-2Ta (at.%) systems with various alloying additions (in at.%). Data from Makineni *et al*., 2015 [140, 141] and Nithin *et al*., 2017 [142].

Base alloy composition (at.%)	Property	Base alloy	+30Ni	+30Ni+2Ti	+30Ni+2Ti+10Cr
Co-10Al-5Mo-2Nb [140]	γ' solvus temperature (°C)	866	990	-	-
	Mass density (g.cm^{-3})	8.36	8.38	-	-
	Specific 0.2% proof stress at 870°C (MPa/g.cm^{-3})	46.7	63.9	-	-
Co-10Al-5Mo-2Ta [141] and [142]	γ' solvus temperature (°C)	928	1014	1066	1078
	Mass density (g.cm^{-3})	8.61	8.65	8.55	8.41
	Specific 0.2% proof stress at 870°C (MPa/g.cm^{-3})	-	64.7	73.9	85.6

From the study by Nithin *et al*. [142], addition of 10 at.% Cr reportedly elicited spherical $L1_2$-γ' precipitates rather than the cuboidal $L1_2$-γ' precipitates observed for the Cr-free alloy. Cr partitioned preferentially to the γ matrix but also influenced Mo and Ta partitioning, such that k_{Mo} decreased from ~1.2 in the base composition (±Ti) to <1, whilst k_{Ta} increased appreciably from ~5.4 in the base composition (±Ti) to ~10 in the presence of Ti and ~14 in the absence of Ti [142].

Pandey *et al*., 2019 [147] investigated the systematic addition of Cr (2, 5 and 8 at.%) to the same low-density, W-free alloy composition, Co-30Ni-10Al-5Mo-2Ta-2Ti (at.%), described above by Nithin *et al*. [142]. The 5Cr alloy achieved the highest γ' solvus temperature for this alloy series (1105°C). This compares with 1066°C for the Cr-free alloy and 1078°C for the 10Cr alloy investigated by Nithin *et al*. [142] (Table 1.2). In terms of mass density, the 8Cr alloy displayed the lowest density of the series (8.44 g.cm^{-3}) [147].

Pandey *et al*., 2019 [147] deduced a trend for Cr substitution on the $L1_2$-γ' lattice in alloy Co-30Ni-10Al-5Mo-2Ta-2Ti (at.%) with increasing alloy Cr content by estimating the Gibbs free energy values of the $L1_2$ γ' compounds. According to these authors, with low Cr content (2 at.%), Cr prefers to substitute only for Mo atoms on B sites in the $L1_2$ lattice. In the

5 at.% Cr alloy, Cr atoms additionally replace excess anti-site Co atoms from the B sites and in the 8 at.% Cr alloy, Cr atoms additionally replace Co atoms from A sites of the $L1_2$ unit cell. This change in site preference with increasing Cr content from 0 to 8 at.% was associated with decreasing lattice misfit from +0.48% to +0.19% and a change in γ' morphology from cuboidal (0Cr) to rounded corners (2Cr and 5Cr alloys) to more spherical (8Cr) [147].

1.3 Summary

Recent studies on γ'-strengthened Co-Al-Mo-Nb/Ta alloy systems have been successful in mitigating the intrinsic problem of low γ' solvus temperature by incorporation of elements Ni, Ti and Cr (Table 1.2). Simultaneously, advances have been made in increasing γ' solvus temperature of Co-Al-W based alloys by specific elemental addition, such as the incorporation of Ni, Ti or Ta, as described in section 1.2.2. Of major significance, the 2008 study by Shinagawa *et al*. [127] showed that increasing Ni:Co ratio in Co-(10-70)Ni-Al-W (at.%) alloys raised γ' solvus temperature and reduced lattice misfit (section 1.2.2). Furthermore, in stabilising the γ' phase, increasing Ni content extended the γ+γ' two-phase field to the low W region of the Co-(10-70)Ni-Al-W (at.%) phase diagram at 900°C, reducing the W content necessary to stabilise the γ-γ' microstructure [127] (section 1.2.8), thereby providing the potential for reduced mass density. Incorporation of 2 at.% Ti or 2 at.% Ta in Co-Al-W alloys also proved efficacious in increasing γ′ solvus temperature [125] and γ′ volume fraction [126] (section 1.2.2).

From section 1.2.5, the high onset temperature for the yield stress anomaly of $Co_3(Al,W)$ purportedly derives from a low complex stacking fault (CSF) energy that impedes cross slip of APB-coupled dislocations from (111) to (010) planes [132]. As such, it is essential to select alloying elements that can raise γ' solvus temperature and increase the CSF energy of the $Co_3(Al,W)$ phase. Both can be achieved by stabilising the $L1_2$ $Co_3(Al,W)$ phase by addition of Ta, Ti or Nb, or by incorporating significant amounts of Ni, as discussed in section 1.2.2. Indeed, addition of Ni to achieve the $L1_2$ phase $(Co_{0.8}Ni_{0.2})_3(Al,W)$ reportedly reduced the onset temperature for the 0.2% yield stress anomaly from ~680°C to ~430°C [122]. From section 1.2.2, the increase in γ' solvus temperature from Ni addition to the ternary Co-Al-W alloy, although modest per at.%, is reportedly ~200°C for large amounts of Ni (~80 at.%) due to its high solubility, suggesting that advantageous high-temperature properties may derive from alloys intermediate between Ni- and Co-based compositions. In contrast, substitution of 20 at.% Cr for Co in the Co-Al-W base alloy destabilised the γ' phase and decreased γ' solvus by

>100°C [122], a potential disadvantage in turbine disc applications, for which Cr incorporation has traditionally been considered critical for oxidation resistance.

A number of studies have reported relatively high γ' solvus temperatures on incorporation of elements such as Ni, Ti or Ta in the Co-Al-W system (section 1.2.2): 1131°C for alloy Co-7Al-8W-4Ti-1Ta (at.%) [135], 1185°C for alloy Co-20Ni-7Al-7W-4Ti-2Ta (at.%) [136] and 1218°C for alloy Co-30Ni-9Al-3Ti-7W-2Ta-0.1B (mole percent) [137]. However, a W content of ~7-10 at.%, as in the Co-Al-W compositions described by Sato *et al*. [120], generally confers a mass density in excess of 9.0 $g.cm^{-3}$ [125], compared with the desired density for Ni-based disc alloys of < 8.5 $g.cm^{-3}$ [139].

In comparison, the highest γ' solvus temperature for the W-free alloys investigated by Makineni *et al*. [140, 141] and Nithin *et al*. [142] (Table 1.2) was achieved by addition of 10 at.% Cr to the base composition Co-30Ni-10Al-5Mo-2Ta-2Ti (at.%). This raised γ' solvus temperature from 1066°C to 1078°C, whilst also increasing specific 0.2% proof stress at 870°C from 73.9 MPa/$g.cm^{-3}$ to 85.6 MPa/$g.cm^{-3}$ (Table 1.2), indicating that Cr is highly beneficial to alloy strength in this W-free alloy system. Furthermore, addition of 10 at.% Cr reduced density from 8.55 $g.cm^{-3}$ for the Cr-free alloy Co-30Ni-10Al-5Mo-2Ta-2Ti (at.%) to 8.41 $g.cm^{-3}$ (Table 1.2), to approach that of Waspaloy (~8.2 $g.cm^{-3}$).

Reducing W concentration in Co-Al-W based alloys has been shown to reduce γ' solvus temperature and γ' volume fraction (Figure 1.29). However, a study by Bocchini *et al*. [146] showed that systematic substitution of Ti (2-8 at.%) in the base alloy Co-10Ni-9Al-9W (at.%), at the expense of an equiatomic ratio of W and Al, produced an almost linear increase in γ' solvus temperature: from ~985°C for the Ti-free alloy to ~1130°C for alloy Co-10Ni-5Al-5W-8Ti (at.%), denoted 8Ti (section 1.2.8 *ii*). Ti addition (2-8 at.%) produced a systematic increase in 0.2% flow stress for the temperature range ambient to 900°C, with an onset temperature for the flow stress anomaly of ~600°C. This compares with an onset temperature of ~700°C for the Ti-free alloy and of ~650°C for the Co-9Al-9W (at.%) alloy (section 1.2.3). For the 8Ti alloy, the peak value for 0.2% flow stress (~810 MPa) appeared significantly higher than that of the Ti-free Co-10Ni-9Al-9W (at.%) alloy (~575 MPa) and of the ternary Co-9Al-9W (at.%) alloy (just under 500 MPa) (section 1.2.3). Therefore, Ti appears a useful addition in Co-Al-W based alloys in permitting reduction of W content whilst raising γ' solvus temperature, increasing 0.2% flow stress and lowering the onset temperature for the 0.2% flow stress anomaly. The concurrent reduction in mass density to a value of 8.84 $g.cm^{-3}$ for the Co-10Ni-

5Al-5W-8Ti (at.%) alloy provides the potential for mass density of higher-order alloys to approach the target density for a Ni-based disc superalloy of < 8.5 g.cm^{-3} [139].

Lass *et al*., 2018 [143] fabricated a range of Co-Ni-Al-Ti based alloys that combined the advantages of increased γ' solvus temperature conferred by Ni, Ti and Ta addition in the Co-Al-W system and the reduced mass density achieved by replacing W with Mo and Nb. Of these alloys, the low W alloy, Co-30Ni-7Al-4Ti-3Mo-2W-1Nb-1Ta (by mole percent) (L19) exhibited a desired combination of high γ' volume fraction (~0.65) and good γ-γ' phase stability at 900°C, as well as high γ' solvus temperature (1126°C) and a mass density of ~8.89 g.cm^{-3}. Evidence suggests that such a combination of alloying elements is likely to provide a basis for future Co-based alloy design for high-temperature aero-engine applications (section 1.2). Commercial Ni-based superalloys are solid solution strengthened (section 1.1.1 *v*) by refractory metal elements such as Mo, W, Nb and/or Ta (section 1.1.2 *v* and *vi*). W is also anticipated to provide solid solution strengthening of γ'-strengthened Co-based superalloys. Studies have shown that systematic increase of W content in model superalloys based on the Co-Al-W system increases γ' solvus temperature as well as γ' volume fraction following ageing at 850 and 900°C (Figure 1.29). Thus, addition of W to the Ni-Co-Al-Ti-Cr quinary alloy system is of interest as W is known to contribute to the formation of γ'-Co_3(Al,W) in Co-Al-W based superalloys, where studies have focussed mainly on the $L1_2$-γ' phase stability at 900°C (section 1.2).

A detailed systematic study on the fundamental quinary system, Ni-Co-Al-Ti-Cr, is therefore essential to determine the effect of variation in Co:Ni ratio on alloy microstructure and critical properties and to provide a baseline against which to compare the influence of higher-order alloying with elements, such as W, that potentially confer superior properties at the proposed new operating temperatures for turbine discs of ~800°C.

2. Effect of Co:Ni Ratio on Elemental Partitioning in γ-γ' Ni-Co-5Al-5Ti-15Cr (at.%) alloys

Atom probe tomography has been used to characterise the effect of varying Ni:Co ratio on elemental phase partitioning at 800°C in γ-γ′ alloys derived from the Ni-Co-Al-Ti-Cr system. In all alloys tested, Al and Ti were found to partition preferentially to the γ′ phase, whereas Co and Cr partitioned preferentially to the γ phase. However, above a critical Co content (~19 at.%), the extent of partitioning of Al and Ti to the γ′ phase reduced. Conversely, Cr partitioned more strongly to the γ phase with Co additions of up to ~19 at.%, above which this preferential segregation was less pronounced. This non-monotonic trend of elemental partitioning behaviour with increasing Co concentration was attributed to a transition in the chemistry of the $L1_2$ γ′ phase from $Ni_3(Ti,Al)$ to $(Ni,Co)_3(Ti,Al)$ and thus to a change in its solute solubility.

2.1 Introduction

As discussed in Chapter 1, the drive to improve aero-engine efficiency imposes higher temperatures and stresses on the alloys from which turbine components are fabricated, requiring new higher-performance alloys to be developed that can sustain these more stringent in-service conditions. The polycrystalline Ni-based superalloys currently deployed as turbine discs typically comprise a Ni-rich solid solution (γ) exhibiting the face-centred cubic (A1) crystal structure strengthened by coherent particles of an intermetallic phase, $Ni_3(Al,Ti)$ (γ'), possessing the $L1_2$ superlattice structure [1]. One method by which superalloys can be designed with higher proof strength and greater creep resistance is through increasing the volume fraction of the strengthening γ' phase for a given temperature [12, 29]. This can be readily achieved through increasing the concentration of γ'-forming elements such as Al and Ti. Ti additions also offer the benefit of increasing the anti-phase boundary energy of the γ' phase whilst not negatively impacting alloy density [148]. However, excessive Ti additions increase the propensity to form the Ni_3Ti (η) phase, which has the $D0_{24}$ crystal structure and is generally considered deleterious to alloy properties [83]. This issue may be overcome through the use of Co-Ti co-additions [149], enabling new superalloy compositions with improved high temperature strength and creep resistance.

In the binary Co-Ti phase diagram (Figure 2.1) [150] a two-phase field exists above 600°C between an A1 Co-rich solid solution and the $L1_2$ Co_3Ti intermetallic phase. As shown in Figure 1.24, the monolithic Co_3Ti compound exhibits an increase in proof stress with

increasing temperature [151]. Indeed, the strength of Co_3Ti has been shown to exceed that of Ni_3Al at temperatures greater than 730°C [152] and is thus anticipated to confer improved high-temperature strength over conventional superalloys. Furthermore, the Co_3Ti intermetallic has the advantage of relatively low cost and low density compared with other candidate $L1_2$ intermetallics such as $Co_3(Al,W)$. Unfortunately, alloys based on the Co-Co_3Ti two-phase field are not currently considered as viable alternatives to Ni-based superalloys as their microstructures are often unstable, precipitating detrimental intermetallic phases and exhibiting discontinuous reaction products at elevated temperature [116, 117, 153]. A further barrier to the commercial use of Co-Co_3Ti based alloys is the low solvus temperature of the γ'-Co_3Ti, which typically lies in the range of 815-872°C [154]. However, simultaneous additions of Co and Ti to conventional Ni-based superalloys have been shown to enable the development of (Ni,Co)-based superalloys that exhibit improved high-temperature properties over conventional superalloys.

Co-Ti binary phase diagram removed for copyright reasons. Copyright holder is ASM International.

Figure 2.1. Binary phase diagram of the Co-Ti alloy system, where the blue and white regions indicate single-phase and two-phase fields respectively. The dashed line in the Co-rich region of the phase diagram identifies the Curie temperature [150].

A partial phase diagram of the quaternary Ni-Al-Co-Ti system has been experimentally derived for temperatures between 750 and 1100°C [155, 156, 157]. It has been reported that a continuous $L1_2$ phase field exists between Ni_3Al and Co_3Ti (γ') along their near-stoichiometric compositions and that a continuous A1 phase field (γ) exists between the Ni-rich and Co-rich

vertices of the phase diagram. Furthermore, for this range of temperatures, a continuous two-phase field of γ and γ' has been shown to exist between the Ni-Ni_3Al and Co-Co_3Ti equilibria, such that any alloy composition within this two-phase field may produce the desirable A1-$L1_2$ microstructure [155, 156, 157]. Consistent with this result, a number of studies have shown that, by incorporating elevated concentrations of Co and Ti into commercial Ni-based superalloy compositions, it is possible to achieve a γ-γ' microstructure that possesses superior high-temperature strength and creep resistance compared with conventional Ni-based superalloys [88, 148, 154, 158, 159]. This effect has been attributed to several mechanisms, most notably to an increase in γ' volume fraction as well as to an increase in the solid solution hardening of γ and γ' by Co and Ti respectively [158].

Critically, the relative concentrations of the different alloying elements in Ni-based superalloys determine the elemental partitioning behaviour between the γ and γ' phases and, therefore, the properties of the alloy. Previous studies have shown that Co partitions preferentially to the γ phase and has a significant influence on the solubility of other alloying elements in the γ and γ' phases of Ni-based superalloys [79, 87, 88, 89]. For example, additions of Co have been found to increase the volume fraction of γ' in commercial Ni-based superalloys [81, 87, 90, 91] and this has been attributed to the effect that Co has in reducing the solubility of Al and Ti in the γ solid solution [81, 89]. This is consistent with a recent study by Oni *et al*. [79], who used atom probe tomography to highlight the differences in elemental partitioning between the γ and γ' phases in three Ni-Al-Co-Ti alloys with varying Co and Ti content.

Chromium is an important addition in polycrystalline Ni-based superalloys as it imparts resistance to oxidation and hot corrosion via the formation of a protective (diffusion-resistant) Cr_2O_3-rich scale [12]. However, high Cr concentrations in the alloy increase the propensity to form deleterious topologically close-packed (TCP) intermetallic phases such as σ [1]. Therefore, it is desirable that the partitioning of Ni, Al, Co and Ti between the γ and γ' phases is assessed in the presence of Cr, as its concentration in the γ phase must be optimised to provide environmental resistance whilst also retaining microstructural stability. Differences observed in the hardness of γ-γ' Ni-Co-Al-Ti-Cr alloys have been attributed to the effect of the Ni:Co ratio on the partitioning of the other elements [160] and therefore an improved understanding of the phase equilibria is critical if optimised compositions are to be designed. To this end, this study aims to determine the influence of Ni:Co ratio on elemental partitioning behaviour in alloys of the Ni-Co-Al-Ti-Cr system.

2.2 Experimental Procedure

2.2.1 Material and heat treatment

The series of model superalloys investigated in the present study was based on the $(Ni,Co)_{75}Al_5Ti_5Cr_{15}$ (at.%) system in which the Ni:Co concentration ratio was varied from 1:0 to 1:3 (Table 2.1). The concentration ratio of Al:Ti was kept at one to allow systematic assessment of the influence of Co on the partitioning of solute elements between the γ and γ′ phases. Additionally, the total Al+Ti content was fixed at 10 at.% to achieve comparable γ' volume fractions in the alloys. The alloys were named according to their nominal at.% Co.

Vacuum arc melting was used to fabricate polycrystalline samples of the seven alloys from raw elements of at least 99.9% purity. Thermal analysis of the as-cast alloys was performed using differential scanning calorimetry (DSC) to determine the critical phase transformation temperatures, knowledge of which was required for the selection of suitable homogenising temperatures. DSC tests were performed using a Netzsch 404 heat-flux calorimeter operating at temperatures of up to 1450°C with a heating rate of 10°C min^{-1}. The alloys were sealed in quartz tubes under an argon atmosphere before being subjected to a homogenisation heat treatment in the single γ phase field at 1250°C for 24 hours to minimise the effect of casting-induced micro-segregation. The homogenisation heat treatment temperature was chosen to be higher than the γ′ solvus temperatures of all of the alloys but sufficiently lower than their solidus temperatures to avoid incipient melting. Following the homogenisation heat treatment, all alloys were subjected to an ageing heat treatment at 800°C for 1000 hours to attain the thermodynamically stable phase distributions at this temperature. The alloy specimens were then air-cooled.

Table 2.1. Nominal chemical compositions of alloys Ni-Co-5Al-5Ti-15Cr (at.%), together with measured compositions and standard deviations (σ) obtained using SEM-EDS. Alloys were aged at 800°C for 1000 hours.

Alloy	Nominal composition (at.%)					Measured composition (at.%)									
	Ni	Co	Al	Ti	Cr	Ni	±σ	Co	±σ	Al	±σ	Ti	±σ	Cr	±σ
0Co	75.0	0.0	5.0	5.0	15.0	74.34	0.06	-	-	5.46	0.07	5.35	0.06	14.85	0.09
9Co	65.6	9.4	5.0	5.0	15.0	64.9	0.3	9.4	0.3	5.41	0.17	5.4	0.2	14.91	0.10
19Co	56.3	18.8	5.0	5.0	15.0	55.9	0.6	18.85	0.15	5.2	0.9	5.21	0.10	14.83	0.11
28Co	46.9	28.1	5.0	5.0	15.0	46.5	0.2	28.42	0.14	5.24	0.16	5.31	0.09	14.54	0.15
38Co	37.5	37.5	5.0	5.0	15.0	37.55	0.04	37.88	0.06	4.69	0.03	5.13	0.06	14.76	0.06
47Co	28.1	46.9	5.0	5.0	15.0	27.78	0.19	47.9	0.3	4.91	0.17	4.92	0.18	14.52	0.17
56Co	18.8	56.3	5.0	5.0	15.0	18.89	0.08	57.02	0.14	4.31	0.05	5.06	0.05	14.71	0.05

2.2.2 Scanning electron microscopy (SEM)

Alloy specimens in the as-homogenised and fully aged conditions were mounted in conductive Bakelite and prepared for metallographical examination by grinding using wet SiC abrasive paper. They were then polished using progressively finer diamond suspensions down to 1 µm. Specimens were subsequently electrolytically etched using a 10% phosphoric acid solution in order to dissolve the γ matrices and to highlight the γ′ precipitates. Microstructural examination of the alloys was performed using an FEI Nova NanoSEM 450 scanning electron microscope in secondary electron mode. Energy dispersive X-ray spectroscopy (EDS) was performed using a Bruker XFlash 6 solid state EDS system to identify the overall compositions of the alloys (Table 2.1), which were obtained from a minimum of 5 large area scans of at least 0.5 × 0.5 mm in size.

To permit estimation of mean γ′ precipitate size, the mounted specimens were re-polished and etched with OP-S (colloidal silica suspension) diluted 1:1 in water. The mean size of γ' precipitates in each aged alloy was quantified by taking back-scattered electron images using the FEI Nova NanoSEM 450 microscope and analysing at least 2,000 precipitates in image analysis software, ImageJ.

2.2.3 Differential scanning calorimetry (DSC)

DSC was performed to determine the γ′ solvus, solidus and liquidus temperatures of the seven model superalloys after the ageing heat treatment of 800°C for 1000 hours. Small discs of 5 mm in diameter and 1 mm in thickness were extracted from each alloy in the fully aged condition using spark erosion. DSC tests on these aged alloy specimens were performed as for the as-cast alloy specimens using a Netzsch 404 heat-flux calorimeter operating at temperatures of up to 1450°C with a heating rate of 10°C min^{-1}. Data analysis was performed using Igor Pro 6.3 software [161].

2.2.4 Atom probe tomography (APT)

Atom probe tomography (APT) was performed to determine the compositions of the γ and γ' phases within the seven model superalloys aged at 800°C for 1000 hours. Cuboidal rods (0.5 × 0.5 × 15 mm) were extracted from each alloy in the fully aged condition using electrical discharge machining (EDM). From these rods, specimens suitable for APT analysis were prepared in the form of sharply pointed needles by a rough electropolish using a 25% perchloric acid solution at a voltage of 15-20 V, followed by fine electropolishing using a more dilute

perchloric acid solution (2%) at a voltage of 15 V. All APT experiments were carried out using a CAMECA local-electrode atom-probe (LEAP) 4000X HR instrument at the Michigan Center for Materials Characterization. The instrument was operated in the high-voltage pulsing mode with the superimposed pulsing voltage at nominally 20% of the steady-state voltage and a detection efficiency of ~36%. Specimen temperatures were maintained at nominally 50 K. Initial data processing was performed using the CAMECA IVAS 3.6.8 software. Data were subsequently processed to deconvolve the overlapping isotopic peaks. Proximity histograms (proxigrams) were generated from the data acquired, which displayed the atomic fraction of each element as a function of its proximity to the γ/γ' interface, as defined using an isoconcentration surface of Al and/or Ti. These surfaces were used as reference points for calculating the proxigrams, which were computed 10 nm either side of the interfaces using a 0.5 nm bin size. Error bars displayed represent one standard deviation (σ) and were calculated using Equation 2.1:

$$\sigma = \sqrt{(C_i(1 - C_i))/N} \qquad \text{Equation 2.1}$$

where C_i is the calculated atomic fraction of each element *i* and *N* is the total number of atoms in each bin [162]. For each alloy, the mean elemental concentrations in the γ and γ' phases were quantified using data points away from the interface, where the deviation from the average value was not more than ~1 at.%. The uncertainty associated with these values was taken to be the standard deviation of the elemental concentrations over the range used to calculate the average values.

The elemental concentration data were used to calculate the volume fraction of the γ' phase in each alloy using the lever rule: $C_i^{\text{alloy}} = (C_i^{\gamma'} . f^{\gamma'}) + (C_i^{\gamma} . (1 - f^{\gamma'}))$, where C_i^{alloy} is the nominal concentration of element *i* in the alloy, $C_i{}^{\gamma}$ and $C_i{}^{\gamma'}$ are the concentrations of the same element in the γ and γ' phases respectively and $f^{\gamma'}$ is the volume fraction of γ' in the alloy. The overall γ' volume fraction in each alloy was determined by rearranging the lever rule (Equation 2.2):

$$f^{\gamma'} = \frac{C_i^{\text{alloy}} - C_i^{\gamma}}{C_i^{\gamma'} - C_i^{\gamma}} \qquad \text{Equation 2.2}$$

Values for $C_i^{\text{alloy}} - C_i^{\gamma}$ were then plotted against values for $C_i^{\gamma'} - C_i^{\gamma}$ for the individual alloying elements and a linear regression analysis performed to determine the line gradient, equivalent to $f^{\gamma'}$.

2.2.5 Computational modelling

The compositions of the γ and γ′ phases in the quinary Ni-Co-Al-Ti-Cr alloys were calculated by the CALPHAD approach using the Thermo-Calc software with the TCNi8 database. Phase equilibria were calculated for 800°C without suppressing the formation of any phases. In addition, the equilibrium phase transition temperatures of each alloy were computed using Thermo-Calc with the TCNi8 database.

2.3 Results

Duplex γ-γ′ microstructures were observed in all alloys in their homogenised condition and following ageing at 800°C with no other phases observed (Figure 2.2). The Co-free alloy (Figure 2.2a) and those alloys containing up to 38 at.% Co (Figure 2.2b-e) exhibited isolated γ′ precipitates. With increasing Co content from 0 to 38 at.%, there appeared a decrease in mean γ' precipitate size, measured as a cube edge length assuming that the precipitates in each alloy adopted a cuboidal morphology. Overall, γ' precipitate size for the aged alloys decreased from ~119 ±4 nm for the 0Co alloy to ~67 ±3 nm for the 38Co alloy. The 47Co and 56Co alloys (Figure 2.2f, g) exhibited elongated γ′ precipitates, suggesting directional coalescence during precipitate growth. It should be noted that the triangular appearance of the precipitates in the 47Co alloy (Figure 2.2f) was consistent with sectioning away from the {100} planes.

It should be noted that raising the Co content to 75 at.% to achieve the Ni-free quaternary alloy (Co-5Al-5Ti-15Cr at.%) appeared to destabilise the γ-γ' microstructure, indicating the need for a critical Ni content (Appendix, section 8.1).

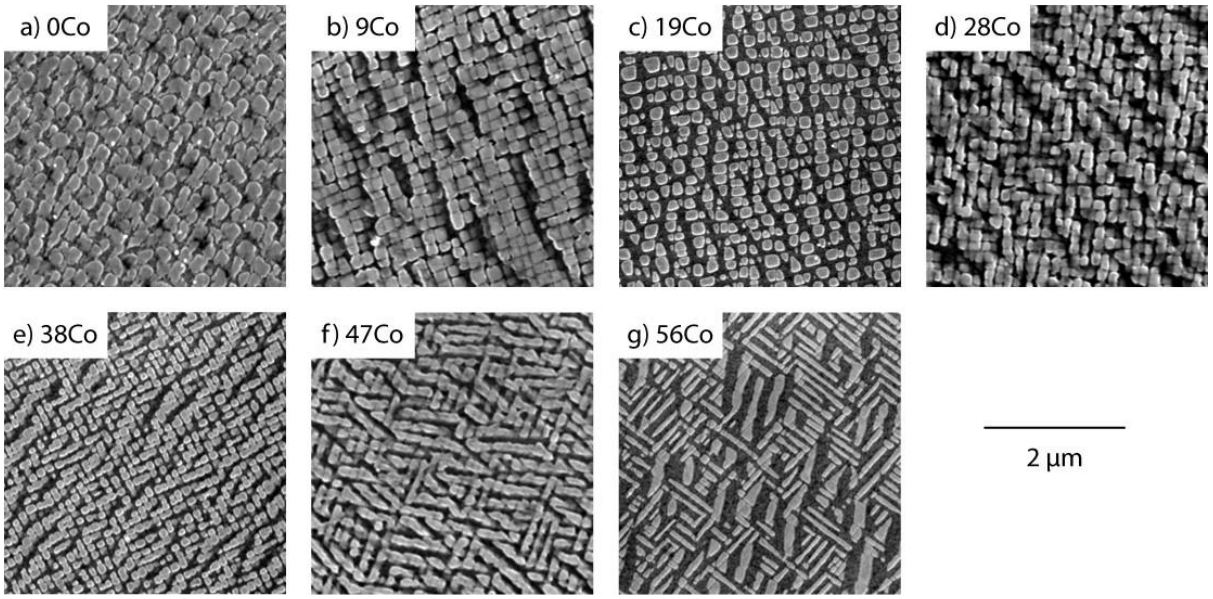

Figure 2.2. Secondary electron images of the A1-$L1_2$ microstructure, showing γ' precipitates embedded in the γ matrix of alloys: (a) 0Co, (b) 9Co, (c) 19Co, (d) 28Co, (e) 38Co, (f) 47Co and (g) 56Co following ageing at 800°C for 1000 hours.

Figure 2.3 shows the volume fraction of the γ′ phase in each of the seven γ-γ' alloys as derived from the experimental APT data as a function of the nominal Co content, compared with predicted values determined using Thermo-Calc with the TCNi8 database. The experimental data indicate that the γ′ volume fraction increased slightly with Co additions of up to 19 at.%, with a subsequent decrease in γ′ volume fraction observed as alloy Co content increased further. The modelled predictions of γ′ volume fraction were consistently lower than experimental values.

2.3.1 Phase transition temperatures

Figure 2.4 shows the γ′ solvus, solidus and liquidus temperatures of the aged alloys as a function of the nominal Co content. The experimental data indicate that the solvus temperature of the γ′ phase decreased with increasing Co concentration, consistent with Thermo-Calc predictions for the alloys of higher Co content. The Co concentration appears to have had a less pronounced effect on the experimentally obtained solidus and liquidus temperatures.

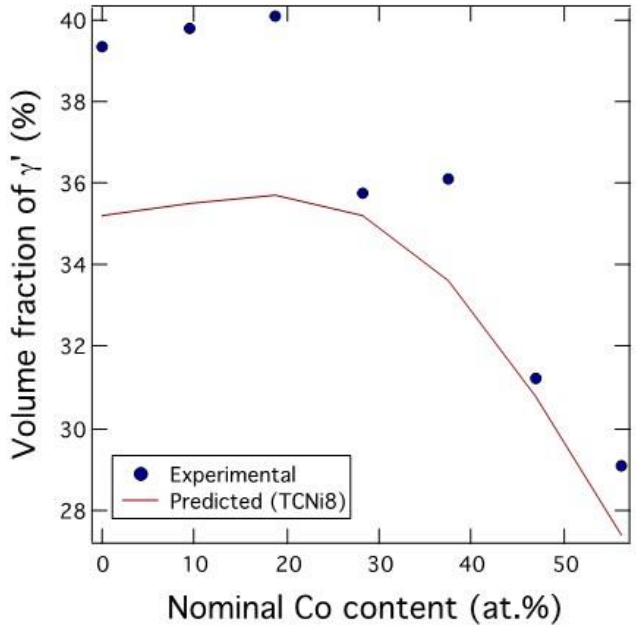

Figure 2.3. Volume fraction of the γ' phase in the Ni-Co-5Al-5Ti-15Cr (at.%) alloys tested as a function of nominal alloy Co content. Experimental data (markers) are compared with thermodynamic model predictions (solid lines) obtained using Thermo-Calc with the TCNi8 database for 800°C.

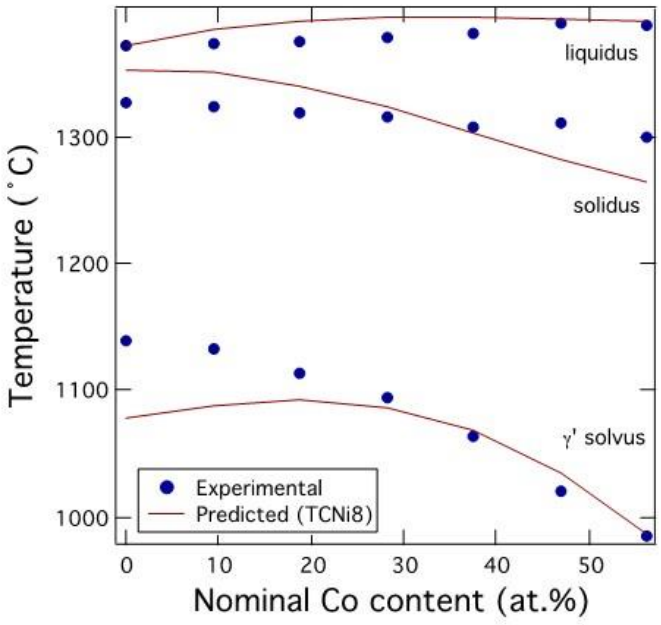

Figure 2.4. Liquidus, solidus and γ' solvus temperatures of the Ni-Co-5Al-5Ti-15Cr (at.%) alloys as a function of nominal alloy Co content. Experimental data (markers) are compared with thermodynamic model predictions (solid lines) obtained using Thermo-Calc with the TCNi8 database.

2.3.2 Elemental phase partitioning

Compositional data obtained from the 0Co alloy were used as a baseline to which corresponding data from the quinary (Co-containing) alloys could be compared. Figure 2.5a displays a 10 nm slice through the reconstruction of the atom probe sample of the aged Co-free alloy, showing the Ni, Al, Ti and Cr solute distributions where each coloured dot represents one atom of a particular solute species. Two phases were identified, pertaining to γ and γ' as indicated. The associated proximity histograms are presented in Figure 2.5b. It can be seen that the concentrations of Ni in the γ and γ' phases were similar, although a slight decrease in Ni concentration at the interface was observed. The other elements showed a marked difference in solute concentration between the γ and γ' phases. The γ phase was enriched with Cr (~23 at.%) and the γ' phase was enriched with Ti (~11 at.%) and Al (~11 at.%).

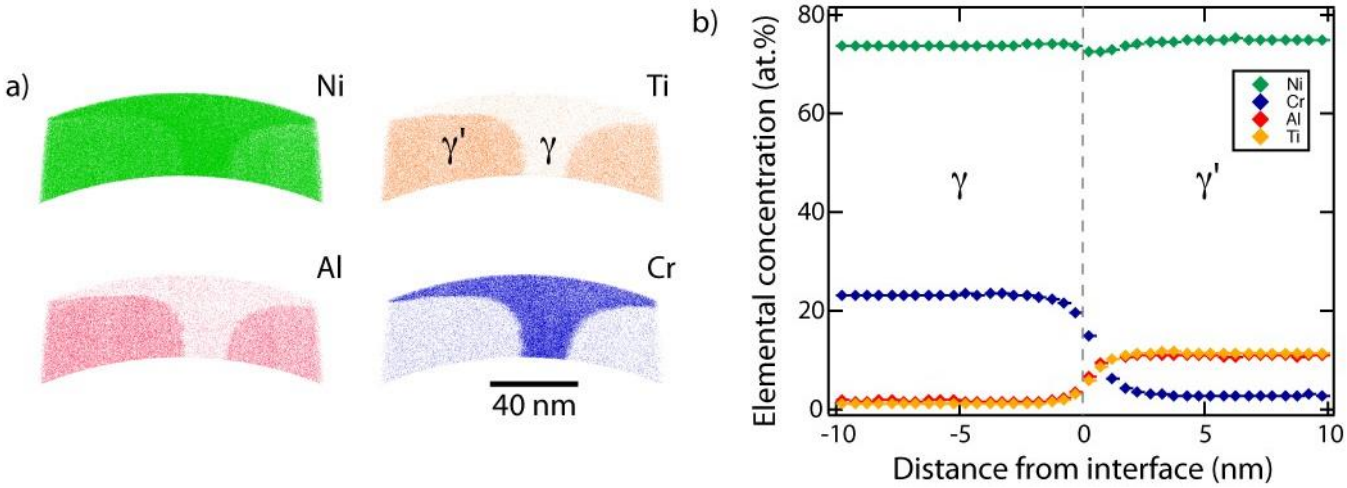

Figure 2.5. (a) Atom probe reconstructions of the spatial distributions of Ni, Ti, Al and Cr atoms within a 10 nm slice through the volume analysed of aged **alloy 0Co**. 100% Al (red), 100% Ti (orange), 100% Cr (blue) ions are shown but only 70% Ni (green) ions are shown so that the γ and γ' phases may be distinguished. (b) Proxigrams showing solute concentration profiles across the γ/γ' interface. Error bars have been included but are smaller than the symbols used.

Figure 2.6a displays a 10 nm slice through the atom probe reconstruction of the aged 56Co alloy, showing the Ni, Ti, Al, Cr and Co solute distributions. It is evident that the γ matrix was rich in Cr and Co and that the γ' precipitates were rich in Ni, Ti and Al. The corresponding proxigrams shown in Figure 2.6b permit an estimate to be obtained for elemental concentration within the γ and γ' phases. Thus, the γ phase comprised *circa*. 59 at.% Co and 21 at.% Cr whilst the γ' phase comprised *circa*. 30 at.% Ni, 12 at.% Ti and 8 at.% Al. The proxigrams also indicated the presence of a diffuse interface between the γ and γ' phases approximately 20 nm in width. In the γ phase approaching the interface, there appeared to be

a slight enrichment in Co and Cr and depletion in Ni, Ti and Al. This may be attributed to the coarsening of the γ' precipitates observed in this alloy (Figure 2.2g). Figures showing the atom probe reconstructions and proximity histograms pertaining to the other five alloys are provided in the Appendix (section 8.2).

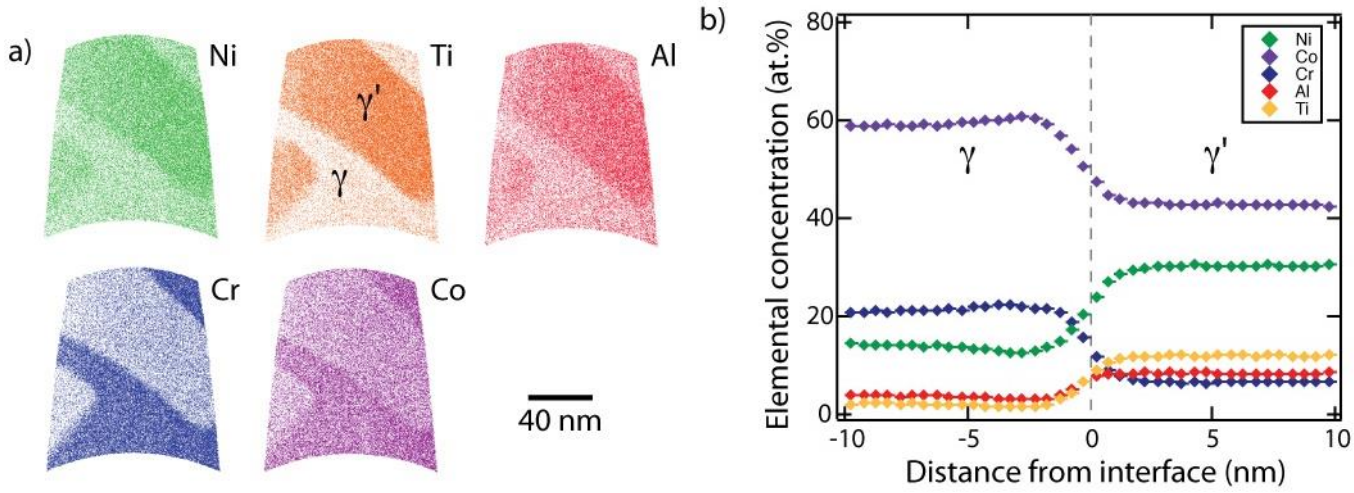

Figure 2.6. (a) Atom probe reconstructions of the spatial distributions of Ni, Ti, Al, Cr and Co atoms within a 10 nm slice through the volume analysed of aged **alloy 56Co**. To distinguish the γ phase from the γ' phase, only a fraction of the ions are shown for each element [10% Ni (green), 30% Al (red), 30% Ti (orange), 20% Cr (blue) and 4% Co (purple)]. (b) Proxigrams showing solute concentration profiles across the γ/γ' interface. Error bars have been included but are smaller than the symbols used.

Comparison of Figure 2.5 and Figure 2.6 indicates that the addition of 56 at.% Co to the Ni-Al-Ti-Cr quaternary alloy caused less extensive partitioning of Al than of Ti to the γ' phase. Increased partitioning of Ni towards the γ' phase was observed in alloy 56Co compared with alloy 0Co.

Table 2.2 shows the mean atomic concentrations of elements within the γ and γ' phases for each alloy, quantified from their respective proxigrams. The elemental partitioning coefficient (k_i) was defined as the ratio of the concentration of element i in the γ' phase ($C_i^{\gamma'}$) to the concentration of the same element in the γ phase (C_i^{γ}) according to (Equation 1.4):

$$k_i = \frac{C_i^{\gamma'}}{C_i^{\gamma}}$$

This parameter is useful in the assessment of preferential phase partitioning of solutes and is displayed for i = Al, Ti, Ni, Cr and Co in Table 2.2. As inferred from k_i values in excess of 1, it is apparent that Ti and Al, and to a lesser extent Ni, segregated preferentially to the γ'

phase. At any given alloy Co content, Ti exhibited a higher k_i than Al, suggesting that preferential partitioning to the γ′ phase was higher for Ti than for Al. Conversely, Cr and Co partitioned preferentially to the γ matrix phase in all alloy compositions, as indicated by k_i values of less than unity. The extent of preferential partitioning of individual alloying elements was observed to be highly dependent on the Ni:Co ratio of the alloy.

Table 2.2. Average chemical compositions (at.%) of the γ and γ' phases and their associated standard deviations in the alloys following ageing at 800°C for 1000 hours, as obtained from the APT proxigram data.

Alloy	Phase	Average composition (at.%)										Partitioning ratio ($C_i^{\gamma'}/C_i^{\gamma}$)									
		Al	±σ	Ti	±σ	Ni	±σ	Cr	±σ	Co	±σ	k_{Al}	±σ	k_{Ti}	±σ	k_{Ni}	±σ	k_{Cr}	±σ	k_{Co}	±σ
0Co	γ	1.77	0.03	1.24	0.03	73.77	0.09	23.23	0.09	-	-	6.15	0.11	9.2	0.2	1.015	0.003	0.124	0.003	-	-
	γ'	10.85	0.07	11.37	0.12	74.9	0.2	2.87	0.08	-	-										
9Co	γ	1.64	0.08	1.00	0.05	60.48	0.18	23.63	0.14	13.25	0.16	6.9	0.4	12.2	0.7	1.180	0.005	0.104	0.005	0.200	0.006
	γ'	11.30	0.16	12.2	0.3	71.39	0.18	2.46	0.11	2.65	0.07										
19Co	γ	1.41	0.08	0.73	0.05	46.75	0.18	24.99	0.08	26.1	0.2	8.0	0.5	16.6	1.1	1.484	0.006	0.080	0.001	0.202	0.004
	γ'	11.27	0.09	12.10	0.05	69.37	0.08	2.00	0.02	5.26	0.10										
28Co	γ	1.74	0.08	0.91	0.07	36.6	0.2	23.82	0.18	36.89	0.18	6.5	0.3	13.5	1.1	1.770	0.011	0.086	0.004	0.260	0.006
	γ'	11.31	0.13	12.22	0.09	64.8	0.2	2.05	0.09	9.6	0.2										
38Co	γ	2.07	0.09	0.95	0.06	25.2	0.3	24.9	0.2	46.8	0.3	5.4	0.3	13.5	0.9	2.28	0.03	0.098	0.004	0.344	0.005
	γ'	11.12	0.19	12.8	0.2	57.5	0.3	2.45	0.09	16.1	0.2										
47Co	γ	3.09	0.18	1.6	0.2	19.8	0.4	21.7	0.3	53.9	0.5	3.3	0.2	7.3	0.9	2.32	0.05	0.173	0.007	0.527	0.009
	γ'	10.26	0.19	11.7	0.3	46.0	0.4	3.75	0.15	28.4	0.4										
56Co	γ	3.72	0.15	2.04	0.18	13.9	0.4	21.2	0.4	59.2	0.4	2.27	0.09	5.9	0.5	2.18	0.06	0.308	0.007	0.723	0.006
	γ'	8.43	0.06	12.0	0.1	30.28	0.15	6.53	0.08	42.79	0.15										

2.3.3 Effects of alloying with cobalt

To elucidate how the partitioning of Al, Ti and Cr between the γ and γ' phases varied with the Ni:Co ratio, the elemental concentrations within both phases are plotted in Figure 2.7 as a function of alloy Co content. Superimposed on these plots as solid lines are the equilibrium elemental concentrations of the phases computed at 800°C using thermodynamic modelling. For each alloy, the thermodynamic modelling predicted the formation of a duplex γ-γ' microstructure with no additional phases.

The experimental data shown in Figure 2.7a indicate that the concentration of Al within the γ phase decreased up to a Co content of ~19 at.% (Ni:Co ratio of 3:1), above which Al concentration increased, inferring a transition in elemental partitioning behaviour at this Ni:Co ratio. Correspondingly, within the γ' phase (Figure 2.7b), an increase in Al concentration was observed initially on addition of Co to the quaternary Ni-Al-Ti-Cr alloy, followed by a decrease in Al concentration as the Co content increased further. The variation in Al concentration with increasing Co content, as predicted by thermodynamic modelling (solid lines in Figure 2.7a, b) followed a similar trend, but suggests that the critical Co content at which there is a transition in partitioning behaviour was higher than that found experimentally.

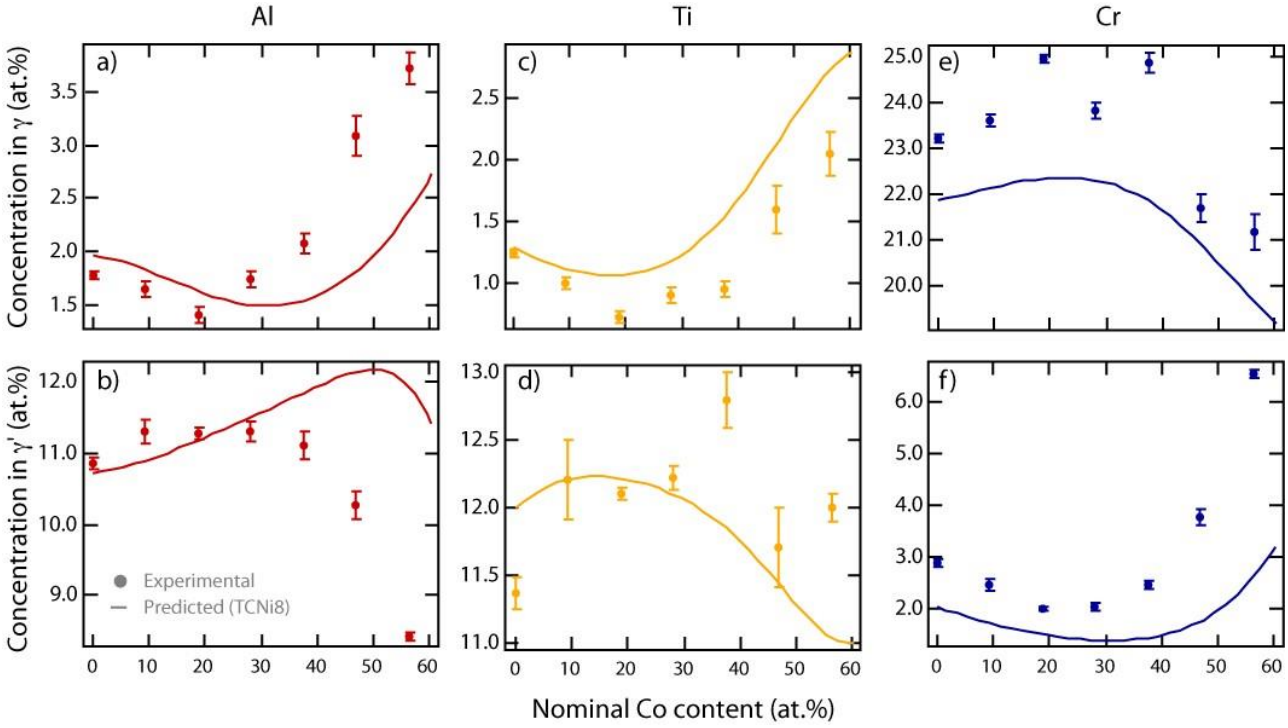

Figure 2.7. Concentration of (a) Al in the γ phase; (b) Al in the γ' phase; (c) Ti in the γ phase; (d) Ti in the γ' phase; (e) Cr in the γ phase; (f) Cr in the γ' phase as a function of nominal alloy Co content. Experimental data (markers) are contrasted with thermodynamic predictions (solid lines) obtained using Thermo-Calc with the TCNi8 database for 800°C.

From the Ti partitioning data (Figure 2.7c) it can be seen that an increasing Co content (up to ~19 at.%) gave rise to a decrease in the Ti concentration within the γ phase, followed by increased Ti concentration as Co content rose further. This suggests that the observed preferential partitioning to the γ' phase occurred to a lesser extent at higher Co content. The thermodynamic modelling data (solid line in Figure 2.7c) predicted a similar transition in phase partitioning behaviour at ~19 at.% Co. However, the concentrations of Ti in the γ phase, as predicted by modelling, were consistently higher than those determined by experiment. For the Ti concentration within the γ' phase of each alloy (Figure 2.7d) experimental data showed no clear correlation between Ti concentration and alloy Co content, whereas corresponding thermodynamic modelling data predicted an increase and then decrease in Ti concentration within the γ' phase as Co content increased.

With respect to the partitioning of Cr, Figure 2.7e indicates that the concentration of Cr within the γ phase increased slightly up to a Co content of ~19 at.%. For alloys with significantly higher Co content, Cr concentration in the γ phase was observed to decrease. Conversely, within the γ′ phase (Figure 2.7f), an initial slight decrease in the Cr concentration was observed with increasing Co content (up to ~19 at.%) followed by an increase in Cr concentration as Co content increased further. The modelling data displayed a comparable trend to the experimental data (Figure 2.7e, f) though the experimentally-determined Cr concentrations in both the γ and γ' phases were consistently higher than those predicted using thermodynamic data.

To summarise the experimental data presented thus far, Figure 2.8 shows how the elemental partitioning coefficients (k_i) were dependent on the Co content of the alloy. From Figure 2.8a, it can be seen that the k_i of Ti was higher than that for Al for each alloy composition tested, with Ti and Al displaying a peak in k_i at a Co content of ~19 at.%. In contrast, Cr exhibited a minimum in the k_i at this critical Co content (~19 at.%) (Figure 2.8b). Figure 2.8c indicates that Ni segregated preferentially to the γ' phase in the presence of Co and did so to a greater extent with increasing Co additions of up to 47 at.%. Furthermore, it appears that Co partitioned to the γ' phase to a greater extent as Co concentration in the alloy increased.

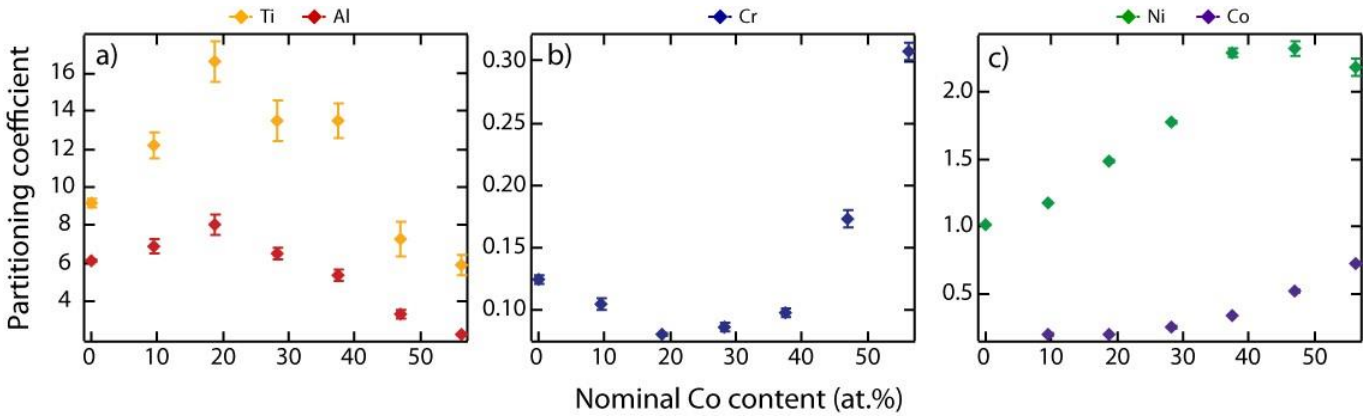

Figure 2.8. Variation in elemental partitioning coefficients (k_i) of (a) Al and Ti; (b) Cr and (c) Ni and Co as a function of nominal alloy Co content.

Figure 2.9 shows the elemental constitution of the two sub-lattices of the γ' phase as a function of alloy Co content, as predicted by thermodynamic modelling. Figure 2.9a, b suggest that, as expected, Ti preferentially occupies the Al sub-lattice. A significant fraction of the Cr concentration predicted to reside in the γ′ phase (solid line in Figure 2.7f) is anticipated to occupy the Al sub-lattice (Figure 2.9c, d). This is suggested by the comparable concentration profiles of Figure 2.7f and Figure 2.9d in addition to the relatively high concentration values calculated for Cr on the Al sub-lattice. Figure 2.9e, f would indicate that, for all alloy Co contents, Co substitutes predominantly onto the Ni sub-lattice.

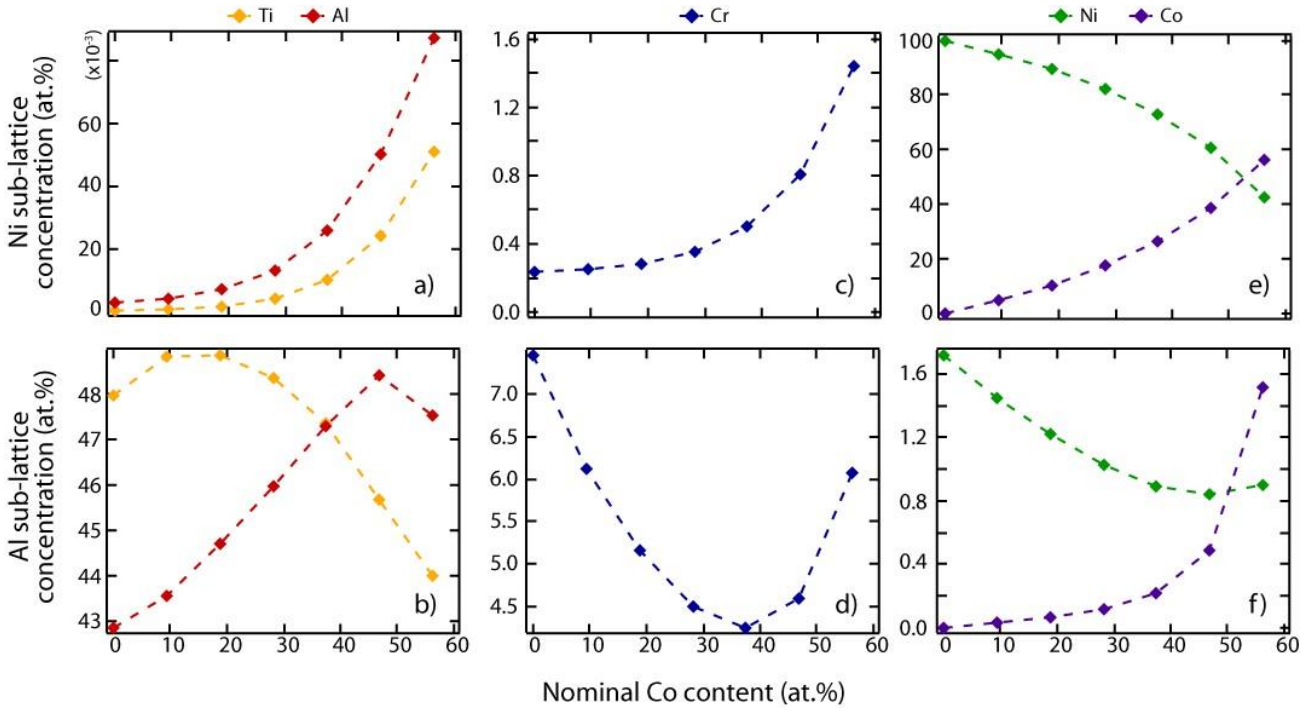

Figure 2.9. Concentration of (a) Al and Ti on the Ni sub-lattice; (b) Al and Ti on the Al sub-lattice; (c) Cr on the Ni sub-lattice; (d) Cr on the Al sub-lattice; (e) Ni and Co on the Ni sub-lattice; (f) Ni and Co on the Al sub-lattice with varying alloy Co content, as predicted by Thermo-Calc with the TCNi8 database for 800°C.

2.4 Discussion

With increasing Co content in γ-γ' Ni-Co-Al-Ti-Cr alloys, both Al and Ti were observed to partition more extensively to the γ' phase up to the Co content of ~19 at.%, after which the preferential segregation of Al and Ti to the γ' phase was less extensive (Figure 2.8a). The inference is that a transition in elemental partitioning behaviour occurs at a critical Co content in the vicinity of 19 at.%. The more extensive degree of partitioning of Al and Ti to the γ′ phase at relatively low Co contents may be attributed to the effect that Co has in reducing the solubility of Al and Ti in the Ni-based γ solid solution [81, 89].

In contrast to Al and Ti, with increasing Co additions up to ~19 at.%, the Cr content in the γ phase increased (Figure 2.7e) accompanied by a concomitant decrease in Cr concentration in the γ′ phase (Figure 2.7f). Increasing concentrations of Cr in the γ phase at relatively low Co content may be due to the increased partitioning of Al and Ti to the γ′ phase (Figure 2.7a, c). For alloys with significantly higher Co content, the concentration of Cr in the γ′ phase appeared to increase (Figure 2.7f) with a concomitant decrease in the γ phase (Figure 2.7e). This suggests that the γ' phase exhibits a higher solubility for Cr in the presence of high Co concentrations.

The non-monotonic dependence of elemental concentration within the γ and γ′ phases on increasing alloy Co content may be explained with reference to the quaternary phase diagram of the Ni-Co-Al-Ti system derived for the temperature range 750-1100°C [155, 156]. In the Ni-Al rich region of the quaternary phase diagram, the $L1_2$ γ′ phase is likely to be $Ni_3(Al,Ti)$. Where Co and Ti content are increased simultaneously, the effect is to shift the alloy composition across the γ-γ′ two-phase field connecting the Ni-Ni_3Al and Co-Co_3Ti equilibria. This plausibly corresponds to a gradual chemical shift of the γ′ phase from Ni_3Al-based to Co_3Ti-based [155, 156]. The resulting difference in phase chemistry of the γ′ would be expected to induce different elemental phase partitioning in low and high Co variants of alloys from the quaternary Ni-Co-Al-Ti system. Indeed, it has been reported that in γ-γ′ Ni-Co-Al-Ti alloys, a simultaneous decrease in the concentration ratios of Ni:Co and Al:Ti corresponds to marked changes in the partitioning coefficients of Al and Ti on ageing at 750°C [79]. However, the compositions at which these transitions occurred were not established in that study as a result of the limited number of samples investigated. It has been well established that Ti can substitute extensively for Al in Ni_3Al whereas Co_3Ti exhibits relatively low solubility for ternary alloying elements such as Al [119]. In the current alloys, the transition in elemental phase partitioning behaviour observed with increasing alloy Co content is thus

putatively attributed to a change in the solute solubility in the γ′ phase, driven by the underlying thermodynamics of the system.

Despite the preferential partitioning of Co towards the γ matrix phase (k_{Co} consistently < 1; Table 2.2), an increase in the partitioning coefficient of Co was observed with its increasing concentration in the alloy (Figure 2.8c). This indicates that the preferential segregation of Co towards the γ phase was occurring to a lesser extent as its concentration in the alloy increased, and that the partitioning of Co toward the γ′ phase was becoming more pronounced. In a recent study published by Oni *et al*., 2016 [79], which examined the atomic site occupancies in γ′ within quaternary Ni-Al-Co-Ti alloys, it was reported that the site preference of Co in the A_3B structure of γ′ changes from a random distribution between the A and B sub-lattices in the 15 at.% Co alloy to the A sub-lattice with alloy Co content of 30 and 55 at.%. This would indicate that, in Ni-Al-Co-Ti alloys, a chemical transition of the γ′ occurs from Ni_3(Al,Ti) to $(Ni,Co)_3$(Al,Ti) at a critical Co content in the range of 15-30 at.%. Thus, in the current study, it is plausible that at Co contents above ~19 at.%, Co preferentially occupies the Ni sub-lattice of the $L1_2$ structure to form $(Ni,Co)_3$(Ti,Al) and this may underlie the observed phase partitioning behaviour at higher Co contents. However, thermodynamic modelling predicted that the Co partitioning to the γ′ phase substitutes predominantly onto the Ni sub-lattice *in all alloys* (Figure 2.9e, f).

It may be inferred from Figure 2.7f that the γ′ phase of alloys comprising Co contents greater than ~19 at.% exhibit rapidly increasing solubility for Cr. With regards to the atomic site preferences of Co and Cr in $L1_2$ Ni_3Al, a first-principles study by Chaudhari *et al*., 2013 [66] suggests that if Co were to reside on the Ni sub-lattice of the γ′ phase, then the most thermodynamically stable atomic configuration would be for Cr to occupy the Al sites of the $L1_2$ lattice. Their study, using density functional theory calculations, indicated that the substitution of Co on to the Ni sub-lattice of the γ′ generates a larger energy barrier for a Cr atom residing on the Al sub-lattice to transfer to the Ni sub-lattice. The implication is that by raising the Co content of the alloy, and with its substitution on to the Ni sub-lattice of the γ′ phase, there is an increase in the thermodynamic driving force for Cr to partition to the Al sites of the Ni_3Al lattice. Furthermore, it has been shown both theoretically and experimentally that in the $L1_2$ Co_3Ti compound, Cr substitutes onto the Ti sub-lattice [117, 119]. Thus, it follows that at higher alloy Co contents (above ~19 at.%), Cr may increasingly readily partition to the γ′ phase in which it occupies the (Ti,Al) sub-lattice of $(Ni,Co)_3$(Ti,Al). This is supported by the thermodynamic predictions of atomic site occupancies in γ′, which indicate that the Cr

partitioning to the γ' phase at higher Co content substitutes preferentially for Ti and Al (Figure 2.9b, d). This substitution of Cr onto the (Ti,Al) sub-lattice may underlie the observed decrease in the preferential partitioning of Ti and Al to the γ′ with Co contents increasing above ~19 at.% (Figure 2.8a).

From Figure 2.8c, it is apparent that a Co content of 56 at.% corresponds to a notable decrease in k_{Ni} and to a concurrent increase in k_{Co} that may suggest the onset of a compositional transition of the γ′ from Ni-based to Co-based. It may be inferred from Table 2.2 that the γ′ phase of alloy 56Co comprises a higher concentration of Co than Ni and is thus Co_3Ti-based. Therefore, it is plausible that, between 47 and 56 at.% Co in the alloy, there is a chemical transition of the γ′ phase occurring from $(Ni,Co)_3(Ti,Al)$ to Co_3Ti.

2.5 Conclusions

Through APT, this study examined the effects that the Ni:Co ratio has on the elemental phase partitioning in alloys from the $(Ni,Co)_{75}Al_5Ti_5Cr_{15}$ (at.%) alloy system at 800°C. The following conclusions were drawn.

- All alloys were observed to exhibit a two-phase γ-γ′ microstructure in which Ni, Al and Ti segregated preferentially to the γ' precipitate phase (k_i > 1) and Cr and Co partitioned preferentially to the γ matrix phase (k_i < 1).
- Ni was observed to partition more strongly to the γ' phase (i.e k_{Ni} increases) with increasing Co additions of up to 47 at.%. However, Co, whilst consistently partitioning preferentially toward the γ matrix (k_{Co} < 1), showed an increased tendency to partition toward the γ' phase as alloy Co content increased (i.e. k_{Co} increases).
- The preferential partitioning of Ti and Al toward the γ′ phase was observed to increase as alloy Co content increased up to ~19 at.%. As Co concentration was raised further, the γ′ solubility for both Ti and Al appeared to decline.
- Cr exhibited a more extensive degree of preferential partitioning toward the γ matrix with increasing Co additions of up to ~19 at.%, above which the concentration of Cr in the γ′ phase appeared to increase.
- The non-monotonic correlation observed between elemental phase partitioning and alloy Co content was attributed to a transition in the composition of the γ′ phase from $Ni_3(Ti,Al)$ towards Co_3Ti via $(Ni,Co)_3(Ti,Al)$.

- The substitution of Co onto the Ni sub-lattice at higher Co contents (greater than 19 at.%) may be responsible for the apparent increase in Cr substitution onto the aluminium sub-lattice and concomitant decrease in the solubility of γ′ for Al and Ti, consistent with the thermodynamic data.
- Although predictions of phase compositions based on thermodynamic equilibrium displayed a similar trend to experimental results with respect to phase partitioning in relation to Co content, the absolute values of transition concentrations differed.
- Alloy γ' volume fraction was observed to increase slightly with increasing Co content up to 19 at.% (to a maximum value of 0.40), corresponding to maximal preferential partitioning of Ti and Al to the γ' phase. With increasing Co content beyond ~19 at.%, a reduction in γ' volume fraction was observed.

3. Effect of Co:Ni Ratio on Lattice Misfit of γ-γ' Ni-Co-5Al-5Ti-15Cr (at.%) alloys

The effect of a systematic increase in Co:Ni ratio on lattice misfit of γ-γ′ alloys of the Ni-Co-Al-Ti-Cr system was investigated. Seven model superalloys of fixed Cr (15 at.%), Ti (5 at.%) and Al (5 at.%) content and varying Co content (0 to 56 at.%) were hot-rolled to achieve a fine grain size and subsequently aged at 800°C for 1000 hours. Neutron diffraction data were obtained for each of the seven model superalloys at room temperature, 400, 600, 700 and 800°C. At each test temperature, alloys of Co content 0-47 at.% exhibited a positive lattice misfit. For alloys of Co content 0-47 at.%, lattice misfit was observed to decrease with increasing test temperature from ambient to 800°C. For a specific test temperature, the magnitude of the lattice misfit was observed to increase as Co content increased from 0-38 at.%.

3.1 Introduction

As discussed in Chapter 1, the exceptional high-temperature strength of Ni-based superalloys currently in service as aero-engine turbine discs derives from the ordered Ni_3Al γ' precipitates (of $L1_2$ crystal structure) coherently embedded in a solid solution hardened γ-Ni matrix phase (of A1 crystal structure). During extended high-temperature exposure, the γ-γ' microstructure evolves such that γ' precipitates can coarsen and change shape, with a concomitant effect on alloy mechanical behaviour. From section 1.1, the geometrically close-packed γ' phase, which is inherently ductile, precipitates coherently with the A1 γ-Ni matrix adopting a cube-cube orientation relationship with the parent γ. In binary and higher-order A1-$L1_2$ Ni alloys, interfacial energies originate predominantly from unfavourable juxtaposition of individual atoms at the γ-γ' inter-phase boundary, where the ordered $L1_2$-Ni_3Al unit cells meet with the disordered A1 γ matrix atom array [163]. The inherent drive to minimise total system interfacial free energy is generally accepted to provide the driving force for high-temperature γ' precipitate coarsening, leading to diffusion of elements from small to large precipitates [164]. One strategy in superalloy design when aiming to maintain stability of the γ' precipitate array at the higher proposed in-service temperatures is to minimise γ-γ' interfacial energy to retard the rate of γ' precipitate coarsening and, for Ni-based superalloys, this has traditionally been achieved by striving for a near-zero γ-γ' lattice misfit [1] (see section 1.1.1 *iv*).

In the classical coarsening theory of Lifshitz-Slyozov-Wagner (LSW) [165, 166], diffusion in the γ matrix phase is assumed to be the rate-limiting factor and γ' precipitate coarsening occurs over time, as described by Equation 3.1:

$$r_t^3 - r_0^3 = K.t \qquad \text{Equation 3.1}$$

where r_t is the mean precipitate radius at time *t*, r_0 is the mean precipitate radius when coarsening commences ($t = 0$) and *K* is the coarsening rate constant [163]. For a finite solute content in the matrix and precipitate phase and finite γ' volume fraction, both applicable for γ-γ' Ni-based superalloys, the coarsening rate [167] that applies to Equation 3.1 is given by:

$$K = \frac{8D(1-C_e)C_eV_m\sigma}{9RT(C_e^{\gamma'}-C_e)^2} \qquad \text{Equation 3.2}$$

where *D* is the effective diffusivity in the γ matrix, C_e is the equilibrium solute concentration (in atomic fraction) of the rate-limiting element in the γ matrix, V_m is the molar volume of γ', σ is the interfacial energy between the γ and γ' phases, R is the universal gas constant, *T* is the absolute temperature and $C_\mathrm{e}^{\gamma'}$ is the equilibrium solute concentration of the rate-limiting element in the γ' precipitate [163]. Equation 3.2 assumes an ideal solution. This LSW relationship of the precipitate radius cubed with time, modified to account for finite precipitate volume fraction, has been demonstrated as representative of γ' precipitate coarsening or Ostwald ripening in γ-γ' Ni alloys [168, 169].

As mentioned in section 1.1.1 *iv* with respect to Ni-based superalloys, alloy composition should be selected so that the γ-γ' lattice misfit is small; this minimises γ-γ' interfacial energy (σ) such that γ' coarsening is retarded [1], in accordance with Equation 3.2. The lattice misfit (δ) between the coherently embedded ordered γ' precipitates and the intervening γ matrix phase is defined according to (Equation 1.1):

$$\delta = 2\,\frac{[a_{\gamma'} - a_\gamma]}{[a_{\gamma'} + a_\gamma]}$$

where a_γ and $a_{\gamma'}$ are the lattice parameters of the γ and γ' phases respectively [1].

Values of lattice misfit for Ni-based blade alloys are reportedly negative at room temperature (i.e. $a_\gamma > a_{\gamma'}$), with misfit magnitude of the order of ~10^{-3} [1, 170, 171]. With increasing temperature, lattice misfit decreases to become more negative (i.e. of greater magnitude) in Ni-based superalloys, presumed due in part to differential thermal expansion between γ and γ' phases [172]. In contrast, $L1_2$-γ' strengthened Co-based alloys reportedly

exhibit a positive lattice misfit at room temperature (i.e. $a_{\gamma'} > a_{\gamma}$) [120, 173, 174], where misfit has been observed to decrease in magnitude as temperature increases and remains positive up to ~1000°C [173, 174].

Mughrabi, 2014 [175] postulates potential benefits of a positive γ-γ' lattice misfit on alloy high-temperature mechanical properties in terms of resistance to creep and fatigue: first, by invoking the model of Svoboda and Lukáš [176] which correlates a smaller magnitude of lattice misfit at high temperature (as reported for γ'-strengthened Co-based alloys) with better overall creep resistance; and secondly, by suggesting that directional coarsening (rafting) of γ' precipitates parallel to the stress axis may hinder propagation of fatigue cracks perpendicular to the stress axis, thereby enhancing fatigue resistance.

As described by Reed, 2006 [1], lattice misfit is dependent on two factors: first, on elemental partitioning of solutes *i* between γ and γ' phases; secondly, on the corresponding influence of solutes *i* on γ and γ' lattice parameters. From Chapter 2, atom probe tomography (APT) on the quinary γ-γ' Ni-(0-56)Co-5Al-5Ti-15Cr (at.%) alloy system (aged at 800°C) showed that as Co:Ni ratio increases, there is a transition in elemental phase partitioning with respect to Ti, Al and Cr at ~19 at.% Co, putatively attributed to a transition in the chemistry of the γ' phase from $Ni_3(Ti,Al)$ to $(Ni,Co)_3(Ti,Al)$. To elucidate the relationship between the elemental partitioning and lattice misfit in this fundamental Ni-Co-5Al-5Ti-15Cr (at.%) system, it is important to quantify the effect of increasing Co:Ni ratio on γ and γ' lattice parameters and resultant lattice misfit for the proposed in-service temperature of 800°C for high-pressure turbine disc applications. To this end, neutron diffraction was performed on each of the seven model superalloy compositions (0Co, 9Co, 19Co, 28Co, 38Co, 47Co, 56Co) investigated in Chapter 2 to determine values of γ and γ' lattice parameter across a range of temperatures (ambient, 400, 600, 700 and 800°C) likely to be experienced by aero-engine turbine disc superalloys in service.

3.2 Experimental Procedure

3.2.1 Materials and homogenisation heat treatment

The model superalloys tested were of the $(Ni,Co)_{75}Al_5Ti_5Cr_{15}$ (at.%) system for which the Ni:Co concentration ratio was varied from 1:0 to ~1:3. The alloys were named according to their nominal atomic concentration of Co: 0Co, 9Co, 19Co, 28Co, 38Co, 47Co and 56Co (Table 3.1). Polycrystalline ingots of the seven alloy compositions were fabricated by vacuum arc melting of raw elements to produce a cast ingot approximately 23 × 23 × 55 mm in size. The attached skull (residual solidified alloy) was cut from the cast ingot. To determine solidus temperatures prior to homogenisation of each alloy ingot, differential scanning calorimetry (DSC) was performed on alloy discs (5 × 1 mm) extracted by spark erosion from 1 mm thick slices cut from the skull area nearest to the cast ingot. A Netzsch 404 heat-flux calorimeter was used to perform DSC for each as-cast alloy, operating at temperatures of up to 1450°C with a heating rate of 10°C min^{-1}. The DSC trace for each of the seven cast alloys was analysed using Igor Pro 6.3 software [161] to determine an appropriate homogenisation heat treatment temperature for the cast alloy ingots. A homogenisation heat treatment temperature of 1250°C was selected to minimise casting-induced micro-segregation. This homogenisation heat treatment temperature was chosen to lie within the γ single-phase field i.e. above the γ′ solvus temperature but sufficiently below the solidus temperature to preclude incipient melting. The cast alloy ingots (23 × 23 × 55 mm) were subjected to homogenisation heat treatment for 48 hours at 1250°C using a Carbolite vacuum furnace.

3.2.2 Hot-rolling of the homogenised alloy ingots

The purpose of hot-working the homogenised alloy ingots was to produce, for each alloy composition, a microstructure with a finer grain size than the millimetre-scale grains that formed as a result of the casting process and subsequent homogenisation heat treatment. A polycrystalline alloy with a small grain size promotes diffraction from all potential crystallographic planes through increasing the probability for all planes to be at the orientation required for diffraction to occur.

In order to set a rolling temperature for the homogenised alloy ingots, DSC was performed on sample alloy discs (5 × 1 mm) as previously carried out on the as-cast specimens. The DSC trace for each homogenised alloy ingot was analysed using Igor Pro 6.3 software [161] to determine γ' solvus and solidus temperatures for each alloy. A rolling temperature

Table 3.1. Nominal and measured chemical compositions (mean ± standard deviation, σ) of the seven model superalloys investigated. Measurements obtained using SEM-EDS on alloys aged at 800°C (1000 hours) were within ±1 at.% of their nominal compositions.

Alloy	Nominal composition (at.%)					Measured composition (at.%)									
	Ni	Co	Al	Ti	Cr	Ni	±σ	Co	±σ	Al	±σ	Ti	±σ	Cr	±σ
0Co	75.0	0.0	5.0	5.0	15.0	74.88	0.12	-	-	4.93	0.08	5.27	0.11	14.9	0.1
9Co	65.6	9.4	5.0	5.0	15.0	65.2	0.2	9.55	0.15	5.09	0.10	5.20	0.05	14.9	0.2
19Co	56.3	18.8	5.0	5.0	15.0	56.21	0.11	18.64	0.18	5.08	0.17	5.27	0.15	14.80	0.20
28Co	46.9	28.1	5.0	5.0	15.0	47.2	0.2	27.86	0.08	5.01	0.19	5.23	0.09	14.8	0.3
38Co	37.5	37.5	5.0	5.0	15.0	37.70	0.13	37.21	0.05	5.01	0.18	5.08	0.11	15.00	0.11
47Co	28.1	46.9	5.0	5.0	15.0	28.43	0.09	46.4	0.4	5.0	0.2	5.2	0.3	15.0	0.2
56Co	18.8	56.3	5.0	5.0	15.0	18.53	0.12	56.35	0.12	4.86	0.11	5.18	0.13	15.09	0.19

was selected for each alloy composition that was effectively 2/3 into the γ single-phase field from the γ' solvus temperature. Three super-solvus hot-rolling temperatures were selected such that alloys were flat-rolled in three batches: 0Co and 9Co were rolled at 1264°C; 19Co and 28Co were rolled at 1251°C; 38Co, 47Co, 56Co were rolled at 1216°C. The box-furnace used in the hot-rolling process was calibrated using an R-type thermocouple prior to hot-rolling to ensure that alloy ingots were rolled at the chosen super-solvus rolling temperature. From the hot-rolling process, flat alloy slabs were obtained ~100 mm in length, ~30 mm wide and 9.6 - 9.9 mm thick.

3.2.3 Ageing hot-rolled alloy specimens at 800°C, 1000 hours

Electrical discharge machining (EDM) was used to extract 4 cylindrical specimens of 7 mm diameter from each of the seven as-rolled slabs. All cylinders were cleaned ultrasonically in acetone and then in ethanol before being encapsulated in silica tubes back-filled with argon. Alloy specimens were inserted into a box-furnace pre-heated to 800°C (temperature measured using a calibrated n-type thermocouple) and aged for 1000 hours. After 1000 hours, samples were removed from the furnace and air-cooled. Thus, 4 cylinders were obtained for each alloy composition ready for neutron diffraction. Additional samples were prepared and aged simultaneously under the same conditions to permit microstructural characterisation of each alloy composition in the aged condition.

3.2.4 Microstructural characterisation of aged alloys prior to neutron diffraction

To determine actual alloy compositions (Table 3.1), the additional aged samples described in the above section were mounted in conductive Bakelite, ground with wet SiC abrasive paper and polished using a progressively finer diamond suspension (from 6 μm down

to 1 µm). The polished samples were electrolytically etched with a 10% phosphoric acid solution to dissolve the γ matrices and highlight γ′ precipitates. Alloy microstructure was examined using a ZEISS GeminiSEM 300 scanning electron microscope in secondary electron (SE) mode. Energy dispersive X-ray spectroscopy (EDS) was carried out using an Oxford Aztec EDS system to determine a mean measured composition for each alloy from 5 large area scans of at least 500 × 500 µm. The measured composition for each alloy was found to be within ±1 at.% of its nominal composition (Table 3.1). The EDS system was calibrated with a nickel strip prior to acquiring large area EDS scans.

3.2.5 Neutron diffraction experiment at the ISIS Neutron and Muon Source

The seven aged model superalloys $(Ni,Co)_{75}Al_5Ti_5Cr_{15}$ (at.%) of varying Co:Ni ratio (0-56 at.% Co) were subjected to neutron diffraction at room temperature, 400, 600, 700 and 800°C to determine values of lattice parameter for individual γ and γ' phases. Thus, lattice misfit could be determined for each alloy composition across a range of temperatures likely to be experienced in service by alloys based on the fundamental Ni-Co-Al-Ti-Cr quinary system. The POLARIS powder diffractometer was used (Figure 3.1), located at the Rutherford Appleton Laboratory ISIS Neutron and Muon Source, UK (RB1810034, October 2018). The POLARIS instrument employed five detector banks, whereby bank 1 collected low-angle diffracted neutrons (corresponding to high *d*-spacing) and bank 5 collected high-angle diffracted neutrons (corresponding to low *d*-spacing).

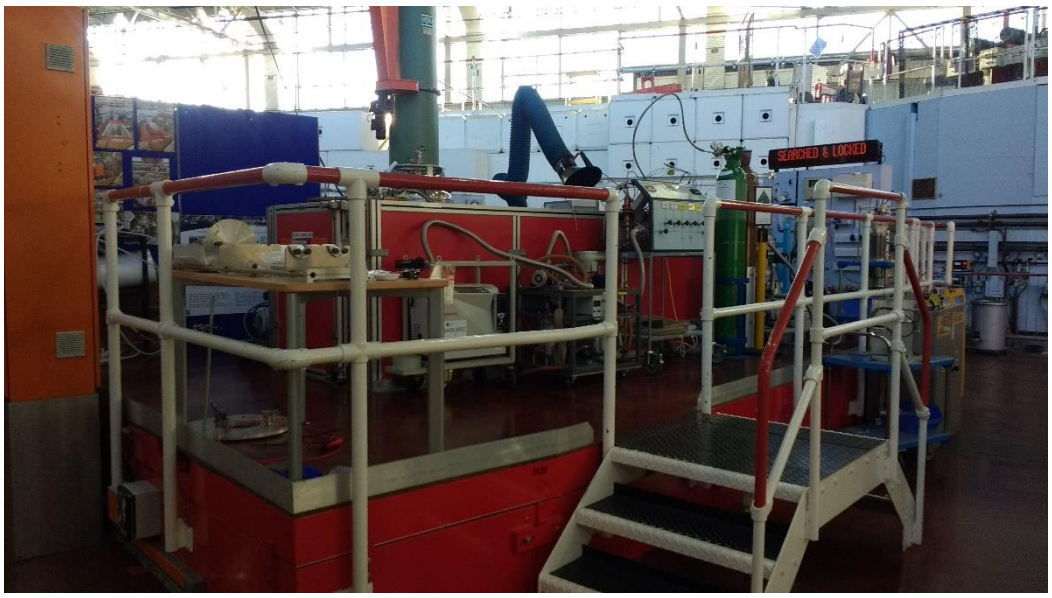

Figure 3.1. POLARIS instrument at the ISIS spallation neutron source of the Rutherford Appleton Laboratory.

One alloy composition was tested at a time, initially at room temperature before being heated to each of the higher test temperatures (400, 600, 700 and 800°C). For each alloy composition, the 4 cylinders obtained (each of length ~10 mm) were stacked in a thin-walled vanadium can of 8 mm diameter (Figure 3.2).

Figure 3.2. 8 mm diameter thin-walled vanadium can containing four aged alloy cylinders for one alloy composition prior to insertion into the sample holder.

Thus, the alloy cylinder stack filled the height of the neutron beam (~40 mm) within the POLARIS instrument. The vanadium can was screwed onto a large sample holder such that two thermocouples were in contact with the vanadium can (Figure 3.3), before the whole assembly was placed vertically inside the instrument furnace. The assembly was loaded into the furnace in such a way that the vanadium can was at the optimal height to receive the full 40 mm beam height. In this way, a diffraction pattern was obtained at room temperature and subsequently at each of the higher temperatures for each alloy composition. The vanadium cans containing the polycrystalline alloy specimens were rotated at ~6°/min within the furnace at room temperature and at the higher test temperatures to obtain a high-quality diffraction pattern by promoting diffraction from all potential crystallographic planes. A 1-hour counting duration was used for each test temperature, deemed sufficient for the superlattice reflections to be captured with good counting statistics.

Figure 3.3. Filled vanadium can (containing alloy cylinders), attached to the sample holder with a thermocouple either side to monitor test temperature.

3.2.6 Analysis of neutron diffraction data

Following acquisition of diffraction data at each test temperature, the data collected during the 1-hour counting period were exported using the Manipulation and Analysis Toolkit for Instrument Data (MANTID) software [177]. The neutron diffraction patterns acquired were then analysed using the General Structure Analysis System (GSAS) software [178]. The Le Bail method of refinement [179] was used to determine lattice parameters of individual γ and γ' phases for each alloy composition. Whilst diffraction data were collected using all five detector banks within the POLARIS instrument, only diffraction patterns obtained from high-angle detector banks 3 (at ~52°), 4 (at ~93°) and 5 (at ~147°) were used in the analysis to acquire the most accurate values of phase lattice parameters.

The accuracy with which lattice parameter can be determined relies on being able to define accurately the *position* of the peaks in the diffraction patterns. Whole pattern fitting was used to refine each neutron diffraction pattern for alloys 0Co to 47Co at each test temperature. Two phases were defined within GSAS: one comprising Ni atoms with space group $Fm\bar{3}m$ (γ phase) and the other comprising Ni and Al atoms (Ni_3Al) with space group $Pm\bar{3}m$ (γ' phase). It should be noted that the raw diffraction data were not manipulated at any stage of the refinement process. Diffraction patterns for the 56Co alloy proved difficult to fit using the Le Bail method of refinement (see section 3.3.4).

The refined lattice parameters of γ and γ' obtained using GSAS permit accurate determination of γ-γ' lattice misfit (δ) according to Equation 1.1. A value of standard deviation was provided with each value of lattice parameter determined using the GSAS software. The uncertainty in the lattice misfit values obtained were calculated using the standard method of error propagation using Equation 3.3:

$$\Delta\delta = |\delta| \sqrt{\left(\frac{\Delta\left(a_{\gamma'} - a_{\gamma}\right)}{\left(a_{\gamma'} - a_{\gamma}\right)}\right)^2 + \left(\frac{\Delta\left(a_{\gamma'} + a_{\gamma}\right)}{\left(a_{\gamma'} + a_{\gamma}\right)}\right)^2} \qquad \text{Equation 3.3}$$

3.3 Results

3.3.1 Microstructural characterisation of Ni-Co-5Al-5Ti-15Cr (at.%) alloys aged at 800°C

Figure 3.4 shows representative SE micrographs of each of the seven model superalloys following hot rolling and subsequent ageing at 800°C for 1000 hours prior to neutron diffraction. Each alloy exhibited a duplex γ-γ' microstructure and similar γ' precipitate morphology to that observed for the same alloy composition (aged at 800°C) investigated by APT (Figure 2.2). The 56Co alloy appeared to indicate a degree of precipitate elongation, whereas the 38Co and 47Co alloys exhibited cuboidal γ' precipitates with a degree of coalescence in the 47Co alloy. The lower Co alloys appeared to exhibit γ' precipitates with more rounded corners.

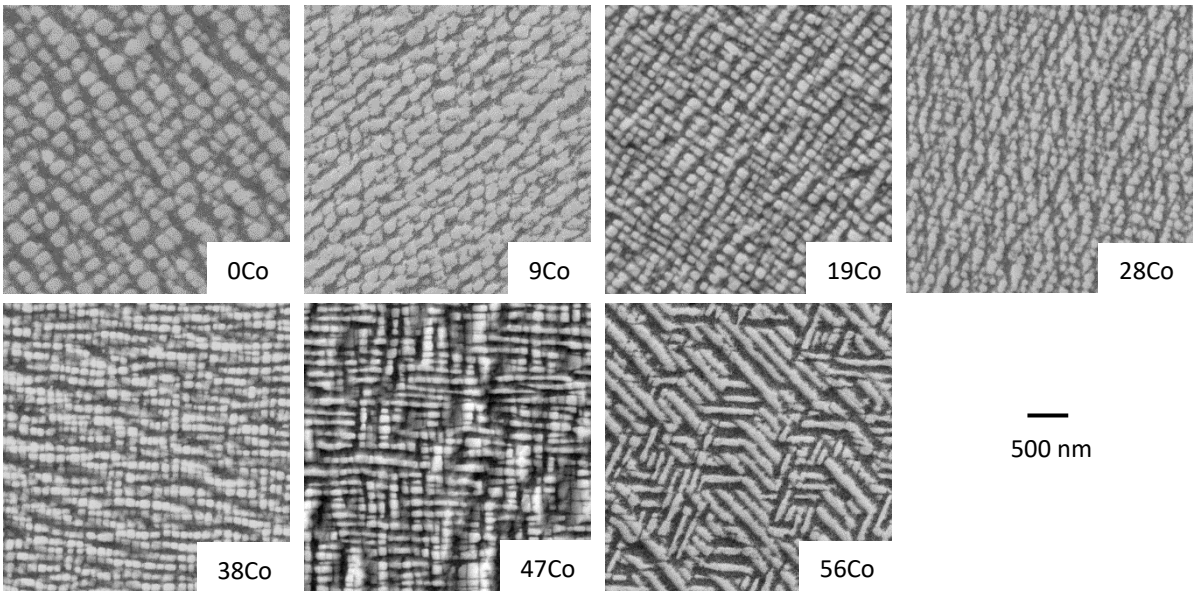

Figure 3.4. Representative SE micrographs of alloy γ-γ' microstructure following hot rolling and subsequent ageing at 800°C for 1000 hours. All alloys exhibited γ' precipitates embedded in a γ matrix.

3.3.2 Lattice parameters of γ and γ' phases for alloys 0Co to 47Co

Lattice parameters of the individual γ and γ' phases were determined for alloys containing 0, 9, 19, 28, 38 and 47 at.% Co at room temperature and at 400, 600, 700 and 800°C. Le Bail refinements of the neutron diffraction patterns were performed using GSAS software and an example of a fitted dataset is given in Figure 3.5. Black crosses indicate experimental data, the red line indicates the Le Bail fit and the green line indicates the background. The blue line indicates any difference between the experimental data and the Le Bail fit.

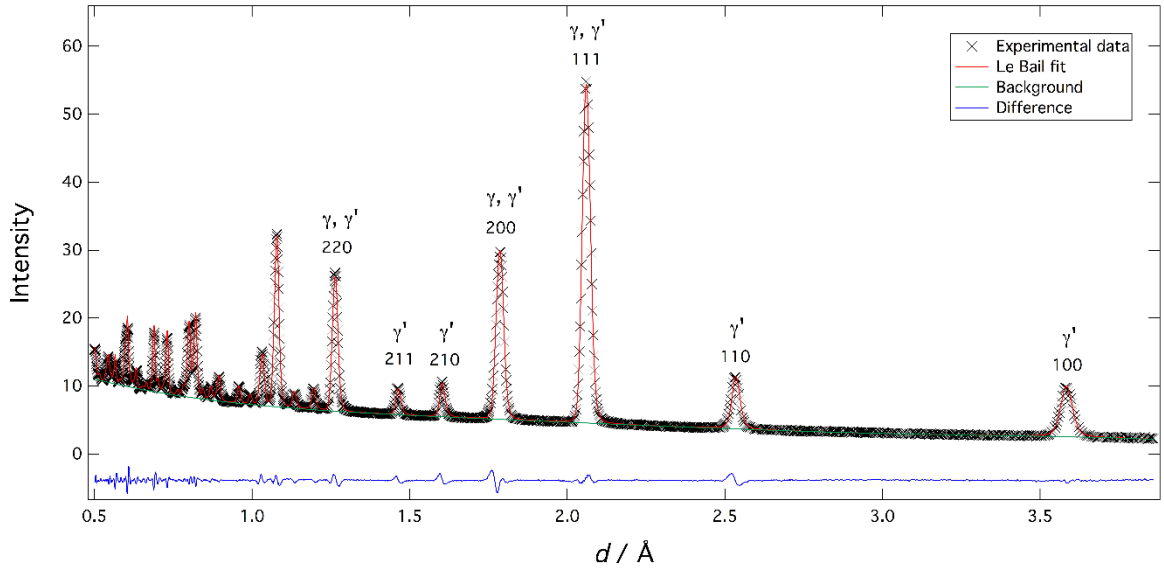

Figure 3.5. Example of Le Bail fit used to determine γ and γ' lattice parameters for each neutron diffraction pattern acquired using the ISIS POLARIS instrument. The pattern shown was for alloy 38Co at room temperature from detector bank 3.

The γ' phase possesses an ordered primitive cubic $L1_2$ superlattice structure of the γ FCC matrix phase. From Figure 3.5, the 111, 200 and 220 are doublet γ and γ' peaks due to scattering from both γ and γ' phases whilst the 100, 110, 210 and 211 peaks are from the γ' superlattice phase only. A face-centred cubic Bravais lattice (cubic F), such as the A1-γ matrix phase, exhibits peaks when *h*, *k* and *l* are all odd integers or all even integers, where *h*, *k* and *l* are the Miller indices of the diffracting (reflecting) planes [180]. Therefore, the γ phase exhibits peaks corresponding to the following reflections, *hkl*: 111, 200, 220, 311, etc. A primitive cubic Bravais lattice (cubic P), such as the $L1_2$-γ' phase, exhibits peaks when *h*, *k* and *l* are all odd, all even or mixed integers [180]. Therefore, the $L1_2$ γ' superlattice phase exhibits peaks corresponding to all the following reflections, *hkl*: 100, 110, 111, 200, 210, 211, 220, 300/221, etc. i.e. no systematic absences occur and thus more peaks are observed for the γ' phase than for the γ phase.

Table 3.2 summarises the values of lattice parameter of the individual γ and γ' phases for alloys 0Co to 47Co acquired at each test temperature. These values are plotted graphically in Figure 3.6 and Figure 3.7 and show the variation in lattice parameter with increasing Co content up to 47 at.%. For each alloy composition, the γ' lattice parameter was observed to be greater than the γ lattice parameter, indicating a positive lattice misfit throughout the compositional range. Increasing test temperature leads to an increase in the lattice parameter of both γ and γ' phases for each alloy composition. The 47Co alloy showed a marked reduction in lattice parameter of γ and γ' phases compared with alloys of lower Co content.

Table 3.2. Values of lattice parameter (Å) of γ and γ' phases for alloys 0Co to 47Co (aged at 800°C, 1000 hours) obtained using neutron diffraction at room temperature (RT), 400°C, 600°C, 700°C and 800°C. Data were obtained from analysing neutron diffraction patterns using the Le Bail method of peak refinement. Values of error of lattice parameter generated by the GSAS software were close to 0.00002 Å for all datasets.

Alloy	Phase	Phase lattice parameter (Å)				
		RT	400°C	600°C	700°C	800°C
0Co	γ	3.55520	3.57339	3.58621	3.59282	3.60024
	γ'	3.57206	3.58918	3.60065	3.60650	3.61223
9Co	γ	3.55757	3.57678	3.58894	3.59565	3.60363
	γ'	3.57595	3.59386	3.60471	3.61058	3.61674
19Co	γ	3.55886	3.57718	3.59040	3.59712	3.60520
	γ'	3.57878	3.59595	3.60780	3.61371	3.61999
28Co	γ	3.55807	3.57607	3.58961	3.59634	3.60421
	γ'	3.57892	3.59589	3.60815	3.61415	3.62030
38Co	γ	3.55794	3.57711	3.58952	3.59642	3.60459
	γ'	3.57906	3.59742	3.60888	3.61520	3.62177
47Co	γ	3.53874	3.55678	3.56956	3.57710	3.58538
	γ'	3.55847	3.57596	3.58831	3.59543	3.60248

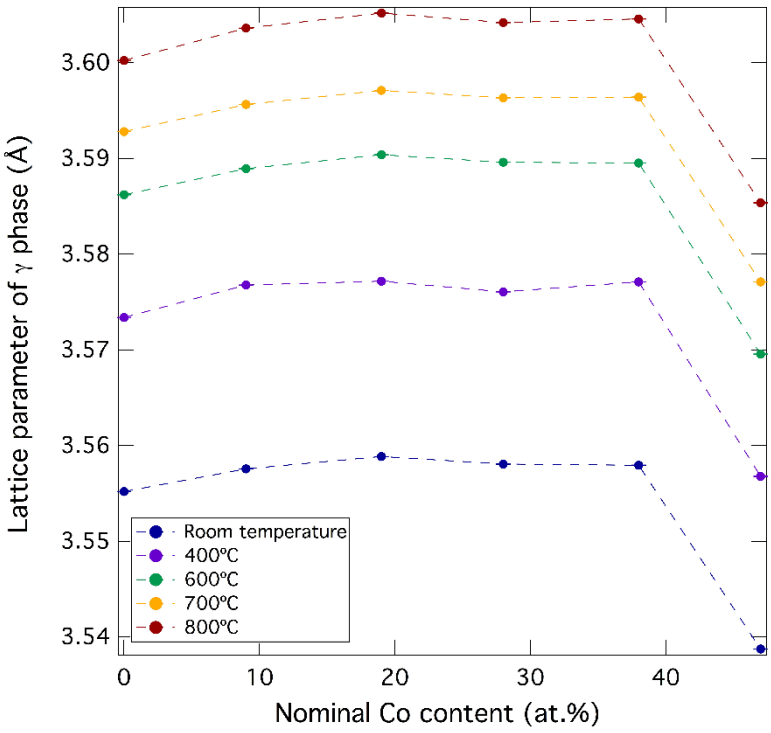

Figure 3.6. Lattice parameter of the **γ phase** as a function of alloy Co content for each test temperature. Error bars are shown but are smaller than the markers. Data from Table 3.2.

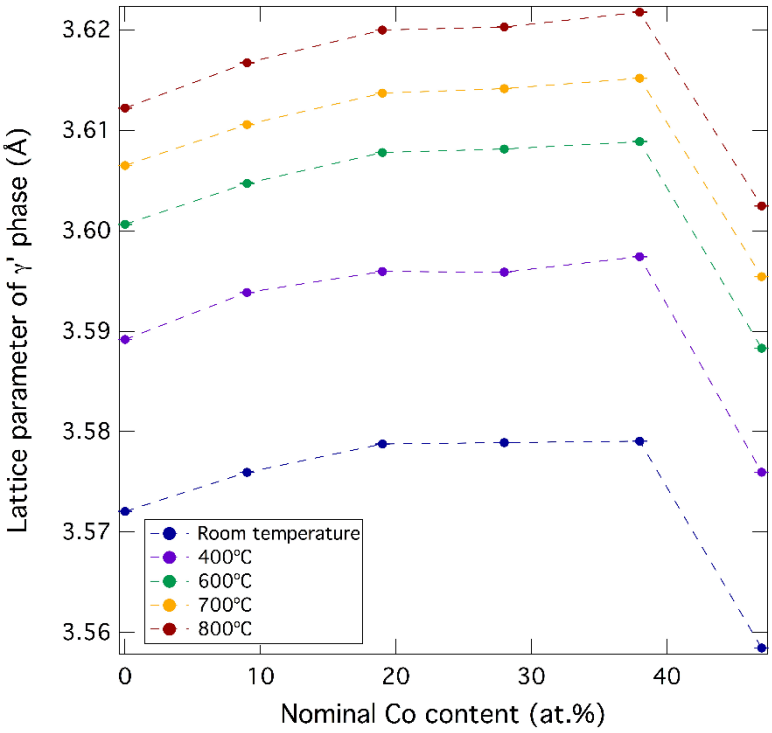

Figure 3.7. Lattice parameter of the **γ' phase** as a function of alloy Co content for each test temperature. Error bars are shown but are smaller than the markers. Data from Table 3.2.

3.3.3 Lattice misfit of alloys 0Co to 47Co

The lattice misfit (δ) for alloys 0Co, 9Co, 19Co, 28Co, 38Co and 47Co was determined for each test temperature from lattice parameter values (Table 3.2) using Equation 1.1. Table 3.3 shows the values of lattice misfit obtained for alloys 0Co-47Co. For each test temperature, alloys 0Co-47Co exhibited a positive lattice misfit i.e. $a_{\gamma'} > a_{\gamma}$. In referring to the lattice misfit, δ, of an alloy, it should be noted that this is technically the constrained lattice misfit, as opposed to the unconstrained misfit i.e. that value of misfit that would be measured if the γ' precipitates were removed (for example by wet chemical electrolysis).

Table 3.3. Values of lattice misfit (%) and associated standard deviations (determined using Equation 3.3) for alloys 0Co to 47Co (aged at 800°C, 1000 hours) for each test temperature: room temperature (RT), 400°C, 600°C, 700°C and 800°C. These values were determined using Equation 1.1 with the lattice parameter values for γ and γ' phases shown in Table 3.2.

Alloy	Alloy lattice misfit δ (%)									
	RT	±σ	400°C	±σ	600°C	±σ	700°C	±σ	800°C	±σ
0Co	0.4731	0.0008	0.4410	0.0007	0.4018	0.0007	0.3803	0.0007	0.3322	0.0008
9Co	0.5154	0.0008	0.4764	0.0007	0.4384	0.0007	0.4143	0.0008	0.3631	0.0008
19Co	0.5582	0.0006	0.5234	0.0006	0.4834	0.0006	0.4600	0.0006	0.4095	0.0006
28Co	0.5841	0.0007	0.5528	0.0006	0.5150	0.0006	0.4940	0.0007	0.4453	0.0008
38Co	0.5919	0.0007	0.5663	0.0007	0.5378	0.0007	0.5208	0.0007	0.4753	0.0008
47Co	0.556	0.001	0.538	0.001	0.5239	0.0009	0.5112	0.0009	0.4757	0.0009

Values of lattice misfit were plotted to show variation in lattice misfit with increasing Co:Ni ratio (Figure 3.8a) and the dependence of lattice misfit on temperature for each alloy composition (Figure 3.8b). All data in Figure 3.8 are from Table 3.3. For a given test temperature, lattice misfit values increased with increasing Co content up to 38Co (Figure 3.8a). However, the 47Co alloy showed a lower lattice misfit than alloy 38Co at all test temperatures except 800°C, for which lattice misfit values were comparable. For a given alloy Co content (Figure 3.8b), lattice misfit decreased with increasing temperature over the temperature range tested, with alloys 0Co-38Co exhibiting a similar trend in temperature-dependence of the lattice misfit. However, the 47Co alloy showed a lesser diminution of lattice misfit with increasing temperature.

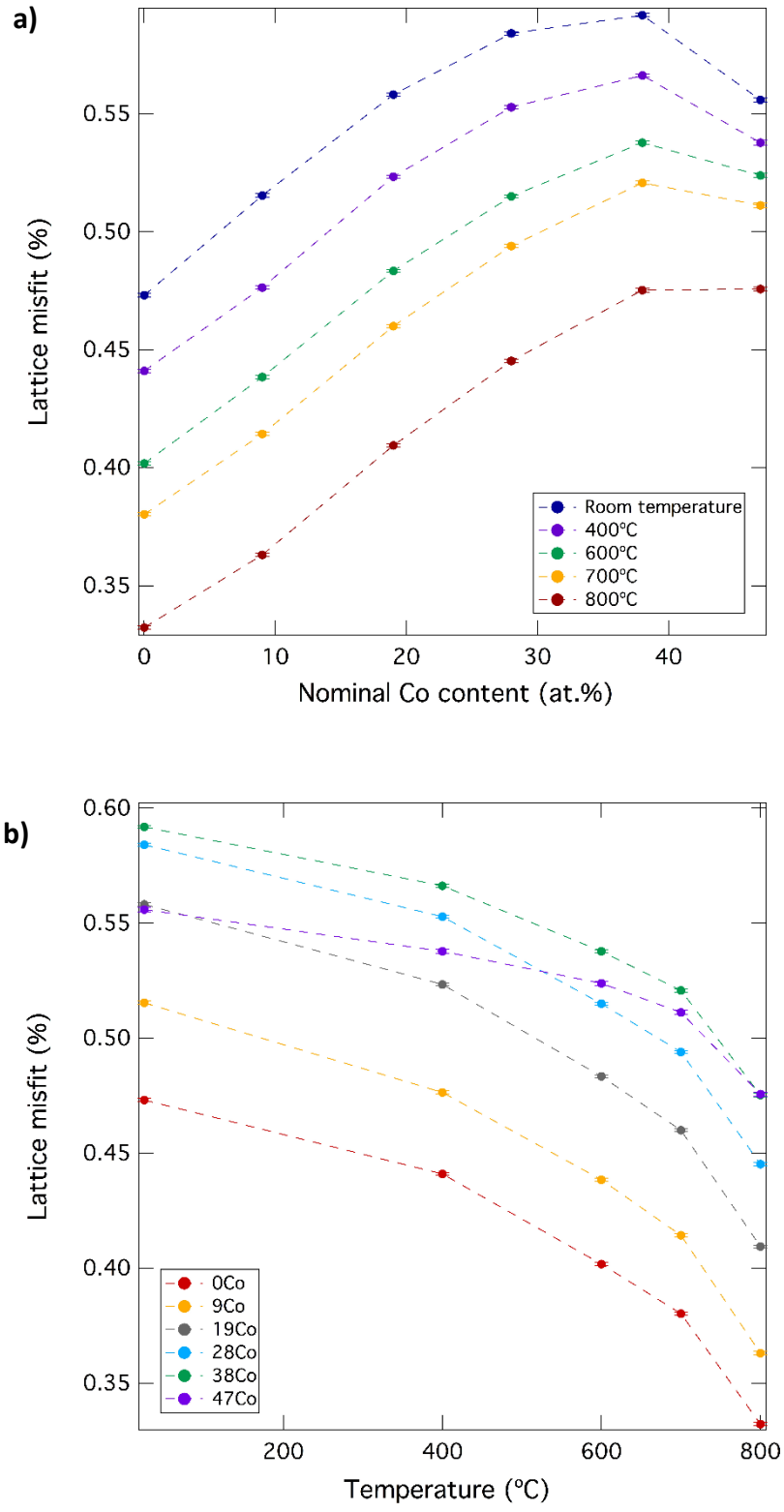

Figure 3.8. Lattice misfit of the model superalloys 0Co to 47Co: a) as a function of alloy Co content for each test temperature; b) as a function of temperature for each alloy Co content. Data are from Table 3.3. Error bars are shown but are smaller than the markers.

3.3.4 Neutron diffraction data for alloy 56Co

Figure 3.9 shows the neutron diffraction pattern for the 56Co alloy (aged at 800°C, 1000 hours) acquired at room temperature. From the profile of the peaks, it would appear that the reflections corresponding to γ and γ' may comprise three peaks, as seen for the 200 reflection. Furthermore, the $L1_2$ superlattice reflections (γ' only) appear to be doublet peaks, as seen for the 210 reflection for the 56Co alloy shown for each test temperature in Figure 3.10. The profile, indicative of two individual but overlapping peaks for each test temperature (ambient, 400, 600, 700 and 800°C), may suggest a strain-induced distortion of the γ' phase. As such, no lattice parameter or lattice misfit values could be derived for the 56Co alloy. The apparent distortion of the γ' phase indicated by the room-temperature diffraction pattern for the 56Co alloy may be related to the elongation of γ' precipitates observed using SEM (Figure 3.4).

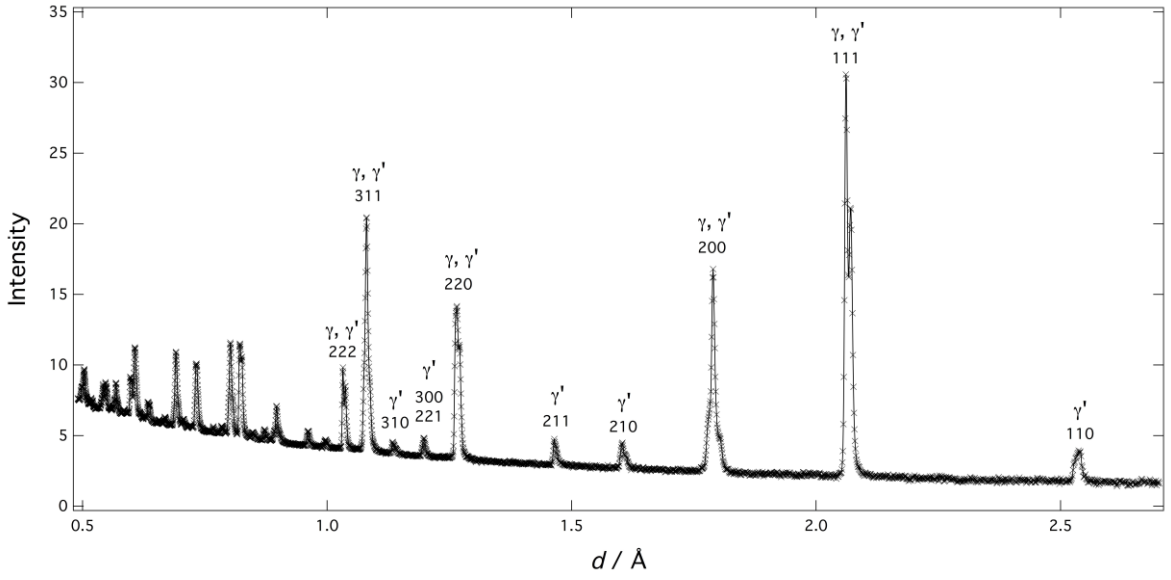

Figure 3.9. Diffraction pattern for the 56Co alloy acquired at room temperature from detector bank 5. It was not possible to achieve a satisfactory Le Bail fit for these data.

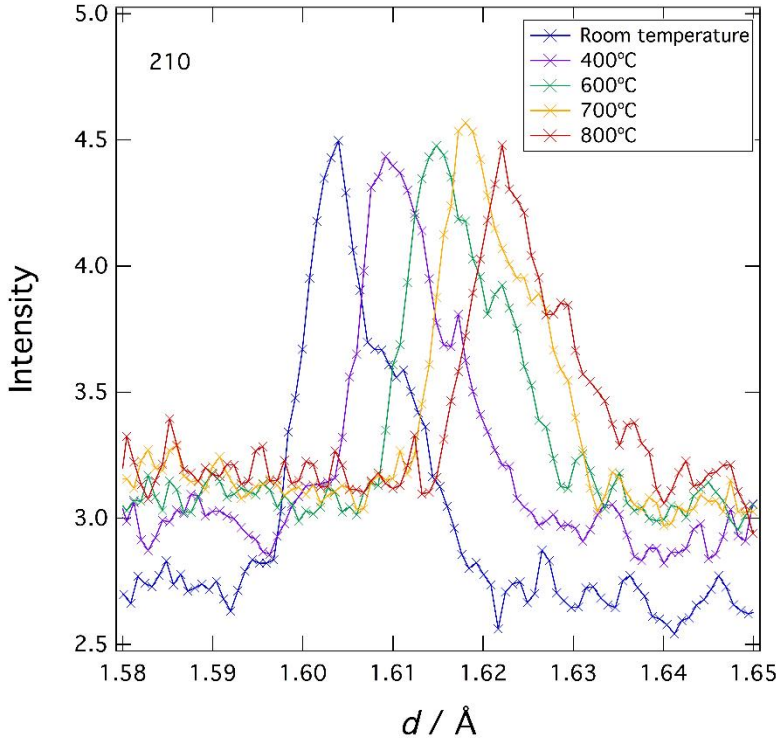

Figure 3.10. Detail of diffraction pattern for the 56Co alloy (from Figure 3.9), showing the room-temperature 210 superlattice reflection (blue line, d-space range 1.58 to 1.65 Å), together with diffraction patterns obtained for the 56Co alloy at the higher test temperatures (for the same d-space range). All data taken from detector bank 5.

3.4 Discussion

Alloys 0Co to 47Co (aged at 800°C for 1000 hours) all exhibited a positive lattice misfit at all test temperatures (room temperature, 400°C, 600°C, 700°C and 800°C). With increasing Co content from 0 to 38 at.%, at any given test temperature, the magnitude of the lattice misfit observed increased (Figure 3.8). The 47Co alloy exhibited a lower lattice misfit than the 38Co alloy at each test temperature, except at 800°C for which the two lattice misfit values were comparable. From the APT study on the same alloy compositions aged at 800°C for 1000 hours (Chapter 2), a non-monotonic relationship was observed between alloy Co content and elemental partitioning of Ti, Al and Cr, with a transition occurring at ~19 at.% Co. Thus, it is difficult to relate directly the steady increase in lattice misfit with increasing Co from 0 to 38 at.% observed at room temperature to the partitioning of Ti, Al and Cr. Although a transition in Ti and Al partitioning was observed as Co content increased beyond ~19 at.% (Figure 2.8), alloy lattice misfit values derived at room temperature continued to increase with increasing Co content beyond 19 at.% (Figure 3.8), in parallel with the increased partitioning of both Ni and Co to the γ' phase observed in the same alloy series (Figure 2.8). From the partitioning data (Figure 2.8), both Co and Ni increasingly partition to the γ' phase with increasing Co

content up to 38 at.%. At higher Co concentrations, the partitioning coefficient for Ni (k_{Ni}) appears to level off then decline as the γ' approaches predominantly Co-based, as for the 56Co (Table 2.2).

For Ni-based superalloys, Equations 1.2 and 1.3 (in section 1.1.1 *iv*) have traditionally been used to predict lattice parameter values for individual γ and γ' phases (a_γ and $a_{\gamma'}$ respectively) using phase elemental content (x_i) and the efficacy of solute per at.% (Γ_i) in expanding the γ and γ' lattice parameters. However, values for $\Gamma_{Co}^{\gamma'}$ in the literature appear inconsistent. Furthermore, literature values of Vegard coefficient are derived for binary alloys only. Therefore, extrapolation of these simplistic relations to a higher-order alloy such as those of the Ni-Co-5Al-5Ti-15Cr (at.%) system may be presumptive, due to the complex interaction of additional alloying elements. Figure 3.11 shows room temperature lattice parameter values derived from the present study using neutron diffraction data (from Figures 3.6 and 3.7) as well as lattice parameter values that would be predicted using APT data from the current study (Chapter 2) in conjunction with the available Vegard coefficients published in the literature for binary alloys [181]. Figure 3.12 shows room temperature lattice misfit values derived from the neutron diffraction data (Figure 3.8) compared with predicted lattice misfit values calculated from the predicted lattice parameter values (Figure 3.11) using Equation 1.1.

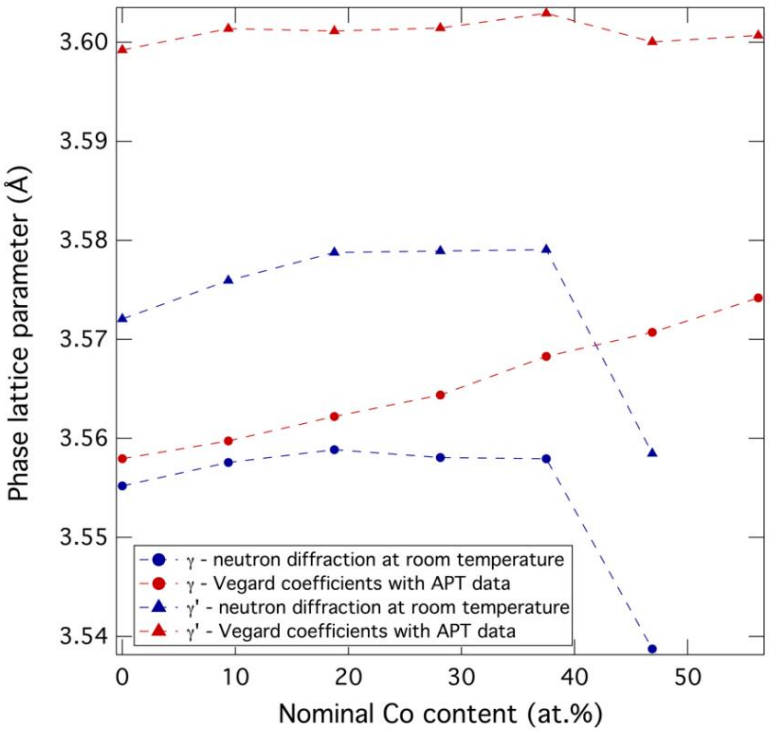

Figure 3.11. Room temperature lattice parameter values derived using neutron diffraction data obtained in the current study for the Ni-Co-5Al-5Ti-15Cr (at.%) alloys (Figures 3.6 and 3.7) compared with lattice parameter values predicted using APT data on the same alloys (Chapter 2) in conjunction with published Vegard coefficients for binary alloys [181].

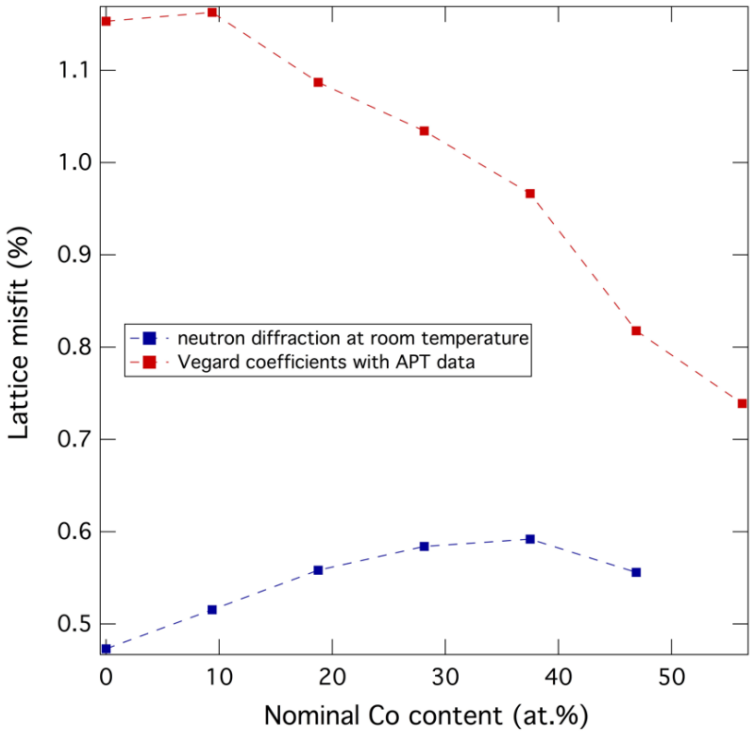

Figure 3.12. Room temperature lattice misfit values derived using neutron diffraction data obtained in the current study for the Ni-Co-5Al-5Ti-15Cr (at.%) alloys (Figure 3.8) compared with predicted lattice misfit values calculated from the predicted lattice parameter values (Figure 3.11) using Equation 1.1.

From the graphs showing the variation in room temperature lattice parameter with increasing alloy Co content for individual γ and γ' phases (Figure 3.6 and Figure 3.7), the gradients were used to calculate values for the expansion of γ and γ' lattice parameters per at.% Co over two ranges: 0-19 at.% and 0-38 at.%. These values are, respectively, 2×10^{-4} Å/at.% and 6×10^{-5} Å/at.% for the γ matrix phase and 4×10^{-4} Å/at.% and 2×10^{-4} Å/at.% for the γ' precipitate phase.

In considering the dependence of alloy lattice misfit on Co:Ni ratio, it is of interest to compare values obtained in the present systematic study with systematic studies by Zenk *et al*., 2016 [182] and Shinagawa *et al*., 2008 [127] on alloys of the Ni-Co-(9-10)Al-7.5W (at.%) system (aged at 900°C) in the presence and absence of Cr (Figure 3.13). From Figure 3.13a, lattice misfit values obtained at room temperature for the 0Cr and 8Cr Ni-Co-(9-10)Al-7.5W alloys increased with increasing Co:Ni ratio. Addition of 8Cr resulted in a systematic shift in values for lattice misfit toward negative lattice misfit values. Thus, the trend showing an increase in lattice misfit with increasing Co:Ni ratio for the Ni-Co-(9-10)Al-7.5W system appears to occur independently of Cr content and in the absence of Ti.

a) Graph showing lattice misfit as a function of Co content in Ni-Co-Al-W ±Cr alloys removed for copyright reasons. Copyright holder is The Minerals, Metals and Materials Society.

b) Graph showing elemental partitioning coefficient as a function of Co content in Ni-Co-Al-W ±Cr alloys removed for copyright reasons. Copyright holder is The Minerals, Metals and Materials Society.

Figure 3.13. Adapted from Zenk *et al*., 2016 [182]. a) variation in γ-γ' lattice misfit with increasing Co:Ni fraction (f_B) for Ni-Co-9Al-7.5W-8Cr (at.%) alloys (black line, alloy Co content labelled in at.%; data, Zenk *et al*. [182]) compared with Cr-free Ni-Co-10Al-7.5W alloys (red line, data from Shinagawa *et al*. [127]). b) elemental partitioning coefficients for the 8Cr (at.%) alloys (solid symbols) [182] and 0Cr alloys (open symbols) [127]. All values were obtained at room temperature for alloys aged at 900°C.

Zenk *et al*. [182] attributed the increase in lattice misfit with increasing Co:Ni ratio of the Ni-Co-Al-W system to the increased partitioning of W to the γ' phase with increasing Co

content (Figure 3.13b). However, in the present study on the Ni-Co-5Al-5Ti-15Cr (at.%) alloy system, a similar trend, of increasing lattice misfit with increasing Co:Ni ratio (up to 38 at.% Co), was observed in the absence of W. Furthermore, this trend of increasing lattice misfit with increasing Co content up to 38 at.% observed in the present study appears to show no direct correlation with the non-monotonic trend in Ti partitioning (Figure 2.7 and Figure 2.8).

The absolute values of lattice misfit obtained by Zenk *et al*. [182] in the presence of 8Cr for the Ni-Co-10Al-7.5W (at.%) system appear significantly lower than the corresponding lattice misfit values derived for the Ni-Co-5Al-5Ti-15Cr (at.%) system for room temperature in the present study. This is plausibly attributed to the relatively high concentration of Ti in the current study and the fact that Ti was shown to partition strongly to the γ' phase (Chapter 2), although the transition in partitioning at ~19 at.% Co cannot be directly related to the values of lattice misfit derived at room temperature for the same alloy series.

For alloys of Co content 0-47 at.%, lattice misfit values decreased with increasing test temperature from ambient to 800°C, which may in part be attributed to a difference in thermal expansion coefficients of the γ and γ' phases. Nathal *et al*., 1985 [172] used high-temperature X-ray diffraction techniques to show that thermal expansion coefficients of the γ' phase in single-crystal Ni-based superalloys were lower than those of the γ phase and thus the lattice misfit tends towards increasingly negative values as temperature increases.

With respect to Ni-based superalloys (section 1.1.1 *iv*), alloy composition should be selected so that the γ-γ' lattice misfit is small; this minimises γ-γ' interfacial energy (σ) such that γ' coarsening is retarded [1] in accordance with Equation 3.2, as modified from the classical coarsening theory of Lifshitz-Slyozov-Wagner (section 3.1). If a similar relation applies to Co-based superalloys, then it may prove serendipitous that lattice misfit values for the quinary Ni-Co-5Al-5Ti-15Cr (at.%) system decrease with increasing temperature from ambient to 800°C for the entire compositional range for which a lattice misfit value could be derived (0-47 at.% Co).

The γ' precipitate morphology of each of the seven $(Ni,Co)_{75}Al_5Ti_5Cr_{15}$ (at.%) alloys following hot rolling and ageing at 800°C for 1000 hours (Figure 3.4) closely resembled that observed in the atom probe tomography study on the same alloy compositions, aged at 800°C for 1000 hours (Chapter 2). From this APT study (Chapter 2), γ' precipitate size decreased with increasing Co content from 0 to 38 at.%: from ~119 nm for the Co-free alloy to ~67 nm for the 38Co alloy. In both alloy series, alloys containing 56 at.% Co showed significant

elongation of the γ' precipitates. This may account for the fact that no lattice misfit values could be derived for the 56Co alloy, with neutron diffraction data for this alloy indicating a strain-distortion of the γ' phase over the temperature range tested (ambient to 800°C). Individual γ' precipitates of the 38Co and 47Co alloys (Figure 3.4) appeared more cuboidal than those of the lower Co alloys, with the 47Co alloy also exhibiting a degree of γ' precipitate elongation. This coalescence of γ' precipitates in the 47Co alloy may account for the reduction in lattice misfit values observed for the 47Co alloy compared with the 38Co alloy for temperatures ambient to 700°C (Figure 3.8).

The equilibrium shapes of single γ' precipitates [183, 184, 185, 186] as well as the precipitate coarsening behaviour in multi-precipitate systems [187, 188, 189, 190] have been studied using integrated computational modelling. Johnson and Cahn, 1984 [191] demonstrated that the equilibrium morphology of an elastically-stressed precipitate with isotropic interfacial energy is not necessarily cubic, even when matrix and precipitate both exhibit cubic crystal structure. This has been termed shape bifurcation [191]. The L' parameter [192] assists in determining the bifurcation behaviour of a precipitate, where:

$$L' \equiv \frac{\overline{g^{el}}\, l}{\sigma}$$

$\overline{g^{el}}$ represents a characteristic strain energy density, l represents a characteristic length of the precipitate that equals the radius of a sphere of the same volume and σ is interfacial energy per unit area. Therefore, L' is a dimensionless parameter characterising the ratio of the elastic energy to the interfacial energy of a precipitate [192]. Differences in precipitate shape for the same value of L' may therefore be used to elucidate the influence of crystal symmetry, variation in elastic stiffness and anisotropy of the interfacial energy and misfit strain [193].

To predict the equilibrium shapes of γ' precipitates, Jokisaari *et al.*, 2017 [193] developed a phase field model using experimental data or first principle calculations to study the ternary Co-Al-W system, for which considerable published data are available compared with other Co-based γ-γ' superalloy systems. These authors suggest that the model should also apply qualitatively to systems with minor alloying additions that do not alter the sign of the misfit strain. The model used resembled the diffuse interface model of Leo *et al.*, 1998 [194]. Jokisaari *et al.* [193] used a phase field free-energy formulation that incorporates interfacial energy (between γ and γ' phases), linear elasticity and anisotropic elastic stiffnesses, whilst also incorporating the diffuse nature of the γ-γ' interface observed experimentally [126, 195]. In

seeking to determine only the equilibrium precipitate shapes, chemical phase energies or chemical diffusion are not directly included but phase chemistry is indirectly addressed through interfacial energy, misfit strain and elastic stiffnesses.

To achieve quantitative predictions of equilibrium shapes for Co-Al-W γ' precipitates, input values of γ-γ' interfacial energy, interface thickness, elastic constants and misfit strain are necessary. Jokisaari *et al*. [193] used density functional theory to calculate the γ-γ' interfacial energy, assumed isotropic, derived by building a supercell structure using the pure Co-Al-W system. The diffuse γ-γ' interface width was taken to approximate to 3-5 nm from APT measurements [126, 195]. In considering the system's elastic behaviour, this model [193] used the room temperature misfit strain value of 0.53% reported by Sato *et al*., 2006 [120] and acknowledges the potential error, due to elastic stress, introduced by misfit strain values calculated using constrained lattice parameters from two-phase materials rather than from single-phase unconstrained values. Because of the potential for elastically driven bifurcation behaviour, both spherical and ellipsoid initial shapes were used [193]. The L' parameter was invoked to characterise the ratio of elastic to interfacial energy of a precipitate.

From the study of single precipitates, using elastic stiffness tensor values at 300 K, Jokisaari *et al*. [193] simulated a range of precipitate sizes for the Co-Al-W system, the smallest of diameter 20 nm (L' value 0.28). A continuous transition from spherical to cuboidal occurred as the equilibrium size of the precipitates increased to 180 nm (L' value 2.8). This is deemed a consequence of the increasing ratio of elastic energy to interfacial energy of the precipitate. For this size range, the final precipitate was shown to exhibit cuboidal symmetry irrespective of whether the initial precipitate morphology was spherical or ellipsoid [193]. In contrast, precipitates of larger size exhibited different behaviour. Those of spherical initial condition preserved the cubic symmetry but precipitates with an ellipsoid initial condition displayed a lower order of symmetry, indicating that the increase in total interfacial energy of the precipitate that occurs with the symmetry change is more than offset by the reduction in elastic energy [193].

According to the model of Jokisaari *et al*. [193], elastic shape instability (or bifurcation behaviour) occurred at certain critical precipitate sizes, the first critical size being between 180-242 nm ($2.8 < L' < 3.9$). Above this size the precipitate equilibrium shape is plate like with low axial anisotropy ratios. A second critical size lies between 277-319 nm ($4.4 < L' < 5.2$), above which precipitates are rod like, with the rod extending along one of the <100> directions

and the ratio of long: short axes becoming greater with increasing precipitate volume. This shape bifurcation purportedly explains the directional coarsening observed experimentally in the absence of applied stress in the Co-Al-W system [138, 195].

The results of Jokisaari *et al*. [193] may be compared with those of Li *et al*., 2004 [192] who investigated systematically the effect of elastic inhomogeneity on the equilibrium states of an isolated precipitate in a Ni alloy model. Li *et al*. [192] studied four different precipitate/matrix stiffness ratios and reported a critical L' for bifurcation within $3 < L' < 4$ for the system with homogeneous moduli. Systems with less stiff precipitates showed one shape bifurcation, but, for the stiffest precipitate system, two shape bifurcations were reported with increasing precipitate size: plate like initially with a small axial anisotropy ratio (which decreased with increasing precipitate stiffness) and then rod like. By comparison, Jokisaari *et al*. [193] report a critical L' between 2.8 and 3.9, showing a similarity to the case of homogeneous moduli reported in [192], in addition to the plate like and rod like shape transitions seen only with the stiffest precipitate in [192]. Jokisaari *et al*. [193] suggest that it is the ratio of elastic constants $C_{1212}^{\gamma'}$ *to* C_{1212}^{γ} that is the critical factor for controlling the axial anisotropy ratio of plate like morphologies and the second bifurcation to rod like morphologies.

The shape bifurcation behaviour described by Jokisaari *et al*. [193] and Li *et al*. [192] may account for the evolution of γ' precipitate morphology from cuboidal to rod like observed in the current study in the Ni-47Co-5Al-5Ti-15Cr (at.%) alloy following ageing for 1000 hours at 800°C (Figure 3.4).

3.5 Conclusions

Using neutron diffraction, this study investigated the effect of increasing Co content (0-56 at.%) on γ and γ' lattice parameters and resultant lattice misfit of $(Ni,Co)_{75}Al_5Ti_5Cr_{15}$ (at.%) alloys (aged at 800°C, 1000 hours) at room temperature, 400, 600, 700 and 800°C. The following conclusions were drawn.

- Alloys of Co content 0 to 47 at.% exhibited a positive lattice misfit at each test temperature. For each test temperature, the magnitude of lattice misfit increased with increasing Co content from 0 to 38 at.%.
- Values of room-temperature lattice parameter expansion (in Å) per at.% Co were calculated for individual γ and γ' phases. These values are, respectively, 6×10^{-5} Å/at.%

and 2×10^{-4} Å/at.% over the 0-38 at.% Co range and 2×10^{-4} Å/at.% and 4×10^{-4} Å/at.% over the 0-19 at.% Co range.

- The increase in room-temperature lattice misfit values with increasing Co content up to 38 at.% appeared to parallel the increased partitioning of Ni and Co to the γ' phase observed over the same Co concentration range in a systematic study using atom probe tomography on the same alloy series (Chapter 2).
- As Co content increased from 38 at.% to approach 47 at.%, a diminution in lattice misfit was observed for test temperatures ambient to 700°C. This diminution was pronounced at room temperature but less pronounced at higher temperatures.
- No lattice parameter or lattice misfit values could be derived for the 56 at.% Co alloy. The 56 at.% Co alloy neutron diffraction patterns obtained for each test temperature (ambient, 400, 600, 700 and 800°C) appeared to indicate a strain-induced distortion of the γ' phase.
- With respect to the effect of temperature on lattice parameter and lattice misfit values, lattice misfit decreased with increasing temperature from ambient to 800°C for alloys containing 0 to 47 at.% Co. Thus, a systematic shift in the lattice misfit-temperature curve toward higher misfit values was apparent as Co content increased from 0 to 38 at.%. However, the 47 at.% Co alloy showed a lesser diminution in lattice misfit with increasing temperature than was observed for the lower Co alloys.

In summary, lattice misfit values were positive for the six $(Ni,Co)_{75}Al_5Ti_5Cr_{15}$ (at.%) alloys with Co content 0 to 47 at.%. Lattice misfit values were observed to decrease with decreasing Co content from 38 to 0 at.% and decrease with increasing temperature from ambient towards the proposed new operating temperatures for turbine discs approaching 800°C.

4. Effect of Co:Ni Ratio on Oxidation Behaviour of γ-γ' Ni-Co-5Al-5Ti-15Cr (at.%) alloys

The effect of a systematic increase in Co:Ni ratio on the oxidation performance of γ-γ′ alloys based on the Ni-Co-Al-Ti-Cr system was investigated. Seven model superalloys of fixed Cr (15 at.%), Ti (5 at.%) and Al (5 at.%) content and varying Co content (0 to 56 at.%) underwent isothermal oxidation in air at 800°C using both thermogravimetric analysis (100 hours) and box-furnace exposure (1000 hours). Following 1000 hours oxidation at 800°C, the 28Co, 38Co and 47Co alloys were observed to exhibit a flat, compact, well-defined external oxide scale and Cr_2O_3 layer with minimal oxygen ingress, together with a distinct Al_2O_3 sub-scale.

4.1 Introduction

As mentioned in Chapter 1, conventional turbine disc rotor components are fabricated from polycrystalline nickel-based superalloys typically comprising a Ni-rich solid solution (γ) of FCC crystal structure (A1), strengthened by coherent $Ni_3(Al,Ti)$ intermetallic precipitates (γ') of $L1_2$ superlattice structure [1]. Refractory elements such as W and Mo have also been incorporated in Ni-based superalloys to confer solid solution strengthening of the γ matrix phase [41]. Cr has traditionally been a critical addition in turbine disc Ni-based superalloys due to its ability to form a protective (diffusion-resistant) Cr_2O_3 scale, imparting resistance to oxidation and hot corrosion at high temperature [5]. High Cr concentrations can, however, encourage formation of the topologically close-packed σ phase, known to be detrimental to alloy strength [8, 11]. Therefore, Cr content must be optimised for adequate environmental resistance whilst retaining an exclusively γ-γ' microstructure. Although highly successful for several decades as aero-engine turbine discs, superalloys based on the Ni-Ni_3Al (A1-$L1_2$) system are approaching the limits of their high-temperature capability.

As mentioned in Chapter 2, a partial phase diagram for the *quaternary* Ni-Al-Co-Ti system experimentally derived for temperatures in the range 750-1100°C [155, 156, 157] has been shown to exhibit a continuous γ-γ' two-phase field between the Ni-Ni_3Al and Co-Co_3Ti equilibria, suggesting that alloy compositions within this two-phase field exhibit the desired A1-$L1_2$ microstructure [155, 156, 157]. Indeed, incorporation of higher concentrations of both Co and Ti in conventional Ni-based superalloy compositions has been shown to elicit a γ-γ' microstructure that confers improved high-temperature strength and creep resistance [88, 148, 154, 158, 159]. This is purportedly due to several mechanisms, notably to the higher γ' volume

fraction conferred by Co-Ti co-addition [148, 154, 158, 159], although the solid solution hardening of γ and γ' by Co and Ti respectively is assumed to contribute to the increased high-temperature yield strength [158]. Although this appears encouraging for novel superalloy design, the higher proposed turbine entry temperatures demanded for improved fuel efficiency inevitably impose a harsher oxidising environment on the superalloys constituting the high-pressure turbine discs. The oxidation resistance of these high Co-Ti candidate superalloys therefore becomes critical.

Crucially, alloys developed for high-temperature applications are engineered to confer surface integrity by oxidising to form a thermally stable, adherent and slow-growing oxide scale free from pores and cracks [63, 196]. Most conventional Ni-based turbine disc alloys are characteristic of chromia-formers [63, 77] i.e. they contain sufficient Cr to establish a continuous Cr_2O_3 scale during oxidation [73, 197] capable of protecting the underlying alloy at temperatures up to approximately 1000°C [72]. However, superalloys that elicit protective Cr_2O_3 scales can undergo accelerated degradation at high temperature in high oxygen partial pressures due to evaporation of Cr_2O_3 to CrO_3, causing metal consumption and recession [72]. This volatilisation becomes significant above approximately 1000°C, and even at lower temperatures in the presence of high velocity gases [197]. In this highly-oxidising environment, alumina-forming alloys appear more robust, as no vapour species exist in the Al-O system with significant vapour pressures [72].

The thermodynamically stable form of Al_2O_3 is the slow-growing α-Al_2O_3 of corundum crystal structure [73]. However, at temperatures below ~1200°C, oxidation of Al_2O_3-forming alloys frequently elicits fast-growing transient metastable Al_2O_3 scales that are crystalline below certain temperature barriers [198]. The metastable γ-, δ- and θ-Al_2O_3 phases transform to the stable α-Al_2O_3 phase providing that activation barriers are overcome. This may be achieved thermally but depends also on the presence of other species [198]. Cr has been reported to accelerate the transformation of metastable θ-Al_2O_3 to α-Al_2O_3 by initial formation of chromia, which is isotypic with α-Al_2O_3 thus providing sites for α-Al_2O_3 nucleation [73, 198]. Ni also reportedly accelerates transformation to α-Al_2O_3 at 850°C and 950°C [198]. Significantly, the faster-growing metastable Al_2O_3 phases possess lower density than α-Al_2O_3 and transformation to the α-Al_2O_3 is associated with a 13% volume reduction [198].

As γ-γ' (A1-$L1_2$) superalloys derived from the two-phase field between the Ni-Ni_3Al and Co-Co_3Ti equilibria of the quaternary Ni-Al-Co-Ti system appear promising candidates

for next-generation higher-temperature turbine discs, elucidation of their high-temperature oxidation behaviour is critical. The current study provides a systematic investigation into the effect of increasing Co:Ni ratio on oxidation performance of model γ-γ' superalloys based on the *quinary* Ni-Co-Al-Ti-Cr system at the higher proposed in-service temperature of 800°C.

4.2 Experimental Procedure

4.2.1 Materials and heat treatment

The model superalloys tested were of the $(Ni,Co)_{75}Al_5Ti_5Cr_{15}$ (at.%) system for which the Ni:Co concentration ratio was varied from 1:0 to ~1:3. The alloys were named according to their nominal atomic concentration of Co: 0Co, 9Co, 19Co, 28Co, 38Co, 47Co and 56Co (Table 4.1). Polycrystalline ingots of the seven alloy compositions were fabricated by vacuum arc melting of raw elements of at least 99.9% purity. To determine solidus and γ' solvus temperatures prior to homogenisation of each alloy ingot, differential scanning calorimetry (DSC) was performed on alloy discs (5 mm × 1 mm) extracted by spark erosion. For this purpose, a Netzsch 404 heat-flux calorimeter was used, operating at temperatures of up to 1450°C with a heating rate of 10°C min^{-1}. The cast alloy ingots were encapsulated in quartz tubes, back-filled with argon before being subjected to a homogenisation heat treatment (1250°C, 24 hours) to minimise casting-induced micro-segregation. This homogenisation heat treatment temperature was chosen to lie within the γ single-phase field, above the γ′ solvus temperatures of the alloys but sufficiently below their solidus temperatures to preclude incipient melting.

Table 4.1. Nominal and measured chemical compositions (mean ± standard deviation, σ) of the seven model superalloys investigated. Measurements obtained using SEM-EDS on alloys in the homogenised condition were within ±1 at.% of their nominal composition.

Alloy	Nominal composition (at.%)					Measured composition (at.%)									
	Ni	Co	Al	Ti	Cr	Ni	±σ	Co	±σ	Al	±σ	Ti	±σ	Cr	±σ
0Co	75.0	0.0	5.0	5.0	15.0	74.96	0.09	-	-	5.01	0.04	5.16	0.02	14.87	0.06
9Co	65.6	9.4	5.0	5.0	15.0	65.55	0.05	9.60	0.03	4.97	0.04	5.13	0.03	14.76	0.09
19Co	56.3	18.8	5.0	5.0	15.0	56.2	0.1	19.08	0.04	4.82	0.07	5.25	0.04	14.65	0.10
28Co	46.9	28.1	5.0	5.0	15.0	46.52	0.10	28.9	0.1	4.80	0.09	5.27	0.03	14.55	0.05
38Co	37.5	37.5	5.0	5.0	15.0	37.42	0.06	38.33	0.11	4.83	0.06	4.92	0.04	14.50	0.05
47Co	28.1	46.9	5.0	5.0	15.0	28.11	0.13	47.24	0.10	4.83	0.12	5.19	0.18	14.63	0.15
56Co	18.8	56.3	5.0	5.0	15.0	18.69	0.16	56.81	0.05	4.8	0.1	5.21	0.08	14.5	0.1

4.2.2 Microstructural characterisation of homogenised alloys prior to oxidation

An alloy specimen of ~1 cm thickness was cut from the end of each homogenised ingot and mounted in conductive Bakelite. Specimens were ground with wet SiC abrasive paper and polished using a progressively finer diamond suspension (from 6 µm down to 1 µm). The polished samples were then electrolytically etched with a 10% phosphoric acid solution to dissolve the γ matrices and highlight γ′ precipitates. Alloy microstructure was examined using an FEI Nova NanoSEM 450 scanning electron microscope (SEM) in secondary electron (SE) mode to verify the presence of a γ/γ′ microstructure with no other phases present. Energy dispersive X-ray spectroscopy (EDS) was carried out using a Bruker XFlash 6 solid state EDS system to determine a mean measured composition for each alloy from a minimum of 5 large area scans of at least 500 × 500 µm (Table 4.1). The measured composition for each alloy was determined to be within ±1 at.% of its nominal composition. The mounted specimens were then re-polished and etched with OP-S (colloidal silica suspension) diluted 1:1 in water to highlight γ grain boundaries for subsequent determination of alloy grain size using a Camscan MX2600 FEGSEM microscope.

4.2.3 Isothermal oxidation of homogenised alloys at 800°C

The seven model superalloys of fixed Cr (15 at.%), Ti (5 at.%) and Al (5 at.%) and varying Co content (0, 9, 19, 28, 38, 47, 56 at.%) were oxidised isothermally at 800°C in air. Each alloy was oxidised using two separate methods: thermogravimetric analysis (TGA) for 100 hours and box-furnace exposure for 1000 hours.

(i) Thermogravimetric analysis of alloys during isothermal oxidation (800°C, 100 hours)

For each alloy composition, a rectangular plate (nominally 10 × 6 × 0.5 mm) was cut from the homogenised alloy ingot using a Secotom-10 cutting machine. Each plate was spark eroded to produce a small hole approximately 2 mm diameter, 1 mm from the top of the sample and equidistant from the sides. For uniform oxidation of each alloy specimen, all surfaces were ground using SiC abrasive paper and polished using a 4000 SiC grit size. All edges and corners were chamfered and polished to achieve the same surface finish. Each specimen plate was then measured using a micrometer accurate to ±0.01 mm to calculate surface area. The specimen alloys were then ultrasonically cleaned in ethanol for 6 minutes and weighed before and after oxidation using a calibrated balance accurate to ±0.01 mg. TGA was performed using a Setaram SETSYS Evolution instrument to permit continual monitoring of alloy mass as

oxidation progressed with time. Alloy specimens for TGA were suspended from a platinum wire attached to an electrical microbalance and air was introduced into the sample chamber during testing at a rate of 30 $ml.s^{-1}$. For each TGA test, specimen mass was recorded every 30 seconds for 100 hours to obtain a graph of mass gain per unit area (specific mass gain) as a function of time. Subsequent data analysis was performed using Igor Pro 6.3 software [161] to assess how the oxidation kinetics may vary with increasing alloy Co:Ni ratio.

(ii) Isothermal box-furnace oxidation of alloys (800°C, 1000 hours)

For each alloy composition, a square plate (nominally 5 × 5 × 1 mm) was cut from the homogenised alloy ingot using a Struers Accutom-5 cutting machine. For uniform oxidation of each alloy plate, all surfaces were polished as for the TGA specimens. Alloy plates for box-furnace exposures were measured using a micrometer accurate to ±0.01 mm, ultrasonically cleaned in ethanol for 6 minutes and then weighed before and after oxidation using a calibrated balance accurate to ±0.01 mg. Alloy plates were placed in individual open alumina crucibles and oxidised for 1000 hours in a box furnace pre-heated to 800°C (temperature measured using a calibrated n-type thermocouple). Specimens were subsequently air-cooled.

4.2.4 Characterisation of oxides following TGA and box-furnace exposure at 800°C

(i) Surface oxides: SEM-EDS point analysis and X-ray diffraction (XRD)

For alloy specimens oxidised by TGA (800°C, 100 hours), the FEI Nova NanoSEM 450 was used in SE mode to examine alloy specimen surfaces (accelerating voltage 5 kV) and SEM-EDS point analysis performed (accelerating voltage 15 kV) to acquire elemental composition data on surface oxide species present. The FEI Nova NanoSEM 450 was used under similar conditions to examine alloy surfaces of the 5 × 5 × 1 mm specimens oxidised by box-furnace exposure (800°C, 1000 hours). X-ray diffraction (XRD) was carried out on TGA-oxidised (100 hours) and box furnace-oxidised (1000 hours) alloy specimens to identify surface oxide phases present. A Bruker D8 Advance X-ray diffractometer was employed, operated at 40 kV and 40 mA with Cu Kα radiation. (A Ni filter of 0.012 mm thickness was added to attenuate the Cu Kβ signal). Data were acquired over a range of $20° < 2\theta < 120°$, with a step size of 0.03° and dwell time of 2 seconds. As diffraction data were collected using a variable divergence slit to achieve a fixed irradiation length, DIFFRAC.EVA software [199] was employed to simulate a fixed divergence slit, corresponding to a constant effective irradiation volume. The Inorganic Crystal Structure Database (ICSD) [200] was consulted to identify

individual phases from peaks in XRD traces. Only the oxides that formed in the external scale were analysed by this method due to the limited penetration depth of the X-rays.

(ii) Cross-sectional SEM-EDS analysis of TGA and box-furnace oxidised alloys (800°C)

Cross-sections were obtained for all alloys oxidised at 800°C by mounting the specimen in conductive Bakelite, grinding using wet SiC abrasive paper (down to 2500 grit size) and polishing using a progressively finer diamond suspension (6 µm down to 0.25 µm). Cross-sectional oxide scale and sub-scale morphology were examined using the FEI Nova NanoSEM 450 in back-scattered electron (BSE) mode to elucidate the effect of a systematic increase in Co content on alloy microstructure.

For specimens oxidised by box-furnace exposure for 1000 hours, the FEI Nova NanoSEM 450 was used to generate ten BSE micrographs from which fifty measurements of oxide scale thickness were taken using ImageJ software. Similarly, ten BSE micrographs were acquired to permit fifty measurements of depth of internal oxidation products using ImageJ software. A ZEISS GeminiSEM 300 microscope equipped with an Oxford Aztec EDS system was then employed to generate SEM-EDS maps for each cross-sectioned alloy specimen under standardised conditions using 50 frames (accelerating voltage 15 kV). For the 0Co and 47Co alloys, EDS linescans were also generated under standardised conditions using the same microscope and EDS system (100 passes). The EDS system had been calibrated using a nickel strip prior to acquiring EDS maps and linescans.

4.2.5 Use of larger specimens to measure mass gain and to elucidate oxidation behaviour

(i) Specific mass gain, XRD and SEM surface analysis

To elucidate the influence of increasing Co:Ni ratio on oxide morphology and mass gain as a result of oxidation, larger specimens (nominally 10 × 6 × 1 mm) were cut using a Secotom-10 cutting machine and then processed as for the 5 × 5 × 1 mm specimens for all seven alloy compositions prior to isothermal box-furnace oxidation. All specimens were weighed before and after oxidation using a calibrated balance accurate to ±0.01 mg. Each specimen was oxidised for 1000 hours in an open alumina crucible in a box furnace pre-heated to 800°C (temperature measured using a calibrated n-type thermocouple). Following oxidation, specimens were air-cooled and XRD used to identify oxide phases present using the Bruker D8 Advance diffractometer with the same experimental parameters as before (section

4.2.4. *i*). Oxide surfaces were examined under SE and BSE modes using the ZEISS GeminiSEM 300 microscope to assess surface morphology over a large area.

(ii) Secondary ion mass spectrometry (SIMS)

Secondary ion mass spectrometry (SIMS) was performed on the 10 × 6 × 1 mm specimens for the oxidised 19Co and 38Co alloys in order to verify the microstructural characteristics observed in EDS maps for the 5 × 5 × 1 mm specimens. To generate a ramped section across the external oxides and internal oxidation products, an FEI FIB200 SIMS instrument equipped with a $^{69}Ga^{+}$ primary ion source was used for milling an angle of 30° to the oxidised specimen surface. A beam energy of 30 kV and a beam current of 330 pA were employed to acquire elemental concentration maps across the ramped sections. The elements Al, Ti and Cr were detected by a quadrupole detector as positively charged secondary ions. For the oxidised 38Co alloy specimen, SIMS elemental count vs. time profiles were obtained from a surface region of approximately 25 × 25 μm using a beam current of 3325 pA.

(iii) SEM examination and EDS linescans

Cross-sections of the 10 × 6 × 1 mm oxidised alloy specimens were then prepared as for the 5 × 5 × 1 mm box-furnace oxidised specimens (section 4.2.4. *ii*) to assess the reproducibility of the oxide morphologies observed. The ZEISS GeminiSEM 300 microscope was used in BSE mode for examining oxide scale and sub-scale morphology (accelerating voltage 15 kV). EDS linescans were generated as before to provide elemental concentration profiles across the oxidation products for alloys 0Co, 19Co, 28Co, 38Co and 47Co.

4.3 Results and Discussion

For all seven model superalloys in their homogenised condition, SEM analysis indicated a γ-γ′ microstructure with no other phases apparent (Figure 4.1). For each alloy, the grain size following homogenisation was of the order of millimetres and therefore too coarse for implementing conventional methods of grain size analysis.

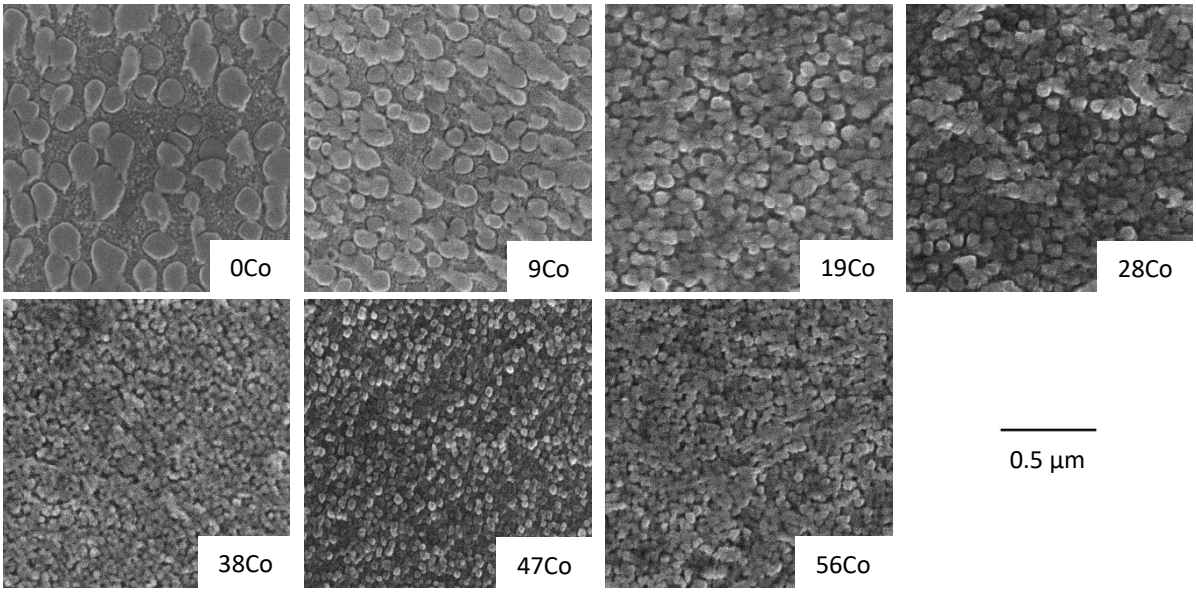

Figure 4.1. Representative SE images of alloy γ-γ' microstructure following homogenisation heat treatment at 1250°C for 24 hours. All alloys exhibited γ' precipitates embedded in a γ matrix with no other phases apparent. An FEI Nova NanoSEM 450 microscope was used.

4.3.1 Thermogravimetric analysis (800°C, 100 hours)

(i) Specific mass gain vs. exposure time

Figure 4.2 shows specific mass gain as a function of time during isothermal TGA oxidation (800°C, 100 hours) for each of the seven model superalloys tested. The initial rate of specific mass gain appeared faster for higher Co alloys (28Co, 38Co, 47Co, 56Co) than for the 0Co, 9Co and 19Co alloys. However, from Figure 4.2 and Table 4.2, there appeared no definitive correlation between final specific mass gain and Co:Ni ratio following 100 hours TGA oxidation. To assess reaction kinetics, Igor Pro software was used to determine a value of *n* (Table 4.2) for each alloy composition according to Equation 4.1:

$$\frac{\Delta m}{S.A.} = A \,.\, t^{\frac{1}{n}} \qquad \text{Equation 4.1}$$

where Δm is mass change (mg), *S.A.* is initial surface area (cm^2), *t* is time (s) and *A* is a constant. An *n* value of 2 would indicate a parabolic relationship between specific mass gain and time, as determined for the 9Co alloy ($n = 2.0628$). The 47Co and 56Co alloys generated *n* values approaching $n = 3$, indicative of cubic kinetics and therefore the formation of a number of new oxide species is implied. Alloys containing between 19 and 38 at.% Co generated *n* values between 2 and 3. For each *n* value, Igor Pro software generated a low standard deviation (Table 4.2). To assess reproducibility of *n* values, an additional 19Co specimen was extracted from

the homogenised bar, prepared as before and subjected to TGA under the same conditions. An *n* value of 2.1047 ± 0.0006 was derived for this specimen, indicating a difference of 0.2 in *n* values obtained from different specimens of the same alloy composition.

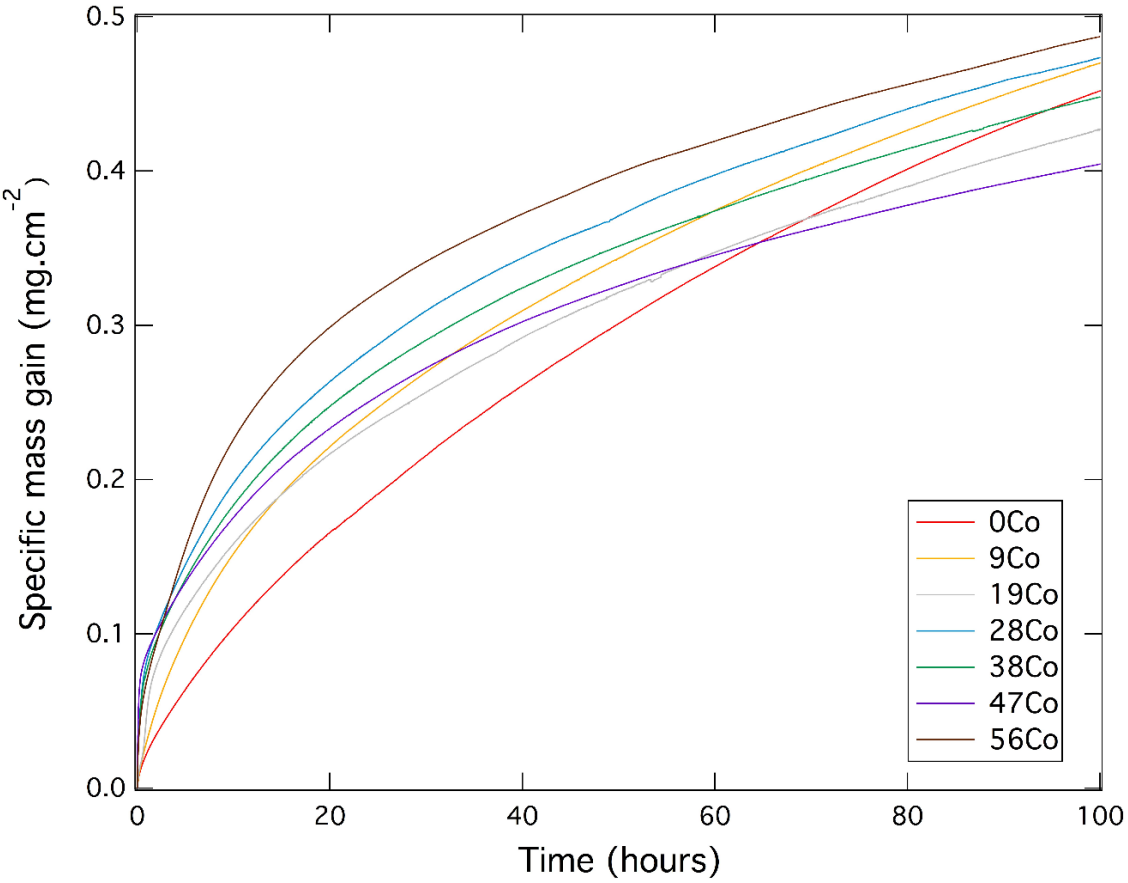

Figure 4.2. TGA data obtained during isothermal oxidation (800°C, 100 hours) for alloys 0Co, 9Co, 19Co, 28Co, 38Co, 47Co and 56Co. Graph shows specific mass gain vs. exposure time.

Table 4.2. Specific mass gain obtained by weighing alloy specimens before and after TGA oxidation (800°C, 100 hours). Also displayed are best-estimate values of *n* (Equation 4.1) generated using Igor Pro software for the TGA data shown in Figure 4.2.

Alloy	**Specific mass gain after cooling (mg.cm^{-2})**	**Best-estimate *n* value ± standard deviation (σ)**
0Co	0.49	1.5891 ± 0.0006
9Co	0.51	2.0628 ± 0.0012
19Co	0.48	2.3295 ± 0.0007
28Co	0.56	2.6611 ± 0.0012
38Co	0.53	2.6367 ± 0.0012
47Co	0.57	2.8450 ± 0.0017
56Co	0.60	2.975 ± 0.004

(ii) Surface oxide phases following TGA: SEM-EDS and XRD

Following TGA oxidation (800°C, 100 hours), all seven model superalloy surfaces were examined under SEM using SE mode (Figure 4.3). The 0Co and 9Co alloys appeared to exhibit a relatively uniform granular oxide morphology, whereas higher Co alloys (19Co, 28Co, 38Co and 47Co) appeared to differentiate two distinct types of surface morphology: areas observed as pale with relatively large grains and contrasting darker areas of apparently smaller grains, possibly indicating the presence of differing surface phases. The 56Co alloy appeared to exhibit pale nodular areas on the oxidised specimen surface, subsequently identified by EDS point analysis as rich in Co (~44 at.%) and oxygen (~52 at.%), plausibly CoO and/or Co_3O_4. The non-uniform surface morphology observed for alloys 19Co, 28Co, 38Co, 47Co and 56Co following TGA suggests a more complex evolution of oxide scale phases than that observed for the 0Co and 9Co alloys.

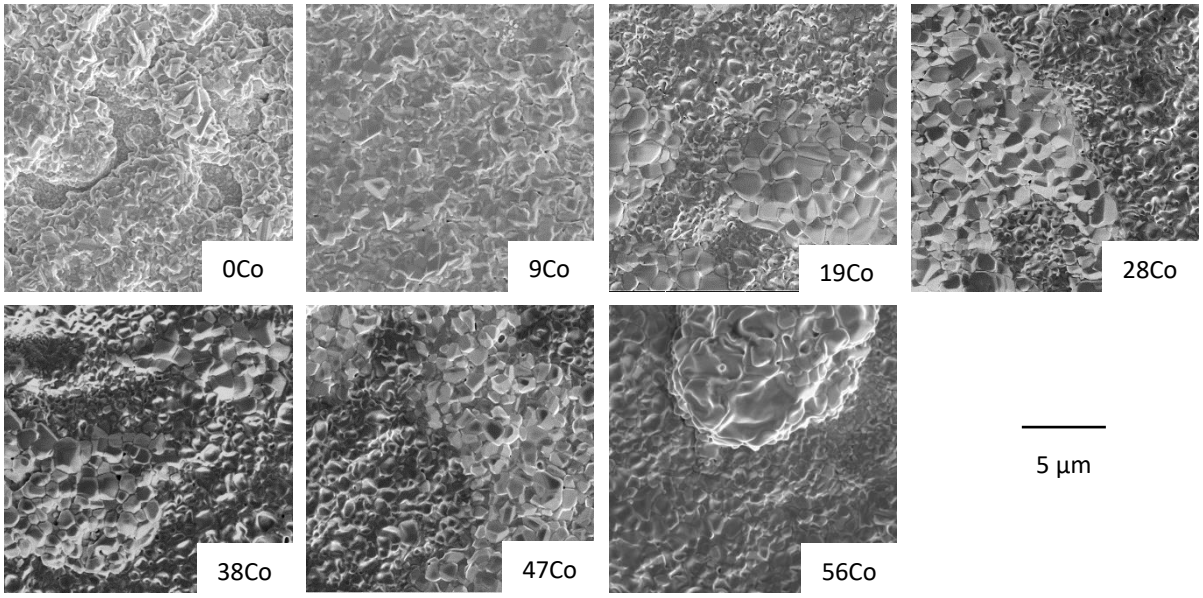

Figure 4.3. SE micrographs of oxidised alloy specimen surfaces following TGA (800°C, 100 hours). Alloys 19Co and above exhibited pale areas and contrasting darker areas of apparently smaller grains. An FEI Nova NanoSEM 450 microscope was used.

Table 4.3 and Figure 4.4 show elemental composition data associated with the two distinct surface morphologies observed for alloys 19Co, 28Co, 38Co, 47Co and 56Co, as indicated by SEM-EDS point analysis. For alloy 19Co and alloys with higher Co content (Table 4.3), areas of pale morphology appeared associated with a combined (Ni+Co) content of ~44-49 at.% and an oxygen content of ~49-54 at.%, implying the presence of (Ni,Co)O. Ni and Co are known to form a continuous range of solid solutions with NiO (lattice parameter, a_{NiO} = 4.17 Å) and CoO (lattice parameter, a_{CoO} = 4.25 Å) being isomorphous, producing a (Ni,Co)O solid solution of variable composition [201]. This (Ni,Co)O surface phase was subsequently identified by XRD analysis for alloys of 19Co and above (Table 4.4), and, from Figure 4.4, appeared to exist predominantly as a (Ni,Co)O for alloys 19Co, 28Co and 38Co, but as a (Co,Ni)O for the 47Co and 56Co alloys. From Figure 4.4, the transition from (Ni,Co)O to (Co,Ni)O was identified as occurring at ~43 at.% Co. The other elements Ti, Cr and Al appeared scarcely present in the pale areas of morphology i.e. their concentrations were too small to quantify accurately by SEM-EDS point analysis. For the areas of dark morphology in alloys 19Co and above, the proportion of Co:Ni appeared to change as follows: 1:1 (19Co); 2:1 (28Co); 2:1 (38Co); 3:1 (47Co) and 6:1 for the 56Co (Table 4.3). These areas of dark morphology appeared to contain a relatively high proportion of Ti (~10–14 at.%) compared with the paler areas.

Table 4.3. Surface SEM-EDS point analysis data for alloys 19Co and above oxidised by TGA (800°C, 100 hours) showing elemental composition (mean ± standard deviation σ) for pale and dark areas of morphology.

Alloy	Morphology	Elemental composition (at.%)							
		Ni	±σ	Co	±σ	O	±σ	Ti	±σ
19Co	Pale	38	5	6.7	1.4	54	7	-	-
	Dark	10.2	1.3	9.9	1.9	57	8	13	3
28Co	Pale	37	9	12	3	49	11	-	-
	Dark	9.9	0.8	17	3	54	5	14	2
38Co	Pale	31	7	16	5	50	12	-	-
	Dark	8.77	1.08	18	2	59	5	11.0	1.4
47Co	Pale	15	8	29	10	50	15	-	-
	Dark	6.2	1.1	20	3	58	12	12	4
56Co	Nodule (pale)	2.5	0.7	44	13	52	14	-	-
	Dark	3.7	0.7	25	3	60	3	10	4

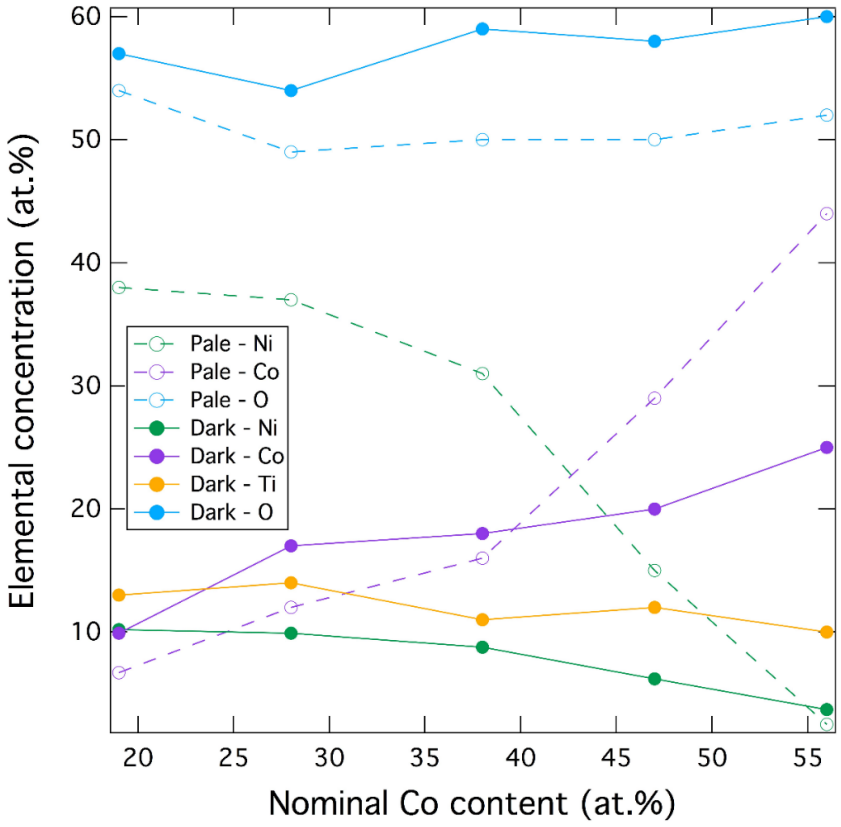

Figure 4.4. Surface SEM-EDS point analysis data for alloys 19Co and above oxidised by TGA (800°C, 100 hours) showing the effect of increasing Co on elemental composition of oxide surface morphologies (data from Table 4.3).

From XRD data (Table 4.4), all alloys appeared to form Cr_2O_3 of corundum crystal structure, with rutile (TiO_2) detected for all alloys except for the 56Co. $NiCr_2O_4/CoCr_2O_4$ spinel phases appeared present in all alloys except for the 0Co, although reference peaks for individual $NiCr_2O_4$ or $CoCr_2O_4$ phases occurred in close proximity such that experimental peaks could not be allocated definitively to either. Similarly, $NiTiO_3/CoTiO_3$ phases appeared present in all alloys except for the 0Co, although reference peaks for individual $NiTiO_3$ or $CoTiO_3$ phases occurred in close proximity such that experimental peaks could not be allocated definitively to either. The 47Co and 56Co alloys appeared to form Co_3O_4 spinel phase (Table 4.4), although it may be noted that reference peaks for Co_3O_4 appeared to overlap with reference peaks corresponding to $NiAl_2O_4$, $CoAl_2O_4$ and $NiCo_2O_4$ spinel phases, such that the latter phases may also be present. Overall, XRD analysis of alloy oxide surfaces detected an increased number of phases with increasing Co:Ni ratio (Table 4.4), consistent with the higher *n* values generated for the higher Co alloys (Table 4.2).

Table 4.4. Surface oxide phases as indicated by XRD data for TGA-oxidised alloys (800°C, 100 hours). For each of the seven alloy compositions, the underlying γ-Ni/Co matrix phase was also detected. The Co content for which (Ni,Co)O transitions to (Co,Ni)O was deduced from Figure 4.4 to be ~43 at.%.

Alloy	**Phases identified by XRD after TGA oxidation (800°C, 100 hours)**					
0Co	Cr_2O_3	TiO_2	-	-	-	-
9Co	Cr_2O_3	TiO_2	$NiCr_2O_4/CoCr_2O_4$	$NiTiO_3/CoTiO_3$	-	-
19Co	Cr_2O_3	TiO_2	$NiCr_2O_4/CoCr_2O_4$	$NiTiO_3/CoTiO_3$	(Ni,Co)O	-
28Co	Cr_2O_3	TiO_2	$NiCr_2O_4/CoCr_2O_4$	$NiTiO_3/CoTiO_3$	(Ni,Co)O	-
38Co	Cr_2O_3	TiO_2	$NiCr_2O_4/CoCr_2O_4$	$NiTiO_3/CoTiO_3$	(Ni,Co)O	-
47Co	Cr_2O_3	TiO_2	$NiCr_2O_4/CoCr_2O_4$	$NiTiO_3/CoTiO_3$	(Co,Ni)O	Co_3O_4
56Co	Cr_2O_3	-	$NiCr_2O_4/CoCr_2O_4$	$NiTiO_3/CoTiO_3$	(Co,Ni)O	Co_3O_4

4.3.2 SEM-BSE cross-sectional analysis following TGA and box-furnace oxidation (800°C)

Figure 4.5 shows representative cross-sectional SEM-BSE micrographs of typical oxide morphologies for all seven alloy compositions following isothermal oxidation at 800°C: a) TGA for 100 hours; b) box-furnace oxidation for 1000 hours. For both oxidation methods, an external oxide scale could be observed overlying a zone of irregular intrusions penetrating toward the alloy interior. This was the case for all seven alloy compositions tested. However, the 47Co alloy exhibited a second type of morphology within the same alloy specimen oxidised for 1000 hours. These two distinct types of morphology for the 47Co were denoted Type I or Type II for the purpose of this study (Figure 4.5b). The 47Co Type I morphology resembled that observed for the 38Co in exhibiting distinct relatively *thin, flat* strata within a compact oxide scale, overlying a zone of conspicuous oxidation products projecting into the alloy interior. In contrast, the Type II 47Co morphology exhibited a relatively *thick, undulating* oxide scale of porous appearance, as observed for the lower Co alloys (0Co, 9Co, 19Co and 28Co). Significantly, the 47Co Type II morphology additionally showed what appeared to be a dense sub-scale, seen as dark on BSE micrographs, overlying a region apparently devoid of internal protrusions. The 38Co, 47Co Type I and 56Co oxide scales appeared to be thinner than those of the 0Co, 9Co, 19Co, 28Co and 47Co Type II morphologies following 1000 hours oxidation. For all alloy morphologies other than 47Co Type II, internal phases elicited by oxidation were observed as irregular intrusions penetrating the alloy interior.

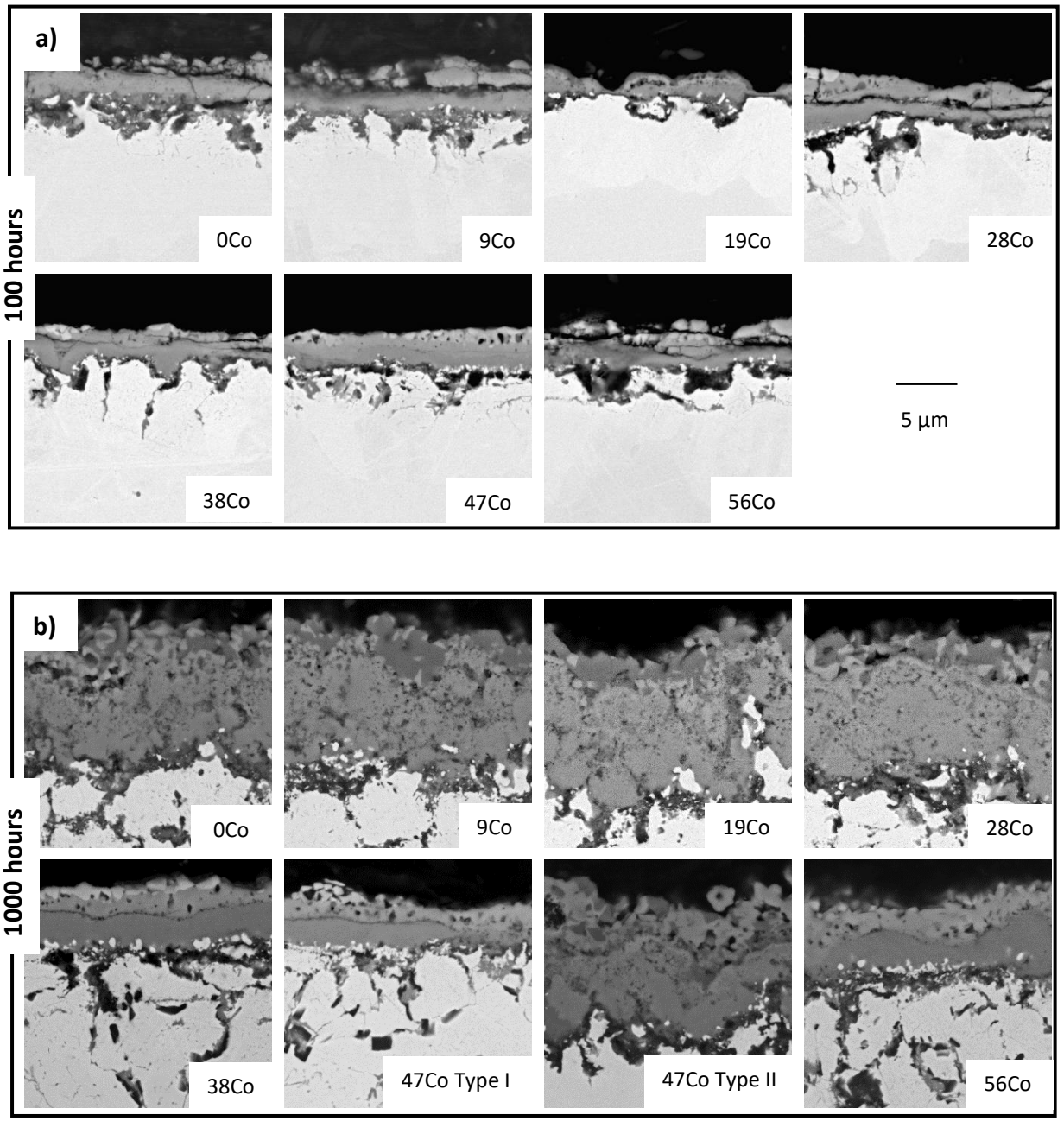

Figure 4.5. Cross-sectional SEM-BSE micrographs showing typical oxide morphologies following isothermal oxidation at 800°C: a) TGA (100 hours); b) box-furnace oxidation (1000 hours, 5 × 5 × 1 mm specimens). An FEI Nova NanoSEM 450 microscope was used. Scale bar applies to (a) and (b).

4.3.3 SEM-EDS cross-sectional analysis following box-furnace oxidation (800°C, 1000 hours)

(i) EDS maps for all seven alloy compositions

Figure 4.6 and Figure 4.7 show cross-sectional SEM-BSE micrographs and corresponding elemental concentration maps for all seven model superalloys following isothermal box-furnace oxidation (800°C, 1000 hours). The EDS maps indicate the distribution of Co, Ni, Al, Ti, Cr, O and N in the oxide scale and alloy interior. A lower magnification than that of Figure 4.5 was selected to highlight the extent of internal penetration of oxidation products.

For the alloys of relatively low Co content (0Co, 9Co, 19Co and 28Co; Figure 4.6), the relatively thick, undulating oxide scale produced appeared to comprise a Cr- and O-rich layer, plausibly Cr_2O_3, beneath an outer layer rich in Ti with associated oxygen, plausibly rutile. All four alloy compositions exhibited, beneath the layer assumed to be Cr_2O_3, a layer rich in Al with associated oxygen, putatively an Al_2O_3 sub-scale. Penetrating deeper into the alloy interior appeared internal oxidation products, indicative of Al_2O_3 and titanium nitride. The 28Co alloy appeared to show a more distinct Al- and O-rich sub-scale, with less internal Ti enrichment compared with the lower Co alloys. Additionally, for the 28Co alloy, there appeared to be less oxygen and nitrogen ingress into the alloy interior than was observed for the lower Co alloys (note the higher magnification for the 28Co alloy).

Figure 4.7 shows the oxide scales observed for alloys of relatively high Co content (38Co, 47Co and 56Co) following 1000 hours box-furnace oxidation at 800°C. The 38Co, 47Co and 56Co oxide morphologies appeared to exhibit distinct layers within the external scale (as in Figure 4.5b), with a well-defined Cr- and O-rich layer, indicative of a continuous Cr_2O_3 scale. All three high Co specimens (38Co, 47Co and 56Co) appeared to demonstrate a more compact Cr_2O_3 scale and a marked reduction in oxygen ingress into the alloy compared with the lower Co alloys. The two distinct types of oxide morphology for the 47Co alloy specimen (Type I and Type II) are evident in Figure 4.7. Whilst each of the high Co alloys (38Co, 47Co and 56Co) appeared to exhibit a sub-scale rich in Al and O, indicative of Al_2O_3, this sub-scale appeared more distinct and compact for the 47Co Type II morphology and was associated with a paucity of conspicuous internal oxidation products. The internal Al- and Ti-rich projections evident in the 38Co, 47Co Type I and 56Co alloy morphologies did not appear associated with oxygen but rather with nitrogen, indicating the presence of nitrides of Al and Ti (Figure 4.7).

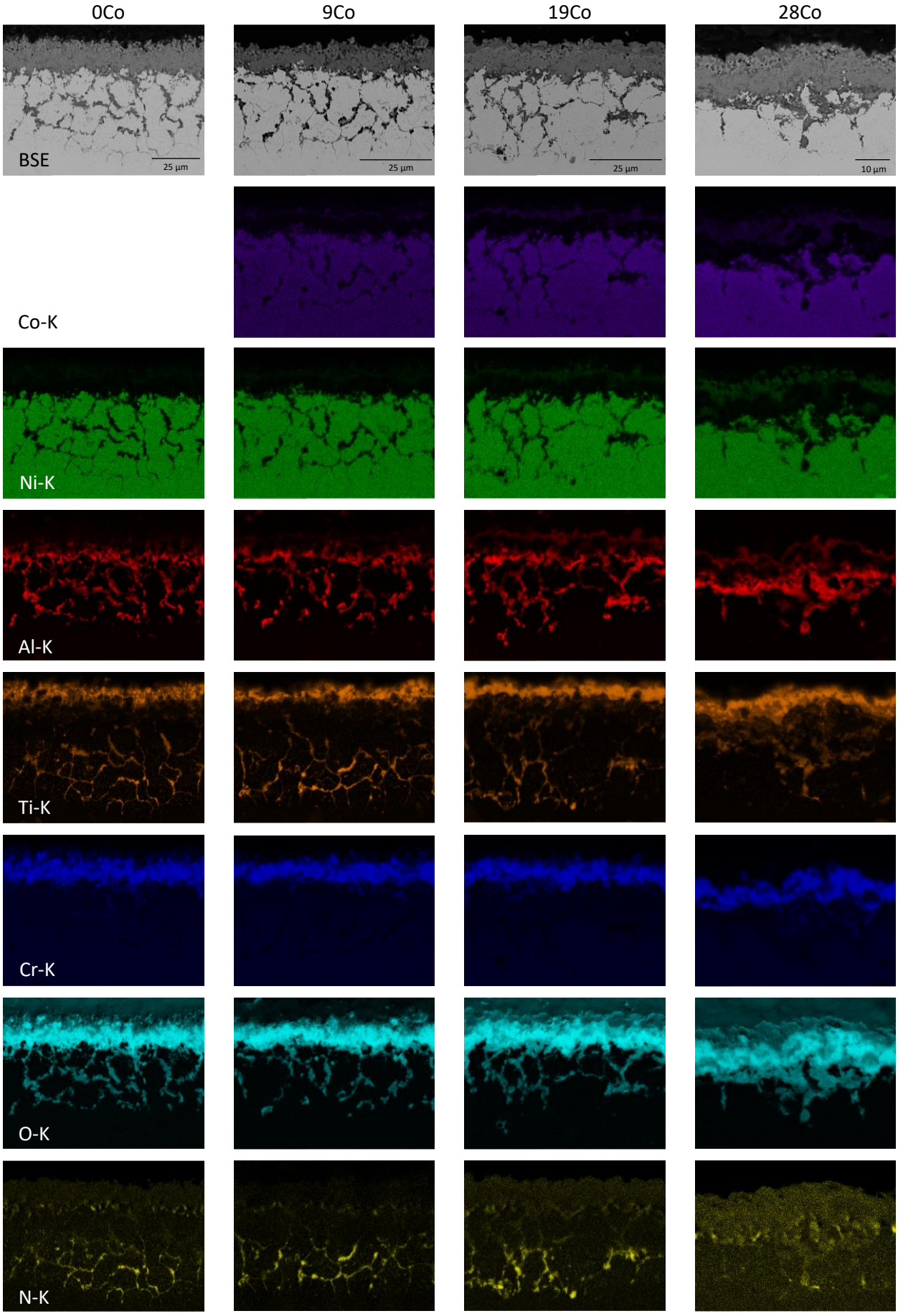

Figure 4.6. Cross-sectional SEM-BSE micrographs and corresponding EDS elemental concentration maps for 0Co, 9Co, 19Co and 28Co following isothermal box-furnace oxidation (800°C, 1000 hours). A ZEISS GeminiSEM 300 microscope was used (5 × 5 × 1 mm specimens). Note differing scale bars.

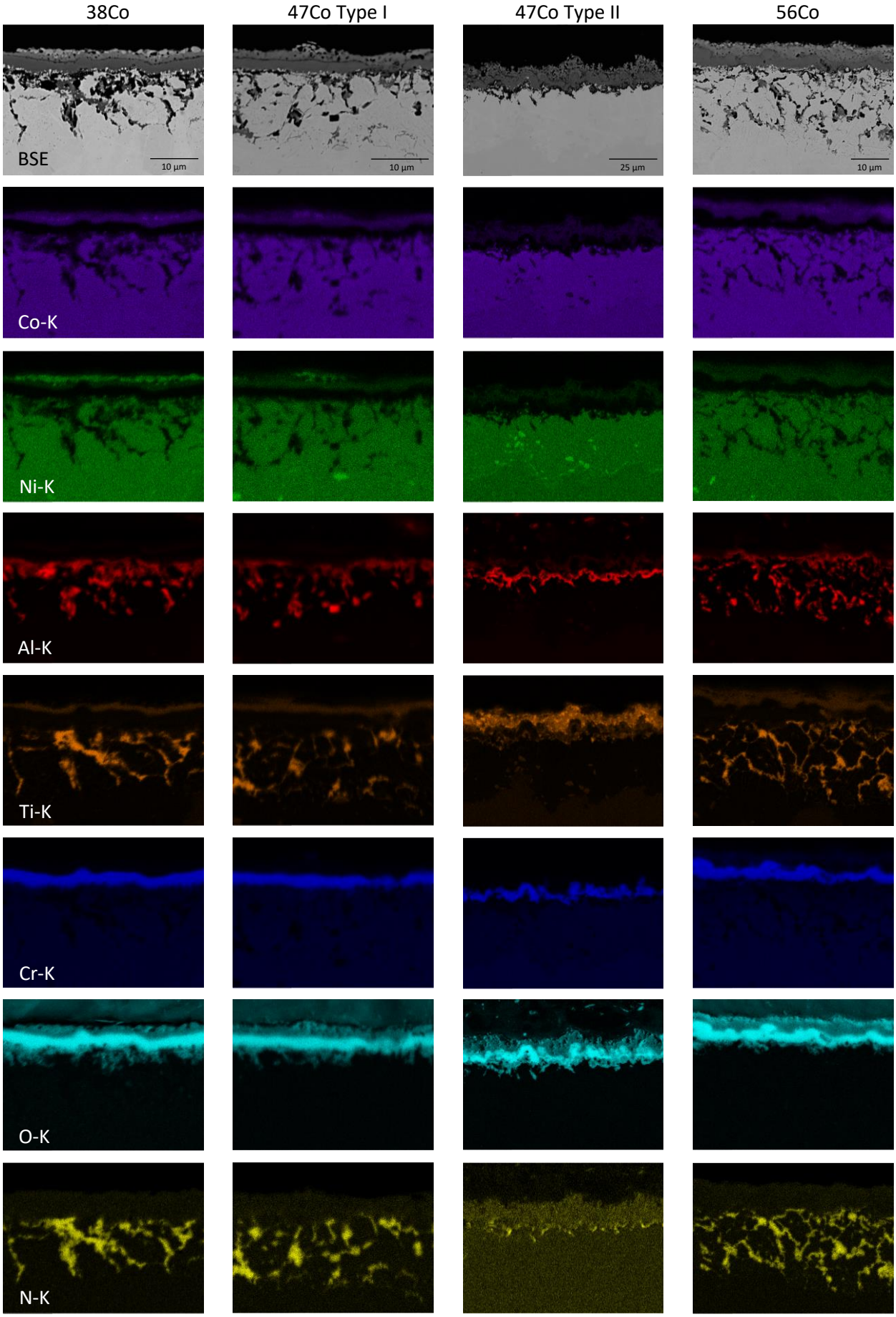

Figure 4.7. Cross-sectional SEM-BSE micrographs and corresponding EDS elemental concentration maps for 38Co, 47Co and 56Co following isothermal box-furnace oxidation (800°C, 1000 hours). A ZEISS GeminiSEM 300 microscope was used (5 × 5 × 1 mm specimens). Note differing scale bars.

With respect to the oxide scale, the 38Co, 47Co Type I and 56Co morphologies appeared to exhibit less surface Ti enrichment than was observed in the 0Co, 9Co, 19Co and 28Co alloys, but a more well-defined surface Co- and Ni-rich layer with some associated oxygen (Figure 4.7). In contrast, the 47Co Type II morphology appeared to show extensive Ti enrichment of the scale surface with some associated oxygen. The micrographs of the 47Co Type II morphology and 56Co alloy indicated the presence of a more undulating Cr_2O_3 scale than was observed for the 47Co Type I morphology or 38Co, which both demonstrated a relatively flat oxide scale and Cr-rich layer (Figure 4.7).

(ii) Measurements of oxide scale thickness and depth of internal oxidation/nitridation products

Figure 4.8 shows measurements taken following 1000 hours box-furnace oxidation at 800°C: a) oxide scale thickness and b) depth of internal oxidation/nitridation products. The 38Co, 47Co Type I and 56Co oxide scales were found to be thinner than the oxide scales of the 0Co, 9Co, 19Co, 28Co and 47Co Type II morphologies (consistent with Figure 4.5b). The 28Co, 38Co, 47Co Type I and 56Co morphologies exhibited a lesser depth of internal oxidation/nitridation products than observed for alloys of lower Co content (Figure 4.8b). The 38Co alloy demonstrated a lesser depth of internal oxidation/nitridation products than the 28Co alloy.

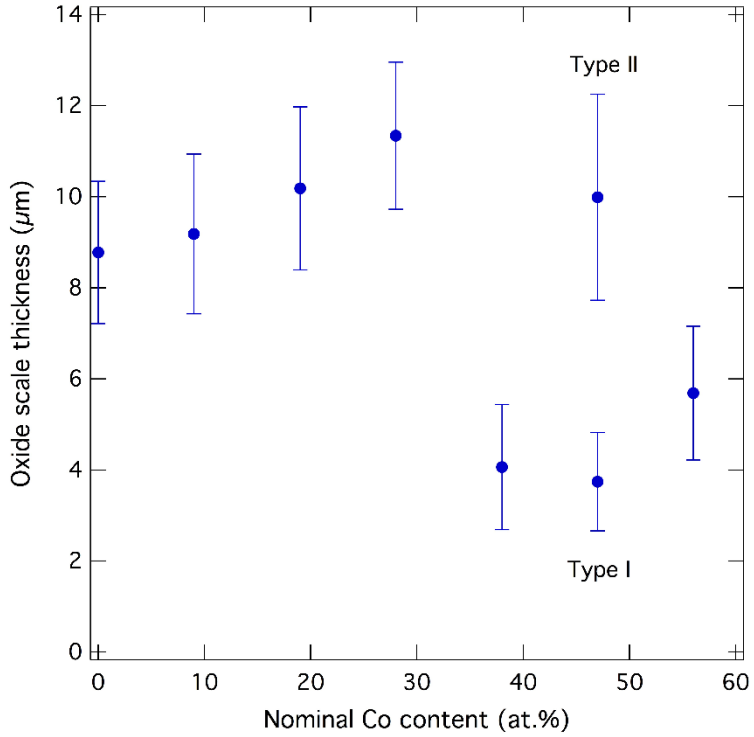

(a)

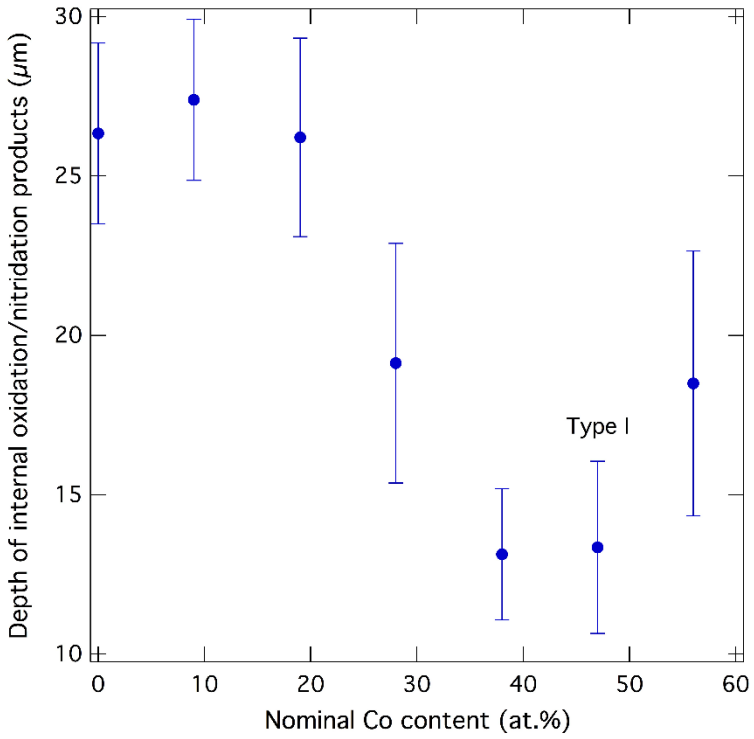

(b)

Figure 4.8. Measurements derived using ImageJ software from BSE micrographs of oxidised alloy cross-sections (800°C, 1000 hours): a) external oxide scale thickness; b) depth of internal oxidation/nitridation products (5 × 5 × 1 mm specimens).

(iii) EDS linescans to elucidate the 47Co Type II oxidation morphology

To investigate further the microstructural characteristics associated with the 47Co Type II morphology, a linescan was performed on an area of this Type II morphology and compared with the 0Co microstructure ($5 \times 5 \times 1$ mm specimens). Figure 4.9 shows SEM-EDS linescans generated for a) 0Co and b) 47Co Type II morphologies following 1000 hours box-furnace oxidation at 800°C. Whereas the 0Co alloy BSE micrograph clearly demonstrates internal projections (Figure 4.9a), the 47Co Type II morphology exhibits an obvious dense (dark) sub-scale on the BSE micrograph and a paucity of internal projections (Figure 4.9b). The elemental concentration profiles obtained for both the 0Co and 47Co Type II morphologies indicate the presence of a Ti-rich outer layer on the external scale. For both morphologies, the underlying layer was identified as Cr- and O-rich, indicative of Cr_2O_3. For the 47Co Type II morphology, the high intensity Al peak beneath the Cr-rich layer (recorded at an x-axis value of ~23 µm) was associated with the presence of oxygen, indicative of an Al_2O_3 sub-scale. This putative Al_2O_3 sub-scale appears protective against further oxidation, as suggested by the apparent lack of internal oxides or nitrides. Beneath this Al-rich sub-scale, a γ'-depleted zone appeared present, as indicated by the predominantly low Al and Ti in the x-axis range 25-48 µm. Of particular interest are two regions at 41-45 µm and 48-51 µm that indicate a relative enhancement of Ni, Ti and Al (and associated depletion in Co and Cr) compared with the plateau region extending internally from 51 µm, which may represent the start of the γ/γ' zone. This Ni-, Ti-, Al-rich sub-surface phase, of unknown crystal structure, appears unlikely to be η-Ni_3Ti as the ternary Ni-Ti-Al phase diagram for 800°C [84] (Figure 1.13) indicates that η-Ni_3Ti has negligible solubility for Al. It may transpire that this sub-surface phase is $L1_2$ γ' that has coarsened during oxidation.

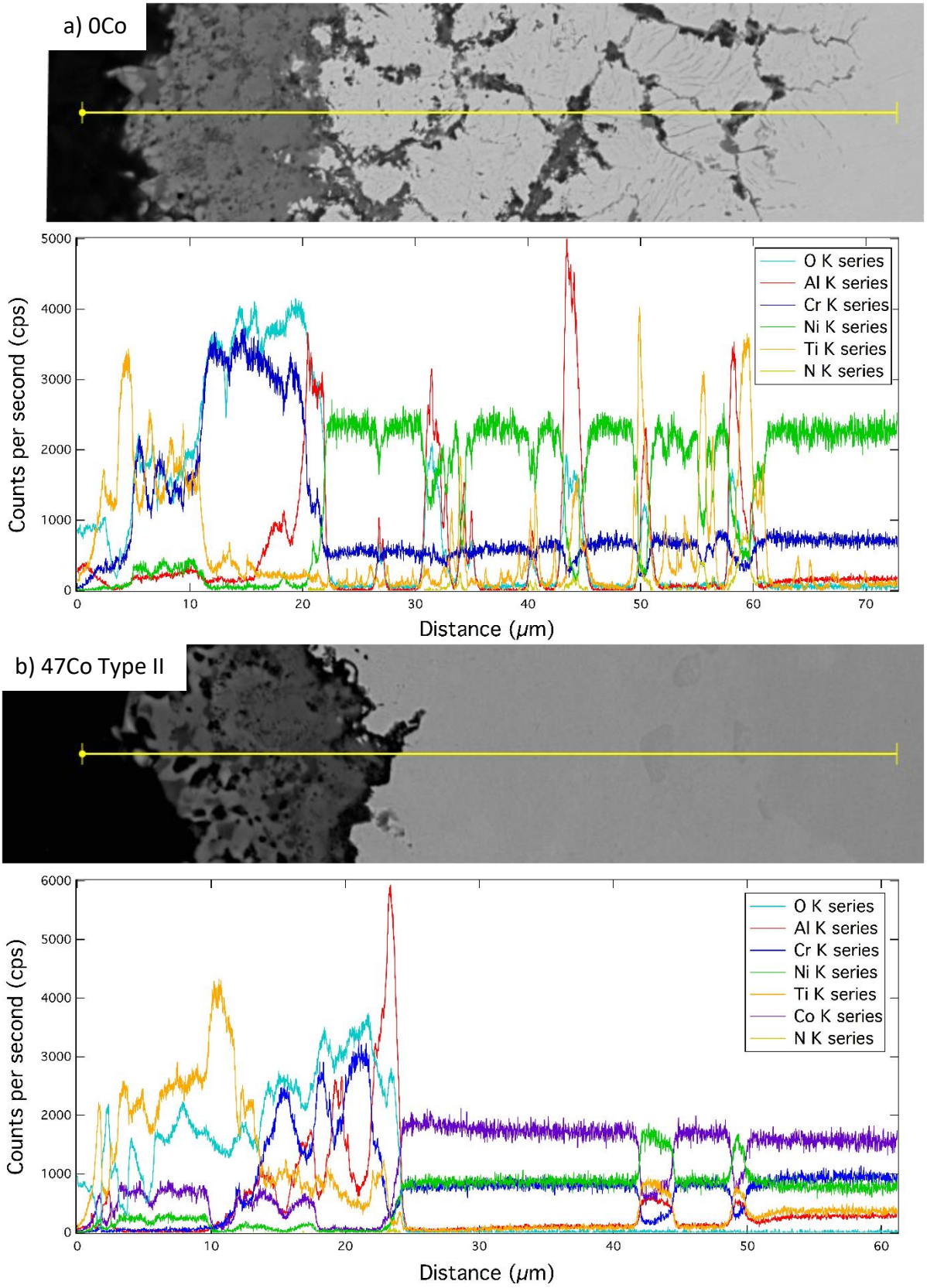

Figure 4.9. Representative SEM-BSE micrograph and corresponding EDS linescan following alloy oxidation (800°C, 1000 hours): a) 0Co showing abundance of internal oxidation products; b) 47Co Type II morphology showing a high intensity Al peak and minimal internal oxidation products. A ZEISS GeminiSEM 300 microscope was used (5 × 5 × 1 mm specimens).

4.3.4 XRD of alloy surfaces following box-furnace oxidation (800°C, 1000 hours)

Figure 4.10 shows the surface phases detected by XRD for the 28Co, 38Co, 47Co and 56Co alloys oxidised at 800°C for 1000 hours, together with micrographs (SE mode) showing the oxidised specimen surfaces. As observed for the TGA-oxidised alloys shown in Figure 4.3, surface micrographs for the 28Co, 38Co and 47Co alloys differentiated two distinct surface morphologies and the 56Co alloy exhibited surface nodules (Figure 4.10). EDS point analysis indicated that these surface nodules were rich in O (~57 at.%) and Co (~39 at.%).

As with the TGA XRD data shown in Table 4.4, all seven model superalloy compositions appeared to be Cr_2O_3-formers and overall, more phases could be detected as Co:Ni ratio increased (Table 4.5). From Table 4.5, it is clear that the XRD data for the 1000-hour oxidation closely corroborated the TGA XRD data with respect to the phases produced. However, no $NiTiO_3/CoTiO_3$ phase was detected in the 9Co alloy following 1000 hours oxidation and no TiO_2 was detected in the 47Co alloy, in contrast to the corresponding TGA-oxidised alloys. The principal peak for rutile occurs at a peak position, 2θ, of ~27° (ICSD record number 9161) and this peak was not detected in the XRD trace for 47Co (1000 hours). For the 56Co alloy, TiO_2 was detected following 1000 hours oxidation, whereas TiO_2 was not detected for the 100-hour TGA-oxidised 56Co alloy. XRD data (Table 4.5) therefore indicate the presence of rutile in all but the 47Co alloy and the presence of $NiTiO_3/CoTiO_3$ in alloys 19Co and above. In light of this, the high-intensity surface Ti evident in the 0Co, 9Co, 19Co and 28Co alloys (Figure 4.6) appears likely to exist predominantly as rutile, whereas the lower intensity surface Ti observed in the 38Co, 47Co Type I and 56Co morphologies (Figure 4.7) appears likely to exist predominantly as $NiTiO_3/CoTiO_3$, as indicated by the presence of a well-pronounced Ni- and Co-rich surface layer in these higher Co alloys.

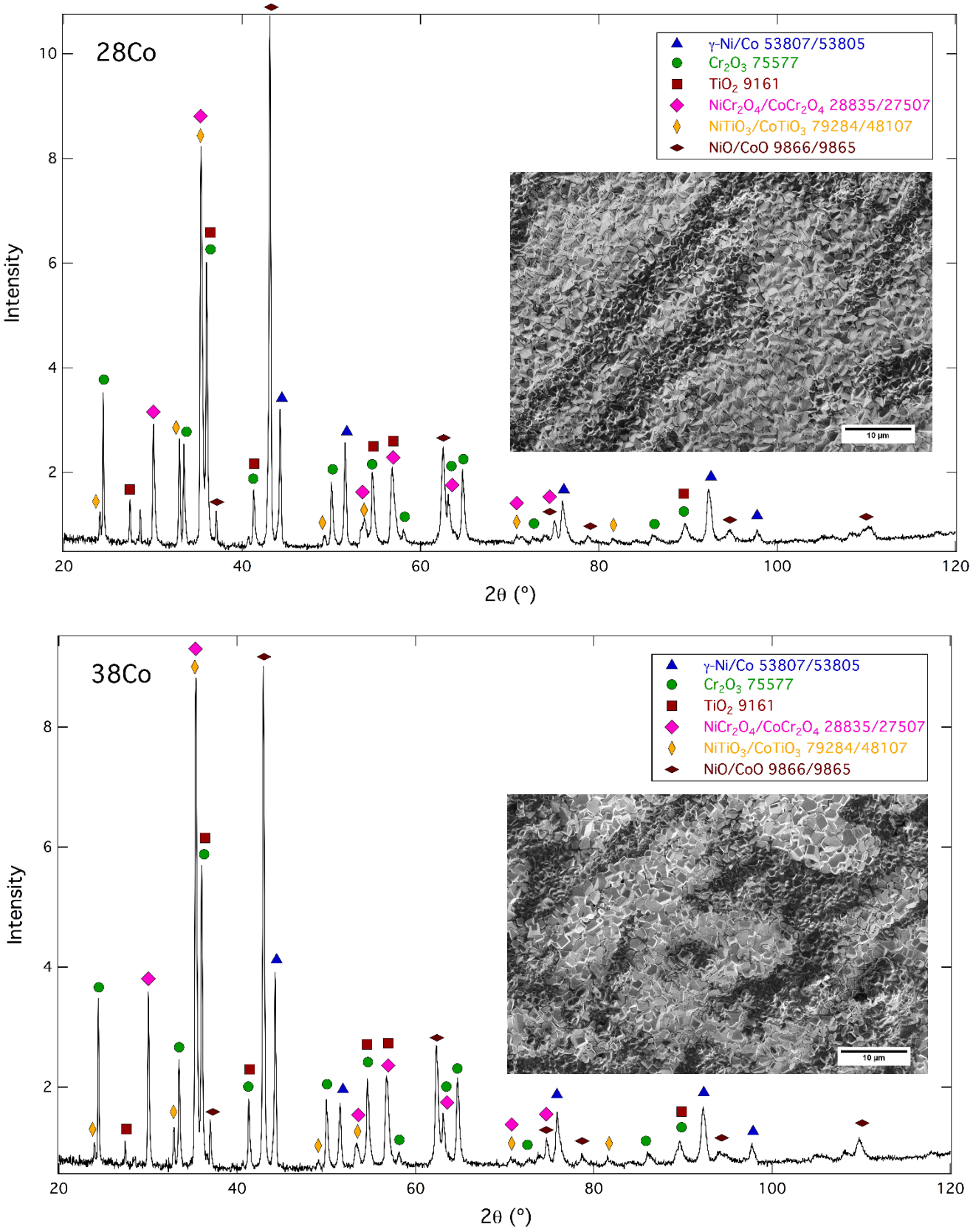

Figure 4.10. XRD traces for alloys 28Co, 38Co, 47Co and 56Co following isothermal box-furnace oxidation (800°C, 1000 hours, 5 × 5 × 1 mm specimens). The key indicates phases and ICSD reference codes (peak identification: 20°< 2θ <120°). Insets show SE images of the oxidised specimen surfaces.

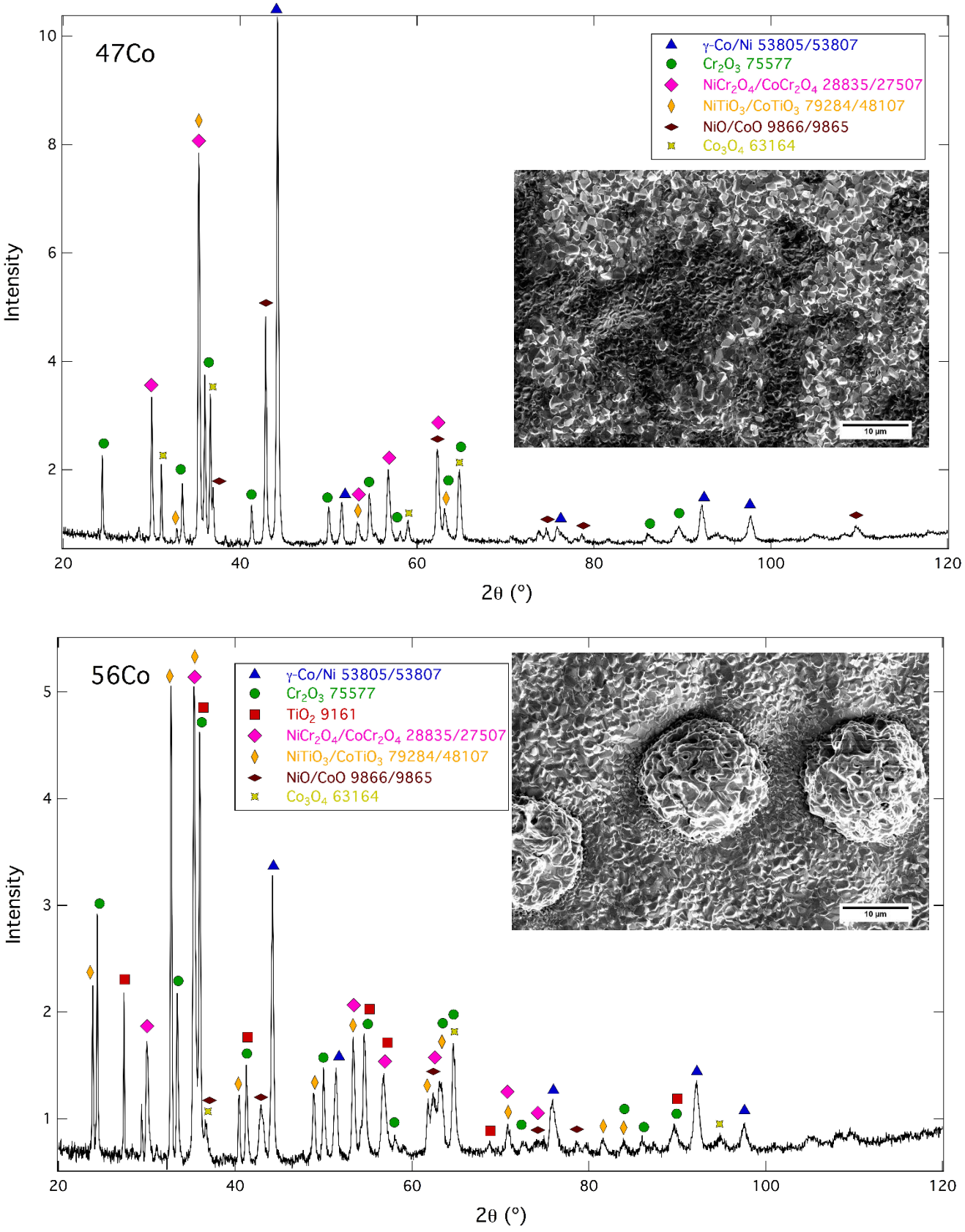

Figure 4.10. Continued.

Table 4.5. Surface oxide phases detected by XRD for all seven alloys oxidised by box-furnace exposure (800°C, 1000 hours). The underlying γ-Ni/Co matrix phase was detected for all seven alloy compositions (5 × 5 × 1 mm specimens). Data corroborate 100-hour TGA XRD data (Table 4.4) except for phases shown in italics.

Alloy	**Phases identified by XRD after box-furnace oxidation (800°C, 1000 hours)**					
0Co	Cr_2O_3	TiO_2	-	-	-	-
9Co	Cr_2O_3	TiO_2	$NiCr_2O_4/CoCr_2O_4$	~~*NiTiO₃/CoTiO₃*~~ *	-	-
19Co	Cr_2O_3	TiO_2	$NiCr_2O_4/CoCr_2O_4$	$NiTiO_3/CoTiO_3$	NiO/CoO	-
28Co	Cr_2O_3	TiO_2	$NiCr_2O_4/CoCr_2O_4$	$NiTiO_3/CoTiO_3$	NiO/CoO	-
38Co	Cr_2O_3	TiO_2	$NiCr_2O_4/CoCr_2O_4$	$NiTiO_3/CoTiO_3$	NiO/CoO	-
47Co	Cr_2O_3	~~*TiO_2*~~ *	$NiCr_2O_4/CoCr_2O_4$	$NiTiO_3/CoTiO_3$	NiO/CoO	Co_3O_4
56Co	Cr_2O_3	*TiO_2* ǂ	$NiCr_2O_4/CoCr_2O_4$	$NiTiO_3/CoTiO_3$	NiO/CoO	Co_3O_4

* Indicated as present in TGA-oxidised alloys only (100 hours)

ǂ Indicated as present in box furnace-oxidised alloys only (1000 hours)

4.3.5 Use of larger specimens to measure mass gain and to elucidate oxidation behaviour

Specimens of larger surface area (10 × 6 × 1 mm) were employed for accurate assessment of specific mass gain and to determine reproducibility of oxide morphologies, in particular for the 47Co Types I and II. SEM-EDS linescans and BSE micrographs were obtained for the 0Co, 19Co, 28Co, 38Co and 47Co alloys following 1000 hours oxidation at 800°C. SIMS elemental concentration maps were generated on the 19Co and 38Co alloys (10 × 6 × 1 mm specimens) to corroborate the EDS data shown in Figure 4.6 and Figure 4.7 for the smaller (5 × 5 × 1 mm) specimens. In addition, a SIMS count vs. time profile was obtained on the 38Co alloy to provide precise chemical analysis of any thin surface oxide layers present, as the 38Co alloy exhibited a uniformly flat, compact Cr_2O_3 scale (Figure 4.7).

(i) Specific mass gain and oxide surface analysis

To assess the influence of increasing Co:Ni ratio on specific mass gain as accurately as possible, larger specimens (10 × 6 × 1 mm) were cut from all seven homogenised alloy bars and processed as for the smaller specimens (5 × 5 × 1 mm) prior to isothermal box-furnace oxidation (800°C, 1000 hours). Specific mass gain data on these larger specimens showed no definitive correlation with alloy Co content (Figure 4.11a). The specific mass gain recorded as a result of oxidation was ~1.1 $mg.cm^{-2}$ for alloys 0Co, 9Co, 19Co, 28Co, 38Co and 47Co. However, alloy 56Co exhibited a specific mass gain of ~1.6 $mg.cm^{-2}$, notably higher than that of the other alloy compositions tested. To investigate this apparent disparity, an additional 10 × 6 × 1 mm specimen was cut, processed and oxidised for each of the higher Co alloys (38Co, 47Co and 56Co). Specific mass gain values for the three repeat specimens were consistent with the values obtained previously for alloys 0-47Co inclusive (Figure 4.11a). The high specific mass gain recorded for the first 10 × 6 × 1 mm 56Co alloy specimen (closed circle, Figure 4.11a) may result from the thick, undulating, pumice-like oxide scale observed (Figure 4.11b). This surface appearance contrasts with the discrete nodules observed for the 56Co specimens of Figure 4.3 and Figure 4.10. EDS point analysis indicated that the 56Co alloy of Figure 4.11b contained high levels of Co (~42 at.%) and O (~53 at.%), suggesting the presence of cobalt oxides. XRD data (not shown) for this 56Co specimen displayed peaks corresponding solely to CoO/NiO, a spinel phase (plausibly Co_3O_4 given the EDS data) and $CoCr_2O_4$/$NiCr_2O_4$, suggesting that this surface oxide layer may have precluded further penetration of X-rays toward the alloy interior. From Figure 4.11, there appeared no discernible correlation between specific mass gain following 1000 hours box-furnace oxidation at 800°C and alloy Co content, corroborating mass gain data obtained following TGA. This lack of obvious correlation between specific mass gain and Ni:Co ratio is not unexpected for an oxidation process involving formation of multiple oxide species.

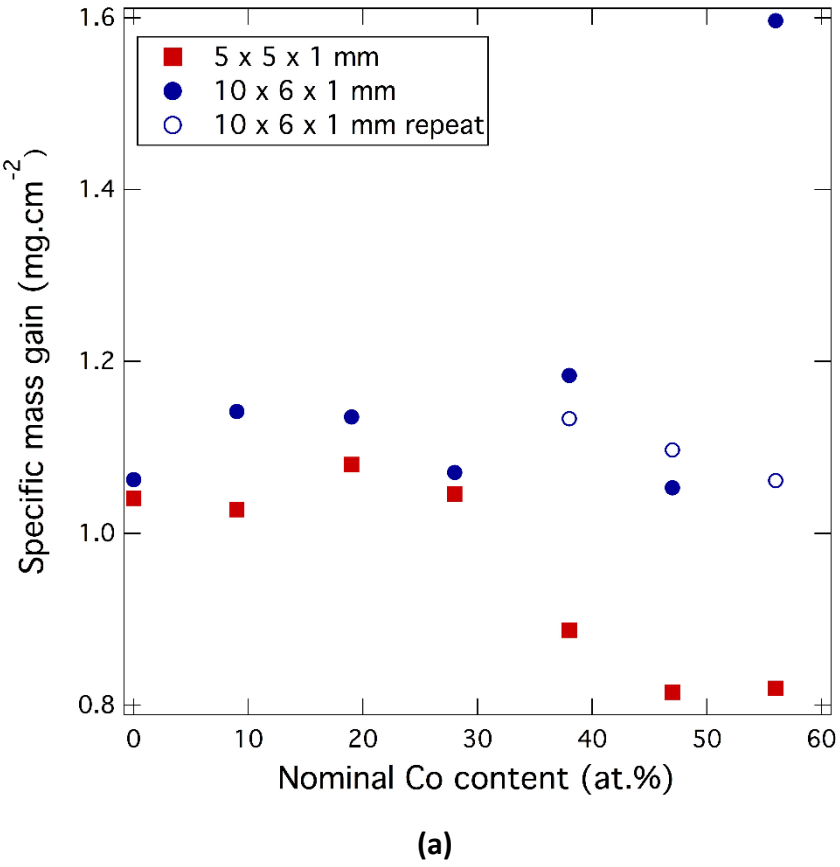

(a)

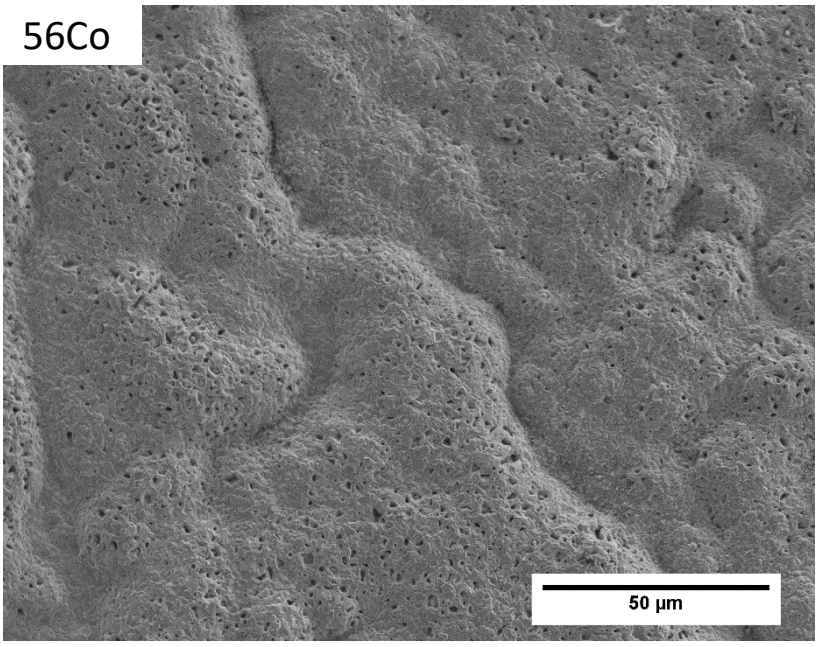

(b)

Figure 4.11. a) Specific mass gain vs. alloy Co content from weighing specimens before and after isothermal box-furnace oxidation (800°C, 1000 hours); b) SE micrograph of the oxidised 56Co surface (10 × 6 × 1 mm specimen) showing high specific mass gain (closed circle).

(ii) SEM-EDS linescans to elucidate the morphology of oxidised 47Co and 38Co alloys

To confirm the reproducibility of the Type I and Type II oxidation morphologies for the 47Co alloy and to investigate whether the 38Co alloy also exhibited two distinct morphologies, SEM-BSE micrographs and EDS linescans were obtained for these 10 × 6 × 1 mm alloy specimens oxidised for 1000 hours at 800°C (Figure 4.12). The 47Co specimen investigated here displayed both Type I and Type II oxidation morphologies within the same specimen, confirming the reproducibility of the microstructural characteristics observed for the 5 × 5 × 1 mm 47Co specimen (Figure 4.5b and Figure 4.7). As with the smaller 47Co specimen linescan (Figure 4.9b), the morphology denoted Type II in this larger 47Co specimen (Figure 4.12a) implies the presence of a dense Al_2O_3 sub-scale (shown as dark on the BSE micrograph) and an apparent lack of internal projections. Islands of relatively high Ni, Ti and Al intensity and low Co and Cr intensity were observed external to the main bulk of the γ/γ' in this larger 47Co alloy specimen in areas exhibiting Type II morphology (at 20-22 μm, Figure 4.12a) or Type I morphology (at 23-24.5 μm, Figure 4.12b). Importantly, the 38Co alloy appeared to exhibit only one type of morphology throughout the alloy specimen (Figure 4.12c). As with the 47Co alloy (Type I and Type II morphologies), the 38Co alloy also displayed the unidentified Ni-, Ti- and Al-rich phase within what appeared to be a γ'-depleted zone. The 47Co Type II morphology (Figure 4.12a) exhibited a more compact oxide scale and Cr-rich layer than was observed for the 5 × 5 × 1 mm specimen (Figure 4.9b) and was more akin to the 38Co and 47Co Type I morphologies with respect to the external scale. Extensive SEM examination of the 38Co alloy cross-section revealed a uniform, flat and compact Cr-rich scale *throughout*. XRD analysis (not shown) on these 10 × 6 × 1 mm specimens confirmed the presence of Cr_2O_3 in alloys 0Co, 9Co, 19Co, 28Co, 38Co and 47Co. The 38Co alloy (Figure 4.12c) exhibited extended depletion of Cr (dark blue, at 8–30 μm on the x-axis) beneath the Cr_2O_3 layer, as may be expected with significant chromia formation.

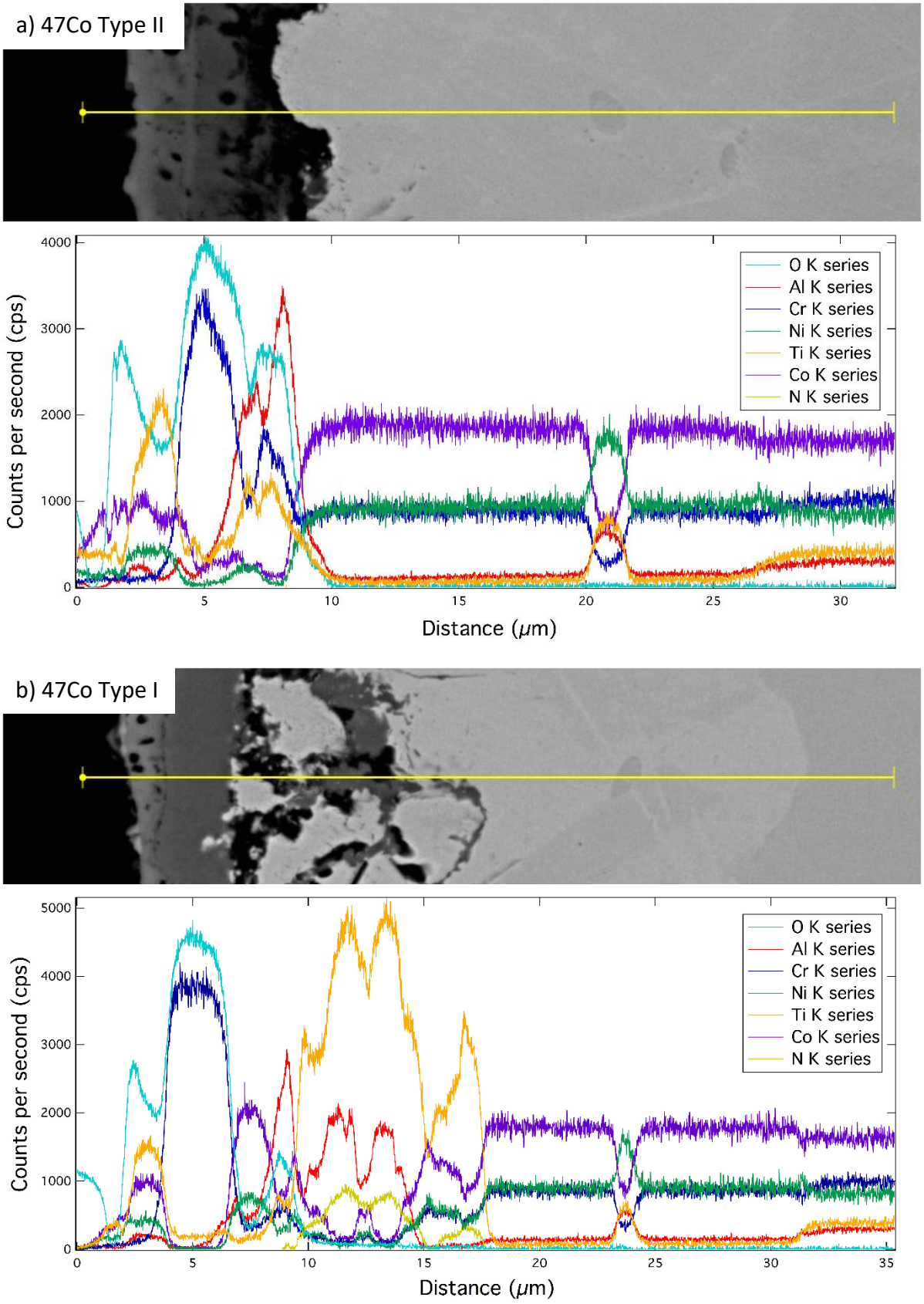

Figure 4.12. Representative SEM-BSE micrograph and corresponding EDS linescan following alloy oxidation (800°C, 1000 hours): a) 47Co Type II morphology showing dense Al- and O-rich sub-scale; b) 47Co Type I morphology; c) 38Co. (b) and (c) exhibit a compact, well-defined Cr- and O-rich layer within the oxide scale. A ZEISS GeminiSEM 300 microscope was used (10 × 6 × 1 mm specimens).

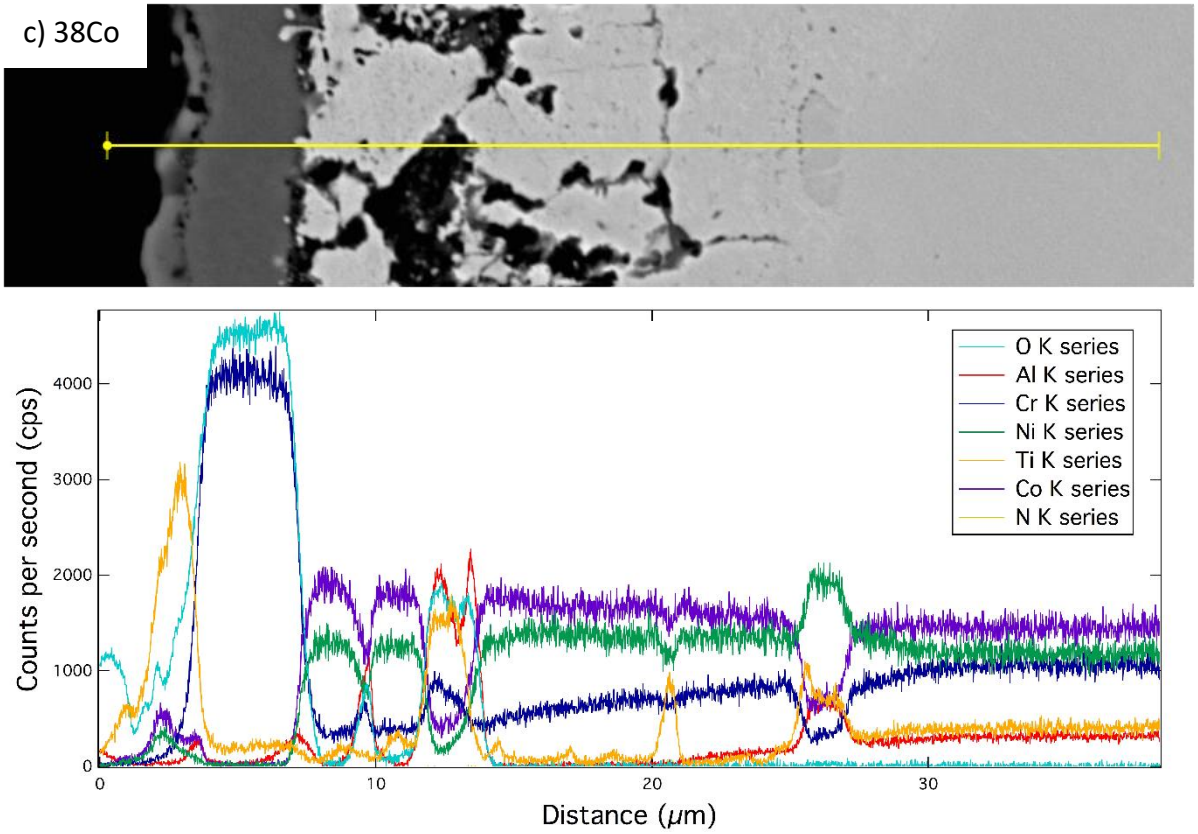

Figure 4.12. Continued.

The differing Type I and Type II morphologies of the 47Co alloy may be related to the differing crystal structures of the metastable Al_2O_3 phases compared with the stable α-Al_2O_3 phase, as described by Birks *et al*. [73]. The metastable γ-, δ- and θ-Al_2O_3 polymorphs reportedly exhibit cubic spinel, tetragonal and monoclinic structures respectively, whereas α-Al_2O_3 exhibits a rhombohedral crystal structure comprising hexagonally close-packed oxide anions with cations occupying two thirds of octahedral interstitial sites [73]. The α-Al_2O_3 phase reportedly develops as a dense layer, whereas the metastable polymorphs reportedly form as whiskers or blades [198]. The differing crystal structures and morphologies of the various alumina phases reportedly contribute to their differential growth rates and, as mentioned in section 4.1, transformation from the metastable aluminas to the α-Al_2O_3 at temperatures lower than 1200°C is readily influenced by the presence of other species such as Cr [198]. As mentioned, Cr is known to accelerate transformation of θ-Al_2O_3 to α-Al_2O_3 by initial formation of chromia, which is isotypic with α-Al_2O_3 providing sites for α-Al_2O_3 nucleation [73, 198].

As described in Chapter 2, a systematic study of the effect of Ni:Co ratio on elemental partitioning for the same series of alloys aged at 800°C for 1000 hours was carried out. The 47Co alloy elicited maximal preferential partitioning of Ni to the γ' phase and substantial

partitioning of Cr to the γ' phase, associated with a relatively high Al concentration in the γ phase (3.09 at.%) compared with lower Co alloys. It is plausible, therefore, that development of the 47Co Type II morphology (dense alumina sub-scale and lack of internal oxidation products) observed in the present study may be related to the role of Co in influencing elemental phase partitioning as described in Chapter 2 for this alloy composition at 800°C. However, it is difficult to correlate directly the elemental partitioning data derived from ageing the alloys for 1000 hours at 800°C in an argon atmosphere (Chapter 2) to the present study, which involved continual evolution of an external oxide scale over the 1000-hour oxidation period at 800°C and concomitant changes in sub-surface composition.

(iii) Secondary ion mass spectrometry (SIMS) on 38Co and 19Co alloys

As the 38Co alloy exhibited a consistently flatter, more compact oxide scale and Cr_2O_3 layer than the lower Co alloys or the 47Co and 56Co alloys (Figure 4.5b, Figure 4.7, Figure 4.8a), SIMS was performed on the 38Co alloy to provide precise chemical analysis of any thin surface oxide layers present. Figure 4.13a shows SIMS elemental count vs. time profiles obtained for the 38Co alloy following oxidation for 1000 hours at 800°C to assess how the profiles for Al and Ti vary in relation to that of the chromia scale (shown in Figure 4.13a as a blue plateau). On sputtering down through the external oxide scale, the Cr-rich layer appeared most dense between 15 and 60 minutes after initiating sputtering. Ti abundance decreased as the Cr-rich layer became apparent. The presence of surface Ti in this 38Co specimen as indicated by the SIMS count vs. time profile is consistent with the evidence of surface Ti apparent on the 38Co EDS map for the smaller (5 × 5 × 1 mm) specimen (Figure 4.7). The aluminium profile observed in Figure 4.13a exhibited a small peak on initial sputtering, indicating the presence of an Al-rich surface layer not easily discernible in the 38Co EDS map (Figure 4.7), but apparent in the 19Co and 28Co EDS maps (Figure 4.6). This small initial peak in Al counts preceded a much larger Al peak, indicative of an Al_2O_3 sub-scale beneath the Cr-rich layer (Figure 4.13a). Figure 4.13b shows an SE micrograph of the crater produced following sputtering to a depth of ~10 µm, exposing pillars resistant to sputtering, plausibly a discontinuous Al_2O_3 sub-scale.

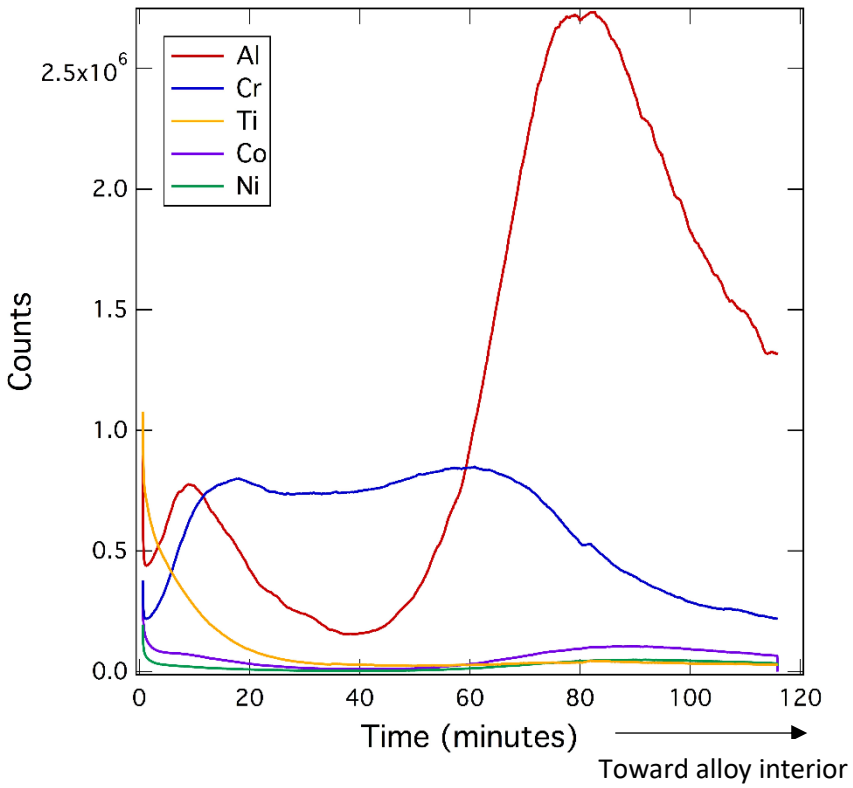

(a)

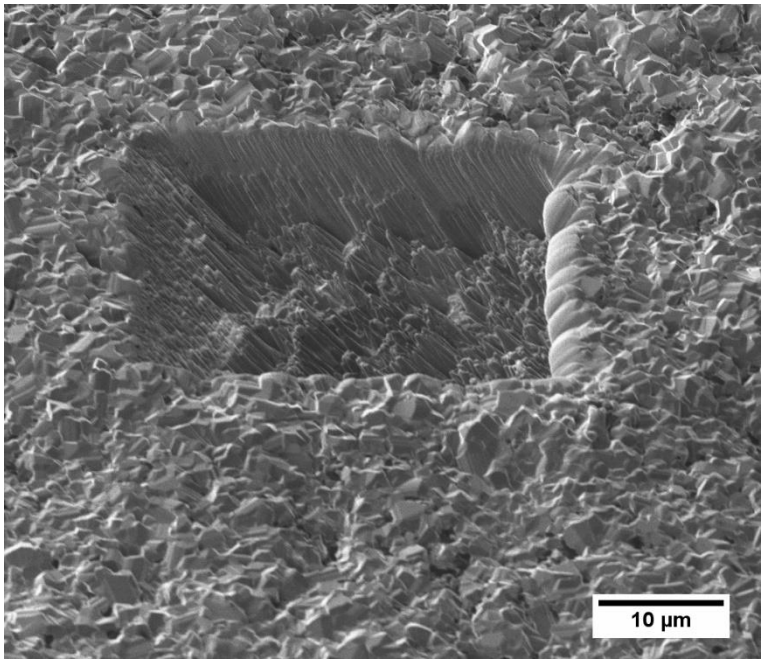

(b)

Figure 4.13. SIMS for the oxidised (800°C, 1000 hours) 38Co alloy: a) elemental count vs. time profiles; b) SE micrograph (tilt 45°) showing crater produced following sputtering of the oxidised surface to obtain (a). Pillars in (b) may correspond to regions of Al_2O_3 sub-scale (10 × 6 × 1 mm specimen).

Figure 4.14 shows SE micrographs of ramps made to a maximum vertical depth of ~17 μm in the 38Co alloy and in the 19Co alloy for comparison, following oxidation at 800°C for 1000 hours. Also displayed are SIMS elemental concentration maps showing the distribution of O, Ti, Cr and Al in the alloy sub-surface. Both alloy compositions appear to exhibit a continuous Cr_2O_3 scale and a discontinuous Al_2O_3 sub-scale. As noted previously, the presence of this Cr_2O_3 scale in the 38Co and 19Co alloys was confirmed by XRD analysis on these larger ($10 \times 6 \times 1$ mm) specimens. The 38Co alloy appears to demonstrate less oxygen penetration into the alloy interior compared with the 19Co alloy, consistent with EDS maps obtained for the smaller specimens (Figure 4.6 and Figure 4.7). The 19Co alloy appears to indicate extensive precipitation of Al_2O_3 beneath the Cr_2O_3 scale (Figure 4.14b), consistent with EDS maps obtained for the smaller ($5 \times 5 \times 1$ mm) 19Co specimen (Figure 4.6). (Rectangular troughs seen in Figure 4.14a indicate areas where SIMS depth profiles (not shown) had been acquired previously).

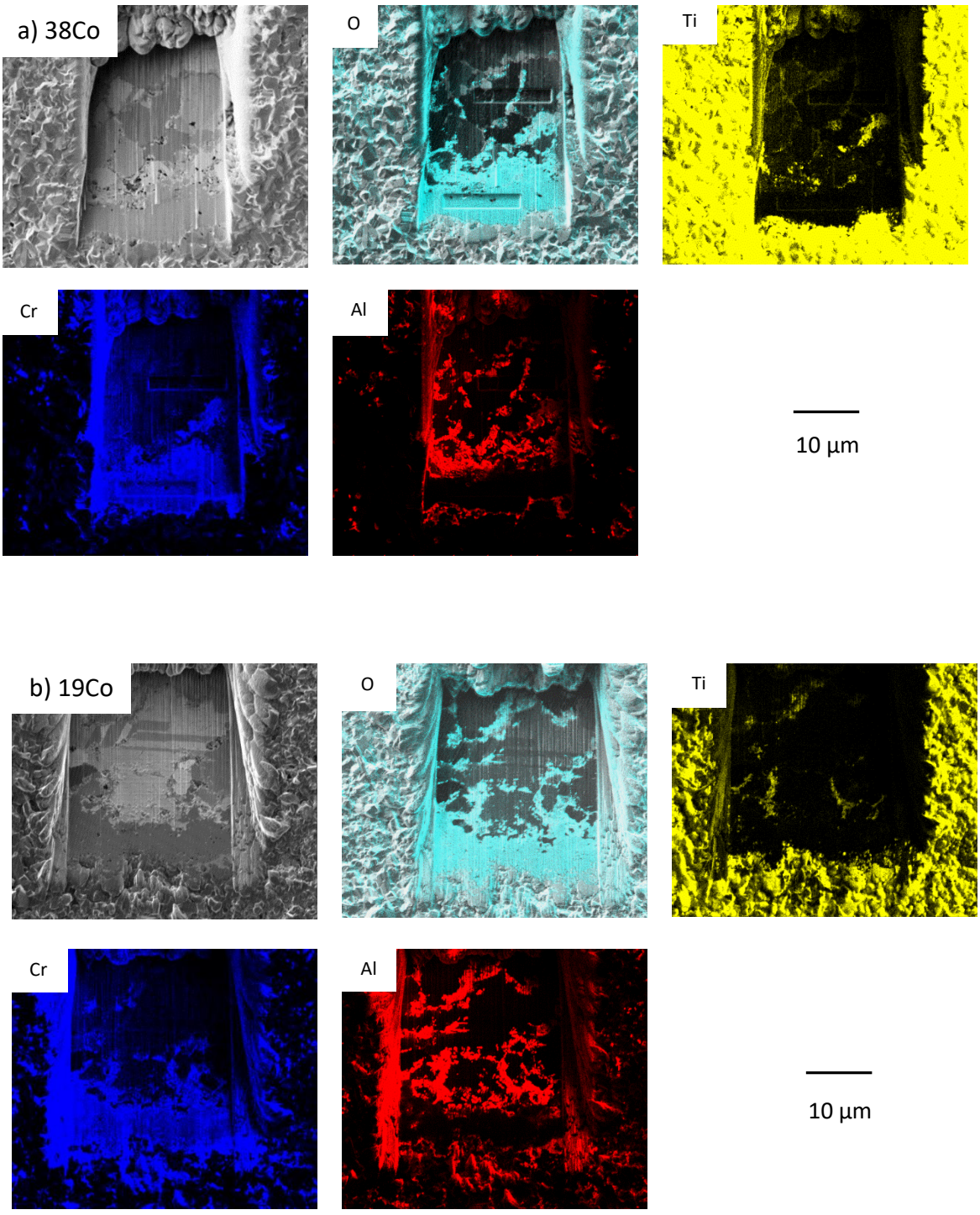

Figure 4.14. SE micrograph and SIMS elemental concentration maps for O, Ti, Cr and Al following alloy oxidation (800°C, 1000 hours): a) 38Co; b) 19Co. Both alloy compositions appeared to exhibit a continuous Cr_2O_3 scale and a discontinuous Al_2O_3 sub-scale (10 × 6 × 1 mm specimens).

(iv) SEM-EDS linescans to elucidate the morphology of oxidised 19Co and 28Co alloys

As the 28Co alloy exhibited microstructural features similar to those of the 47Co Type II morphology in terms of the distinct Al- and O-rich sub-scale and limited nitrogen and oxygen ingress into the alloy interior (Figure 4.6 and Figure 4.7), EDS linescans were obtained on the 10 × 6 × 1 mm specimens to compare the 28Co alloy with the 19Co and 0Co alloys. Figure 4.15 shows representative BSE micrographs and corresponding EDS linescans for alloys 0Co, 19Co and 28Co following isothermal box-furnace oxidation at 800°C for 1000 hours. The 0Co and 19Co specimens both demonstrated a similar undulating, porous-looking external scale to those seen in Figure 4.5b, Figure 4.6 and Figure 4.9a for these alloy compositions and internal oxidation products were clearly visible. The 28Co alloy appeared to exhibit a more compact, uniform Cr_2O_3 layer (Figure 4.15c) compared with the 0Co and 19Co alloys (Figure 4.15a, b) in contrast to the thick porous-looking scale observed in the smaller 28Co specimen (Figure 4.5b and Figure 4.6). Indeed, from Figure 4.15c, the larger 28Co specimen (10 × 6 × 1 mm) displayed the relatively thin, dense and well-defined external scale and Cr_2O_3 layer characteristic of the 38Co alloy (Figure 4.5b, Figure 4.7 and Figure 4.12c) and desirable for good oxidation resistance.

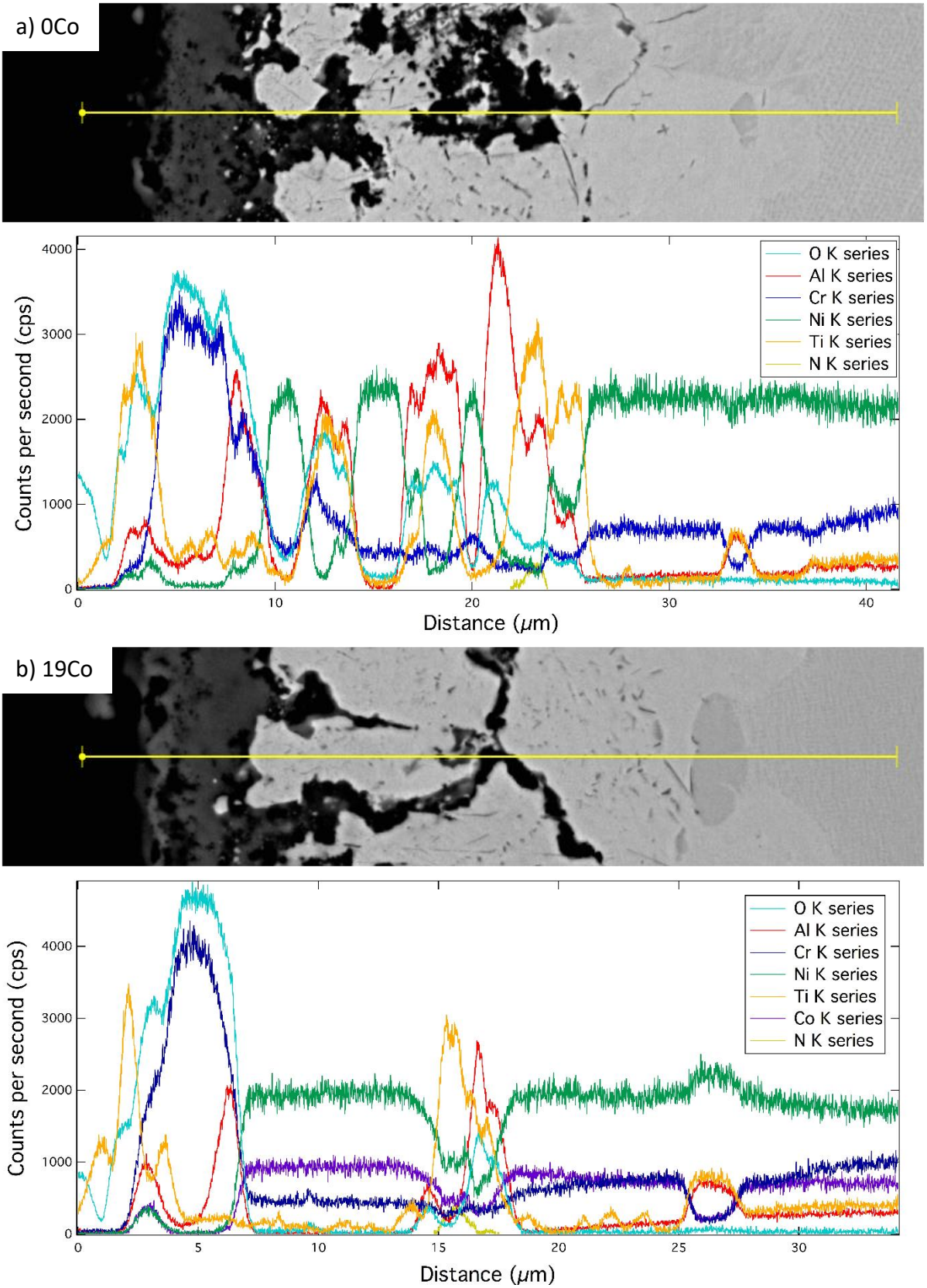

Figure 4.15. Representative SEM-BSE micrograph and corresponding EDS linescan following alloy oxidation (800°C, 1000 hours): a) 0Co; b) 19Co; c) 28Co. The 28Co alloy exhibits a compact, well-defined Cr- and O-rich layer within the oxide scale, as seen for the 38Co alloy and 47Co Type I morphology (Figure 4.12). A ZEISS GeminiSEM 300 microscope was used (10 × 6 × 1 mm specimens).

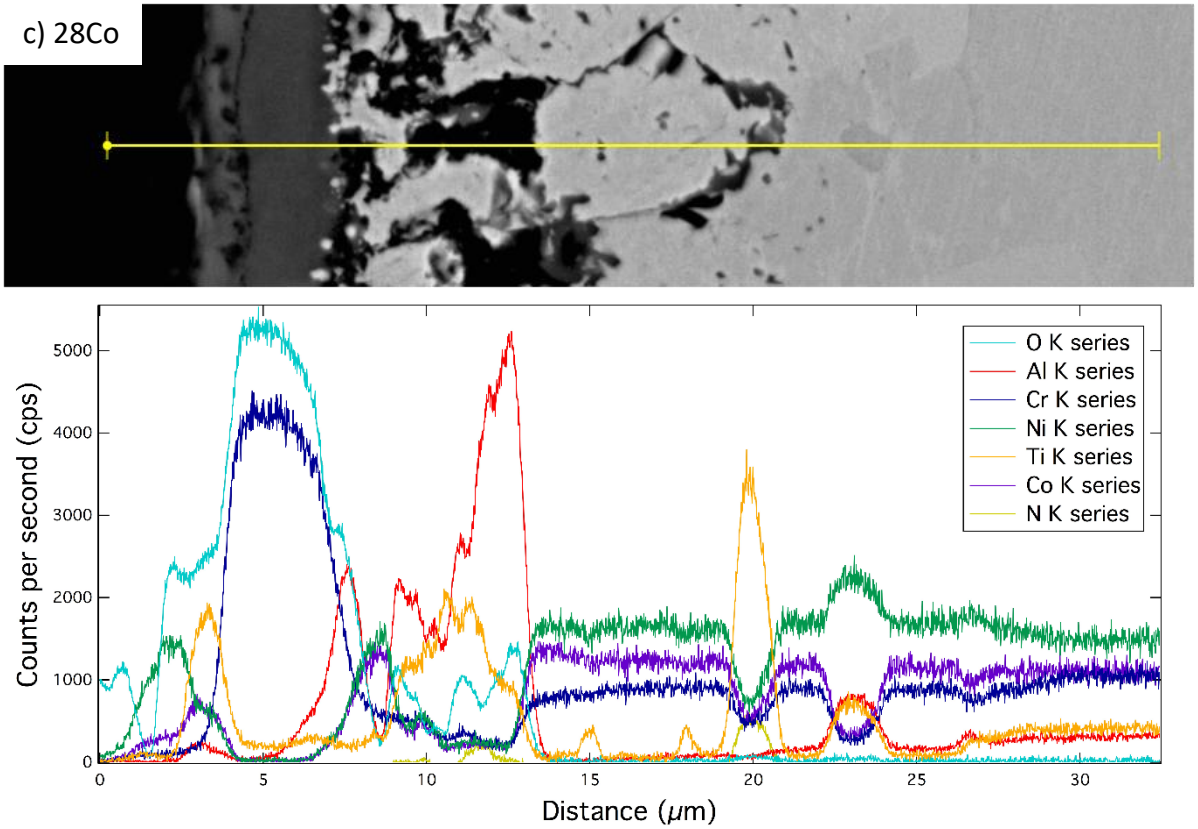

Figure 4.15. Continued.

4.4 Conclusions

- From 100 hours TGA at 800°C, the kinetics of oxide scale growth appeared to indicate a parabolic relationship between specific mass gain and time for the 9Co alloy (n = 2.0628), whereas the 47Co and 56Co alloys generated n values approaching n = 3, indicative of cubic kinetics and therefore of the formation of a number of new oxide species.
- XRD data on the 1000-hour box-furnace oxidised specimens (5 × 5 × 1 mm) closely corroborated XRD data on the 100-hour TGA exposures and confirmed the presence of Cr_2O_3 for all seven alloy compositions. An increasing number of surface phases was detected as Co:Ni ratio increased.
- Following 100 hours or 1000 hours oxidation at 800°C, SEM-BSE examination revealed the presence of an external oxide scale overlying a zone of irregular oxidation products in all seven alloy compositions.
- However, the 47Co alloy elicited two distinct morphologies following 1000 hours oxidation at 800°C: Type I resembling the 38Co alloy with thin, flat strata within a compact scale overlying a zone of conspicuous oxidation products; in contrast, Type II

exhibited a paucity of internal oxidation products beneath what appeared to be a dense Al_2O_3 sub-scale. This effect was found to be reproducible on oxidation of a larger 47Co alloy specimen (10 × 6 × 1 mm), as mentioned below.

- SEM-EDS maps of alloys 0Co, 9Co, 19Co and 28Co (5 × 5 × 1 mm specimens) following 1000 hours oxidation at 800°C revealed a thick, undulating external scale comprising a Ti-rich surface layer above a putative Cr_2O_3 layer overlying a sub-scale rich in Al and associated O. This putative Al_2O_3 sub-scale appeared more distinct in the 28Co alloy, which displayed less oxygen and nitrogen ingress into the alloy interior than alloys of lower Co content.
- SEM-EDS maps of the 38Co, 47Co Type I and 56Co morphologies taken following 1000 hours oxidation at 800°C revealed distinct layers within a compact external scale, putatively a continuous Cr_2O_3 layer beneath an outer layer comprising oxides rich in Co, Ni and Ti. A reduction in oxygen ingress was observed for these higher Co alloys compared with the lower Co alloys, with the 38Co, 47Co Type I and 56Co morphologies exhibiting internal Al- and Ti-rich projections apparently associated with nitrogen.
- SEM cross-sectional analysis of larger alloy specimens (10 × 6 × 1 mm) oxidised for 1000 hours at 800°C confirmed the evolution of Type I and Type II morphologies within a single 47Co specimen and confirmed the presence of only one type of microstructure for the 38Co alloy.
- SEM cross-sectional analysis of the 28Co alloy (10 × 6 × 1 mm specimen) revealed a consistently compact, well-defined external scale, characteristic of the 38Co alloy. This contrasts with the thick, undulating scale observed for the smaller (5 × 5 × 1 mm) 28Co specimen. An EDS linescan for the 10 × 6 × 1 mm 28Co specimen showed a well-defined Cr- and O-rich layer within the compact external scale, as observed for the 38Co alloy.
- A SIMS depth profile and elemental concentration maps for the 38Co alloy (10 × 6 × 1 mm specimen) oxidised for 1000 hours at 800°C indicated the presence of a discontinuous Al_2O_3 sub-scale beneath the well-defined Cr_2O_3 layer.
- Thus, the 28Co, 38Co and 47Co alloys were observed to elicit a flat, compact, well-defined external scale and Cr_2O_3 layer with minimal oxygen ingress following 1000 hours oxidation at 800°C. The presence of an Al_2O_3 sub-scale in the 28Co, 38Co and 47Co alloys suggests that manipulating the aluminium content within this Co

concentration range to facilitate formation of a continuous Al_2O_3 sub-scale may enhance oxidation resistance and resistance to fatigue crack initiation by precluding both oxygen and nitrogen ingress.

5. Effect of Co:Ni Ratio on Microstructure and Properties of Ni-Co-5Al-5Ti-15Cr-3W (at.%) alloys

The influence of 3 at.% W addition to the base alloy Ni-Co-5Al-5Ti-15Cr (at.%) system was investigated by examining the effect of a systematic increase in Co:Ni ratio on the resultant microstructure and critical properties. 3 at.% W was substituted for an equiatomic ratio of Ni and Co to fabricate a series of six alloys of composition $(Ni,Co)_{72}Al_5Ti_5Cr_{15}W_3$ (at.%), denoted 0Co-3W, 17Co-3W, 27Co-3W, 36Co-3W, 45Co-3W and 55Co-3W. Alloys were homogenised at 1250°C and subsequently aged for 1000 hours at 800°C. For alloys with 3 at.% W added, values of γ' solvus temperature were consistently higher than corresponding values for the W-free alloys but followed the same trend of decreasing γ' solvus temperature with increasing Co:Ni ratio. Addition of 3 at.% W increased mass density from ~8.1 $g.cm^{-3}$ for the W-free Ni-Co-5Al-5Ti-15Cr (at.%) alloy series to ~8.5 $g.cm^{-3}$ for the alloy series containing 3 at.% W. The alloy of composition Ni-17Co-5Al-5Ti-15Cr-3W (at.%) exhibited a combination of high γ′ solvus temperature (1143°C) and high Vickers microhardness (~424 HV). Alloy Ni-27Co-5Al-5Ti-15Cr-3W displayed a relatively high γ′ solvus temperature (1122°C) and a Vickers microhardness of ~436 HV.

5.1 Introduction

First reported by Lee, 1971 [2], γ-γ′ two phase alloys based on the ternary Co-Al-W system and strengthened by ordered $L1_2$ γ' precipitates of $Co_3(Al,W)$ have been extensively investigated in recent years. Renewed interest in these alloys was triggered by a report by Sato *et al*., 2006 [120] who observed an A1-$L1_2$ two-phase microstructure in the Co-9Al-7.5W (at.%) alloy aged at 900°C for 72 hours (section 1.2.1). Alloys based on the Co-Al-W system reportedly exhibit higher solidus and liquidus temperatures than conventional Ni-based superalloys and display less segregation during solidification [202].

Although the γ′-$Co_3(Al,W)$ phase in the Co-Al-W system is reportedly metastable at 900°C following extended ageing [121], Ta, Ti, Nb and high concentrations of Ni are efficacious in stabilising the γ′-$Co_3(Al,W)$ phase and raising γ′ solvus temperature, as reflected in the preferential partitioning of these elements to the $L1_2$-γ′ phase (section 1.2.2). In contrast, addition of 20 at.% Cr reportedly decreased γ′ solvus temperature by >100°C in the Co-Al-W system, destabilising the γ′ phase (section 1.2.2). This is an important consideration in turbine disc alloys, for which Cr addition has traditionally been considered critical for oxidation

resistance. Significantly, Shinagawa *et al*. [127] reported that increasing Ni:Co ratio in the Co-(10-70)Ni-Al-W (at.%) alloy system raised γ' solvus temperature and reduced lattice misfit (section 1.2.2). In stabilising the γ' phase, increasing Ni content reportedly extended the γ+γ' two-phase field to the low W region of the Co-(10-70)Ni-Al-W (at.%) phase diagram at 900°C, reducing the amount of W needed to stabilise the γ-γ' microstructure [127] thereby providing the potential for reduced mass density. Addition of 2 at.% Ti or 2 at.% Ta to the ternary Co-Al-W system was also shown to be efficacious in increasing γ′ solvus temperature [125] and γ′ volume fraction [126] (section 1.2.2).

As with a number of $L1_2$ compounds, the $Co_3(Al,W)$ yield stress anomaly is attributed to thermal activation of cross slip of APB-coupled superpartial dislocations from (111) to (010) planes [132] (section 1.1.1. *i*). From section 1.2.5, the high onset temperature of the yield stress anomaly for $Co_3(Al,W)$ is likely to derive from a low complex stacking fault (CSF) energy that impedes cross slip of APB-coupled dislocations from (111) to (010) planes [132]. As discussed in section 1.2.2, a number of elements including Ti, Ta, Nb and high concentrations of Ni are known to stabilise the $L1_2$ $Co_3(Al,W)$ phase, raising γ' solvus temperature and plausibly increasing CSF energy of the $L1_2$ $Co_3(Al,W)$ phase [122]. Thus, selective elemental addition, likely to increase CSF energy, may reduce onset temperature of the 0.2% yield stress anomaly, potentially broadening the temperature range over which alloy strength is increased.

Recently, high γ' solvus temperatures have been reported for higher-order Co-based alloys: 1131°C for alloy Co-7Al-8W-4Ti-1Ta (at.%) [135], 1185°C for alloy Co-20Ni-7Al-7W-4Ti-2Ta (at.%) [136] and 1218°C for alloy Co-30Ni-9Al-3Ti-7W-2Ta-0.1B (mole percent) [137]. However, mass density remains an issue for Co alloys based on the compositions described by Sato *et al*. [120], which traditionally possess a high W content (~7-10 at.%), conferring mass density values in excess of 9.0 $g.cm^{-3}$ [125] compared with the desired density for Ni-based disc superalloys of < 8.5 $g.cm^{-3}$ [139].

Several studies have shown that systematic reduction of W in low-order Co-Al-W based alloys reduces γ' solvus temperature and γ' volume fraction (Figure 1.29). This reduction in γ' solvus temperature and volume fraction appeared particularly steep for the low W range (4-2 at.%). Reducing W concentration from 4 to 2 at.% in alloy Co-10Ni-6Al-W-6Ti (at.%) reduced γ' solvus temperature from ~1020°C to ~940°C and reduced γ' volume fraction from ~0.58 to ~0.19 [145]. However, systematic incorporation of Ti (2-8 at.%) into the base alloy Co-10Ni-9Al-9W (at.%), (at the expense of an equiatomic ratio of W and Al) produced an almost linear

increase in γ' solvus temperature: overall from ~985°C for the 0Ti alloy to ~1130°C for the Co-10Ni-5Al-5W-8Ti (at.%) alloy (denoted 8Ti) [146]. Ti addition (2-8 at.%) produced a systematic increase in 0.2% flow stress for the temperature range ambient to 900°C, with an onset temperature for the flow stress anomaly ~600°C [146], compared with ~700°C for the Ti-free alloy and ~650°C for the ternary Co-9Al-9W (at.%) alloy (section 1.2.3). The alloy of lowest W content (8Ti) exhibited a peak 0.2% flow stress value of ~810 MPa i.e. significantly higher than that of the 0Ti base alloy (~575 MPa) [146] and of the ternary Co-9Al-9W (at.%) alloy (just under 500 MPa) (section 1.2.3). Thus, addition of Ti in Co-Al-W based alloys is beneficial in permitting reduced W content whilst raising γ' solvus temperature, increasing 0.2% flow stress and lowering the onset temperature for the 0.2% flow stress anomaly. The simultaneous reduction in mass density (to 8.84 $g.cm^{-3}$ for the Co-10Ni-5Al-5W-8Ti (at.%) alloy) provides the potential for density values of higher-order alloys to approach the target density for a Ni-based disc superalloy of < 8.5 $g.cm^{-3}$ [139].

From section 2.1, high Co-Ti co-addition to conventional Ni-based superalloy compositions reportedly elicits a γ-γ' microstructure with improved high-temperature strength and creep resistance [88, 148, 154, 158, 159], associated with an increase in γ' volume fraction [148, 154, 158, 159], although solid solution hardening of γ and γ' by Ti may contribute to the increased high-temperature yield strength [158]. Conventional Ni-based disc alloys are solid solution strengthened (section 1.1.1 *v*) by refractory metal elements including Mo, W, Nb and/or Ta (section 1.1.2 *v* and *vi*). W is also anticipated to provide solid solution strengthening of γ'-hardened alloys based on the Co-Al-W system. A systematic increase in W in such alloys has been shown to increase γ' solvus temperature and volume fraction following ageing at 850 and 900°C (Figure 1.29). Therefore, addition of W to the Ni-Co-Al-Ti-Cr quinary system is of interest as W is known to contribute to the formation of an $L1_2$ γ'-Co_3(Al,W) phase in Co-Al-W based alloys, where studies have focussed principally on $L1_2$-γ' phase stability at 900°C (section 1.2).

A direct comparison of the effect of a systematic increase in Co:Ni ratio on the fundamental senary Ni-Co-5Al-5Ti-15Cr-3W (at.%) and W-free quinary systems is therefore essential to determine the influence of low W content on microstructural evolution and critical properties following ageing at 800°C.

5.2 Experimental Procedure

5.2.1 Materials and heat treatment

The series of model superalloys investigated in the present study were of the $(Ni,Co)_{72}Al_5Ti_5Cr_{15}W_3$ (at.%) system in which the Ni:Co concentration ratio was varied from 1:0 to 1:3 (Table 5.1). 3 at.% W was added at the expense of 1.5 at.% Co and 1.5 at.% Ni to retain the same alloy Co:Ni ratio as in the quinary series of alloys. The W content in each of the six model superalloys investigated (3 at.%) equates to ~9.3% W by weight. The alloys were named according to their nominal atomic percent Co and W i.e. 0Co-3W, 17Co-3W, 27Co-3W, 36Co-3W, 45Co-3W and 55Co-3W.

Vacuum arc melting was used to fabricate polycrystalline bars of the six alloy compositions from raw elements of at least 99.9% purity. (A binary 80Ni-20W alloy was used for incorporation of W). Differential scanning calorimetry (DSC) was performed on cast alloy discs (1 mm thickness × 5 mm diameter) cut from each alloy bar to determine the critical phase transformation temperatures for selection of an appropriate solutioning (homogenisation) heat treatment temperature for each of the six model superalloys. DSC tests were performed using a Netzsch 404 heat-flux calorimeter operating at temperatures of up to 1450°C with a heating rate of 10°C min^{-1}. From the DSC traces for each alloy, a homogenisation heat treatment temperature was selected such that it was higher than the γ′ solvus temperature but sufficiently lower than its solidus temperature to avoid incipient melting.

The six W-containing alloy bars were sealed in quartz tubes under an argon atmosphere to minimise oxidation of the alloy surface during subsequent heat treatment. The alloy bars were then subjected to a homogenisation heat treatment in the single γ phase field at 1250°C (measured using a calibrated n-type thermocouple) for 48 hours to minimise the effect of casting-induced micro-segregation. The homogenised alloy bars were subsequently air-cooled and sample specimens cut from each alloy bar for scanning electron microscopy (SEM), X-ray diffraction (XRD) and DSC. The six homogenised W-containing alloy bars were then re-sealed in quartz tubes under an argon atmosphere prior to ageing at 800°C (temperature measured using a calibrated n-type thermocouple) for 1000 hours to attain the thermodynamically stable phase distributions at this temperature. The six aged alloy bars were subsequently air-cooled and sample specimens cut from each alloy bar for SEM, XRD, DSC and Vickers microhardness.

Table 5.1. Nominal and measured chemical compositions of the Ni-Co-5Al-5Ti-15Cr-3W (at.%) alloy series (mean ± standard deviation, σ). For each alloy, the measured composition was within ±1.1 at.% of its nominal composition. Measurements were taken using SEM-EDS on alloys in the homogenised condition (1250°C, 48 hours).

Alloy	Nominal composition (at.%)						Measured composition (at.%)											
	Ni	Co	Al	Ti	Cr	W	Ni	±σ	Co	±σ	Al	±σ	Ti	±σ	Cr	±σ	W	±σ
0Co-3W	72.0	0.0	5.0	5.0	15.0	3.0	70.91	0.19	-	-	5.17	0.11	5.11	0.04	15.72	0.18	3.07	0.15
17Co-3W	54.8	17.3	5.0	5.0	15.0	3.0	53.8	0.3	17.32	0.05	5.0	0.2	5.11	0.04	15.60	0.03	3.16	0.17
27Co-3W	45.4	26.6	5.0	5.0	15.0	3.0	44.6	0.3	26.5	0.2	5.06	0.18	5.10	0.11	15.62	0.07	3.1	0.3
36Co-3W	36.0	36.0	5.0	5.0	15.0	3.0	35.1	0.2	35.72	0.16	5.05	0.07	5.13	0.09	15.74	0.13	3.22	0.11
45Co-3W	26.6	45.4	5.0	5.0	15.0	3.0	26.0	0.2	45.24	0.09	4.92	0.20	5.1	0.2	15.7	0.2	3.02	0.18
55Co-3W	17.3	54.8	5.0	5.0	15.0	3.0	16.7	0.2	54.5	0.2	5.04	0.14	5.2	0.2	15.63	0.04	2.99	0.08

5.2.2 Scanning electron microscopy (SEM)

Alloy specimens of composition $(Ni,Co)_{72}Al_5Ti_5Cr_{15}W_3$ (at.%) in both the homogenised condition and the aged condition were mounted in conductive Bakelite and ground using wet SiC abrasive paper. The twelve alloy specimens were then polished using progressively finer diamond suspensions down to 1 μm. Specimens were subsequently electrolytically etched using a 10% phosphoric acid solution to dissolve the γ matrices and highlight the γ' precipitates. Microstructural examination of these specimens was carried out using a ZEISS GeminiSEM 300 scanning electron microscope in secondary electron (SE) mode (in-lens mode). Energy dispersive X-ray spectroscopy (EDS) was performed using the Oxford Aztec system to measure the actual compositions of the alloys (Table 5.1), which were obtained from a minimum of 4 large area scans of at least 500 × 500 μm. The EDS system had been calibrated using a nickel strip prior to acquiring EDS data.

5.2.3 X-ray diffraction (XRD) for assisting in γ-γ' phase identification

Plates 2 mm thick were cut from each alloy bar of composition $(Ni,Co)_{72}Al_5Ti_5Cr_{15}W_3$ (at.%) in the homogenised condition as well as in the aged condition (800°C, 1000 hours) and each of the twelve cut specimens was polished down with 4000 grit SiC paper. X-ray diffraction (XRD) was carried out on all twelve alloy specimens to confirm the presence of a γ-γ' microstructure. A Bruker D8 Advance X-ray diffractometer was employed, operated at 40 kV and 40 mA with Cu Kα radiation. (A Ni filter of 0.012 mm thickness was added to attenuate the Cu Kβ signal). Data were acquired over a range of $20° < 2\theta < 120°$, with a step size of 0.03° and dwell time of 2 seconds. The Inorganic Crystal Structure Database (ICSD) [200] was consulted to identify individual phases from peaks in XRD traces.

5.2.4 Differential scanning calorimetry (DSC)

To determine the γ' solvus, solidus and liquidus temperatures for each of the six $(Ni,Co)_{72}Al_5Ti_5Cr_{15}W_3$ (at.%) alloy compositions in both homogenised and aged conditions, DSC was performed on twelve small discs, six of which were extracted following homogenisation heat treatment (1250°C, 48 hours) and six of which were extracted following the subsequent ageing heat treatment (800°C, 1000 hours). All twelve discs (1 mm thickness × 5 mm diameter) were extracted using spark erosion. DSC tests on the alloy specimens were performed as for the cast alloy specimens using a Netzsch 404 heat-flux calorimeter operating at temperatures of up to 1450°C with a heating rate of 10°C min^{-1}. An empty crucible was run

in the DSC under the same conditions and the data obtained were taken as a representative background and subtracted from the thermal data acquired for each of the six alloys tested.

For direct comparison with the W-free quinary Ni-Co-5Al-5Ti-15Cr (at.%) alloys in the homogenised condition, it was necessary to carry out DSC on each of the seven quinary alloys (denoted 0Co, 9Co, 19Co, 28Co, 38Co, 47Co and 56Co) homogenised at 1250°C for 24 hours. DSC was performed using the same calorimeter and heating rate as for the W-containing alloys. Data analysis for both the W-containing and W-free alloys was performed using Igor Pro 6.3 software [161].

5.2.5 Vickers microhardness

Following ageing of the six W-containing $(Ni,Co)_{72}Al_5Ti_5Cr_{15}W_3$ (at.%) alloy bars at 800°C for 1000 hours, a section of each was cut and mounted in conductive Bakelite. Samples were then ground and polished down to a 0.25 µm diamond finish. Vickers microhardness measurements were performed at room temperature with an applied load of 3 kg and an indentation dwell time of 15 seconds. For each aged alloy specimen, ten indentations were made across the whole sample (i.e. across multiple grains) and then measured to determine the Vickers microhardness (HV).

To compare Vickers microhardness values with microhardness values obtained for the W-free $(Ni,Co)_{75}Al_5Ti_5Cr_{15}$ (at.%) alloys aged in the same way (800°C for 1000 hours), samples were cut from all seven aged W-free bars (fabricated as in Chapter 2), which were then ground and polished down to a 0.25 µm diamond finish, as for the W-containing alloys. Vickers microhardness measurements were then carried out at room temperature as for the W-containing specimens.

As alloy grain size influences microhardness, it was important to ensure a similar grain size for the W-containing and W-free alloys. Therefore, specimens of both series were processed in the same way i.e. fabricated by arc-melting and then homogenised at 1250°C, prior to ageing at 800°C for 1000 hours. SEM examination of the aged W-free alloys confirmed a grain size on the scale of millimetres.

5.2.6 Mass density

The mass density of the W-containing $(Ni,Co)_{72}Al_5Ti_5Cr_{15}W_3$ (at.%) alloys was measured at room temperature and compared with the mass density of the W-free

$(Ni,Co)_{75}Al_5Ti_5Cr_{15}$ (at.%) alloys also obtained at room temperature. To measure the mass density of the six W-containing alloys, a section (nominally 7.5 mm in length) was cut from each aged bar and, from each section, a 5 mm diameter cylinder was extracted using electrical discharge machining (EDM). The mass density of each alloy cylinder was determined using Archimedes' Principle by means of ethanol displacement.

To measure the mass density for each alloy based on the *quinary* Ni-Co-5Al-5Ti-15Cr (at.%) system, a new batch of alloys was fabricated (arc-melted) and homogenised (at 1250°C) as in Chapter 2. The actual composition of each of the $(Ni,Co)_{75}Al_5Ti_5Cr_{15}$ (at.%) alloys following homogenisation was confirmed by SEM-EDS to be within ±1 at.% of its nominal composition. Alloys were subsequently aged at 800°C for 1000 hours and air-cooled. From each aged alloy bar, one cylinder of nominally 5 mm diameter and 7.5 mm length was extracted using EDM. The mass density of each cylinder was determined by using Archimedes' Principle as for the W-containing alloys.

5.3 Results and Discussion

5.3.1 Microstructural characterisation of alloys following homogenisation heat treatment

Figure 5.1 shows a representative SE (in-lens) micrograph for each of the six W-containing $(Ni,Co)_{72}Al_5Ti_5Cr_{15}W_3$ (at.%) alloys following homogenisation heat treatment (1250°C for 48 hours). A γ-γ' microstructure was apparent for all six alloy compositions and an overall reduction in γ' precipitate size was observed with increasing Co content. On examination of $(Ni,Co)_{72}Al_5Ti_5Cr_{15}W_3$ (at.%) alloy microstructures in back-scattered electron (BSE) mode, no extra phases were evident. XRD analysis confirmed the presence of a γ-γ′ microstructure for each of the six alloys investigated: 0Co-3W, 17Co-3W, 27Co-3W, 36Co-3W, 45Co-3W and 55Co-3W.

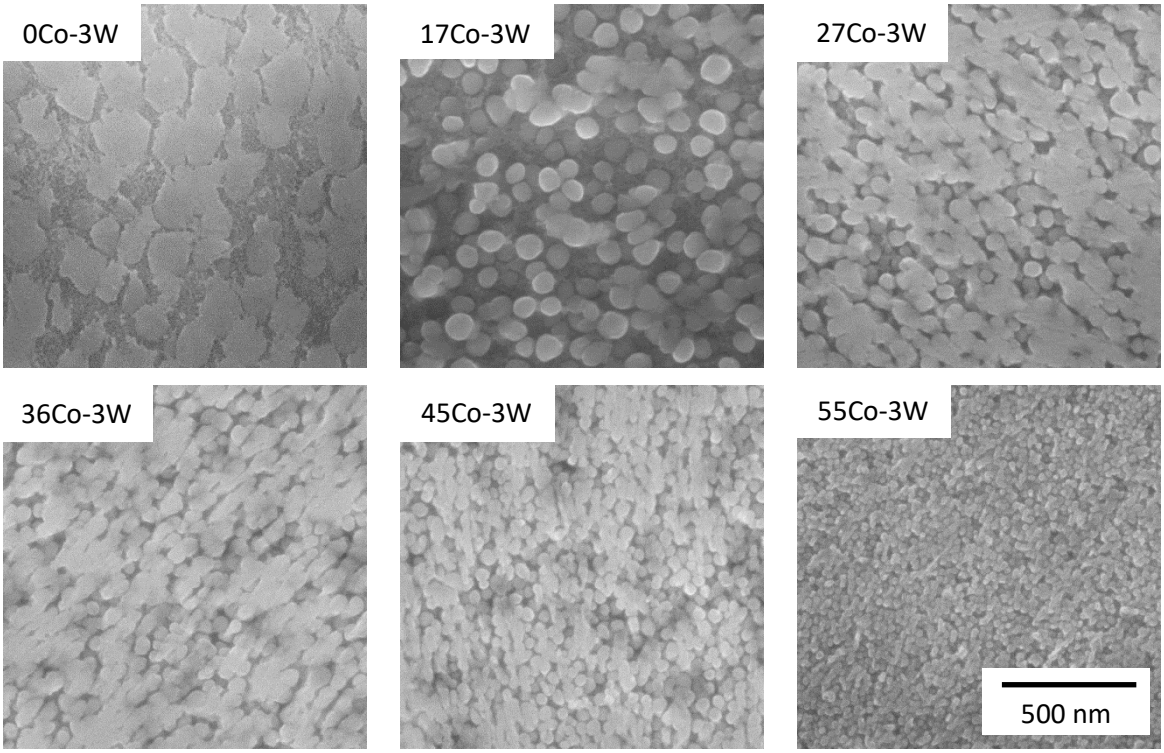

Figure 5.1. Representative SE (in-lens) micrographs of the Ni-Co-5Al-Ti-15Cr-3W (at.%) alloy series following homogenisation heat treatment at 1250°C for 48 hours. All six alloys display a γ-γ' duplex microstructure.

DSC traces obtained for the W-containing $(Ni,Co)_{72}Al_5Ti_5Cr_{15}W_3$ (at.%) alloys and W-free $(Ni,Co)_{75}Al_5Ti_5Cr_{15}$ (at.%) alloys following homogenisation heat treatment (1250°C) are shown in Figure 5.2a and Figure 5.2b respectively. In the current study, the γ' solvus temperature for each alloy was taken to be at the position on its DSC curve equivalent to that arrowed in red in Figure 5.2a. From Figure 5.2, the alloy melting process can be observed as an endothermic event such that the solidus temperature was taken to be the point where the DSC curve starts to fall off rapidly on heating and the liquidus temperature was taken as the point at which the DSC curve recovers its pre-solidus trend. For both alloy series (Figure 5.2a, b), γ' solvus temperature was observed to decrease with increasing Co content. The 0Co-3W alloy exhibited the highest γ' solvus temperature (1170°C, arrowed) out of both alloy series.

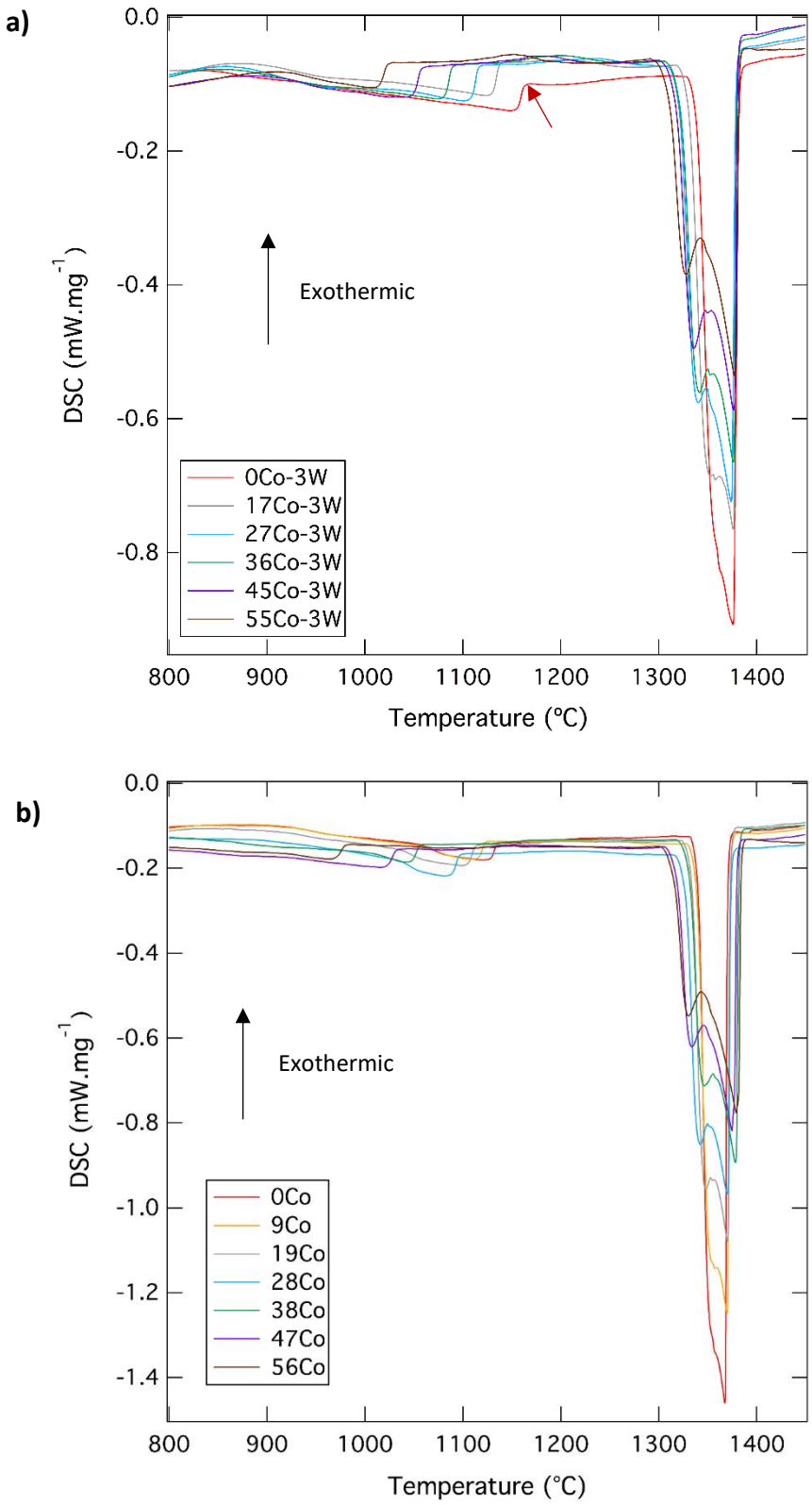

Figure 5.2. DSC traces obtained for: a) Ni-Co-5Al-5Ti-15Cr-3W (at.%) alloy series (homogenised at 1250°C, 48 hours); b) W-free Ni-Co-5Al-5Ti-15Cr (at.%) alloy series (homogenised at 1250°C, 24 hours). Samples were heated from 800°C to 1450°C at 10°C min^{-1}. The 0Co-3W alloy displays the highest γ' solvus temperature obtained (1170°C) out of both alloy series (arrowed in red).

The phase transition temperatures recorded from the DSC traces for the W-containing $(Ni,Co)_{72}Al_5Ti_5Cr_{15}W_3$ (at.%) alloys and W-free $(Ni,Co)_{75}Al_5Ti_5Cr_{15}$ (at.%) alloys following homogenisation heat treatment (1250°C) are compared in Table 5.2 and are plotted graphically in Figure 5.3. Addition of 3 at.% W increased the γ' solvus temperature over the entire alloy series by between 22 and 46°C. The greatest improvement in γ' solvus temperature (a 46°C increase) was observed for the addition of 3 at.% W to the 56Co quinary alloy (from 983 to 1029°C). For both the W-containing and W-free alloy series, the decrease in γ' solvus temperature with increasing Co content is consistent with the reduction in γ' precipitate size apparent in their corresponding micrographs (Figure 5.1 and Figure 4.1).

The solidus temperatures decrease slightly with increasing Co content for both W-containing and W-free alloy series following homogenisation at 1250°C (Figure 5.3). The liquidus temperatures appear less influenced by variation in Co content for both W-containing and W-free alloy series. The trends for γ' solvus and solidus temperatures in both the W-containing and W-free alloy series (Figure 5.3) appear consistent with those reported by Shinagawa *et al*., 2008 [127] for the Co-Ni-10Al-7.5/10W (at.%) alloy series homogenised at 1300°C for 24 hours (Figure 1.22a). Absolute values of γ' solvus and solidus temperatures obtained in the present study for the 3 at.% W-containing alloys may be compared with the Co-Ni-10Al-7.5W (at.%) alloys of Shinagawa *et al*. [127]. For example, alloy 42.5Co-40Ni-10Al-7.5W (at.%) [127] appears to have a γ′ solvus temperature of ~1060°C (Figure 1.22a) and this compares well with alloy 45Co-3W in the present study, which exhibits a γ′ solvus temperature of 1064°C (Table 5.2). For the same alloys, solidus temperature was estimated to be ~1440°C for the 42.5Co-40Ni-10Al-7.5W (at.%) alloy [127] compared with the lower solidus temperature of 1300°C for the 45Co-3W alloy in the present study (Table 5.2).

Table 5.2. Values of γ' solvus, solidus and liquidus temperatures following alloy homogenisation for the Ni-Co-5Al-5Ti-15Cr-3W (at.%) alloy series (1250°C, 48 hours) and for the W-free quinary alloy series (1250°C, 24 hours). All values were acquired using DSC with the same calorimeter and heating rate. Values were extracted from the DSC traces shown in Figure 5.2.

Alloy	Ni-Co-5Al-5Ti-15Cr (at.%) quinary alloys			Alloy	Ni-Co-5Al-5Ti-15Cr-3W (at.%) senary alloys		
	γ' solvus (°C)	Solidus (°C)	Liquidus (°C)		γ' solvus (°C)	Solidus (°C)	Liquidus (°C)
0Co	1140	1331	1377	0Co-3W	1170	1328	1390
9Co	1126	1328	1380	-	-	-	-
19Co	1118	1323	1380	17Co-3W	1144	1318	1387
28Co	1101	1316	1380	27Co-3W	1123	1308	1386
38Co	1059	1318	1387	36Co-3W	1095	1306	1386
47Co	1035	1305	1386	45Co-3W	1064	1300	1386
56Co	983	1300	1390	55Co-3W	1029	1291	1387

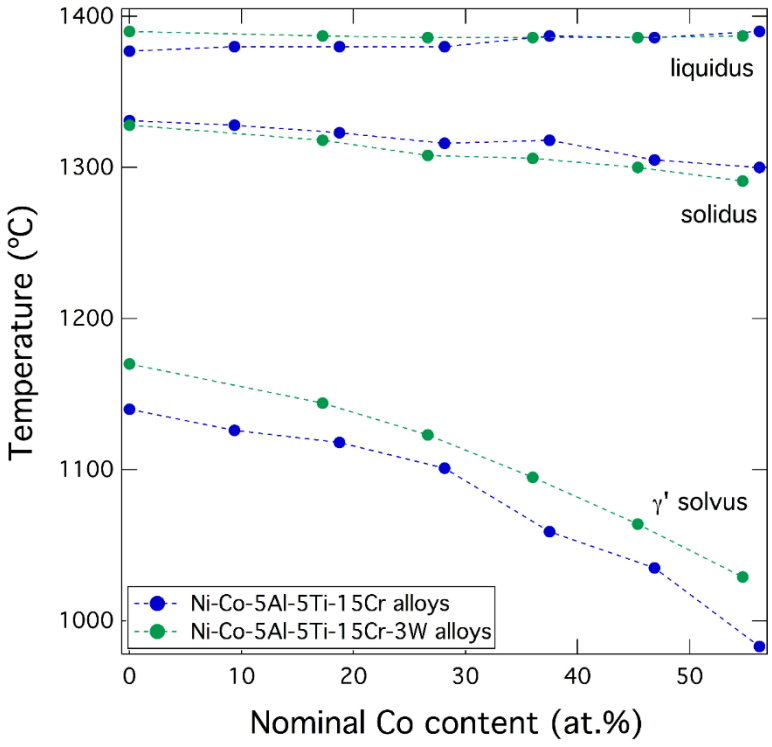

Figure 5.3. Liquidus, solidus and γ' solvus temperatures as a function of nominal alloy Co content for the senary Ni-Co-5Al-5Ti-15Cr-3W (at.%) alloy series (green) compared with the W-free quinary Ni-Co-5Al-5Ti-15Cr (at.%) alloy series (blue), following homogenisation heat treatment of both series at 1250°C. Data from Figure 5.2 and Table 5.2.

5.3.2 Microstructural characterisation of alloys aged at 800°C for 1000 hours

Figure 5.4 shows representative SE (in-lens) micrographs for each of the six W-containing alloys $(Ni,Co)_{72}Al_5Ti_5Cr_{15}W_3$ (at.%) aged at 800°C for 1000 hours. Each alloy composition appeared to show a γ-γ' microstructure as confirmed by XRD analysis. For alloys of Co content 0-27 at.%, γ' precipitates with rounded corners were observed (Figure 5.4a-c), whereas alloys with Co content between 36 and 55 at.% appeared to comprise γ' precipitates that were nearer to cuboidal (Figure 5.4d, e) or cuboidal (Figure 5.4f). The 45Co-3W and 55Co-3W alloys (Figure 5.4e, f), did not appear to exhibit the same degree of coalescence or elongation of γ' precipitates observed for the aged 47Co and 56Co W-free $(Ni,Co)_{75}Al_5Ti_5Cr_{15}$ (at.%) quinary alloys (Figure 2.2f, g).

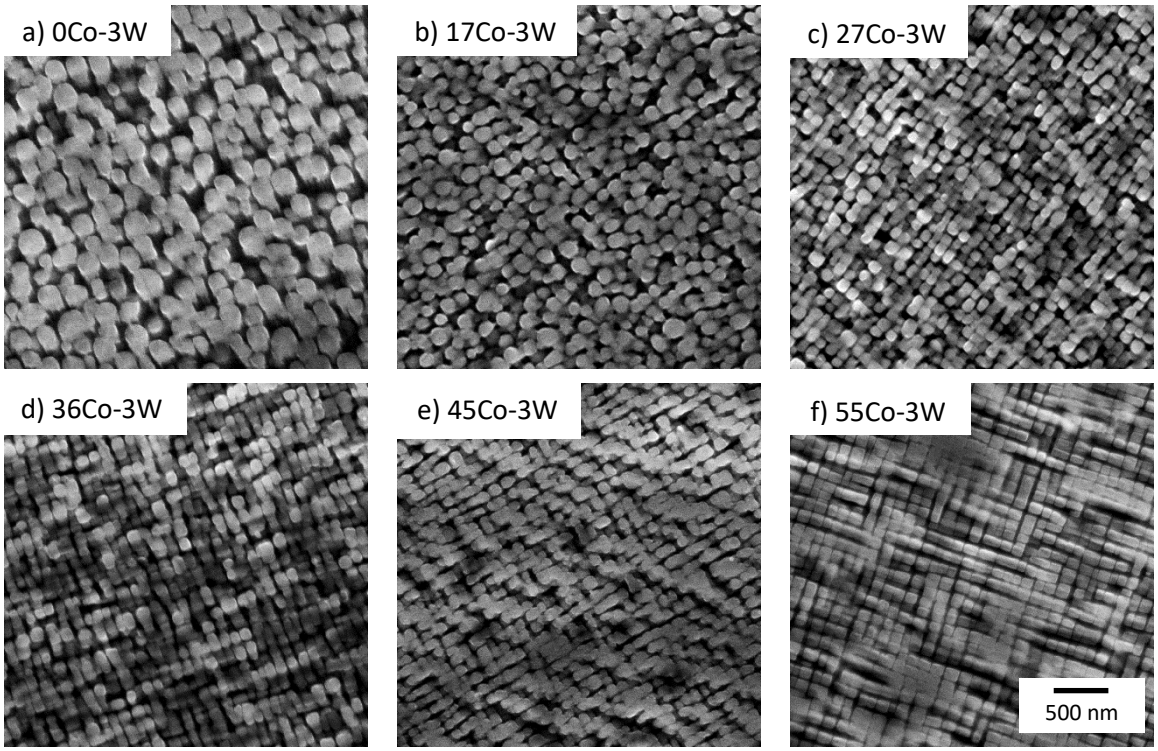

Figure 5.4. Representative SE (in-lens) micrographs of the Ni-Co-5Al-Ti-15Cr-3W (at.%) alloy series following ageing at 800°C for 1000 hours. All six alloys exhibit a γ-γ' duplex microstructure.

The phase transition temperatures after ageing (800°C, 1000 hours) of the W-containing $(Ni,Co)_{72}Al_5Ti_5Cr_{15}W_3$ (at.%) alloys and W-free $(Ni,Co)_{75}Al_5Ti_5Cr_{15}$ (at.%) alloys are shown in Table 5.3 and plotted in Figure 5.5 and were found to be in close agreement with values recorded following homogenisation at 1250°C (Table 5.2 and Figure 5.3). γ' solvus temperature was higher for the W-containing alloys than for the corresponding W-free quinary alloys in the aged condition, as for the homogenised condition. Figure 5.6 elucidates how small the discrepancy is between phase transition temperatures obtained after homogenisation (1250°C, 48 hours) and those obtained after subsequent ageing (800°C, 1000 hours) in this study.

Table 5.3. Values of γ' solvus, solidus and liquidus temperatures following ageing of the Ni-Co-5Al-5Ti-15Cr-3W (at.%) alloy series and the W-free quinary alloy series at 800°C (1000 hours). All values were acquired using DSC with the same calorimeter and heating rate. (These values are plotted graphically in Figure 2.4 for the quinary alloy series.)

Alloy	Ni-Co-5Al-5Ti-15Cr (at.%) quinary alloys			Alloy	Ni-Co-5Al-5Ti-15Cr-3W (at.%) senary alloys		
	γ' solvus (°C)	Solidus (°C)	Liquidus (°C)		γ' solvus (°C)	Solidus (°C)	Liquidus (°C)
0Co	1139	1327	1371	0Co-3W	1168	1328	1386
9Co	1133	1323	1373	-	-	-	-
19Co	1113	1318	1375	17Co-3W	1143	1318	1386
28Co	1094	1316	1378	27Co-3W	1122	1309	1386
38Co	1064	1307	1381	36Co-3W	1095	1305	1387
47Co	1021	1310	1389	45Co-3W	1068	1299	1387
56Co	985	1299	1387	55Co-3W	1033	1291	1389

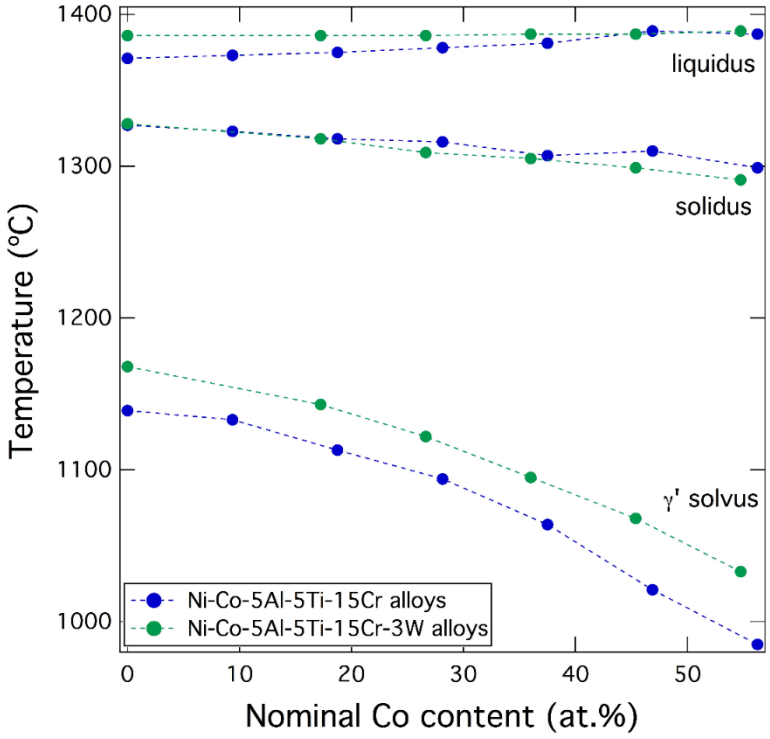

Figure 5.5. Liquidus, solidus and γ' solvus temperatures as a function of nominal alloy Co content for the senary Ni-Co-5Al-5Ti-15Cr-3W (at.%) alloy series (green) compared with the W-free quinary Ni-Co-5Al-5Ti-15Cr (at.%) alloy series (blue) following ageing of both series at 800°C (1000 hours). Data taken from Table 5.3.

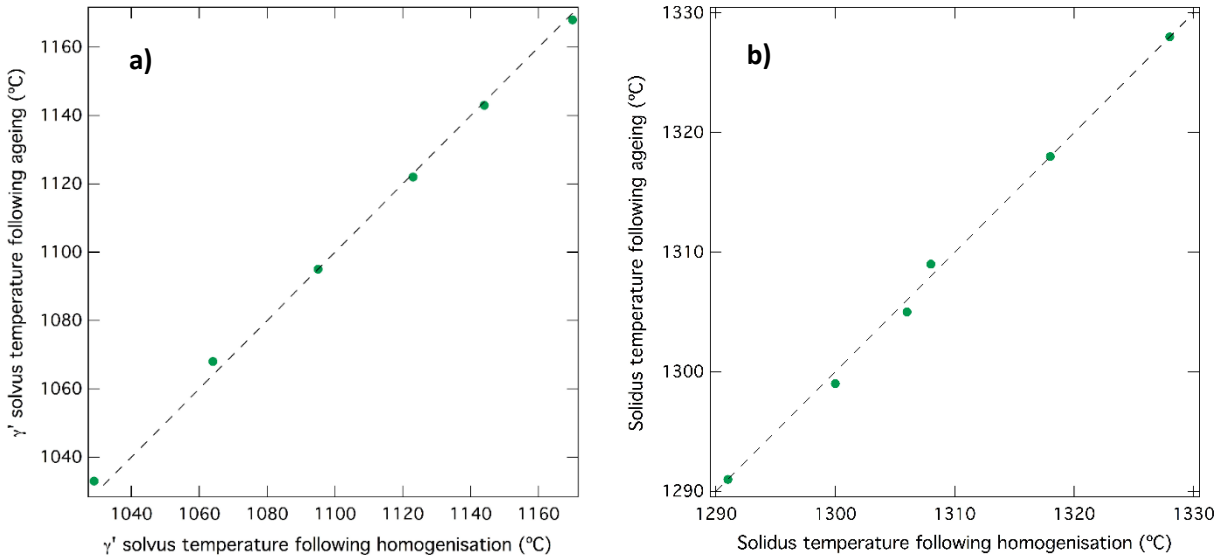

Figure 5.6. Graph showing correlation between measured phase transition temperatures for the aged and homogenised Ni-Co-5Al-5Ti-15Cr-3W (at.%) alloys: a) γ' solvus temperature; b) solidus temperature. Data from Table 5.2 and Table 5.3.

5.3.3 Vickers microhardness of aged alloys

Figure 5.7 compares Vickers microhardness values for the W-containing $(Ni,Co)_{72}Al_5Ti_5Cr_{15}W_3$ (at.%) alloy series and W-free $(Ni,Co)_{75}Al_5Ti_5Cr_{15}$ (at.%) alloy series as a function of alloy Co content. All alloys were aged at 800°C for 1000 hours. For the quinary W-free alloys (blue markers), an increase in Vickers microhardness was observed as Co content increased from 0 to 19 at.%, whereas values for the 19Co, 28Co and 38Co alloys appeared comparable at ~425 HV ($kgf.mm^{-2}$). A marked decrease in microhardness was observed with further addition of Co up to 56 at.%. The relatively large standard deviation for the 56Co alloy may be attributed to the orientation of the rod-like (elongated) γ' precipitates observed in Figure 2.2g. For the W-containing alloys (green markers), an increase in Vickers microhardness was apparent as Co content increased from 0 to 27 at.%. Further addition of Co (up to 55 at.%) appeared to produce a decline in microhardness values.

The Vickers microhardness values for the W-containing alloys 17Co-3W, 27Co-3W and 36Co-3W were comparable to the Vickers microhardness values for the corresponding W-free alloys. The Vickers microhardness values for the W-containing alloys of Co content 45 and 55 at.% were found to be notably higher than the microhardness values for the corresponding W-free quinary alloys. The 55Co-3W alloy was associated with a relatively small standard deviation, consistent with the lesser degree of γ′ precipitate coalescence observed compared with the W-free 56Co alloy (Figure 5.4f and Figure 2.2g).

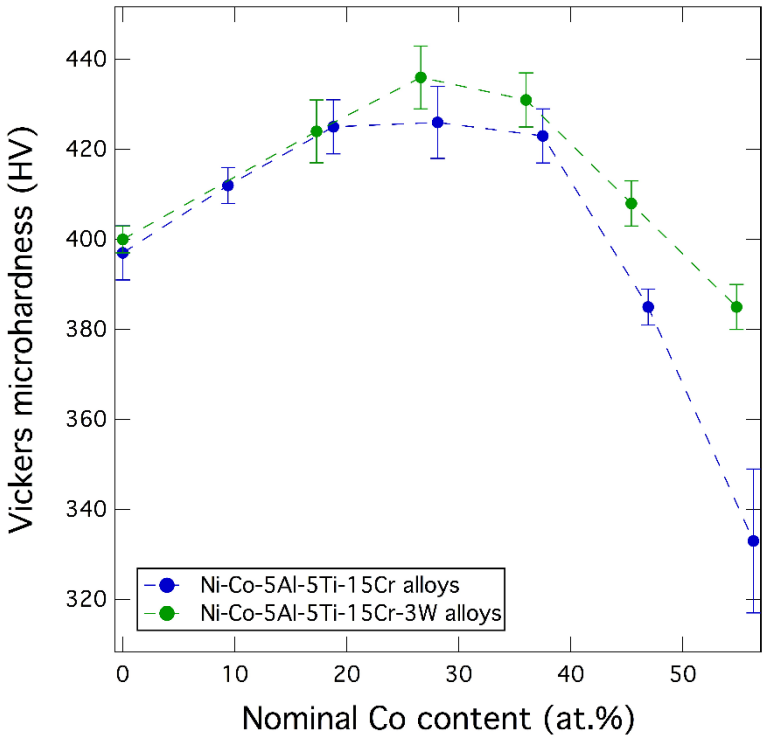

Figure 5.7. Vickers microhardness values (HV in kgf.mm^{-2}) obtained at room temperature as a function of alloy Co content for the senary Ni-Co-5Al-5Ti-15Cr-3W (at.%) alloy series (green) and W-free quinary Ni-Co-5Al-5Ti-15Cr (at.%) alloy series (blue). Both alloy series were aged at 800°C for 1000 hours. Mean values ±1 standard deviation.

5.3.4 Mass density

The mass density of the W-containing $(Ni,Co)_{72}Al_5Ti_5Cr_{15}W_3$ (at.%) alloys was measured and compared with mass density values obtained for the W-free quinary $(Ni,Co)_{75}Al_5Ti_5Cr_{15}$ (at.%) alloys (Figure 5.8). All alloys were aged at 800°C for 1000 hours. The mass density of the W-containing alloys was measured at room temperature and found to be consistent at ~8.5 g.cm^{-3}, whilst the mass density of the W-free quinary alloys was measured at room temperature and found to be ~8.1 g.cm^{-3}. For each alloy series, there appears little discernible influence of Co content on alloy mass density, consistent with the similar atomic mass of Co and Ni. These values compare with a value of ~8.2 g.cm^{-3} for the mass density of the Ni-based superalloy Waspaloy.

Figure 5.8 provides a comparison of the W-containing $(Ni,Co)_{72}Al_5Ti_5Cr_{15}W_3$ (at.%) alloy series and the W-free $(Ni,Co)_{75}Al_5Ti_5Cr_{15}$ (at.%) alloy series in terms of both mass density and γ′ solvus temperature as a function of increasing Co content. The 0Co-3W alloy exhibits the highest γ′ solvus temperature (1168°C) and a mass density of 8.52 g.cm^{-3}. In view of the comparable Vickers microhardness values for alloys 27Co-3W, 36Co-3W and the W-

free alloys 28Co and 38Co (Figure 5.7), it is of note that both W-containing alloys exhibit a mass density of 8.54 g.cm^{-3} compared with 8.08 g.cm^{-3} for the W-free 28Co and 38Co alloys i.e. a 0.46 g.cm^{-3} increase. Addition of 3 at.% W to the quinary 28Co and 38Co alloys produced an increase in γ′ solvus temperature from 1094°C (28Co) and 1064°C (38Co) to 1122°C (27Co-3W) and 1095°C (36Co-3W) i.e. an increase of ~30°C (Figure 5.8).

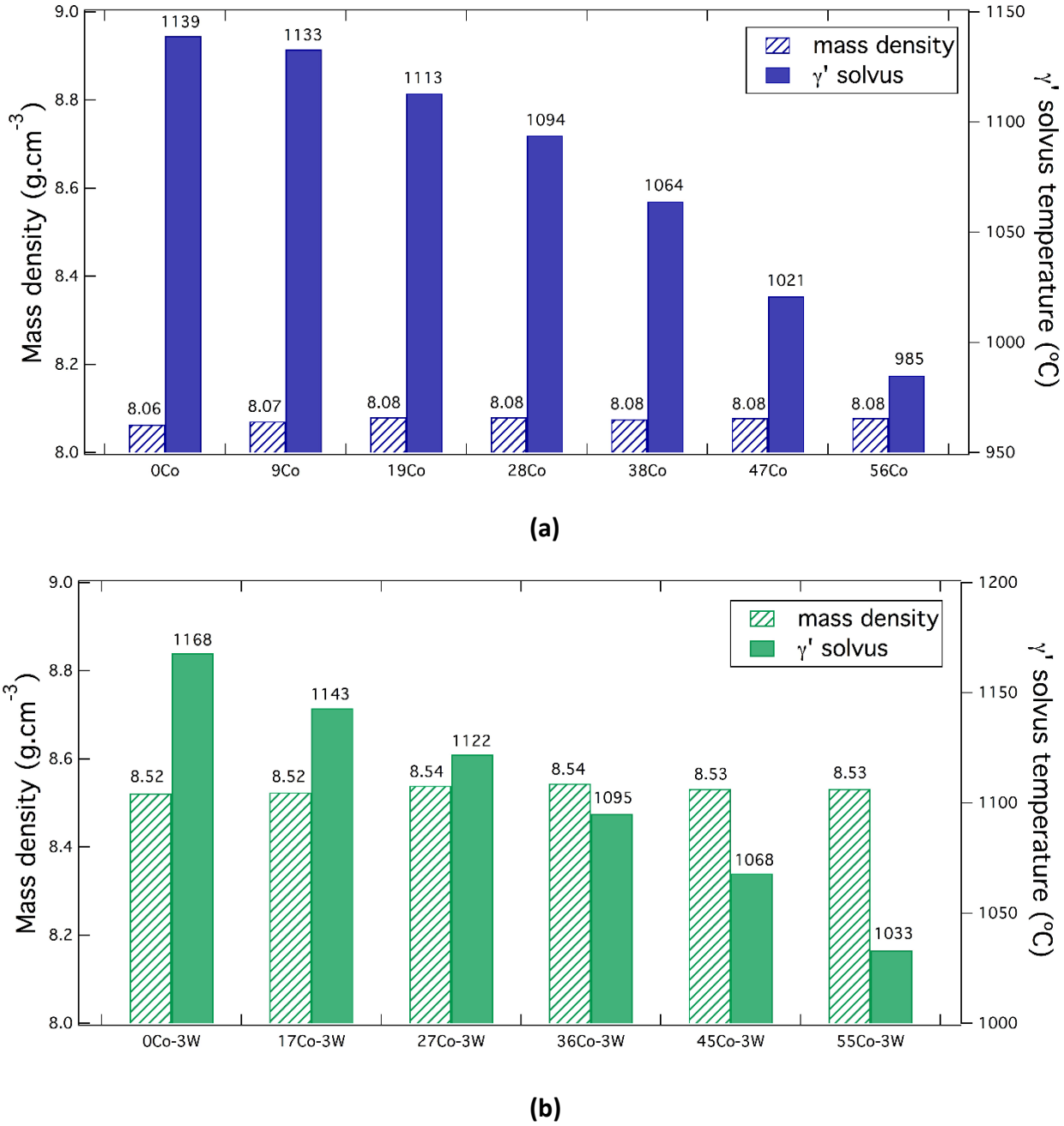

Figure 5.8. Mass density and γ' solvus temperature of: a) the W-free quinary Ni-Co-5Al-5Ti-15Cr (at.%) alloy series; b) the senary Ni-Co-5Al-5Ti-15Cr-3W (at.%) alloy series following ageing of both series at 800°C for 1000 hours.

5.4 Conclusions

- All six W-containing $(Ni,Co)_{72}Al_5Ti_5Cr_{15}W_3$ (at.%) alloys (Co content 0, 17, 27, 36, 45 and 55 at.%) exhibited a γ-γ′ microstructure following the homogenisation heat treatment (1250°C, 48 hours) and following subsequent ageing for 1000 hours at 800°C.
- For the W-containing alloy series, γ′ solvus and solidus temperatures recorded following homogenisation heat treatment were in close agreement with values recorded following ageing at 800°C. This was also the case for the W-free alloy series, $(Ni,Co)_{75}Al_5Ti_5Cr_{15}$ (at.%).
- For the W-containing and W-free alloy series, γ′ solvus temperature decreased with increasing Co content. The γ′ solvus temperature of each W-containing alloy was higher than that of the corresponding W-free alloy. A slight decrease in solidus temperature was observed with increasing Co content in both alloy series.
- 3 at.% W addition to the quinary Ni-Co-5Al-5Ti-15Cr (at.%) alloy series led to an increase in alloy mass density from ~8.1 $g.cm^{-3}$ to ~8.5 $g.cm^{-3}$.
- For the quinary W-free alloys, an increase in Vickers microhardness was observed as Co content increased from 0 to 19 at.%. Values for the 19Co, 28Co and 38Co alloys peaked and appeared comparable at ~425 HV ($kgf.mm^{-2}$). Higher concentrations of Co (up to 56 at.%) produced a marked decrease in microhardness. All alloys were aged at 800°C for 1000 hours.
- For the W-containing alloys, Vickers microhardness appeared to increase as Co content increased from 0 to 27 at.%. Higher concentrations of Co (up to 55 at.%) appeared to produce a decline in microhardness values. The Vickers microhardness values for the W-containing alloys 17Co-3W, 27Co-3W and 36Co-3W were comparable to the Vickers microhardness values for the corresponding W-free alloys.
- For the W-free alloys, the 19Co alloy exhibited an optimal combination of high γ′ solvus temperature (1113°C) and maximal Vickers microhardness (~425 HV). For the W-containing alloys, the 27Co-3W alloy exhibited a γ′ solvus temperature of 1122°C (with Vickers microhardness of ~436 HV), although the 17Co-3W alloy exhibited a higher γ′ solvus temperature, of 1143°C (with Vickers microhardness of ~424 HV).

6. Final Summary and Further Work

6.1 Summary

The excellent high-temperature strength exhibited by conventional Ni-based superalloys currently in service as aero-engine turbine discs originates from their γ-γ' two phase microstructure, wherein $L1_2$ precipitates (γ') based on Ni_3Al are embedded coherently in an FCC (A1) Ni-rich solid solution matrix. Between 8 and 12 alloying additions are typically incorporated to optimise the critical balance of high-temperature strength, oxidation resistance and creep resistance. Although the mainstay of commercial air travel for over half a century, the polycrystalline Ni-based superalloys currently deployed as aero-engine turbine discs are operating at temperatures approaching their theoretical high-temperature limits. To achieve greater thermal efficiency and reduce emissions in future aero-engine designs, next-generation turbine disc superalloys must be engineered to sustain the necessary higher operating temperatures (approaching 800°C), whilst maintaining mechanical integrity and excellent oxidation resistance in a high-stress environment without the application of a protective coating.

Studies on the emerging γ'-strengthened Co-based superalloys have made significant advances in mitigating the problem of high mass density in Co-Al-W based systems and of low γ' solvus temperature in Co-Al-Mo-Nb/Ta based systems by incorporation of elements such as Ni, Ti or Cr. A detailed analysis of the effect of systematic variation in Co:Ni ratio on the fundamental quinary system, Ni-Co-Al-Ti-Cr, is therefore essential to establish a baseline against which to compare the effect of higher order alloying, for example with refractory metals such as W, that potentially confer superior high-temperature properties.

Seven γ'-strengthened model superalloys of composition $(Ni,Co)_{75}Al_5Ti_5Cr_{15}$ (at.%) were arc-melted and subjected to a homogenisation heat treatment (1250°C) before subsequent processing for analysis using atom probe tomography (APT), neutron diffraction and high-temperature oxidation at 800°C. For the purpose of this study, these seven model superalloys were denoted by their nominal atomic concentration of Co (at.%) i.e. 0Co, 9Co, 19Co, 28Co, 38Co, 47Co and 56Co. Following ageing at 800°C for 1000 hours, a γ-γ' duplex microstructure was observed in all seven alloys with no other phases observed. In alloys of Co content 0-38 at.%, isolated cuboidal γ' precipitates were observed, whereas alloys containing 47 and 56 at.% Co exhibited elongated γ' precipitates suggesting directional coalescence during precipitate growth. Pushing the Co content to 75 at.% to achieve the Ni-free quaternary alloy (Co-5Al-5Ti-15Cr at.%) appeared to destabilise the γ-γ' microstructure, indicating the need for a critical

Ni content (Appendix 8.1). Therefore, alloys of 0-56 at.% Co were selected for atom probe tomography, neutron diffraction and oxidation in this systematic study.

For the aged quinary alloy series $(Ni,Co)_{75}Al_5Ti_5Cr_{15}$ (at.%), γ' solvus temperature was observed to decrease with increasing Co:Ni ratio (from 1139°C for the 0Co alloy to 985°C for the 56Co alloy) whilst alloy mass density remained fairly constant across the alloy series (at ~8.1 $g.cm^{-3}$). Atom probe tomography on all seven aged alloys (0-56 at.% Co) indicated preferential partitioning of Ni, Al and Ti to the γ' phase whereas Cr and Co partitioned preferentially to the γ matrix phase. The extent of partitioning of both Ti and Al to the γ' phase increased up to 19 at.% Co, above which the γ' phase solubility for both Ti and Al appeared to decline. Concomitantly, the extent of partitioning of Cr to the γ matrix increased up to 19 at.% Co, above which the concentration of Cr in the γ' phase appeared to increase, suggesting a greater γ' phase solubility for Cr at high Co concentrations. The more extensive degree of partitioning of Ti and Al to the γ' phase with increasing Co content up to ~19 at.% is putatively attributed to the influence of Co at low concentrations in reducing the solubility of Al and Ti in the Ni-based γ solid solution. In addition, the observed decrease in the preferential partitioning of Al and Ti to the γ' with increasing Co content above ~19 at.% is plausibly attributed to an increased tendency for Cr to substitute onto the (Ti,Al) sub-lattice of $(Ni,Co)_3(Ti,Al)$ for Co content above ~19 at.%. The non-monotonic correlation between elemental partitioning and alloy Co content is attributed to a transition in the composition of the γ' from $Ni_3(Ti,Al)$ toward Co_3Ti via $(Ni,Co)_3(Ti,Al)$. Alloy γ' volume fraction was observed to increase slightly with increasing Co content up to 19 at.% (to a maximal value of 0.40), corresponding to maximal preferential partitioning of Al and Ti to the γ' phase. As Co content increased beyond ~19 at.%, γ' volume fraction was observed to decrease, with values of volume fraction for the 28Co and 38Co alloys of ~0.36.

To elucidate the relationship between elemental partitioning and lattice misfit in this fundamental $(Ni,Co)_{75}Al_5Ti_5Cr_{15}$ (at.%) system, it was necessary to quantify the influence of a systematic increase in Co:Ni ratio on γ and γ' lattice parameters and resultant lattice misfit for the proposed higher operating temperatures (approaching 800°C) for next-generation aero-engine turbine discs. The POLARIS instrument at the Rutherford Appleton Laboratory was used to perform neutron diffraction on each of the seven model superalloy compositions (0Co, 9Co, 19Co, 28Co, 38Co, 47Co and 56Co) across a temperature range (ambient to 800°C) likely to be experienced by aero-engine turbine disc superalloys in service. To acquire high quality

diffraction patterns, all seven model superalloys were homogenised at 1250°C and then hot-rolled to achieve a fine grain size before ageing at 800°C for 1000 hours.

Alloys of 0, 9, 19, 28, 38 and 47 at.% Co exhibited a positive lattice misfit at each test temperature (room temperature, 400, 600, 700 and 800°C). For each test temperature, the magnitude of lattice misfit was observed to increase as Co content increased from 0-38 at.%, although pushing the Co content higher (to 47 at.%) resulted in a reduction in lattice misfit for temperatures from ambient to 700°C. Thus, room temperature misfit values increased with increasing Co content up to 38 at.%, appearing to follow the increased partitioning of Ni (and of Co to a lesser extent) to the γ' phase with increasing Co up to the 38-47 at.% range (Chapter 2). Diffraction patterns for the 56Co alloy for temperatures ambient, 400, 600, 700 and 800°C suggest the occurrence of a strain-induced distortion of the γ' phase and therefore no lattice parameter or lattice misfit values could be derived for the 56Co alloy.

Values of lattice misfit decreased with increasing test temperature from ambient to 800°C for the six alloys of Co content 0-47 at.%. A systematic increase in Co from 0 to 38 at.% produced a systematic shift in the curve of lattice misfit versus temperature to higher misfit values, although the corresponding curve for the 47Co alloy appeared aberrant. In Ni-based superalloy design, a small magnitude of lattice misfit is generally considered desirable to minimise γ-γ' interfacial energy and retard γ' coarsening. In the fundamental $(Ni,Co)_{75}Al_5Ti_5Cr_{15}$ (at.%) system investigated, alloys 0Co, 9Co, 19Co and 28Co are Ni-based, suggesting that lower values of lattice misfit are desirable. If a similar principle applies with respect to Co-based superalloy design i.e. that a low lattice misfit is desirable to retard γ' coarsening, then it may prove beneficial that values of lattice misfit decreased with increasing test temperature from ambient to 800°C for the entire compositional range for which a lattice misfit value could be derived (0-47 at.%).

Few detailed systematic studies analysing the high-temperature oxidation performance of γ-γ' alloys of the Ni-Co-Al-Ti-Cr system appear in the literature. Crucially, the current study investigates the effect of a systematic increase in Co:Ni ratio on the evolution of oxides of γ-γ' alloys of the quinary system, $(Ni,Co)_{75}Al_5Ti_5Cr_{15}$ (at.%) following oxidation at 800°C. The seven model superalloys of Co content 0, 9, 19, 28, 38, 47 and 56 at.% Co were subjected to isothermal oxidation in air at 800°C using box furnace exposure (1000 hours) as well as thermogravimetric analysis (TGA) for 100 hours. Following 1000 hours oxidation at 800°C, the 28, 38 and 47 at.% Co alloys were observed to exhibit a flat, compact and well-defined

external oxide scale and Cr_2O_3 layer with minimal oxygen ingress, together with a distinct Al_2O_3 subscale.

The 47Co alloy elicited two distinct morphologies following 1000 hours oxidation at 800°C: Type I resembled the 38Co alloy with thin, flat strata within a compact scale overlying a zone of conspicuous oxidation products; Type II displayed a paucity of internal oxidation products beneath what appeared to be a dense Al_2O_3 sub-scale. The observation of two distinct morphologies within a single specimen of the 47Co alloy was found to be reproducible on oxidation of a larger 47Co alloy specimen (10 × 6 × 1 mm) under the same conditions. SEM cross-sectional analysis of the 28Co alloy larger specimen (10 × 6 × 1 mm) revealed a well-defined Cr- and O-rich layer within a consistently compact external scale, as was observed for the 38Co alloy.

Thus, the 28Co, 38Co and 47Co alloys can elicit a flat, compact, well-defined external scale and Cr_2O_3 layer with minimal oxygen ingress following 1000 hours oxidation at 800°C. The presence of an Al_2O_3 sub-scale in the 28Co, 38Co and 47Co alloys suggests that manipulating the aluminium content within this Co concentration range to facilitate formation of a continuous Al_2O_3 sub-scale may enhance oxidation resistance and resistance to fatigue crack initiation by precluding both oxygen and nitrogen ingress.

The influence of 3 at.% W addition to the base alloy Ni-Co-5Al-5Ti-15Cr (at.%) was investigated by examining the effect of a systematic increase in Co:Ni ratio on the resultant microstructure, phase transition temperatures (γ' solvus, solidus and liquidus), mass density and Vickers microhardness. All six W-containing alloys, denoted by their nominal atomic concentration of Co (at.%), 0Co-3W, 17Co-3W, 27Co-3W, 36Co-3W, 45Co-3W and 55Co-3W, exhibited a γ-γ′ microstructure following homogenisation heat treatment at 1250°C and following subsequent ageing for 1000 hours at 800°C. For the aged W-containing alloys, γ' precipitates appeared more rounded for alloys of Co content 0-27 at.%, but progressively more cuboidal with increasing Co content up to 55 at.%, although the high Co alloys did not appear to exhibit the same extent of coalescence of γ' precipitates as the aged W-free 47Co and 56Co quinary alloys.

With the incorporation of 3 at.% W, values of γ' solvus temperature appeared consistently higher than corresponding values for the W-free alloys, but followed a similar trend of decreasing γ' solvus temperature with increasing Co:Ni ratio over the entire alloy series. Addition of 3 at.% W increased alloy mass density from ~8.1 $g.cm^{-3}$ for the W-free alloys to

~8.5 g.cm^{-3} for all six W-containing alloys, as might be expected. These values compare with a value of ~8.2 g.cm^{-3} for the mass density of the Ni-based superalloy, Waspaloy.

For the W-free alloys, Vickers microhardness values were observed to increase as Co content increased from 0 to 19 at.%, with a peak microhardness value for all three alloys, 19Co, 28Co and 38Co, of ~425 HV (kgf.mm^{-2}). For the alloys containing 3 at.%W, Vickers microhardness appeared to increase as Co content increased from 0 to 27 at.%, with microhardness values for alloys 17Co-3W, 27Co-3W and 36Co-3W appearing comparable to those values obtained for the corresponding W-free alloys (19Co, 28Co and 38Co). All alloys were aged at 800°C for 1000 hours. As Co concentration increased further, a reduction in microhardness values was observed, which was particularly pronounced for the quinary (W-free) alloy series.

Of the W-free alloys, the 19Co alloy exhibited an optimal combination of high γ′ solvus temperature (1113°C) and maximal Vickers microhardness (~425 HV). Of the W-containing alloys, the 27Co-3W alloy exhibited a γ′ solvus temperature of 1122°C (Vickers microhardness ~436 HV), although the 17Co-3W alloy exhibited a higher γ′ solvus temperature of 1143°C (Vickers microhardness ~424 HV).

This work represents the first detailed systematic study on the fundamental quinary Ni-Co-Al-Ti-Cr alloy system describing the effect of variation in Co:Ni ratio on the evolution of surface oxides and on the partitioning of elements to γ and γ' phases and associated lattice misfit. Incorporation of 3 at.% W into the base alloy Ni-Co-5Al-5Ti-15Cr (at.%) enabled a systematic comparison between the fundamental properties of the senary and W-free quinary alloy systems with respect to the influence of increasing Co:Ni ratio.

6.2 Further Work

Given the increased γ' solvus temperature, moderate increase in mass density (to ~8.5 $g.cm^{-3}$) and anticipated improvement in solid solution strengthening conferred by 3 at.% W addition to the quinary alloy series Ni-Co-5Al-5Ti-15Cr (at.%), then atom probe tomography on the senary alloy series may prove useful to determine the composition of γ and γ' phases and γ' volume fraction within each alloy following ageing for 1000 hours at 800°C. Quantifying γ' volume fraction by means of APT would permit comparison of the senary W-containing alloy series with other low-W Co-Ni-Al-Ti based alloys documented in the literature.

In view of the higher operating temperatures (approaching 800°C) proposed for next-generation turbine discs, other further work may include investigation of the influence of higher-order alloying with elements such as Mo, Nb and Ta in the low-W alloy series, Ni-Co-5Al-5Ti-15Cr-3W (at.%) with respect to the resultant microstructural characteristics and critical properties at 800°C. Elucidation of the effect of a systematic increase in Co:Ni ratio on microstructure and properties of the quinary and senary alloy systems investigated in the current study enables selection of particular Co:Ni ratios for which optimal values of γ' volume fraction, lattice misfit, γ' solvus, solidus and liquidus temperatures, mass density and Vickers microhardness have been derived. Investigation of the oxidation behaviour of the quinary alloy series indicated that the 28Co, 38Co and 47Co alloys exhibited promising oxidation characteristics at 800°C. This facilitates selection of alloying element concentration in γ'-strengthened (Ni,Co)-based superalloys likely to achieve an optimal combination of excellent high-temperature strength, a slow rate of γ' coarsening and good oxidation resistance, all fundamental requirements for high-pressure turbine discs designed for service at the higher operating temperatures approaching 800°C.

7. References

[1] R. Reed, The Superalloys: Fundamentals and Applications, Cambridge: Cambridge University Press, 2006.

[2] C. Lee, "Precipitation-Hardening Characteristics of Ternary Cobalt-Aluminum-x Alloys," PhD dissertation, The University of Arizona, 1971.

[3] C. Sims, "Superalloys: Genesis and Character," in *Superalloys II: High-Temperature Materials for Aerospace and Industrial Power*, New York, Wiley, 1987, pp. 3-26.

[4] N. Stoloff, "Fundamentals of Strengthening," in *Superalloys II: High-Temperature Materials for Aerospace and Industrial Power*, New York, Wiley, 1987, pp. 61-96.

[5] B. Geddes, H. Leon and X. Huang, Superalloys: Alloying and Performance, Ohio: ASM International, 2010.

[6] R. Decker, "The Evolution of Wrought Age-Hardenable Superalloys," *JOM*, pp. 32-36, 2006.

[7] A. Jena and M. Chaturvedi, "Review: The Role of Alloying Elements in the Design of Nickel-Base Superalloys," *Journal of Materials Science*, vol. 19, pp. 3121-3139, 1984.

[8] C. Sims, "Prediction of Phase Composition," in *Superalloys II: High-Temperature Materials for Aerospace and Industrial Power*, New York, Wiley, 1987, pp. 217-240.

[9] J. Belan, "GCP and TCP Phases Presented in Nickel-Base Superalloys," *Materials Today: Proceedings*, vol. 3, pp. 936-941, 2016.

[10] W. Betteridge and J. Heslop, The Nimonic Alloys and Other Nickel-Base High-Temperature Alloys, London: Edward Arnold, 1974.

[11] E. Ross and C. Sims, "Nickel-Base Alloys," in *Superalloys II: High-Temperature Materials for Aerospace and Industrial Power*, New York, Wiley, 1987, pp. 97-133.

[12] R. Decker, "Strengthening Mechanisms in Nickel-Base Superalloys," in *Steel Strengthening Mechanisms Symposium*, Zurich, 1969.

[13] G. Stoeckinger and J. Neumann, "Determination of the Order in the Intermetallic Phase Ni_3Al as a Function of Temperature," *Journal of Applied Crystallography*, vol. 3, pp. 32-38, 1970.

[14] F. Bremer, M. Beyss, E. Karthaus, A. Hellwig, T. Schober, J. Welter and H. Wenzl, "Experimental Analysis of the Ni-Al Phase Diagram," *Journal of Crystal Growth*, vol. 87, pp. 185-192, 1988.

[15] I. Ansara, N. Dupin, H. Lukas and B. Sundman, Ni-Al Phase Diagram, ASM Alloy Phase Diagrams Database, P. Villars, editor-in-chief, H. Okamoto and K. Cenzual,

section editors: http://www.asminternational.org, ASM International, Materials Park, OH, 2016.

[16] D. Hull and D. Bacon, Introduction to Dislocations, Oxford: Butterworth-Heinemann, 2011.

[17] D. Pope and S. Ezz, "Mechanical Properties of Ni_3Al and Nickel-Base Alloys with High Volume fraction of γ'," *International Metals Reviews,* vol. 29, no. 3, pp. 136-167, 1984.

[18] A. Vattre, B. Devincre and A. Roos, "Dislocation Dynamics Simulations of Precipitation Hardening in Ni-Based Superalloys with high γ' volume fraction," *Intermetallics,* vol. 17, pp. 988-994, 2009.

[19] R. Taunt and B. Ralph, "Observations of the Fine Structure of Superdislocations in Ni_3Al by Field-Ion Microscopy," *Philosophical Magazine,* vol. 30, no. 6, pp. 1379-1394, 1974.

[20] P. Thornton, R. Davies and T. Johnston, "The Temperature Dependence of the Flow Stress of the γ' Phase Based Upon Ni_3Al," *Metallurgical Transactions,* vol. 1, pp. 207-218, 1970.

[21] P. Hirsch, "A Model of the Anomalous Yield Stress for (111) Slip in $L1_2$ Alloys," *Progress in Materials Science,* vol. 36, pp. 63-88, 1992.

[22] B. Kear, "Dislocation Configurations and Work Hardening in Cu_3Au Crystals," *Acta Metallurgica,* vol. 12, pp. 555-569, 1964.

[23] V. Paidar, D. Pope and V. Vitek, "A Theory of the Anomalous Yield Behavior in $L1_2$ Ordered Alloys," *Acta Metallurgica,* vol. 32, no. 3, pp. 435-448, 1984.

[24] B. Kear and H. Wilsdorf, "Dislocation Configurations in Plastically Deformed Polycrystalline Cu_3Au Alloys," *Transactions of the Metallurgical Society of AIME,* vol. 224, pp. 382-386, 1962.

[25] K. Hemker and M. Mills, "Measurements of Antiphase Boundary and Complex Stacking Fault Energies in Binary and B-Doped Ni_3Al using TEM," *Philosophical Magazine A,* vol. 68, no. 2, pp. 305-324, 1993.

[26] A. Staton-Bevan and R. Rawlings, "The Deformation Behaviour of Single-Crystal Ni_3(Al,Ti)," *Physica Status Solidi (a),* vol. 29, pp. 613-622, 1975.

[27] N. Baluc, R. Schaublin and K. Hemker, "Methods for Determining Precise Values of Antiphase Boundary Energies in Ni_3Al," *Philosophical Magazine Letters,* vol. 64, no. 5, pp. 327-334, 1991.

[28] X. Yu and C. Wang, "Effect of Alloying Element on Dislocation Cross-Slip in γ'-Ni_3Al: A First-Principles Study," *Philosophical Magazine,* vol. 92, no. 32, pp. 4028-4039, 2012.

[29] T. Gibbons and B. Hopkins, "Creep Behaviour and Microstructure of Ni-Cr Base Alloys," *Metal Science,* vol. 18, no. 5, pp. 273-280, 1984.

[30] M. Hardy, B. Zirbel, G. Shen and R. Shankar, "Developing Damage Tolerance and Creep Resistance in a High Strength Nickel Alloy for Disc Applications," in *Superalloys 2004, TMS*, Pennsylvania, 2004.

[31] T. Murakumo, Y. Koizumi, K. Kobayashi and H. Harada, "Creep Strength of Ni-Base Single-Crystal Superalloys on the γ/γ' Tie-Line," in *Superalloys 2004, TMS*, Pennsylvania, 2004.

[32] R. Kozar, A. Suzuki, W. Milligan, J. Schirra, M. Savage and T. Pollock, "Strengthening Mechanisms in Polycrystalline Multimodal Nickel-Base Superalloys," *Metallurgical and Materials Transactions A,* vol. 40A, pp. 1588-1603, 2009.

[33] D. Collins and H. Stone, "A Modelling Approach to Yield Strength Optimisation in a Nickel-Base Superalloy," *International Journal of Plasticity,* vol. 54, pp. 96-112, 2014.

[34] B. Reppich, "Some New Aspects Concerning Particle Hardening Mechanisms in γ' Precipitating Ni-Base Alloys - I. Theoretical Concept," *Acta Metallurgica,* vol. 30, pp. 87-94, 1982.

[35] B. Reppich, P. Schepp and G. Wehner, "Some New Aspects Concerning Particle Hardening Mechanisms in γ' Precipitating Nickel-Base Alloys - II. Experiments," *Acta Metallurgica,* vol. 30, pp. 95-104, 1982.

[36] R. Mitchell, M. Hardy, M. Preuss and S. Tin, "Development of γ' Morphology in P/M Rotor Disc Alloys During Heat Treatment," in *Superalloys 2004, TMS*, Pennsylvania, 2004.

[37] M. Jackson and R. Reed, "Heat Treatment of UDIMET 720Li: The Effect of Microstructure on Properties," *Materials Science and Engineering A,* vol. 259, pp. 85-97, 1999.

[38] E. Galindo-Nava, L. Connor and C. Rae, "On the Prediction of the Yield Stress of Unimodal and Multimodal γ' Nickel-Base Superalloys," *Acta Materialia,* vol. 98, pp. 377-390, 2015.

[39] H. Li, J. Sun, M. Hardy, H. Evans, S. Williams, T. Doel and P. Bowen, "Effects of Microstructure on High Temperature Dwell Fatigue Crack Growth in a Coarse Grain PM Nickel Based Superalloy," *Acta Materialia,* vol. 90, pp. 355-369, 2015.

[40] R. Ricks, A. Porter and R. Ecob, "The Growth of γ' Precipitates in Nickel-Base Superalloys," *Acta Metallurgica,* vol. 31, pp. 43-53, 1983.

[41] T. Pollock and S. Tin, "Nickel-Based Superalloys for Advanced Turbine Engines: Chemistry, Microstructure and Properties," *Journal of Propulsion and Power,* vol. 22, no. 2, pp. 361-374, 2006.

[42] V. Gerold and H. Haberkorn, "On the Critical Resolved Shear Stress of Solid Solutions Containing Coherent Precipitates," *Physica Status Solidi (b),* vol. 16, no. 2, pp. 675-684, 1966.

[43] A. Porter, R. Ecob and R. Ricks, "Coherency Strain Fields: Magnitude and Symmetry," *Journal of Microscopy,* vol. 129, no. 3, pp. 327-336, 1983.

[44] A. Ardell and R. Nicholson, "The Coarsening of γ' in Ni-Al Alloys," *Journal of Physics and Chemistry of Solids,* vol. 27, pp. 1793-1804, 1966.

[45] D. Grose and G. Ansell, "The Influence of Coherency Strain on the Elevated Temperature Tensile Behavior of Ni-15Cr-Al-Ti-Mo Alloys," *Metallurgical Transactions A,* vol. 12A, pp. 1631-1645, 1981.

[46] S. Floreen, "Mechanical Behaviour," in *Superalloys II: High-Temperature Materials for Aerospace and Industrial Power,* New York, Wiley, 1987, pp. 241-262.

[47] R. Mitchell, M. Preuss, M. Hardy and S. Tin, "Influence of Composition and Cooling Rate on Constrained and Unconstrained Lattice Parameters in Advanced Polycrystalline Nickel-base Superalloys," *Materials Science and Engineering A,* vol. 423, pp. 282-291, 2006.

[48] R. Mitchell and M. Preuss, "Inter-Relationships between Composition, γ' Morphology, Hardness, and γ-γ' Mismatch in Advanced Polycrystalline Nickel-Base Superalloys during Aging at 800°C," *Metallurgical and Materials Transactions A,* vol. 38A, pp. 615-627, 2007.

[49] R. Mitchell, M. Preuss, S. Tin and M. Hardy, "The Influence of Cooling Rate from Temperatures Above the γ' Solvus on Morphology, Mismatch and Hardness in Advanced Polycrystalline Nickel-base Superalloys," *Materials Science and Engineering A,* vol. 473, pp. 158-165, 2008.

[50] P. Nash, Phase Diagrams of Binary Nickel Alloys, Ohio: ASM International, 1991.

[51] Y. Mishima, S. Ochiai, N. Hamao, M. Yodogawa and T. Suzuki, "Solid Solution Hardening of Ni_3Al with Ternary Additions," *Transactions of the Japan Institute of Metals,* vol. 27, no. 9, pp. 648-655, 1986.

[52] Y. Mishima, S. Ochiai, N. Hamao, M. Yodogawa and T. Suzuki, "Solid Solution Hardening of Nickel - Role of Transition Metal and B-Subgroup Solutes," *Transactions of the Japan Institute of Metals,* vol. 27, no. 9, pp. 656-664, 1986.

[53] H. Rehman, Solid Solution Strengthening and Diffusion in Nickel- and Cobalt-Based Superalloys, Erlangen: FAU University Press, 2016.

[54] W. Callister and D. Rethwisch, Fundamentals of Materials Science and Engineering: An Integrated Approach, Third Edition, Asia: Wiley, 2008.

[55] P. Kotval, "The Microstructure of Superalloys," *Metallography,* vol. 1, pp. 251-285, 1969.

[56] S. Hong and C. Laird, "Mechanisms of Slip Mode Modification in F.C.C. Solid Solutions," *Acta Metallurgica et Materialia,* vol. 38, no. 8, pp. 1581-1594, 1990.

[57] F. Mohamed and T. Langdon, "The Transition from Dislocation Climb to Viscous Glide in Creep of Solid Solution Alloys," *Acta Metallurgica,* vol. 22, pp. 779-788, 1974.

[58] P. Gallagher, "The Influence of Alloying, Temperature, and Related Effects on the Stacking Fault Energy," *Metallurgical Transactions,* vol. 1, pp. 2429-2461, 1970.

[59] C. Tian, G. Han, C. Cui and X. Sun, "Effects of Stacking Fault Energy on the Creep Behaviors of Ni-Base Superalloy," *Materials and Design,* vol. 64, pp. 316-323, 2014.

[60] R. Dreshfield, "Estimation of Gamma Phase Composition in Nickel-Base Superalloys (Based on Geometric Analysis of a Four-Component Phase Diagram)," NASA Technical Note, Lewis Research Center, Cleveland, Ohio, 1970.

[61] M. McLean, G. Webster, F. Nabarro and A. Cottrell, "Nickel-Base Superalloys: Current Status and Potential [and Discussion]," *Philosophical Transactions of the Royal Society A,* vol. 351, pp. 419-433, 1995.

[62] P. Bagot, O. Silk, J. Douglas, S. Pedrazzini, D. Crudden, T. Martin, M. Hardy, M. Moody and R. Reed, "An Atom Probe Tomography Study of Site Preference and Partitioning in a Nickel-Based Superalloy," *Acta Materialia,* vol. 125, pp. 156-165, 2017.

[63] J. Chen, P. Rogers and J. Little, "Oxidation Behavior of Several Chromia-Forming Commercial Nickel-Base Superalloys," *Oxidation of Metals,* vol. 47, no. 5/6, pp. 381-410, 1997.

[64] F. Stott, "Influence of Alloy Additions on Oxidation," *Materials Science and Technology,* vol. 5, pp. 734-740, 1989.

[65] B. Gleeson and M. Harper, "The Long-Term, Cyclic-Oxidation Behavior of Selected Chromia-Forming Alloys," *Oxidation of Metals,* vol. 49, no. 3/4, pp. 373-399, 1998.

[66] M. Chaudhari, J. Tiley, R. Banerjee and J. Du, "Site Preference and Interaction Energies of Co and Cr in Gamma Prime Ni_3Al: A First-Principles Study," *Modelling and Simulation in Materials Science and Engineering,* vol. 21, pp. 1-20, 2013.

[67] R. Rawlings and A. Staton-Bevan, "The Alloying Behaviour and Mechanical Properties of Polycrystalline Ni_3Al (γ' Phase) with Ternary Additions," *Journal of Materials Science,* vol. 10, pp. 505-514, 1975.

[68] O. Gorbatov, I. Lomaev, Y. Gornostyrev, A. Ruban, D. Furrer, V. Venkatesh, D. Novikov and S. Burlatsky, "Effect of Composition on Antiphase Boundary Energy in

Ni_3Al Based Alloys: Ab initio Calculations," *Physical Review B,* vol. 93, pp. 1-8, 2016.

[69] R. Mitchell, C. Rae and S. Tin, "Grain Boundary Transformations During Isothermal Exposure of Powder Metallurgy Nickel Base Superalloys for Turbine Disc Applications," *Materials Science and Technology,* vol. 21, no. 1, pp. 125-132, 2005.

[70] K. Owusu-Boahen, M. Bamberger, S. Dirnfeld, B. Prinz and J. Klodt, "Precipitation Hardening in Nickel Based Superalloys: Effect of Alloying," *Materials Science and Technology,* vol. 12, pp. 290-294, 1996.

[71] C. Giggins and F. Pettit, "Oxidation of Ni-Cr-Al Alloys Between 1000° and 1200°C," *Journal of The Electrochemical Society,* vol. 118, no. 11, pp. 1782-1790, 1971.

[72] J. Smialek and G. Meier, "High-Temperature Oxidation," in *Superalloys II: High-Temperature Materials for Aerospace and Industrial Power,* New York, Wiley, 1987, pp. 293-326.

[73] N. Birks, G. Meier and F. Pettit, Introduction to the High-Temperature Oxidation of Metals, 2nd Edition, New York: Cambridge University Press, 2006.

[74] M. Pandey and D. Satyanarayana, "Effect of Gamma Prime Depletion on Creep Behaviour of a Nickel Base Superalloy (Inconel Alloy X-750)," *Bulletin of Materials Science,* vol. 19, no. 6, pp. 1009-1015, 1996.

[75] C. Lund and H. Wagner, "Oxidation of Nickel- and Cobalt-Base Superalloys," Defense Metals Information Center, Columbus, Ohio, 1965.

[76] S. Cruchley, M. Taylor, H. Evans, M. Hardy and D. Child, "Characterisation of Subsurface Oxidation Damage in Ni Based Superalloy, RR1000," *Materials Science and Technology,* vol. 30, no. 15, pp. 1884-1889, 2014.

[77] S. Cruchley, H. Evans, M. Taylor, M. Hardy and S. Stekovic, "Chromia Layer Growth on a Ni-Based Superalloy: Sub-Parabolic Kinetics and the Role of Titanium," *Corrosion Science,* vol. 75, pp. 58-66, 2013.

[78] R. Dreshfield and J. Wallace, "The Gamma-Gamma Prime Region of the Ni-Al-Cr-Ti-W-Mo System at 850°C," *Metallurgical Transactions,* vol. 5, pp. 71-78, 1974.

[79] A. Oni, S. Broderick, K. Rajan and J. LeBeau, "Atom Site Preference and γ'/γ Mismatch Strain in Ni-Al-Co-Ti Superalloys," *Intermetallics,* vol. 73, pp. 72-78, 2016.

[80] W. Loomis, J. Freeman and D. Sponseller, "The Influence of Molybdenum on the γ' Phase in Experimental Nickel-Base Superalloys," *Metallurgical Transactions,* vol. 3, pp. 989-1000, 1972.

[81] J. Heslop, "Wrought Nickel-Chromium Heat-Resisting Alloys Containing Cobalt," *Cobalt,* vol. 24, pp. 128-137, 1964.

[82] Y. Mishima, S. Ochiai and T. Suzuki, "Lattice parameters of Ni (γ), Ni_3Al (γ') and Ni_3Ga (γ') Solid Solutions with Additions of Transition and B-Subgroup Elements," *Acta Metallurgica,* vol. 33, no. 6, pp. 1161-1169, 1985.

[83] G. Bouse, "Eta (η) and Platelet Phases in Investment Cast Superalloys," in *Superalloys 1996, TMS,* Pennsylvania, 1996.

[84] K. Povarova, A. Antonova, B. Burmistrov and O. Skachkov, Al-Ni-Ti Phase Diagram, ASM Alloy Phase Diagrams Database, P. Villars, editor-in-chief, H. Okamoto and K. Cenzual, section editors: http://www.asminternational.org, ASM International, Materials Park, OH, 2016.

[85] H. Nagai and M. Okabayashi, "Deleterious Effect of Ti Addition on the Oxidation Resistance of Ni-20Cr Alloy," *Transactions of the Japan Institute of Metals,* vol. 22, no. 10, pp. 691-698, 1981.

[86] Y. Yuan, Y. Gu, C. Cui, T. Osada, Z. Zhong, T. Tetsui, T. Yokokawa and H. Harada, "Influence of Co Content on Stacking Fault Energy in Ni-Co Base Disk Superalloys," *Journal of Materials Research,* vol. 26, no. 22, pp. 2833-2837, 2011.

[87] R. Jarrett and J. Tien, "Effects of Cobalt on Structure, Microchemistry and Properties of a Wrought Nickel-Base Superalloy," *Metallurgical Transactions A,* vol. 13A, pp. 1021-1032, 1982.

[88] Y. Gu, C. Cui, D. Ping, H. Harada, T. Fukuda and J. Fujioka, "Creep Behavior of New Kinds of Ni-Co-Base Superalloys," *Materials Science and Engineering A,* Vols. 510-511, pp. 250-255, 2009.

[89] J. Tien and R. Jarett, "Effects of Cobalt in Nickel-Base Superalloys," NASA Lewis Reseach Center, New York, 1983.

[90] G. Maurer, L. Jackman and J. Domingue, "Role of Cobalt in Waspaloy," in *Superalloys 1980, TMS,* Pennsylvania, 1980.

[91] M. Nathal, R. Maier and L. Ebert, "The Influence of Cobalt on the Tensile and Stress-Rupture Properties of the Nickel-Base Superalloy MAR-M247," *Metallurgical Transactions A,* vol. 13A, pp. 1767-1774, 1982.

[92] J. Donaldson and S. Clark, Cobalt in Superalloys, The Monograph Series, The Cobalt Development Institute, 1985.

[93] A. Janotti, M. Krcmar, C. Fu and R. Reed, "Solute Diffusion in Metals: Larger Atoms Can Move Faster," *Physical Review Letters,* vol. 92, no. 8, pp. 1-4, 2004.

[94] S. Liu, M. Wen, Z. Li, W. Liu, P. Yan and C. Wang, "Partitioning and Diffusion of Transition Metal Solutes in Ternary Model Ni-Based Single Crystal Superalloys," *Materials & Design,* vol. 130, pp. 157-165, 2017.

[95] S. Shang, C. Zacherl, H. Fang, Y. Wang, Y. Du and Z. Liu, "Effects of Alloying Element and Temperature on the Stacking Fault Energies of Dilute Ni-Base Superalloys," *Journal of Physics: Condensed Matter*, vol. 24, pp. 1-14, 2012.

[96] M. Durand-Charre, The Microstructure of Superalloys, London: CRC Press, 1997.

[97] M. Chandran and S. Sondhi, "First-Principle Calculation of APB Energy in Ni-Based Binary and Ternary Alloys," *Modelling and Simulation in Materials Science and Engineering,* vol. 19, pp. 1-7, 2011.

[98] R. Holt and W. Wallace, "Impurities and Trace Elements in Nickel-Base Superalloys," *International Metals Reviews,* vol. 21, no. 1, pp. 1-24, 1976.

[99] P. Mignanelli, N. Jones, M. Hardy and H. Stone, "The Influence of Al:Nb Ratio on the Microstructure and Mechanical Response of Quaternary Ni-Cr-Al-Nb Alloys," *Materials Science & Engineering A,* vol. 612, pp. 179-186, 2014.

[100] R. Cozar and A. Pineau, "Morphology of γ' and γ" Precipitates and Thermal Stability of Inconel 718 Type Alloys," *Metallurgical Transactions,* vol. 4, pp. 47-59, 1973.

[101] M. Dehmas, J. Lacaze, A. Niang and B. Viguier, "TEM Study of High-Temperature Precipitation of Delta Phase in Inconel 718 Alloy," *Advances in Materials Science and Engineering,* pp. 1-9, 2011.

[102] A. Sinha, "Topologically Close-Packed Structures of Transition Metal Alloys," *Progress in Materials Science,* vol. 15, no. 2, pp. 81-185, 1972.

[103] C. Rae and R. Reed, "The Precipitation of Topologically Close-Packed Phases in Rhenium-Containing Superalloys," *Acta Materialia,* vol. 49, pp. 4113-4125, 2001.

[104] F. Frank and J. Kasper, "Complex Alloy Structures Regarded as Sphere Packings. I. Definitions and Basic Principles," *Acta Crystallographica,* vol. 11, pp. 184-190, 1958.

[105] R. Darolia, D. Lahrman and R. Field, "Formation of Topologically Closed Packed Phases in Nickel Base Single Crystal Superalloys," in *Superalloys 1988, TMS*, Pennsylvania, 1988.

[106] P. Keefe, S. Mancuso and G. Maurer, "Effects of Heat Treatment and Chemistry on the Long-Term Phase Stability of a High Strength Nickel-Based Superalloy," in *Superalloys 1992, TMS*, Pennsylvania, 1992.

[107] F. Stott, "The Protective Action of Oxide Scales in Gaseous Environments at High Temperature," *Reports on Progress in Physics,* vol. 50, pp. 861-913, 1987.

[108] C. Tedmon, "The Effect of Oxide Volatilization on the Oxidation Kinetics of Cr and Fe-Cr Alloys," *Journal of The Electrochemical Society,* vol. 113, no. 8, pp. 766-768, 1966.

[109] C. Sullivan, M. Donachie and F. Morral, Cobalt-base Superalloys - 1970, Cobalt Monograph Series, London: Cobalt Information Centre, 1970.

[110] D. Coutsouradis, A. Davin and M. Lamberigts, "Cobalt-based Superalloys for Applications in Gas Turbines," *Materials Science and Engineering,* vol. 88, pp. 11-19, 1987.

[111] A. Beltran, "Cobalt-Base Alloys," in *Superalloys II: High-Temperature Materials for Aerospace and Industrial Power,* New York, Wiley, 1987, pp. 135-163.

[112] A. Beltran, "The Oxidation and Hot-Corrosion Resistance of Cobalt-Base Superalloys," *Cobalt,* vol. 46, pp. 3-14, 1970.

[113] D. Klarstrom, "Wrought Cobalt-base Superalloys," *Journal of Materials Engineering and Performance,* vol. 2, no. 4, pp. 523-530, 1993.

[114] H. Ohtani, M. Yamano and M. Hasebe, Co-Al Phase Diagram, ASM Alloy Phase Diagrams Database, P. Villars, editor-in-chief, H. Okamoto and K. Cenzual, section editors: http://www.asminternational.org, ASM International, Materials Park, OH, 2016.

[115] M. Korchynsky and R. Fountain, "Precipitation Phenomena in Cobalt-Tantalum Alloys," *Transactions of the Metallurgical Society of AIME,* vol. 215, pp. 1033-1043, 1959.

[116] J. Blaise, P. Viatour and J. Drapier, "On the Stability and Precipitation of the Co_3Ti Phase in Co-Ti Alloys," *Cobalt,* vol. 49, pp. 192-195, 1970.

[117] P. Viatour, J. Drapier and D. Coutsouradis, "Stability of the γ'-Co_3Ti Compound in Simple and Complex Cobalt Alloys," *Cobalt,* vol. 3, pp. 67-74, 1973.

[118] S. Neumeier, L. Freund and M. Goken, "Novel Wrought γ/γ' Cobalt Base Superalloys with High Strength and Improved Oxidation Resistance," *Scripta Materialia,* vol. 109, pp. 104-107, 2015.

[119] Y. Liu, T. Takasugi and O. Izumi, "Alloying Behavior of Co_3Ti," *Metallurgical Transactions A,* vol. 17A, pp. 1433-1439, 1986.

[120] J. Sato, T. Omori, K. Oikawa, I. Ohnuma, R. Kainuma and K. Ishida, "Cobalt-Base High-Temperature Alloys," *Science,* vol. 312, pp. 90-91, 2006.

[121] S. Kobayashi, Y. Tsukamoto, T. Takasugi, H. Chinen, T. Omori, K. Ishida and S. Zaefferer, "Determination of Phase Equilibria in the Co-rich Co-Al-W Ternary System with a Diffusion-Couple Technique," *Intermetallics,* vol. 17, pp. 1085-1089, 2009.

[122] A. Suzuki, H. Inui and T. Pollock, "$L1_2$-Strengthened Cobalt-Base Superalloys," *Annual Review of Materials Research,* vol. 45, pp. 345-368, 2015.

[123] J. Sato, K. Oikawa, R. Kainuma and K. Ishida, "Experimental Verification of Magnetically Induced Phase Separation in αCo Phase and Thermodynamic

Calculations of Phase Equilibria in the Co-W System," *Materials Transactions, The Japan Institute of Metals,* vol. 46, no. 6, pp. 1199-1207, 2005.

[124] T. Omori, K. Oikawa, J. Sato, I. Ohnuma, U. Kattner, R. Kainuma and K. Ishida, "Partition Behavior of Alloying Elements and Phase Transformation Temperatures in Co-Al-W-base Quaternary Systems," *Intermetallics,* vol. 32, pp. 274-283, 2013.

[125] H. Yan, V. Vorontsov and D. Dye, "Alloying Effects in Polycrystalline γ' Strengthened Co-Al-W Base Alloys," *Intermetallics,* vol. 48, pp. 44-53, 2014.

[126] I. Povstugar, P. Choi, S. Neumeier, A. Bauer, C. Zenk, M. Goken and D. Raabe, "Elemental Partitioning and Mechanical Properties of Ti- and Ta-containing Co-Al-W-base Superalloys Studied by Atom Probe Tomography and Nanoindentation," *Acta Materialia,* vol. 78, pp. 78-85, 2014.

[127] K. Shinagawa, T. Omori, J. Sato, K. Oikawa, I. Ohnuma, R. Kainuma and K. Ishida, "Phase Equilibria and Microstructure on γ' Phase in Co-Ni-Al-W System," *The Japan Institute of Metals, Materials Transactions,* vol. 49, no. 6, pp. 1474-1479, 2008.

[128] J. Zhu, M. Titus and T. Pollock, "Experimental Investigation and Thermodynamic Modeling of the Co-Rich Region in the Co-Al-Ni-W Quaternary System," *Journal of Phase Equilibria and Diffusion,* vol. 35, no. 5, pp. 595-611, 2014.

[129] A. Suzuki, G. DeNolf and T. Pollock, "Flow Stress Anomalies in γ/γ' Two-phase Co-Al-W-base Alloys," *Scripta Materialia,* vol. 56, pp. 385-388, 2007.

[130] A. Suzuki and T. Pollock, "High-temperature Strength and Deformation of γ/γ' Two-phase Co-Al-W-base Alloys," *Acta Materialia,* vol. 56, pp. 1288-1297, 2008.

[131] T. Gabb and R. Dreshfield, "Superalloy Data," in *Superalloys II: High-Temperature Materials for Aerospace and Industrial Power,* New York, Wiley, 1987, pp. 575-597.

[132] N. Okamoto, T. Oohashi, H. Adachi, K. Kishida, H. Inui and P. Veyssiere, "Plastic Deformation of Polycrystals of $Co_3(Al,W)$ with the $L1_2$ Structure," *Philosophical Magazine,* vol. 91, no. 28, pp. 3667-3684, 2011.

[133] Y. Oya-Seimiya, T. Shinoda and T. Suzuki, "Low Temperature Strength Anomaly of $L1_2$ Type Intermetallic Compounds Co_3Ti and Pt_3Al," *Materials Transactions,* vol. 37, no. 9, pp. 1464-1470, 1996.

[134] R. Mulford and D. Pope, "The Yield Stress of $Ni_3(Al,W)$," *Acta Metallurgica,* vol. 21, pp. 1375-1380, 1973.

[135] F. Xue, H. Zhou, X. Ding, M. Wang and Q. Feng, "Improved High Temperature γ' Stability of Co-Al-W-base Alloys Containing Ti and Ta," *Materials Letters,* vol. 112, pp. 215-218, 2013.

[136] H. Zhou, W. Li, F. Xue, L. Zhang, X. Qu and Q. Feng, "Alloying Effects on Microstructural Stability and γ' Phase Nano-hardness in Co-Al-W-Ta-Ti-base Superalloys," in *Superalloys 2016*, *TMS*, Pennsylvania, 2016.

[137] E. Lass, "Application of Computational Thermodynamics to the Design of a Co-Ni-Based γ'-Strengthened Superalloy," *Metallurgical and Materials Transactions A,* vol. 48A, pp. 2443-2459, 2017.

[138] F. Pyczak, A. Bauer, M. Goken, U. Lorenz, S. Neumeier, M. Oehring, J. Paul, N. Schell, A. Schreyer, A. Stark and F. Symanzik, "The Effect of Tungsten Content on the Properties of $L1_2$-hardened Co-Al-W Alloys," *Journal of Alloys and Compounds,* vol. 632, pp. 110-115, 2015.

[139] M. Knop, P. Mulvey, F. Ismail, A. Radecka, K. Rahman, T. Lindley, B. Shollock, M. Hardy, M. Moody, T. Martin, P. Bagot and D. Dye, "A New Polycrystalline Co-Ni Superalloy," *Journal of The Minerals, Metals and Materials Society,* vol. 66, no. 12, pp. 2495-2501, 2014.

[140] S. Makineni, B. Nithin and K. Chattopadhyay, "Synthesis of a New Tungsten-free γ-γ' Cobalt-based Superalloy by Tuning Alloying Additions," *Acta Materialia,* vol. 85, pp. 85-94, 2015.

[141] S. Makineni, A. Samanta, T. Rojhirunsakool, T. Alam, B. Nithin, A. Singh, R. Banerjee and K. Chattopadhyay, "A New Class of High Strength High Temperature Cobalt Based γ-γ' Co-Mo-Al Alloys Stabilized with Ta Addition," *Acta Materialia,* vol. 97, pp. 29-40, 2015.

[142] B. Nithin, A. Samanta, S. Makineni, T. Alam, P. Pandey, A. Singh, R. Banerjee and K. Chattopadhyay, "Effect of Cr Addition on γ-γ' Cobalt-based Co-Mo-Al-Ta Class of Superalloys: A Combined Experimental and Computational Study," *Journal of Materials Science,* vol. 52, pp. 11036-11047, 2017.

[143] E. Lass, D. Sauza, D. Dunand and D. Seidman, "Multicomponent γ'-strengthened Co-based Superalloys with Increased Solvus Temperatures and Reduced Mass Densities," *Acta Materialia,* vol. 147, pp. 284-295, 2018.

[144] M. Ooshima, K. Tanaka, N. Okamoto, K. Kishida and H. Inui, "Effects of Quaternary Alloying Elements on the γ' Solvus Temperature of Co-Al-W Based Alloys with fcc/$L1_2$ Two-Phase Microstructures," *Journal of Alloys and Compounds,* vol. 508, pp. 71-78, 2010.

[145] P. Bocchini, C. Sudbrack, D. Sauza, R. Noebe, D. Seidman and D. Dunand, "Effect of Tungsten Concentration on Microstructures of Co-10Ni-6Al-(0,2,4,6)W-6Ti (at%) Cobalt-based Superalloys," *Materials Science and Engineering A,* vol. 700, pp. 481-486, 2017.

[146] P. Bocchini, C. Sudbrack, R. Noebe, D. Dunand and D. Seidman, "Effects of Titanium Substitutions for Aluminum and Tungsten in Co-10Ni-9Al-9W (at%) Superalloys," *Materials Science and Engineering A,* vol. 705, pp. 122-132, 2017.

[147] P. Pandey, S. Makineni, A. Samanta, A. Sharma, S. Das, B. Nithin, C. Srivastava, A. Singh, D. Raabe, B. Gault and K. Chattopadhyay, "Elemental Site Occupancy in the $L1_2$ A_3B Ordered Intermetallic Phase in Co-based Superalloys and its Influence on the Microstructure," *Acta Materialia,* vol. 163, pp. 140-153, 2019.

[148] N. Jones, K. Christofidou, P. Mignanelli, J. Minshull, M. Hardy and H. Stone, "Influence of Elevated Co and Ti Levels on Polycrystalline Powder Processed Ni-base Superalloy," *Materials Science and Technology,* vol. 30, no. 15, pp. 1853-1861, 2014.

[149] C. Cui, Y. Gu, D. Ping, H. Harada and T. Fukuda, "The Evolution of η Phase in Ni-Co Base Superalloys," *Materials Science and Engineering A,* vol. 485, pp. 651-656, 2008.

[150] J. Murray, Co-Ti Phase Diagram, ASM Alloy Phase Diagrams Database, P. Villars, editor-in-chief, H. Okamoto and K. Cenzual, section editors: http://www.asminternational.org, ASM International, Materials Park, OH, 2016.

[151] P. Thornton and R. Davies, "The Temperature Dependence of the Flow Stress of Gamma Prime Phases Having the $L1_2$ Structure," *Metallurgical Transactions,* vol. 1, pp. 549-550, 1970.

[152] D. Wee, O. Noguchi, Y. Oya and T. Suzuki, "New $L1_2$ Ordered Alloys Having the Positive Temperature Dependence of Strength," *Materials Transactions, The Japan Institute of Metals,* vol. 21, pp. 237-247, 1980.

[153] P. Viatour, J. Drapier, D. Coutsouradis and L. Habraken, "Structure and Properties of CM-7, a Wrought Precipitation-Hardening Cobalt-Base Alloy," *Cobalt,* vol. 51, pp. 67-76, 1971.

[154] C. Cui, D. Ping, Y. Gu and H. Harada, "A New Co-Base Superalloy Strengthened by γ' Phase," *Materials Transactions, The Japan Institute of Metals,* vol. 47, no. 8, pp. 2099-2102, 2006.

[155] C. Cui, Y. Gu, D. Ping and H. Harada, "Phase Constituents in Ni-Al-Co-Ti Quaternary Alloys," *Intermetallics,* vol. 16, pp. 910-916, 2008.

[156] V. Raghavan, "Al-Co-Ni-Ti (Aluminum-Cobalt-Nickel-Titanium)," *Journal of Phase Equilibria and Diffusion,* vol. 30, no. 2, pp. 199-200, 2009.

[157] J. Minshull, S. Neumeier, M. Tucker and H. Stone, "A1-$L1_2$ Structures in the Al-Co-Ni-Ti Quaternary Phase System," *Advanced Materials Research,* vol. 278, pp. 399-404, 2011.

[158] C. Cui, Y. Gu, H. Harada and A. Sato, "Microstructure and Yield Strength of UDIMET 720LI Alloyed with Co-16.9 Wt Pct Ti," *Metallurgical and Materials Transactions A,* vol. 36A, pp. 2921-2927, 2005.

[159] Y. Gu, H. Harada, C. Cui, D. Ping, A. Sato and J. Fujioka, "New Ni-Co-base Disk Superalloys with Higher Strength and Creep Resistance," *Scripta Materialia,* vol. 55, pp. 815-818, 2006.

[160] K. Christofidou, N. Jones, E. Pickering, R. Flacau, M. Hardy and H. Stone, "The Microstructure and Hardness of Ni-Co-Al-Ti-Cr Quinary Alloys," *Journal of Alloys and Compounds,* vol. 688, pp. 542-552, 2016.

[161] Wavemetrics Igor Pro, [Online]. Available: https://www.wavemetrics.com/. [Accessed 23 March 2017].

[162] O. Hellman, J. Vandenbroucke, J. Rusing, D. Isheim and D. Seidman, "Analysis of Three-dimensional Atom-probe Data by the Proximity Histogram," *Microscopy and Microanalysis,* vol. 6, pp. 437-444, 2000.

[163] S. Meher, M. Carroll, T. Pollock and L. Carroll, "Designing Nickel Base Alloys for Microstructural Stability Through Low γ-γ' Interfacial Energy and Lattice Misfit," *Materials and Design,* vol. 140, pp. 249-256, 2018.

[164] D. Porter and K. Easterling, Phase Transformations in Metals and Alloys, 2nd Edition, Cheltenham: Nelson Thornes, 2001.

[165] I. Lifshitz and V. Slyozov, "The Kinetics of Precipitation from Supersaturated Solid Solutions," *Journal of Physics and Chemistry of Solids,* vol. 19, no. 1/2, pp. 35-50, 1961.

[166] C. Wagner, "Theorie der Alterung von Niederschlägen durch Umlösen (Ostwald-Reifung)," *Zeitschrift für Elektrochemie,* vol. 65, no. 7/8, pp. 581-591, 1961.

[167] H. Calderon, P. Voorhees, J. Murray and G. Kostorz, "Ostwald Ripening in Concentrated Alloys," *Acta Metallurgica et Materialia,* vol. 42, no. 3, pp. 991-1000, 1994.

[168] A. Baldan, "Progress in Ostwald Ripening Theories and their Applications to Nickel-base Superalloys, Part I: Ostwald Ripening Theories," *Journal of Materials Science,* vol. 37, pp. 2171-2202, 2002.

[169] A. Baldan, "Progress in Ostwald Ripening Theories and their Applications to the γ'-precipitates in Nickel-base Superalloys, Part II: Nickel-base Superalloys," *Journal of Materials Science,* vol. 37, pp. 2379-2405, 2002.

[170] T. Pollock and R. Field, "Chapter 63: Dislocations and High-Temperature Plastic Deformation of Superalloy Single Crystals," *Dislocations in Solids,* vol. 11, pp. 547-618, 2002.

[171] H. Mughrabi, "Microstructural Aspects of High Temperature Deformation of Monocrystalline Nickel Base Superalloys: Some Open Problems," *Materials Science and Technology,* vol. 25, no. 2, pp. 191-204, 2009.

[172] M. Nathal, R. Mackay and R. Garlick, "Temperature Dependence of γ-γ' Lattice Mismatch in Nickel-base Superalloys," *Materials Science and Engineering,* vol. 75, pp. 195-205, 1985.

[173] K. Tanaka, M. Ooshima, N. Tsuno, A. Sato and H. Inui, "Creep Deformation of Single Crystals of New Co-Al-W-based Alloys With fcc/$L1_2$ Two-phase Microstructures," *Philosophical Magazine,* vol. 92, no. 32, pp. 4011-4027, 2012.

[174] F. Pyczak, A. Bauer, M. Goken, S. Neumeier, U. Lorenz, M. Oehring, N. Schell, A. Schreyer, A. Stark and F. Symanzik, "Plastic Deformation Mechanisms in a Crept $L1_2$ Hardened Co-base Superalloy," *Materials Science and Engineering A,* vol. 571, pp. 13-18, 2013.

[175] H. Mughrabi, "The Importance of Sign and Magnitude of γ/γ' Lattice Misfit in Superalloys - With Special Reference to the New γ'-hardened Cobalt-base Superalloys," *Acta Materialia,* vol. 81, pp. 21-29, 2014.

[176] J. Svoboda and P. Lukáš, "Model of Creep in <001>-oriented Superalloy Single Crystals," *Acta Materialia,* vol. 46, no. 10, pp. 3421-3431, 1998.

[177] O. Arnold, J. Bilheux, J. Borreguero, A. Buts, S. Campbell, L. Chapon, M. Doucet, N. Draper, R. F. Leal, M. Gigg, V. Lynch, A. Markvardsen, D. Mikkelson, R. Mikkelson, R. Miller, K. Palmen, P. Parker, G. Passos and T. Perring et al., "Mantid - Data Analysis and Visualization Package for Neutron Scattering and μ SR Experiments," *Nuclear Instruments and Methods in Physics Research A,* vol. 764, pp. 156-166, 2014.

[178] A. Larson and R. VonDreele, "General Structure Analysis System (GSAS)," Los Alamos National Laboratory Report LAUR 86-748, 2004.

[179] A. LeBail, "Whole Powder Pattern Decomposition Methods and Applications: a Retrospection," *Powder Diffraction,* vol. 20, no. 4, pp. 316-326, 2005.

[180] C. Hammond, The Basics of Crystallography and Diffraction, 4th Edition, Oxford: Oxford University Press, 2015.

[181] P. Caron, "High γ' Solvus New Generation Nickel-based Superalloys for Single Crystal Turbine Blade Applications," in *Superalloys 2000, TMS,* Pennsylvania, 2000.

[182] C. Zenk, S. Neumeier, M. Kolb, N. Volz, S. Fries, O. Dolotko, I. Povstugar, D. Raabe and M. Goken, "The Role of the Base Element in γ' Strengthened Cobalt/Nickel-base Superalloys," in *Superalloys 2016, TMS,* Pennsylvania, 2016.

[183] R. Mueller and D. Gross, "3D Simulation of Equilibrium Morphologies of Precipitates," *Computational Materials Science,* vol. 11, pp. 35-44, 1998.

[184] R. Mueller and D. Gross, "3D Inhomogeneous, Misfitting Second Phase Particles - Equilibrium Shapes and Morphological Development," *Computational Materials Science,* vol. 16, pp. 53-60, 1999.

[185] M. Thompson and P. Voorhees, "Equilibrium Particle Morphologies in Elastically Stressed Coherent Solids," *Acta Materialia,* vol. 47, no. 3, pp. 983-996, 1999.

[186] X. Li, J. Lowengrub, Q. Nie, V. Cristini and P. Leo, "Microstructure Evolution in Three-Dimensional Inhomogeneous Elastic Media," *Metallurgical and Materials Transactions A,* vol. 34A, pp. 1421-1431, 2003.

[187] J. Zhu, T. Wang, A. Ardell, S. Zhou, Z. Liu and L. Chen, "Three-dimensional Phase-field Simulations of Coarsening Kinetics of γ' Particles in Binary Ni-Al Alloys," *Acta Materialia,* vol. 52, pp. 2837-2845, 2004.

[188] T. Wang, G. Sheng, Z. Liu and L. Chen, "Coarsening Kinetics of γ' Precipitates in the Ni-Al-Mo System," *Acta Materialia,* vol. 56, pp. 5544-5551, 2008.

[189] Y. Tsukada, Y. Murata, T. Koyama and M. Morinaga, "Phase-Field Simulation of the Effect of Elastic Inhomogeneity on Microstructure Evolution in Ni-Based Superalloys," *Materials Transactions, The Japan Institute of Metals,* vol. 50, no. 4, pp. 744-748, 2009.

[190] J. Kundin, L. Mushongera, T. Goehler and H. Emmerich, "Phase-field Modeling of the γ'-coarsening Behavior in Ni-based Superalloys," *Acta Materialia,* vol. 60, pp. 3758-3772, 2012.

[191] W. Johnson and J. Cahn, "Elastically Induced Shape Bifurcations of Inclusions," *Acta Metallurgica,* vol. 32, no. 11, pp. 1925-1933, 1984.

[192] X. Li, K. Thornton, Q. Nie, P. Voorhees and J. Lowengrub, "Two- and Three-Dimensional Equilibrium Morphology of a Misfitting Particle and the Gibbs-Thomson Effect," *Acta Materialia,* vol. 52, pp. 5829-5843, 2004.

[193] A. Jokisaari, S. Naghavi, C. Wolverton, P. Voorhees and O. Heinonen, "Predicting the Morphologies of γ' Precipitates in Cobalt-based Superalloys," *Acta Materialia,* vol. 141, pp. 273-284, 2017.

[194] P. Leo, J. Lowengrub and H. Jou, "A Diffuse Interface Model for Microstructural Evolution in Elastically Stressed Solids," *Acta Materialia,* vol. 46, no. 6, pp. 2113-2130, 1998.

[195] S. Meher, S. Nag, J. Tiley, A. Goel and R. Banerjee, "Coarsening Kinetics of γ' Precipitates in Cobalt-base Alloys," *Acta Materialia* , vol. 61, pp. 4266-4276, 2013.

[196] R. Prescott and M. Graham, "The Formation of Aluminum Oxide Scales on High-Temperature Alloys," *Oxidation of Metals,* vol. 38, no. 3/4, pp. 233-254, 1992.

[197] F. Pettit and G. Meier, "Oxidation and Hot Corrosion of Superalloys," in *Superalloys 1984, TMS*, Pennsylvania, 1984.

[198] D. Young, High Temperature Oxidation and Corrosion of Metals, Oxford: Elsevier, 2008.

[199] DIFFRAC.EVA, [Online]. Available: https://www.bruker.com/products/x-ray-diffraction-and-elemental-analysis/x-ray-diffraction/xrd-software/eva/overview.html . [Accessed 9 August 2019].

[200] Inorganic Crystal Structure Database (ICSD), [Online]. Available: https://icsd.psds.ac.uk/search/basic.xhtml . [Accessed 8 August 2019].

[201] G. Wood, "High-Temperature Oxidation of Alloys," *Oxidation of Metals,* vol. 2, no. 1, pp. 11-57, 1970.

[202] T. Pollock, J. Dibbern, M. Tsunekane, J. Zhu and A. Suzuki, "New Co-based γ-γ′ High-temperature Alloys," *Journal of the Minerals, Metals and Materials Society,* vol. 62, no. 1, pp. 58-63, 2010.

8. Appendix

8.1 Ni-free alloy Co-5Al-5Ti-15Cr (at.%) aged at 800°C for 1000 hours

The Ni-free alloy of the $(Ni,Co)_{75}Al_5Ti_5Cr_{15}$ (at.%) system, containing 75 at.% Co, was fabricated, homogenised (1250°C, 24 hours) and aged (800°C, 1000 hours) in the same way as the seven model superalloys investigated in Chapter 2. A specimen was cut from the aged Co-5Al-5Ti-15Cr (at.%) alloy bar, mounted in conductive Bakelite and prepared for metallographic examination by grinding using wet SiC abrasive paper. The specimen was then polished using progressively finer diamond suspensions down to 0.25 μm. Microstructural examination of the Ni-free alloy was performed using a ZEISS GeminiSEM 300 scanning electron microscope in back-scattered electron (BSE) mode. Energy dispersive X-ray spectroscopy (EDS) was performed using an Oxford Aztec EDS system to identify the overall alloy composition, which was obtained from 5 large area scans of at least 500 × 500 μm. The measured composition was found to be within ±1 at.% of its nominal composition. EDS elemental concentrations maps were also generated using the ZEISS GeminiSEM 300 microscope equipped with the Oxford Aztec EDS system.

An alloy specimen was prepared for atom probe tomography (APT) in the same way as for the seven model superalloys investigated in Chapter 2 (section 2.2.4). APT was performed to determine the compositions of phases within the Ni-free Co-5Al-5Ti-15Cr (at.%) alloy aged at 800°C (1000 hours). APT was carried out using the CAMECA local-electrode atom-probe (LEAP) 4000X instrument, with the same experimental parameters as before (section 2.2.4), at the Michigan Center for Materials Characterization in collaboration with the Marquis Research Group, Department of Materials Science and Engineering, University of Michigan.

Figure 8.1 shows a BSE micrograph of the Co-5Al-5Ti-15Cr (at.%) alloy following ageing at 800°C for 1000 hours, together with the corresponding EDS elemental concentration maps for Cr, Co, Ti and Al. The dark grey phase appears rich in Ti and Al whilst the pale grey phase appears rich in Cr. Co appears more evenly distributed between the two phases.

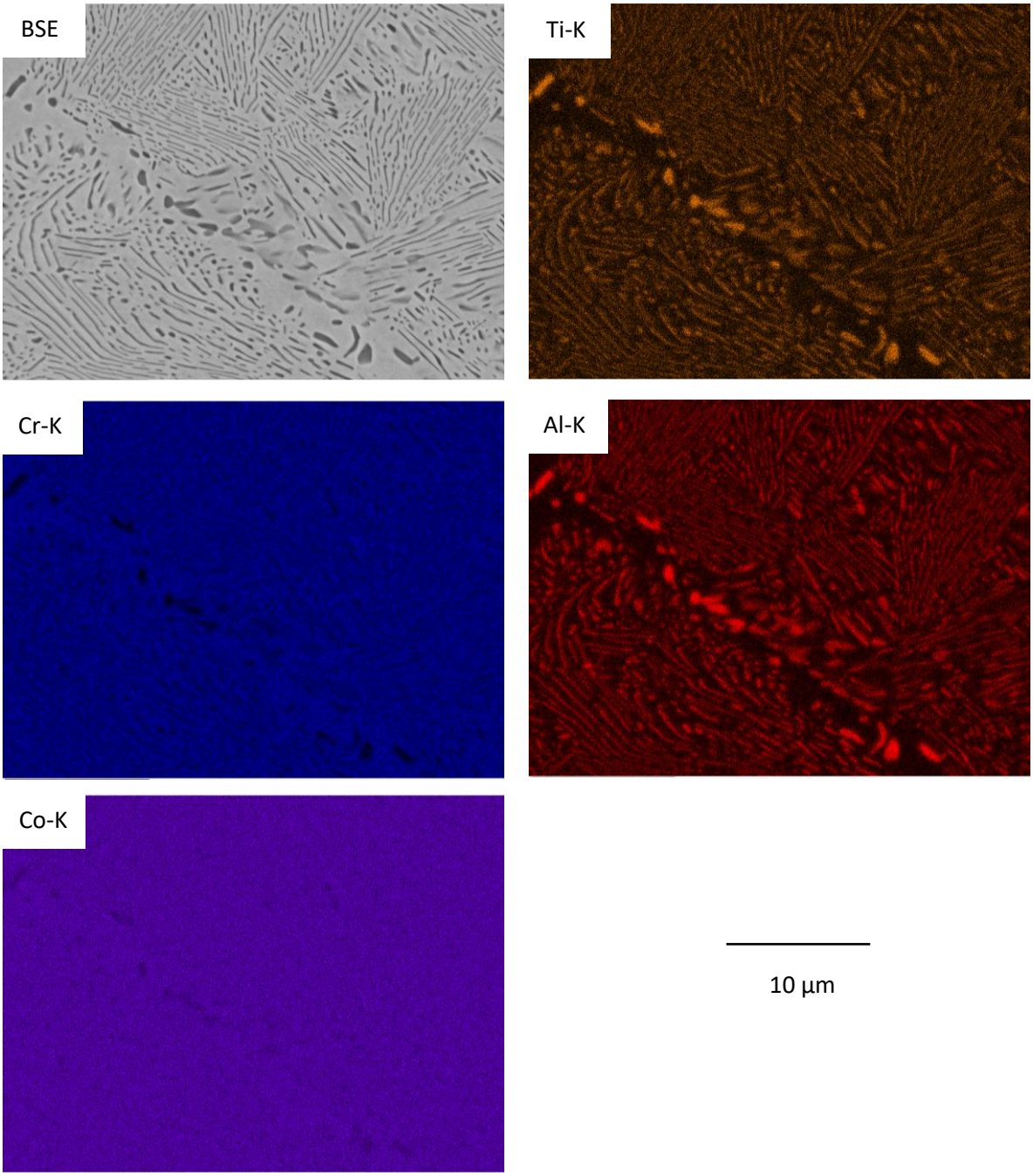

Figure 8.1. BSE micrograph of the Ni-free alloy Co-5Al-5Ti-15Cr (at.%) following ageing at 800°C for 1000 hours, together with corresponding EDS elemental concentration maps for Cr, Co, Ti and Al.

Figure 8.2a displays the atom probe reconstruction of the aged Co-5Al-5Ti-15Cr (at.%) alloy, showing the Cr, Al and Ti solute distributions. From Figure 8.2a, one phase appears rich in Ti and Al and the other appears rich in Cr. The corresponding proximity histograms (Figure 8.2b) permit an estimate of the elemental composition of each phase and these compositions are shown in Table 8.1.

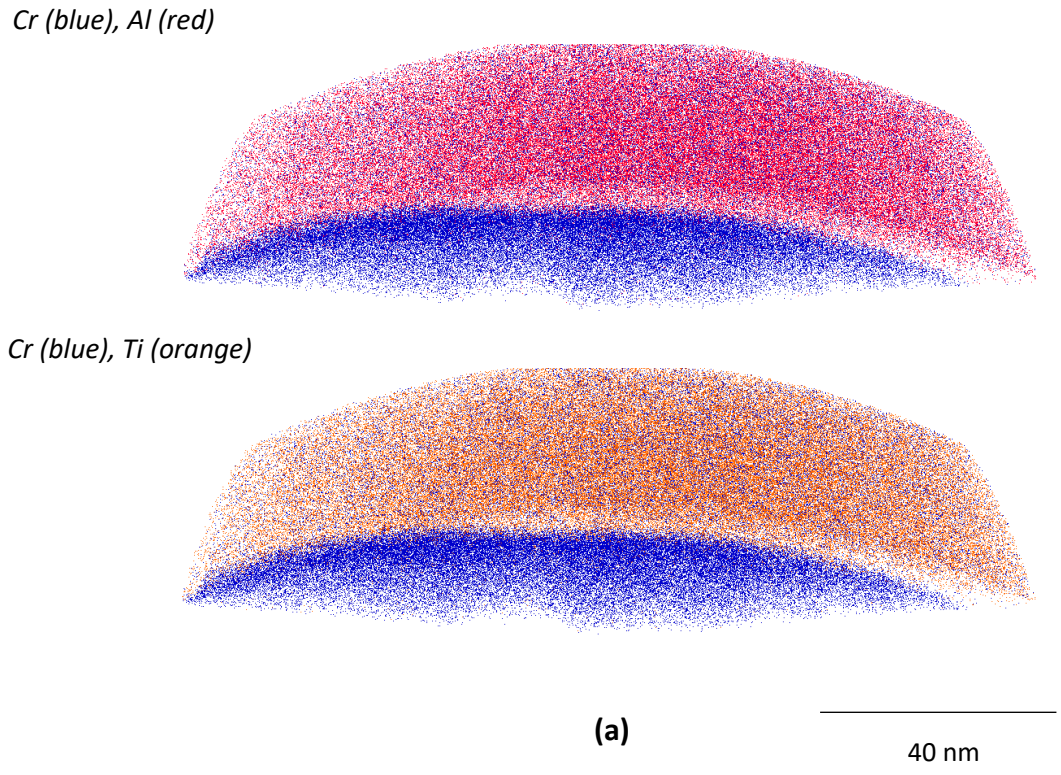

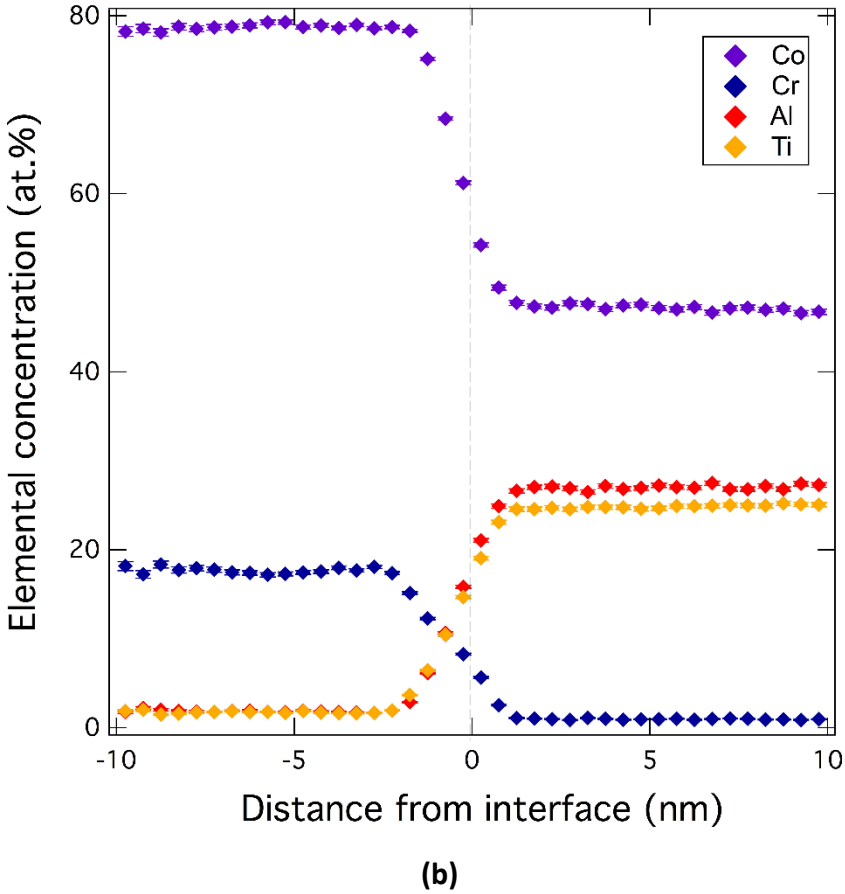

Figure 8.2. (a) Atom probe reconstruction of the volume analysed of the Ni-free alloy Co-5Al-5Ti-15Cr (at.%) aged at 800°C (1000 hours) showing Cr (blue), Al (red) and Ti (orange) ions; (b) Proximity histograms showing solute concentration profiles across the phase interface. Error bars have been included but are smaller than the symbols used.

Table 8.1. Average elemental compositions (at.%) of the two phases identified and their associated standard deviations in the Ni-free alloy Co-5Al-5Ti-15Cr (at.%) aged at 800°C (1000 hours), as obtained from the APT proximity histogram data.

Phase	Average composition (at.%)							
	Al	±σ	Ti	±σ	Cr	±σ	Co	±σ
Cr-rich	1.85	0.14	1.73	0.13	17.7	0.4	78.7	0.3
Al, Ti-rich	27.0	0.2	24.85	0.20	0.96	0.07	47.2	0.3

8.2 Atom probe reconstructions and proximity histograms of alloys aged at 800°C

Figures 8.3-8.7 show atom probe reconstructions and proximity histograms for five of the seven quinary alloys, Ni-Co-5Al-5Ti-15Cr (at.%), documented in Chapter 2 (9Co, 19Co, 28Co, 38Co and 47Co). As stated in Chapter 2, all five alloys were homogenised at 1250°C (24 hours) and then aged at 800°C for 1000 hours. Atom probe tomography was performed on the aged alloys at the Michigan Center for Materials Characterization in collaboration with the Marquis Research Group, Department of Materials Science and Engineering, University of Michigan.

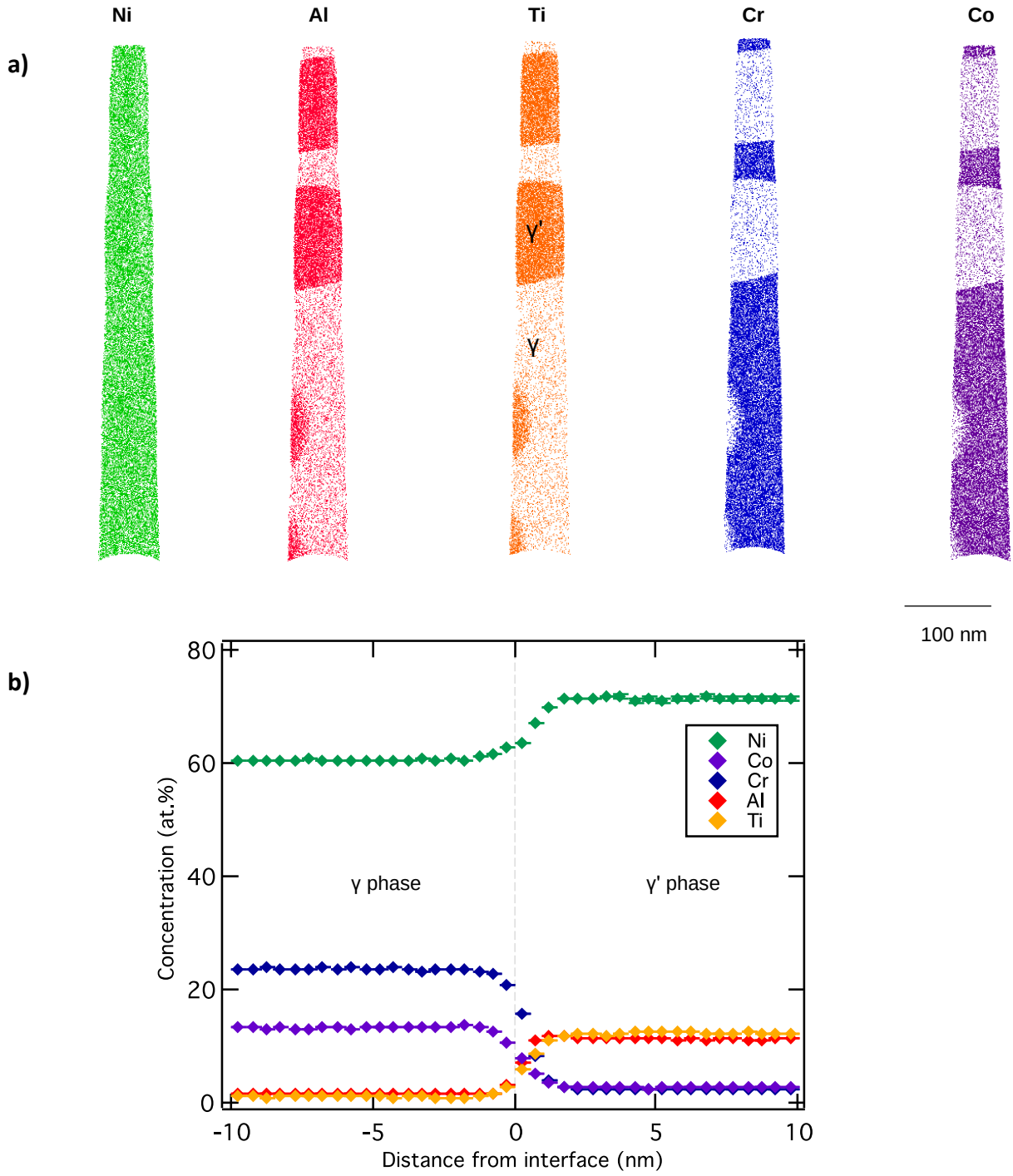

Figure 8.3. (a) Atom probe reconstructions of a 10 nm slice through the volume of aged **alloy 9Co**. To distinguish the γ phase from the γ' phase, only a fraction of the ions is shown for each element [0.5% of Ni ions (green), 5% of Al ions (red), 5% of Ti ions (orange), 2% of Cr ions (blue) and 3% of Co ions (purple)]. (b) Proximity histograms showing solute concentration profiles across the γ/γ' interface. Error bars have been included but are smaller than the symbols used.

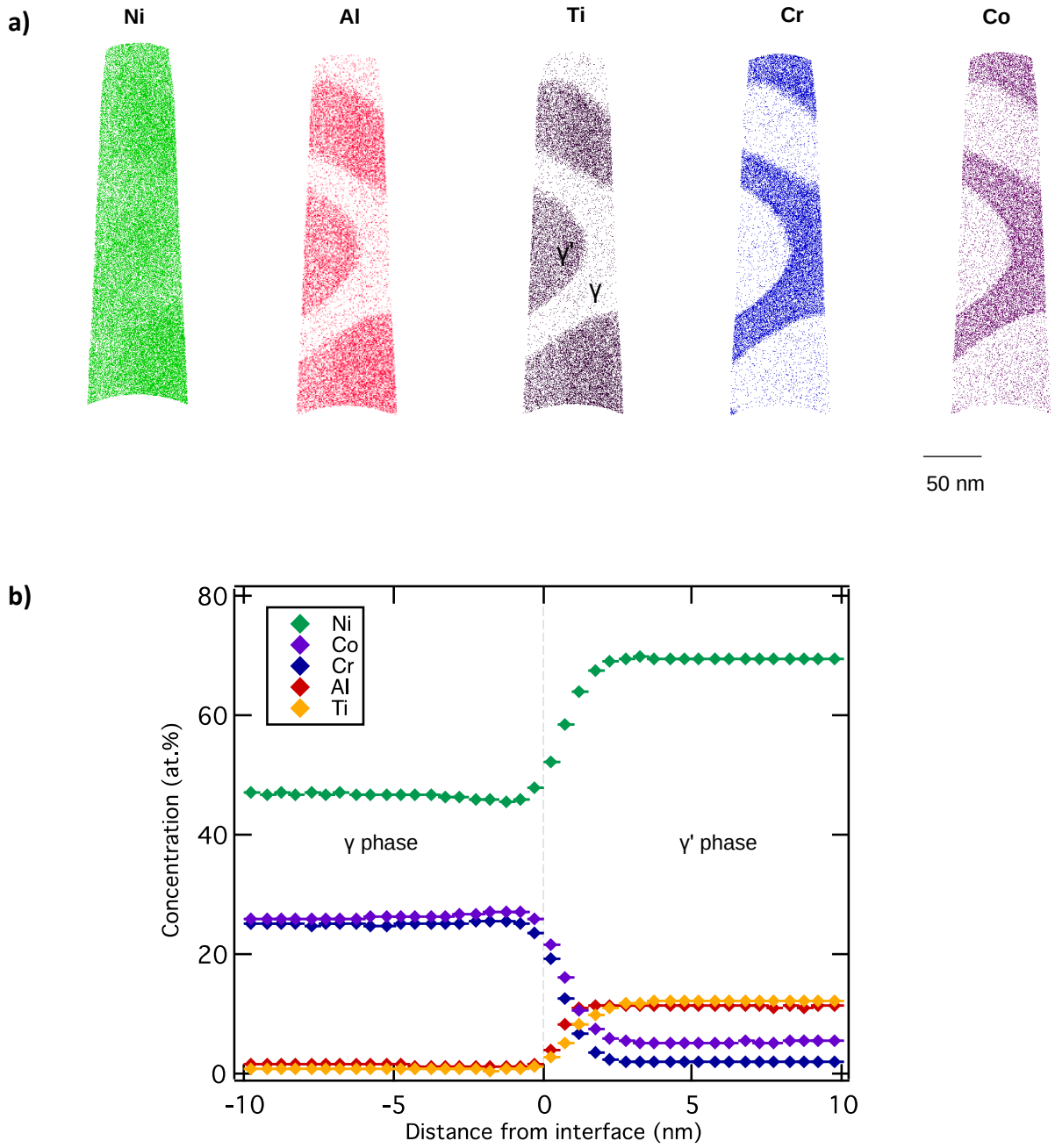

Figure 8.4. (a) Atom probe reconstructions of a 10 nm slice through the volume of aged **alloy 19Co**. To distinguish the γ phase from the γ' phase, only a fraction of the ions is shown for each element [1.5% of Ni ions (green), 5% of Al ions (red), 5% of Ti ions (black), 3% of Cr ions (blue) and 2% of Co ions (purple)]. (b) Proximity histograms showing solute concentration profiles across the γ/γ' interface. Error bars have been included but are smaller than the symbols used.

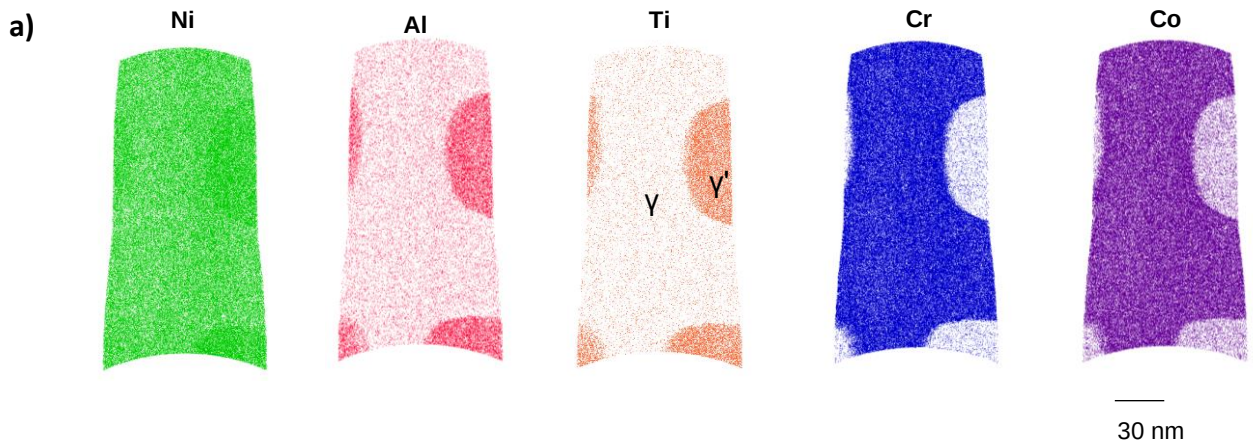

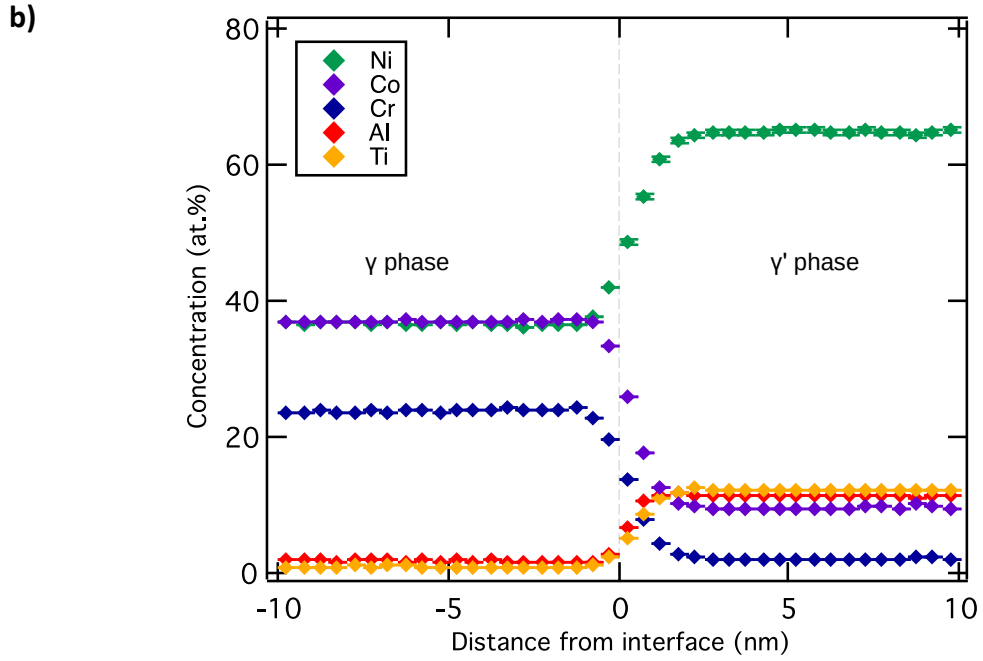

Figure 8.5. (a) Atom probe reconstructions of a 10 nm slice through the volume of aged **alloy 28Co**. To distinguish the γ phase from the γ' phase, only a fraction of the ions is shown for each element [7% of Ni ions (green), 20% of Al ions (red), 20% of Ti ions (orange), 20% of Cr ions (blue) and 10% of Co ions (purple)]. (b) Proximity histograms showing solute concentration profiles across the γ/γ' interface. Error bars have been included but are smaller than the symbols used.

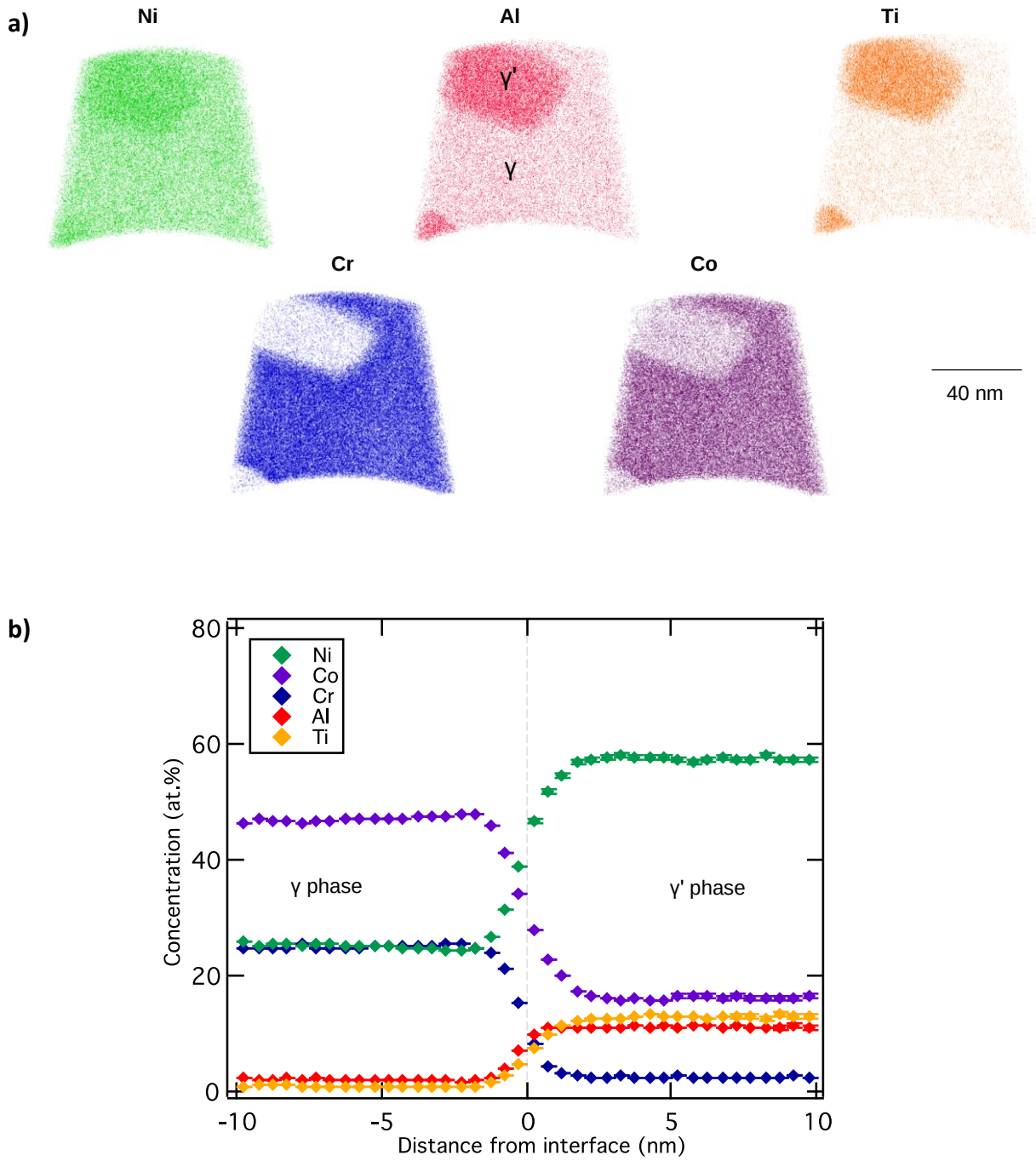

Figure 8.6. (a) Atom probe reconstructions of a 10 nm slice through the volume of aged **alloy 38Co**. To distinguish the γ phase from the γ' phase, only a fraction of the ions is shown for each element [10% of Ni ions (green), 50% of Al ions (red), 50% of Ti ions (orange), 30% of Cr ions (blue) and 10% of Co ions (purple)]. (b) Proximity histograms showing solute concentration profiles across the γ/γ' interface. Error bars have been included but are smaller than the symbols used.

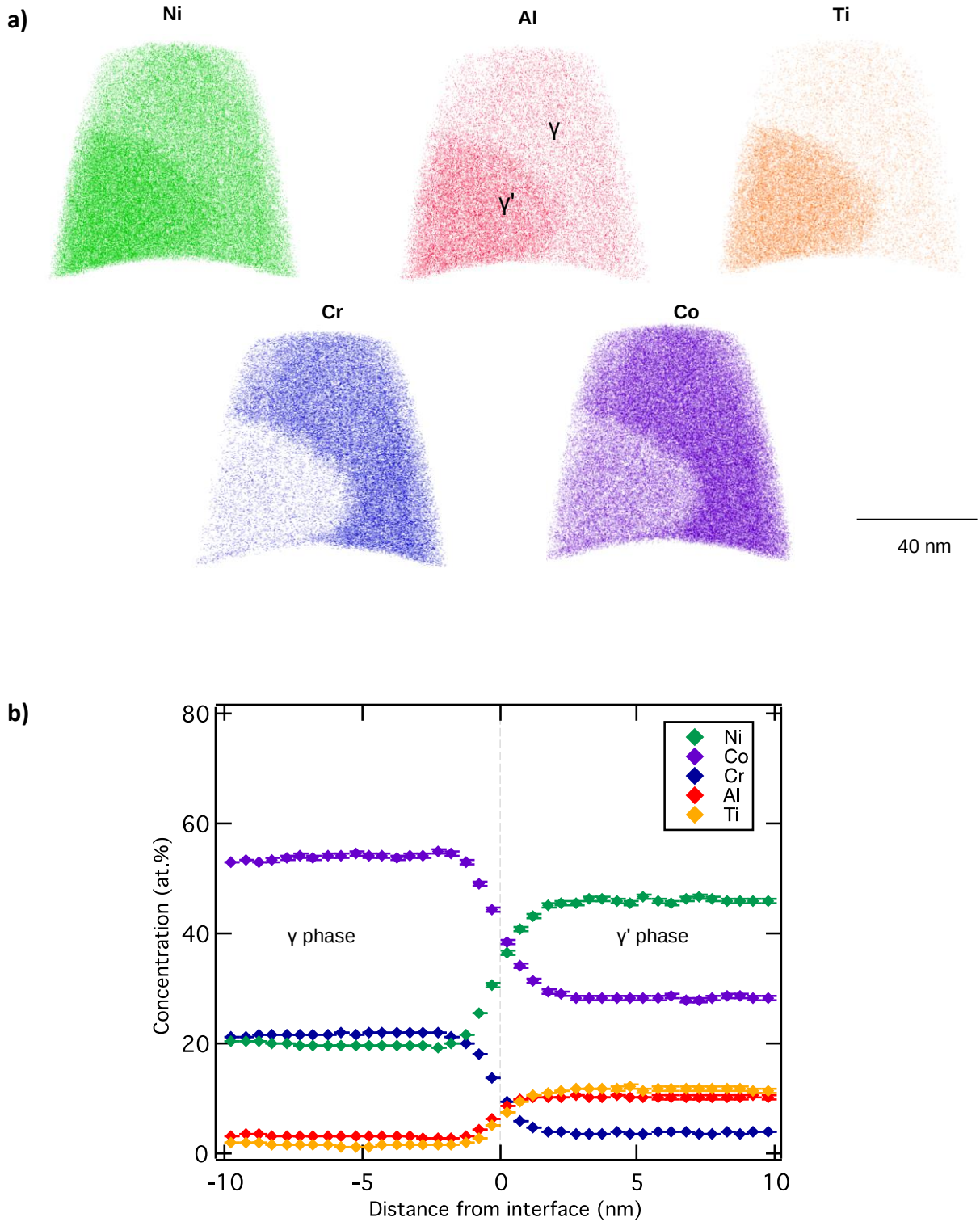

Figure 8.7. (a) Atom probe reconstructions of a 10 nm slice through the volume of aged **alloy 47Co**. To distinguish the γ phase from the γ' phase, only a fraction of the ions is shown for each element [30% of Ni ions (green), 50% of Al ions (red), 50% of Ti ions (orange), 30% of Cr ions (blue) and 20% of Co ions (purple)]. (b) Proximity histograms showing solute concentration profiles across the γ/γ' interface. Error bars have been included but are smaller than the symbols used.